The University Of Sheffield.

# Dynamics of Nonlinear Polariton Wavepackets and Pattern Formation in Microcavity Structures

Jasmin Kaur Chana

A thesis submitted for the degree of Doctor of Philosophy

Department of Physics and Astronomy

University of Sheffield
June 2016

# Abstract

Nonlinear wavepackets, such as solitons, are seen in many areas of physics. A promising medium where they could be used in both classical and quantum computational devices is the exciton-polariton system. Exciton-polaritons are quasi-particles consisting of strongly coupled excitons and photons. Polariton-polariton interactions result in a system with a high degree of nonlinearity.

In this thesis, the dynamics of nonlinear wavepackets and pattern formation in several microcavity structures are studied. Initially, the formation of a polariton condensate in a periodic potential induced by a Surface Acoustic Wave (SAW) is investigated, with a particular focus on the role played by phonons absorbed as polaritons scatter between certain states. This process can result in the formation of "gap solitons". It is further suggested that reflections of the SAW from features on the sample can contribute to pattern formation in the emission spot.

Later chapters focus on nonlinear wavepackets propagating with high momentum which could be used for the transmission of signals across a polaritonic chip. Patterns of bright dissipative polariton solitons are studied in planar microcavities. Arrays can be generated with solitons arranged either along or perpendicular to the propagation direction, with different localisation mechanisms employed in each case.

Finally, the dynamics of soliton-like wavepackets propagating through quasi one dimensional microwire structures are investigated. Measurements of the quantum properties of these nonlinear wavepackets reveal non-classical behaviour. Multi-peak patterns are observed as the excitation power is increased, accompanied by discontinuities in phase between the peaks for higher power cases. At high excitation powers, broadening of the energy spectrum is observed in a similar manner to the supercontinuum generation which has previously been seen in optical fibres.

# Publications

**Spatial Patterns of Dissipative Polariton Solitons in Semiconductor Microcavities**
J. K. Chana, M. Sich, F. Fras, A. V. Gorbach, D. V. Skryabin, E. Cancellieri, E. A. Cerda-Méndez, K. Biermann, R. Hey, P. V. Santos, M. S. Skolnick and D. N. Krizhanovskii
*Physical Review Letters*, **115**, 256401 (2015)

**Logic Gates with Bright Dissipative Polariton Solitons in Bragg Cavity Systems**
E. Cancellieri, J. K. Chana, M. Sich, D. N. Krizhanovskii, M. S. Skolnick and D. M. Whittaker
*Physical Review B*, **92**, 174528 (2015)

**Effects of Spin-Dependent Interactions on Polarization of Bright Polariton Solitons**
M. Sich, F. Fras, J. K. Chana, A. V. Gorbach, R. Hartley, D. V. Skryabin, S. S. Gavrilov, E. A. Cerda-Méndez, K. Biermann, R. Hey, P. V. Santos, M. S. Skolnick and D. N. Krizhanovskii
*Physical Review Letters*, **112**, 046403 (2014)

## Conference Presentations

**Exciton-Polariton Solitons in Quasi-1D Microwires**
J. K. Chana, M. Sich, E. Cancellieri, O. A. Egorov, D. N. Krizhanovskii, M. S. Skolnick
*Oral Presentation at UK Semiconductors 2015, Sheffield, UK*

**Bright Soliton Patterns in Semiconductor Microcavities**
J. K. Chana, M. Sich, F. Fras, E. Cancellieri, A. V. Gorbach, D. V. Skryabin, E. A. Cerda-Méndez, K. Biermann, R. Hey, P. V. Santos, M. S. Skolnick, D. N. Krizhanovskii
*Oral Presentation at PLMCN15, Montpellier, France (2014)*

**Bright Exciton-Polariton Solitons and Trains in Microwires**
J. K. Chana, M. Sich, F. Fras, E. Cancellieri, A. V. Gorbach, D. V. Skryabin, M. S. Skolnick, D. N. Krizhanovskii
*Oral Presentation at UK Semiconductors 2014, Sheffield, UK*

**Soliton-Soliton Interactions in Bright Polariton Soliton Trains**
M. Sich, F. Fras, J. K. Chana, A. V. Gorbach, D. V. Skryabin, E. A. Cerda-Méndez, K. Biermann, R. Hey, P. V. Santos, M. S. Skolnick, D. N. Krizhanovskii
*Poster presentation at OECS13, Rome, Italy (2013)*

**Phonon Assisted Polariton Parametric Scattering in Semiconductor Microcavities Subjected to Surface Acoustic Waves**
J. K. Chana, F. Fras, E. A. Cerda-Méndez, K. Biermann, R. Hey, P. V. Santos, M. S. Skolnick, D. N. Krizhanovskii
*Poster presentation at PLMCN14, Crete (2013)*
*Poster Presentation at UK Semiconductors 2013, Sheffield, UK*

# Acknowledgements

I would like to thank my supervisors, Dr Dmitry Krizhanovskii and Prof. Maurice Skolnick for giving me the opportunity to work on this research project, as well as for their guidance and support throughout. I would particularly like to thank Maksym Sich for all his help both in and out of the lab, from keeping the laser pulsing to insightful discussions about how best to interpret the experimental results. For teaching me all the experimental techniques I needed when I first started, I am grateful to the polariton group, especially Paul Walker, Lloyd Tinkler and Francois Fras. Working in the LDSD group has been both productive and enjoyable, so thank you all for making it such a friendly and supportive environment.

My thanks go to Chris Vickers, Pete Robinson and Phil Taylor for keeping the lab supplied with helium and for emergency cryostat repairs; also to Ed Clarke for growing the wafer and Ben Royall for fabricating the microwires on the sample used in my final experimental chapter; and of course to EPSRC for funding me during my PhD.

Much of the work presented in this thesis has benefited from the contributions of collaborators. I would like to thank Edgar Cerda-Mendez and Paulo Santos for the loan of their Surface Acoustic Wave sample and for fruitful discussions of my results. I am extremely grateful to Dmitry Skryabin and Andrey Gorbach for carrying out numerical simulations to support my results on patterns of dissipative solitons; and to Oleg Egorov whose simulations on wavepackets in microwires both supported my results and helped to guide the direction of the experimental work.

Thank you to all my friends and family for your patience while I disappeared into a lab and for all the good times when I came out of it. I would particularly like to thank my boyfriend Michael for being there for me throughout, for celebrating with me when things went well and keeping me going when there were problems. Finally, a huge thank you goes to my parents and brother for your unwavering support, not only during my PhD but also in all the years before it. Thank you for teaching me not to be bounded by the expectations of others and for always backing me, whichever direction I decided to take my life in. Knowing that you will always support me has given me the freedom to pursue my ambitions and get to where I am now.

# Contents


**1 Introduction** **13**

**2 Background** **15**

2.1 Microcavity Polaritons . . . 15
2.1.1 Nonlinearity and Polariton-Polariton Interactions . . . 18
2.1.2 Polaritons in Quasi-1D Cavities . . . 20
2.1.3 Polaritons in Periodic Potentials . . . 21
2.2 Polariton Condensates . . . 22
2.2.1 Parametric Scattering . . . 23
2.2.2 Experimental Observation . . . 24
2.2.3 Bistability . . . 25
2.2.4 Superfluidity and Vortices . . . 26
2.2.5 Condensates in Periodic Potentials . . . 29
2.3 Solitons . . . 31
2.3.1 Non-linear Media . . . 31
2.3.2 Temporal Optical Solitons . . . 33
2.3.3 Soliton Arrays . . . 35
2.3.4 Supercontinuum Generation . . . 37
2.3.5 Spatial Solitons in Planar Waveguides . . . 37
2.3.6 Matter-wave Solitons . . . 39
2.3.7 Dissipative Solitons . . . 40
2.4 Polariton Solitons . . . 40
2.4.1 Bright Solitons . . . 43
2.4.2 Dark Solitons . . . 46
2.4.3 Gap Solitons . . . 47
2.5 Quantum Effects . . . 48
2.5.1 Squeezed States . . . 49
2.5.2 Emission Statistics . . . 50
2.5.3 Pair Correlations . . . 52
2.6 Polaritonic Devices . . . 53

**3 Methods** **59**

3.1 Samples . . . 59
3.1.1 Sample for Surface Acoustic Wave Experiments . . . 59

3.1.2 Sample for Bright Dissipative Soliton Patterns . . . 60
3.1.3 Sample for Nonlinear Wavepackets in Microwires . . . 60
3.2 Sample cooling . . . 61
3.3 Optical Setups . . . 62
3.3.1 Transmission and Reflection configurations . . . 62
3.3.2 Continuous wave excitation . . . 64
3.3.3 Pulsed excitation . . . 65
3.3.4 Imaging Optics . . . 67
3.3.5 Two-dimensional imaging . . . 67
3.3.6 Detectors . . . 70
3.4 Measurement Techniques . . . 72
3.4.1 Hanbury Brown and Twiss . . . 72
3.4.2 Measurement of phase . . . 73
3.4.3 Measurement of $g^{(2)}$ using streak camera . . . 74

**4 Phonon-Assisted Scattering in Gap Soliton Formation 79**
4.1 Application of a SAW . . . 80
4.2 Intensity Correlations . . . 84
4.2.1 Measurements with a y-SAW . . . 84
4.2.2 Phonon assisted scattering . . . 85
4.2.3 Measurements of Interference with 2 SAWs . . . 87
4.2.4 Alternatives for S' state formation . . . 87
4.3 Additional Interference Patterns . . . 90
4.3.1 Observations . . . 90
4.3.2 Discussion . . . 92
4.3.3 SAW Reflection . . . 93
4.3.4 Further Discussion . . . 94
4.4 Conclusions . . . 97

**5 Formation of Soliton Patterns in a Dissipative System 99**
5.1 Setup . . . 100
5.2 Multi-peak Patterns Along X . . . 101
5.2.1 Soliton Trains . . . 101
5.2.2 Power Dependence of Peak Positions . . . 105
5.2.3 X-Arrays . . . 107
5.2.4 Nucleation of Arrays . . . 110
5.2.5 Nonlinear Wavepackets in Microwires . . . 111
5.3 Y-Arrays . . . 112
5.4 Discussion . . . 116
5.4.1 Soliton Separation . . . 116
5.4.2 Relationship of Pump and WB . . . 117
5.4.3 Mechanisms for Soliton Formation . . . 118
5.5 Conclusions . . . 119

**6 Nonlinear Wavepackets in Microwires** **121**
6.1 Sample characterisation . . . 122
6.2 Dynamics of Self-focussing Wavepackets . . . 123
6.2.1 Single mode . . . 125
6.2.2 Multi mode . . . 125
6.2.3 Excitation Conditions . . . 127
6.2.4 Dynamics of E-**k** profiles . . . 129
6.2.5 Secondary parametric scattering . . . 130
6.3 Wavepacket Arrays . . . 131
6.3.1 Array dynamics . . . 134
6.3.2 Continuum . . . 137
6.3.3 Wavepacket collision . . . 138
6.4 Phase profiles . . . 138
6.4.1 Temporal Evolution . . . 139
6.4.2 Power dependence . . . 142
6.4.3 Discussion of phase observations . . . 145
6.5 Quantum properties . . . 145
6.6 Nonlinear Wavepackets in Short Wires . . . 149
6.6.1 Dynamics of single wavepackets . . . 150
6.6.2 Wavepacket arrays . . . 154
6.6.3 Excitation conditions . . . 154
6.6.4 Femtosecond vs Picosecond Laser Pulses . . . 156
6.7 Planar cavities . . . 159
6.8 Polariton Interaction Coefficient . . . 161
6.9 Summary and Conclusions . . . 162
6.9.1 Conclusions . . . 163

**7 Conclusions** **165**
7.1 Future directions . . . 166
7.1.1 Quantum Properties in Microwires . . . 166
7.1.2 Polariton Polarisation in Microwires . . . 166
7.1.3 Dissipative Solitons in Microwires . . . 167
7.1.4 Continuous Wave Soliton Generation . . . 167
7.1.5 Dark Solitons in Microwires . . . 167

**A Fourier Transform Relations** **169**
A.1 Gaussian Wavepacket . . . 169
A.2 Multiple Peaks . . . 170

**B Simulations of Dissipative Soliton Patterns** **171**
B.1 Soliton Trains . . . 171
B.1.1 Numerical Model . . . 173
B.1.2 Nucleation of Arrays . . . 174
B.2 Y-arrays . . . 174

# Chapter 1

# Introduction

The wide-spread desire for increased computational power has led to a demand for ever-faster and smaller technological devices. Many of these devices make use of nonlinear behaviour. For example, rather than linearly amplifying an input signal, transistors used in logical electronic circuits switch "on" and "off" as the input crosses some threshold [1]. In analogue electronics, amplification stages often include some negative feedback to stabilise the output, effectively altering the degree of amplification of an input depending on the power at the output. In optical systems such as fibers, nonlinearities such as an intensity dependent refractive index can be used to stabilise the shape of a beam or pulse of light [2, 3, 4]. In systems with stronger nonlinearities, significant effects would be seen over shorter distances, so that smaller devices could be made.

The speed of a device depends both on the time it takes to carry out an operation and the time that elapses between operations while the device is reset. The time taken to carry out operations in some electronic components, such as transistors based on p-n junctions, is determined by the drift velocity of the electron and hole carriers when an electromagnetic field is applied. The response time of such components could be increased by using lighter carriers which can be accelerated more quickly, such as photons. However, the low nonlinearity of photonic systems is not ideal for making smaller devices. A compromise can be reached by using half-light, half-matter carriers such as exciton-polaritons [5]: these have a strong non-linearity due to interactions from their excitonic component while their low mass ($\sim 10^{-5}\ m_e$, where $m_e$ is the mass of an electron) allows for a fast response time.

Factors affecting the reset time of a device will vary depending on the nature of the device and the operations it performs. An example of a simple circuit could be a series of regularly spaced pulses propagating along some communication line to arrive at a detector: this could be used as a clocking device. Here, the "operation" would be the detection of a pulse while the "reset time" would be the spacing between pulses. In order to avoid detection errors, two neighbouring pulses must be resolvable so must maintain some separation. However, pulses propagating through a dispersive medium such as an optical fiber will tend to spread out, increasing the overlap between neighbouring pulses. Detection errors can be avoided by making sure the pulses are sufficiently separated at the start of the communication line so that they are still resolvable at the detector, but this limits the reset time of the device. A preferable solution would be to stabilise the wavepacket shape so that it does not spread

as it propagates, allowing a closer packing of pulses. These shape maintaining wavepackets are known as solitons and work is ongoing to study their dynamics in a variety of systems.

Certain computational problems, such as the factorisation of large numbers, could be made more efficient by exploiting quantum mechanical effects. While classical computers perform operations using "bits" which can take values of 0 or 1, quantum computers would use "qubits" which can exist in a 0 state, a 1 state or a superposition of the two. While the number of operations required to factorise a large number N using a classical computer increases exponentially, algorithms using quantum computing have been developed in which the number of operations only scales as a polynomial [6]. By utilising the superposition of the outcomes, complex problems may therefore be able to be solved more efficiently.

The 0 and 1 states can be mapped to those of any two level system. For example, the polarisation degree of freedom associated with polaritons could be used in a qubit, where right and left circular polarisations map onto the two states of the qubit. Practical qubits need to be initialised, manipulated during operations and their final state read out, all of which can be achieved optically in a polariton system. Interactions between a qubit and its surroundings should be minimised in order to maintain the coherence of the qubit during operations. While polaritons will interact with their surroundings, for example by scattering with phonons, these scattering rates are slow compared to the polariton-polariton interactions used in computing operations. This, coupled with the spontaneous appearance of coherence in macroscopically occupied polariton states, makes the polariton system a promising candidate for use in quantum computing applications.

In this thesis, I study the properties of nonlinear polariton wavepackets which may later be able to be implemented in classical computational devices. Some investigation is also made into the quantum properties of such wavepackets, demonstrating their potential for quantum computing applications. In Chapter 4, the parametric scattering mechanism for the formation of a polariton condensate in a periodic potential induced by a Surface Acoustic Wave (SAW) is investigated. The resulting macroscopically occupied states are known as "gap solitons" as they form within a bandgap induced by the periodic potential. The polariton population is spatially modulated into an array of condensates whose interactions can be tuned by varying the SAW amplitude: such a configuration could be used as an array of memory elements or bits with tunable interactions in a device.

Chapters 5 and 6 focus on nonlinear wavepackets propagating with high momentum which could be used for the transmission of signals across a polaritonic chip. Chapter 5 builds on previous observations of single bright dissipative polariton solitons [7], demonstrating the generation of soliton arrays [8]. The closely packed soliton peaks could be used in a clocking device with a 100 GHz repetition rate.

In Chapter 6, the dynamics of soliton-like wavepackets propagating through quasi-one-dimensional microwire structures are studied. Changes in behaviour with excitation conditions, such as the emergence of multi-peak patterns at high excitation powers, are also investigated. The wire structure could be more practical than a planar cavity (used in Chapter 5) for use in a polariton circuit as the wires could be used to route the signals around other devices on the chip where necessary. Measurements of the quantum properties of these nonlinear wavepackets reveal non-classical behaviour, suggesting the possibility of implementing these wavepackets in a quantum computational device.

# Chapter 2

# Background

## 2.1 Microcavity Polaritons

Polaritons are bosonic quasi-particles formed by the strong coupling of photons and excitons. Excitons are bound electron-hole pairs which can be generated by exciting an electron from the valence band to the conduction band in a semiconductor. This electron and the resulting hole in the valence band form a bound pair due to the Coulomb interaction between them. The energy required to excite an exciton can be provided by absorbing a photon whose energy is equal to the difference between the energy of the exciton and that of the electron in the valence band. The subsequent recombination of the electron and hole results in the emission of a photon.

The strong coupling of photons and excitons was first predicted by Pekar in 1957 [9] while the theory of polaritons in bulk semiconductors was further developed by Hopfield [10]. These three-dimensional polaritons have also been studied experimentally [11], although two-dimensional microcavity polaritons (described below) provide greater flexibility. For example, in a three-dimensional crystal, the exciton energy is defined by bandgap of the bulk material while in a two-dimensional quantum well, the exciton energy can be tuned by changing the width of the fabricated quantum well. In addition, polaritons propagating through a three-dimensional crystal will only couple to photons with the same energy and wavevector [12, 11] while in a two-dimensional system only the in-plane component of the wavevector needs to be matched.

Photons can be trapped in microcavities consisting of two Distributed Bragg Reflectors (DBRs) separated by a spacer layer (see figure 2.1). The DBRs consist of alternating layers of two materials with different refractive indices, such as GaAs and AlGaAs. At the boundary between each layer, a portion of the light will be reflected. The layers have an optical thickness of $\frac{\lambda}{4}$, where $\lambda$ is the wavelength of light, so that the light reflected from each boundary is in phase and will interfere constructively to give an overall strong reflection from the DBR stack. The DBRs are designed to reflect light with a particular wavelength $\lambda$ and if their separation is tuned to a multiple of $\frac{\lambda}{2}$, standing waves form within the cavity. By positioning quantum wells at the antinodes of this standing wave, an exciton trapped in one of the wells can couple to a photon confined in the cavity.

Figure 2.1 illustrates a typical energy-$k_x$ dispersion where the momentum along the in-

plane axis x is given by $\hbar k_x$. While the uncoupled exciton and photon modes will cross, as the coupling is increased new anti-crossing modes emerge. The splitting between the two resulting modes is known as the Rabi splitting; if this is larger than the linewidth of the exciton and photon bands, the system is said to be in the strong coupling regime. The new modes are the upper and lower polariton branches and were first observed by Weisbuch *et al* [12]. The DBRs have a reflectivity of less than 1, allowing some light to escape from the system to a detector.

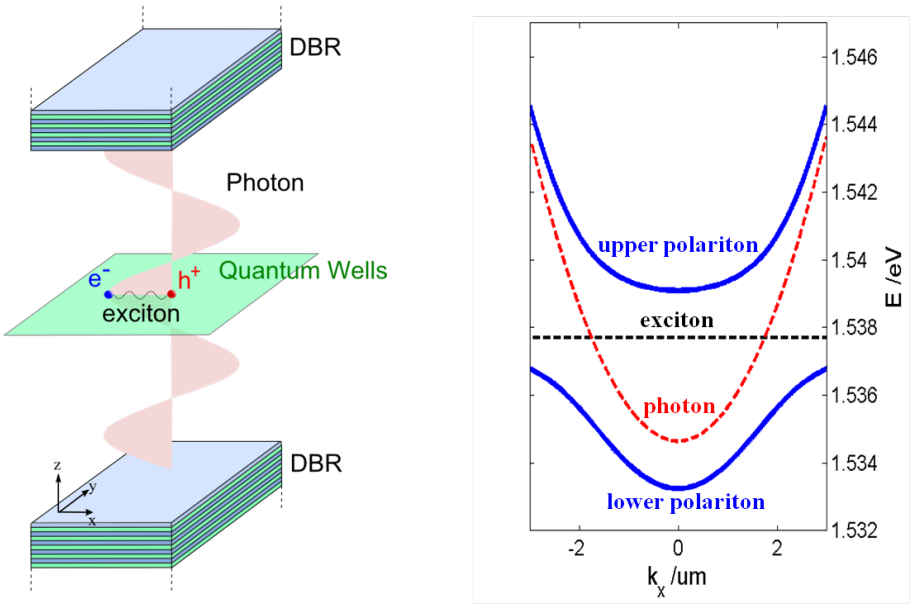


**Figure 2.1: Microcavity polaritons.** **(a)** Schematic of a microcavity with quantum wells positioned at an antinode. **(b)** Polariton dispersion. The dotted lines show the photonic and excitonic dispersions in the case of no coupling while the solid lines show the polariton dispersion arising in the strong coupling regime.

In addition to illustrating the relationship between the energy and k vector (and hence momentum), the E-**k** dispersion of a collection of particles can be used to extract other properties of the system. The velocity $v$ of propagating quasi-particles is proportional to the first derivative of the E-**k** dispersion

$$v(k_x) = \frac{2\pi}{h}\frac{dE}{dk_x} \tag{2.1}$$

as illustrated in Fig 2.2b. The change in velocity with k vector can be quantified by looking at the second derivative of the dispersion. This is related to the effective mass $m^*$ used to describe the polariton quasi-particles, which is given by

$$m^* = \frac{\hbar^2}{\frac{d^2E(k_x)}{dk_x^2}} \tag{2.2}$$

The curvature of the dispersion and the effective mass are shown as a function of k vector in Figure 2.2 (c,d).

Similar properties are used to describe wavepackets in photonic systems, such as optical

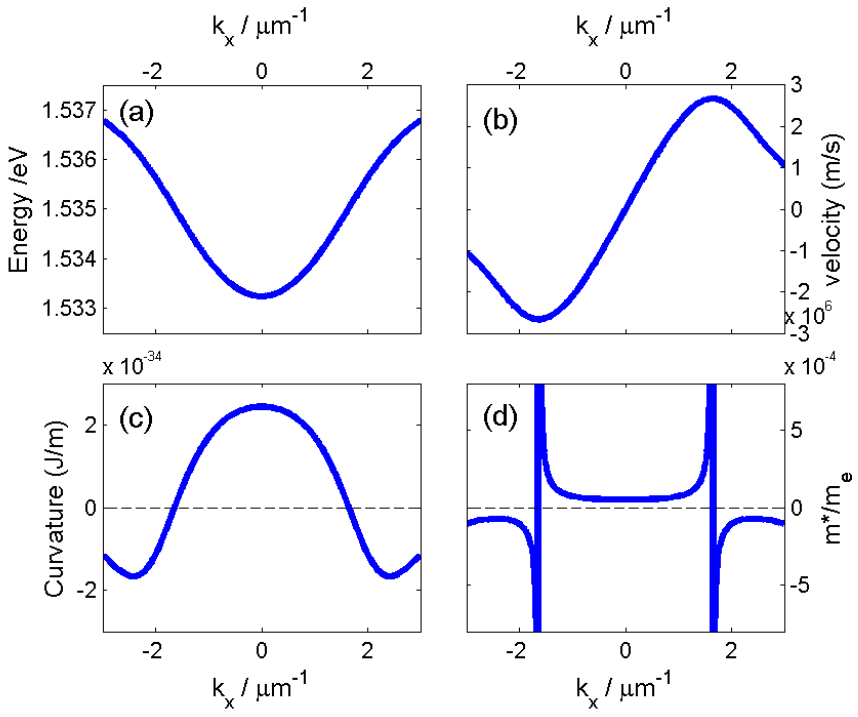


**Figure 2.2: Properties from dispersion (a)** Lower polariton branch energy as a function of $k_x$ ($E(k_x)$ dispersion). **(b)** Polariton velocity as a function of $k_x$, proportional to gradient of $E(k_x)$. **(c)** Curvature of $E(k_x)$ **(d)** Polariton effective mass as a function of $k_x$ in units of electronic mass $m_e$. This is inversely proportional to the curvature shown in (c). In (c,d), black dashed lines mark the zero curvature point.

fibers. Here, the group velocity $v_g$ is defined in terms of the parameter $\beta = n\omega/c$ as $v_g = (d\beta/d\omega)^{-1}$, where $n$ is the refractive index of the medium, $\omega$ is the optical frequency of the light and $c$ is the speed of light in a vacuum. The wavepacket can be broadened due to variations in $v_g$ around the frequency $\omega_0$ quantified by the Group Velocity Dispersion (GVD) parameter $\beta_2 = (d^2\beta/d\omega^2)_{\omega_0}$ [4]. Regions with a positive GVD parameter are described as having "normal dispersion" while those with a negative GVD parameter have "anomalous dispersion" [13]. Analogous definitions can be made in the polariton system, where regions of negative effective mass are described as having "normal dispersion" while those with positive effective mass are described as having "anomalous dispersion". The boundary between regions of anomalous dispersion and normal dispersion is known as the zero GVD point in optical systems and is referred to the point of inflection for polariton systems. At this point, the curvature of the dispersion (Figure 2.2c) goes to zero.

A splitting in energy between TE (no electric field in the z direction, perpendicular to the plane of the quantum wells) and TM (no magnetic field in the z direction) modes is often seen in microcavity systems [14]. This is due to differences in the boundary conditions for electric and magnetic fields at the DBR interfaces, so these fields penetrate into the DBR to different extents. The effective cavity length, and hence the confinement energy, is therefore different for the two modes, leading to an energy splitting which varies with in-plane momentum [15].

Polariton systems are now an active area of research [5]. They have been shown to exhibit phenomena including the formation of condensates with superfluid behaviour (§2.2), [16, 17] and soliton formation (§2.4, [18]). Pattern formation has been studied extensively, looking at systems such as vortex lattices in condensates [19, 20] and polarisation patterns [21]. Much of this work has been done on monolithic microcavities in GaAs based systems at cryogenic temperatures. Now, novel polariton systems are being developed, including semiconductor waveguides [22], tunable open microcavities [23, 24], and microcavities made from materials which can operate at room temperature such as ZnO [25], GaN [26] and organic polymers [27]. Progress is being made towards the development of polaritonic devices, exploiting the combination of properties including fast propagation, long-range coherence and control of the spin degree of freedom (§2.6).

### 2.1.1 Nonlinearity and Polariton-Polariton Interactions

Interactions between particles result in nonlinear behaviour: the higher the particle density, the stronger the interactions which modify the potential felt by the particles. In a polariton system, there are several contributions to polariton-polariton interactions, leading to nonlinearities. A polariton is a quasi-particle including an exciton (itself a quasi-particle consisting of a bound electron-hole pair), a photon, and their coupling interaction. Nonlinearities associated with these constituent parts, such as exciton-exciton scattering and saturation of the exciton-photon coupling (oscillator strength), are inherited by the polariton state resulting in a highly nonlinear system.

Polaritons interact strongly with each other due to their excitonic component. Excitons will scatter elastically due to Coulomb interactions. In addition to the classical dipole interaction, there are contributions from exchange interactions: a quantum mechanical effect

involving interactions between indistinguishable particles. For example, two particles $\alpha$ and $\beta$ can collide and be detected in separate positions A and B. For indistinguishable particles, there is no way of knowing whether the particle detected at A is $\alpha$ or $\beta$. Each outcome is described by a wavefunction and for indistinguishable outcomes, the wavefunctions interfere. For bosonic particles, they interfere constructively so that bosonic particles are likely to coalesce: this is known as bosonic stimulation. For fermionic particles, the wavefunctions interfere destructively so that the particles are never seen to meet, which looks like a repulsive interaction [28].

It has been found that exciton-exciton scattering is dominated by short-range electron-electron and hole-hole exchange interactions [29]. As it is the exchange of the fermionic particles which make up the exciton which contribute the most, the dominant interaction is repulsive. Studies of polaritonic systems reveal similar behaviour [30].

Interactions between polaritons are spin dependent: those with the same spin will strongly repel, but there can be a weak attraction between polaritons with opposite spin [31, 30]. In this work, polaritons are resonantly excited with circularly polarised photons which carry orbital angular momentum of $\pm 1$ for $\sigma\pm$ polarisation. This angular momentum is transferred to the polariton, so that polaritons excited with $\sigma\pm$ polarised photons have a pseudo-spin (total angular momentum) of $\pm 1$ [5].

In addition to the direct interactions described so far, polaritons can interact indirectly via dark exciton and biexciton states [30]. These indirect interactions can greatly modify the behaviour of the polariton system, for example it has been theoretically proposed that interactions involving high k vector components of the uncoupled exciton reservoir can lead to attraction between polaritons [32]. For the right conditions, the strength of this attraction is predicted to be comparable to the Coulomb repulsion normally felt by polaritons.

As mentioned above, exchange interactions between indistinguishable bosons mean it is favourable for these particles to coalesce. If a certain state is populated by bosons, bosonic stimulation increases the likelihood of more bosons being scattered into this state. The bosonic nature of polaritons means that stimulated scattering is a significant factor in polariton dynamics, provided that the density is high enough for the short-range boson exchange interactions to be significant [31].

If the polariton density is too high, the bosonic excitonic component undergoes a phase transition to a fermionic electron-hole plasma (at the Mott density) [33]. This occurs when the exciton wavefunctions overlap. As the system approaches this regime, the exciton population starts to saturate due to phase-space filling: the fermionic nature of electrons and holes limits the number of particles allowed in each state due to Pauli exclusion, reducing the number of carriers available to form excitons [34]. An additional effect is that the Coulomb interaction within a given exciton can be screened by the electron-hole plasma as well as other excitons, reducing the oscillator strength [35].

While there are many contributions to interactions between polaritons, exchange interactions perhaps have the most significant effect. There is interplay between the bosonic exchange interactions between polaritons and the fermionic exchange interactions between their constituent electrons and holes. These effects can be observed in the same experiments, for example a certain polariton state in E-k space can become macroscopically occupied due to bosonic stimulation, but the population may then spread out spatially due to repulsion

between the fermionic electron and hole components.

### 2.1.2 Polaritons in Quasi-1D Cavities

The planar microcavity structures described so far can be modified to make them quasi-one dimensional, confining the polaritons to mesas which are typically a few microns wide and $\geq 100$ μm long. This results in a quantised dispersion as illustrated in Figure 2.3. Polariton confinement can be achieved by etching through the cavity including the quantum wells [36] to confine both the photonic and excitonic modes, although just confining the photonic mode is sufficient, for example by etching through the top DBR only [37].

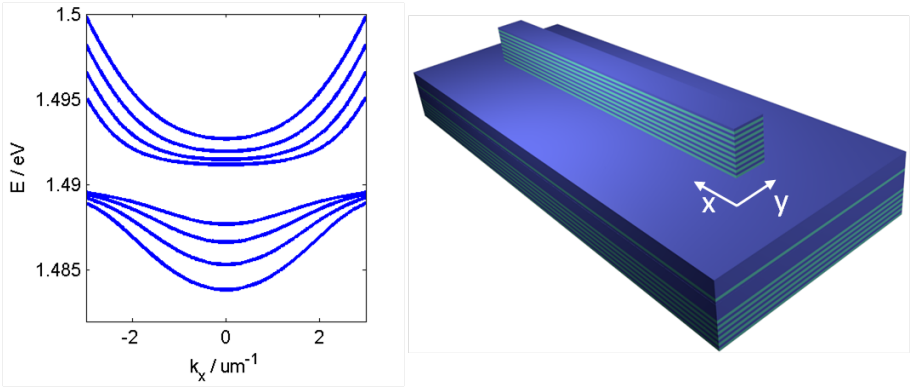


**Figure 2.3: Polaritons in microwires:** when confined in a quasi-one dimensional structure such as a microwire (right), quantisation results in several polariton modes (left).

At high excitation powers, macroscopically occupied states can be generated in a planar cavity via an Optical Parametric Oscillator (OPO) configuration, although phase matching requirements limit the states which can be populated in this manner: three states with equal separation in energy and momentum need to be available (see §2.2.1). In the quasi-1D system, the multi-mode structure of the dispersion opens up new scattering paths for the OPO process as scattering can occur between different modes of the lower polariton branch. Some paths are forbidden due to parity conservation constraints: the product of the final states must have even parity, matching the even parity of the product of two polaritons initialised in the same state [38]. Despite these constraints, new processes become available such as an energy degenerate OPO resulting in a pair of correlated beams with equal emission intensity [39].

#### Polarisation

For 1D wires [40], polarisation splitting can occur between modes polarised along (X) or across (Y) the wires. This arises from the different boundary conditions that apply to magnetic and electric fields crossing the interface between the wire and the vacuum. For X (Y) polarised modes, the main component of the electric field is along (across) the wire while the main component of the magnetic field is across (along) the wire. At the interface between the wire and the air, the normal component of the **D** and **B** fields as well as the parallel components of the **E** and **H** fields must be continuous. Here, **D** is the electric displacement, **E** is the applied electric field, **H** is the magnetic field strengh while **B** is the

magnetic flux density. Due to the different boundary conditions, Y polarised modes are better confined and so have higher energies than the X polarised modes whose main electric field penetrates out of the confined cavity.

### 2.1.3 Polaritons in Periodic Potentials

A spatially periodic system can be described as a lattice consisting of many repeats of a unit cell which are separated by a certain distance (the lattice vector). The reciprocal space (the wavevectors making up the pattern) will also have a periodic distribution made up of repeats of a reciprocal unit cell, known as the Brillouin zone. For polaritons subjected to a periodic potential, the Brillouin zone consists of the polariton spectrum for an unmodulated cavity as illustrated in Figure 2.4a. The repeats are separated by a reciprocal lattice vector, which in this case is the zone width in k space, which is equal to the k vector of the SAW ($k_{SAW}$).

The k space can be visualized in a "repeated zone" scheme covering multiple brillouin zones, where the lower polariton branches (LPBs) extend into neighbouring zones (used in Fig. 2.4). All the information is contained in a single repeat of this (from $-0.5 < k/k_{SAW} < 0.5$ in Fig. 2.4). This structure can alternatively be represented by a "reduced zone" scheme where only the first brillouin zone is shown (i.e. from $-0.5 < k/k_{SAW} < 0.5$ in Fig. 2.4). Here, the appearance of multiple branches can be described as the LPBs folding back on themselves as they cross the brillouin zone boundary. It can be seen that for each k vector, there are multiple lower polariton states coming from different branch repeats. As the amplitude of the applied periodic potential increases, energy gaps open up leading to anticrossing of the branches (Fig. 2.4, [41]).

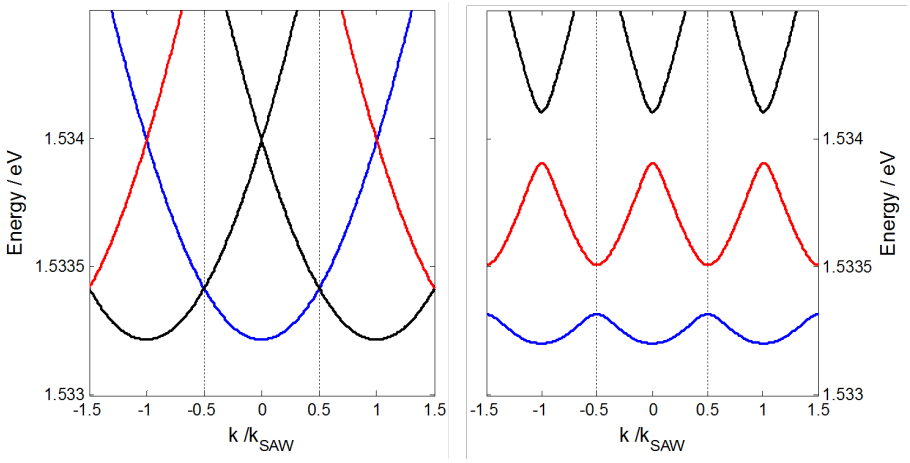


**Figure 2.4: Polariton dispersion in periodic potential:** in a periodic potential, the dispersion is constructed from repeats of the polariton spectrum centred at wavevectors separated by the lattice wavevector (a). As the amplitude of the periodic potential is increased, energy gaps open up so that the resulting branches anticross (b). All dispersion information can be found by looking at one brillouin zone of the k space (between the dashed lines). Here, 3 repeats are shown, looking at the first 3 branches.

**Experimental observation**

The polariton dispersion can be observed by looking at the far-field photo-luminescence at low pump power. The periodic dispersion consisting of Brillouin zones has been experimentally observed for static 1D potentials [42] as well as for dynamic potentials which are periodic in one [41] or two [43] dimensions.

The dynamic potentials cited here are generated using a surface acoustic wave (SAW), which modulates both the quantum well bandgap and the photonic cavity resonance (see §3.1.1). With one SAW, the periodic potential corresponds to a mini-brillouin zone (MBZ) of width $k_{SAW}$ resulting in folding of the dispersion at the edge of the MBZ [41]. The resulting branches of the dispersion anticross with energy gaps approximately equal to the peak-to-peak amplitude of the potential modulation. The low energy branches are flattened and redshifted compared to the case with no SAW. The flattening indicates localisation of the polaritons. The energy shift can be numerically reproduced by treating the SAW as a population of coherent phonons [44]. With 2 perpendicular SAWs, a square MBZ is generated [43]. The dispersion is detected along the diagonal of the square and is folded at edges separated by $\sqrt{2k_{SAW}}$.

## 2.2 Polariton Condensates

The concept of a Bose-Einstein Condensate (BEC) was first developed theoretically for non-interacting bosons, where the particles accumulate in the ground state of the system. The transition to a BEC can be thought of as the point where the wavefunctions of neighbouring particles overlap, which requires the particle separation to be smaller than the de Broglie wavelength $\lambda_{DB} = \sqrt{2\pi\hbar^2/mk_BT}$. The de Broglie wavelength drops as the particle mass increases, so lighter particles can form a condensate at lower densities.

In 3-dimensional systems, BECs can form as the chemical potential (energy change as more particles are added to the state) drops to zero at a finite temperature $T_{BEC}$ given by

$$T_{BEC} = \frac{2\pi\hbar^2}{mk_B}\left(\frac{\rho}{2.612}\right)^{\frac{2}{3}} \tag{2.3}$$

where $m$ is the particle mass, $\rho$ is the number density, $\hbar$ is Planck's constant divided by $2\pi$ and $k_B$ is Boltzmann's constant [16, 17].

It was found that the superfluid properties of liquid helium, which had been observed experimentally, qualitatively matched the predicted behaviour of a BEC when weak interactions were introduced between the bosons [45]. This motivated the generalisation of BEC theory to include interacting bosons, widening the definition of a BEC to include the macroscopic occupation of any single quantum state in equilibrium [46]. The transition to a BEC was found to be associated with the spontaneous appearance of long range order and coherence [47], something which is often considered sufficient evidence to claim the appearance of a condensate.

BECs were first generated experimentally in an atomic vapour of rubidium-87 in a 3-dimensional trap, where the temperature was reduced to below 170 nK [48]. Condensation should not occur at finite temperatures in an infinite 2-dimensional system as the chemical

potential diverges at low temperature, but for a finite system this has been observed in excitonic systems with spatially varying potentials [49, 50].

Polaritonic condensates are good candidates for use in devices (see §2.6) as they are relatively easy to excite. As polaritons are far lighter than atoms ($10^{-5}$ $m_e$ vs $10^4$ $m_e$, where $m_e$ is the mass of an electron), the critical density needed to make a polariton condensate is much lower and $T_{BEC}$ is higher. The density of a polariton condensate is limited as the excitons at high density will undergo a phase transition (Mott transition) to a fermionic electron-hole plasma [33]. Here, the strong coupling regime collapses so the polariton states are lost. The density for this phase transition is much higher than the critical density for polariton condensation [17]. As shown by equation 2.3, the low particle mass increases $T_{BEC}$, so that polariton condensates will form at a few Kelvin (K), making them accessible using standard cryogenic techniques. This is in contrast to atomic condensates, where laser cooling is required to reach μK temperatures. Polaritonic systems are also easier to observe experimentally as the properties of the light escaping from the microcavities map directly to those of the polaritons within the cavities, allowing direct detection.

BECs have attracted much interest as they exhibit quantum effects on a macroscopic scale. Their coherence properties make them good candidates for qubits for quantum computing [51]: they have superfluid-like properties, supporting persistent currents which would be useful for lossless signal propagation [52]; and they have recently been shown to support dark solitons in which a wavepacket of low density propagates across the high density condensate (see §2.4.2), whose shape-maintaining properties make them useful for signalling. Polariton condensates have the additional property of emitting coherent light with a well defined frequency and polarisation: a property shared with lasers [53].

### 2.2.1 Parametric Scattering

In several phenomena observed in the polariton system, including bright soliton formation and some observations of polariton condensates, states are populated by a parametric scattering mechanism (see Figure 2.5). In one scattering event, two particles in the "pump" state scatter into separate "signal" and "idler" states. If the polariton scattering to the idler state gains energy $\Delta E = \hbar\omega_{idler} - \hbar\omega_{pump}$ and momentum $\Delta p = \hbar k_{idler} - \hbar k_{pump}$, then the polariton scattering to the signal state must lose energy $\Delta E$ and momentum $\Delta p$ thereby conserving the total energy and momentum. Similarly, the total phase should also be conserved during the scattering event.

Scattering to a particular pair of signal and idler states can be enhanced by bosonic stimulated scattering, where the likelihood of a particle scattering into a given state increases if that state is already occupied (see §2.1.1). This can lead to macroscopic occupation of a single state, such as a polariton condensate [54, 55]. A particular pair of signal and idler states can therefore be selected by injecting a small population of polaritons into, for example, the signal state using a second laser (the probe). This stimulates scattering of polaritons from the pump state into the selected signal state while the related idler also becomes populated to conserve energy and momentum. This configuration is known as the Optical Parametric Amplifier (OPA) and has been demonstrated in a polariton system by Savvidis *et al* [56]. In this setup, two lasers were used: a strong pump beam with k vector

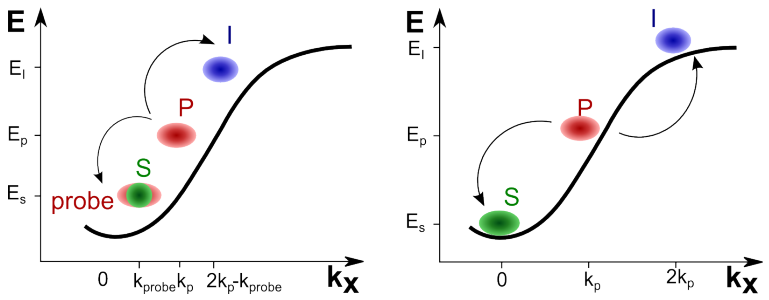


**Figure 2.5: Parametric Scattering Left: OPA configuration.** A high density of polaritons is injected in the pump (P) state. A low density of polaritons is injected by a second laser (probe): this stimulates the scattering of polaritons out of the pump state into signal (S) and idler (I) states, amplifying the probe signal. **Right: OPO configuration.** A high density of polaritons is injected in the pump (P) state near the point of inflection of the lower polariton branch. As polaritons accumulate at the bottom of the LPB, this spontaneously stimulates scattering into signal and idler states with no need for a probe laser.

$k_{pump}$ and a weak probe beam at $k_{probe} = 0$. The small population of polaritons at k=0 was amplified by nearly two orders of magnitude by the OPA process while the corresponding idler state at $k = 2k_{pump}$ also became macroscopically occupied.

It is also possible to generate signal and idler states with no probe; this is the Optical Parametric Oscillator (OPO) configuration [57, 58]. Polaritons are injected with a k vector $k_{pump}$ close to the point of inflection (see Figure 2.5b). Due to the curved shape of the lower polariton branch (LPB), states at k=0, $k_{pump}$ and $2k_{pump}$ which are equally spaced in energy are simultaneously resonant with the LPB. At high pump power, a parametric instability is triggered which results in occupation of the k=0 state, stimulating further scattering to this ground state (See §2.2.3). The OPO configuration can be more reliably realised by pumping at a slightly higher energy than the polariton dispersion [16]: as the population increases, the repulsive polariton-polariton interactions blueshift the LPB into resonance with the pump. While the signal and idler polaritons generated in a scattering event must have a fixed phase relative to each other, in general this is linked neither to the phase of the coherent pump laser nor the phase of signal-idler pairs from other scattering events. Observations of spatial and temporal coherence in the signal state are therefore attributed to a phase transition to a condensate-like phase [58].

### 2.2.2 Experimental Observation

The first experimental observation of a polariton condensate was made in 2006 by Kasprzak *et al* [59]. The system was pumped non-resonantly with a high energy laser, injecting polaritons incoherently into the system. Due to the short polariton lifetime, the reservoir did not reach thermal equilibrium with the host material as the interactions with phonons were slow. However, the polariton gas became internally thermalised due to fast polariton-polariton interactions.

For low excitation powers, the short polariton lifetime limits the number of scattering events with phonons so that few polaritons can relax to low k vectors and instead accumulate at the point of inflection in the LPB; this is known as the bottleneck effect [60]. With high excitation powers, polariton-polariton scattering dominates providing an alternative

relaxation path leading to suppression of this effect [61].

In the experiment [59], as the pump intensity was increased, the density of this thermalised incoherent polariton gas rose and the population of the ground state started to increase. Above a threshold intensity, the ground state population increased exponentially due to stimulated scattering (§2.1.1) and became macroscopically occupied. Both the temporal and spatial coherence of the system were found to increase above the threshold with the spatial coherence extending over the entire condensate. This emergence of long range coherence was taken to be one of the signatures of condensate formation. Below threshold, the system was unpolarized while above threshold the condensate showed a high degree of linear polarization, which could be understood as a macroscopic number of polaritons described by a single linearly polarised wavefunction.

Later experiments using non-resonantly injected polaritons have revealed behaviour such as long-range interactions resulting in the phase locking of spatially separated condensates [62] and pattern formation when several pump spots are used [63]. Wertz *et al* showed that when a condensate is formed in a tight pump spot, the strong Coulomb repulsion starts to eject polaritons from the spot [36]. These maintain their original energy but increase their k vector as they accelerate away from the high intensity pump: as the polariton density decreases, the lower polariton branch redshifts, bringing higher k vectors into resonance with the condensate energy. This change in resonant k vector depending on the spatial position enhances the polariton acceleration away from the pump spot.

Polaritons can also be resonantly injected by tuning the pump laser into quasi-resonance (i.e. slightly blueshifted) with part of the LPB. This can be used to inject a polariton fluid at the pump k vector [54, 55], or can be set up in an optical parametric oscillator (OPO) configuration where scattering from a pump around the point of inflection populates a condensate at around k=0 (see §2.2.1). There is historically some debate about whether such macroscopically occupied polariton states should actually be referred to as BEC as they are non-equilibrium systems. These states do however show many of the characteristics associated with BEC, such as long range coherence, and are commonly referred to as "polariton condensates" [17].

The effect of polariton-polariton interactions on the coherence of an OPO condensate was investigated by Krizhanovskii *et al* [64]. The energy of the condensate at a given real-space position depends on the polariton density at that position as the repulsive polariton-polariton interactions introduce an intensity-dependent blueshift. The local polariton density depends on the location within a non-uniform pump spot (which typically has a gaussian intensity profile in experiments) as well as defects on the sample. The resulting non-uniformity of the spatial profile inhibits spatial coherence and also reduces temporal coherence as it broadens the energy distribution. The coherence of the signal state is affected by polariton-polariton interactions in all 3 macroscopically occupied states (signal, idler and pump) as they are parametrically linked.

### 2.2.3 Bistability

It was shown by Baas *et al* [65] that bistability of the polariton density as a function of the pump power can exist in polariton systems. This behaviour was derived by drawing

an equivalence between the energy shift due to polariton-polariton interactions and the refractive index in an optical Kerr medium, which changes as a function of photon number (see §2.3.1). The evolution of the polariton population over time was investigated to find steady state solutions of the injected population density as the excitation power was varied. A plot of the polariton population as a function of excitation power revealed an S-shaped curve, so for some range of excitation powers both high density states and low density states were stable (see Fig 2.6a). The threshold of this bistable region was shown to depend on the angle of the exciting pump beam. This model describes the bistability of one macroscopically occupied state, in this case the pump state.

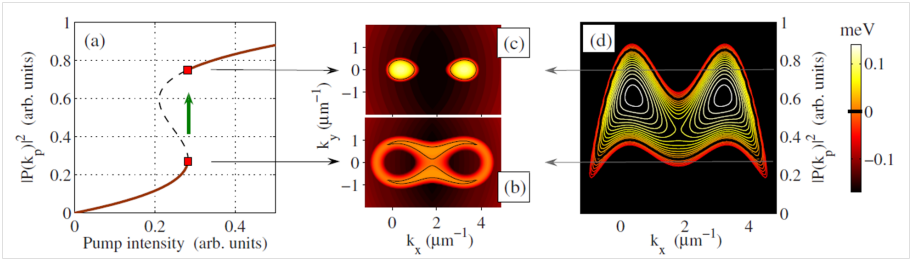


**Figure 2.6: Bistability and Gain Profile.** (a) Population of the pump state $|P(k_p)|$ as a function of applied pump intensity. Solid red lines indicate stable solutions while the black dashed line shows unstable solutions. (b,c) Polariton decay rate as a function of in-plane wavevectors $k_x$ and $k_y$ for two values of $|P(k_p)|$ indicated on (a). (d) Polariton decay rate as a function of in-plane wavevector $k_x$ and pump state population $|P(k_p)|$. Notably, yellow regions correspond to growth of the polariton population while red regions correspond to decay.
Reprinted Figure 4 with permission from [Krizhanovskii *et al*, Phys Rev B, **77**, 115336 (2008)]. Copyright (2008) by the American Physical Society

In addition to pump only bistability, the polariton system can exhibit parametric instability. The eigenenergies of the scattered polaritons have a real part describing the energy-k vector relationship and an imaginary part describing the polariton decay rate at different k-vectors (see Figure 2.6(b-d) for **k** and population dependence of the decay rate). When the pump state is in the upper branch of its bistability loop, the sign of the decay rate changes (i.e. there is gain) at k=0 and k=2$k_{pump}$. The sharp increase in the amplitude of the electromagnetic field in the microcavity triggers this parametric instability. The relationship between the decay rate and the pump population and k vector has been investigated in both one [66] and two [67] dimensions. The onset of the parametric scattering processes (OPA, OPO) described in §2.2.1 was found to be linked to the population of the pump state, and so to the pump-only bistability.

### 2.2.4 Superfluidity and Vortices

Superfluidity has been associated with Bose-Einstein condensation since the 1930s [68] and superfluid-like behaviour has now been observed in polariton condensates. Signatures of superfluidity, such as diffusionless motion and the frictionless flow past static defect obstacles, have been demonstrated by Amo *et al* [54]. Spectrally resolved measurements showed that the condensate maintained a well defined k vector as it propagated. This was in contrast to the low excitation case where Rayleigh scattering quickly resulted in a circle of occupied k states, thus demonstrating a suppression of scattering in the condensate regime.

Further observations were made of condensate wavepackets moving at high velocities ($\sim 10^6$ m s$^{-1}$) in a later paper [69] where a continuous wave pump injected polaritons at k $\sim 1$ μm$^{-1}$ while a pulsed trigger at a higher k vector was used to stimulate parametric scattering. This configuration, combined with nonlinear interactions, lead to the population of a linear dispersion rather than the parabolic lower polariton branch. It is noted that while this spectrum bears some resemblence to the Bogoliubov spectrum describing elementary excitations of a superfluid (see below), the observed spectrum has a different origin and describes the wavepacket itself, rather than only its excitations. On collisions with defects, these wavepackets again maintained a well defined k vector, indicating the suppression of scattering.

The relationship between the energy and momentum of excitations of a superfluid in equilibrium was studied theoretically by Bogoliubov [45]. The linear relationship between these quantities is now known as a "Bogoliubov spectrum", where the gradient is given by the speed of sound. For the non-equiblium polariton system, it has been found that the energy is independent of the k vector for low k vectors although the linear relation is recovered at high k vectors, approaching the Bogoliubov spectrum [70]. The spectra of excitations in polariton condensates have been studied and were found to be consistent with a Bogoliubov spectrum [71].

### Vortices

If a portion of a superfluid is given some angular momentum, this cannot be sustained over the whole superfluid region and instead remains localised in a vortex. A quantised vortex of order $m$ is a confined region carrying $m$ units of angular momentum while a closed path around the vortex gains a phase shift of $2m\pi$ ($m$ takes integer values). The particle density drops to zero at the centre of the vortex where the phase is singular, then rises to that of the superfluid background over a distance known as the healing length. The healing length can be found by equating the kinetic energy of the vortex with the potential energy in the superfluid.

Vortices in exciton-polariton condensates were first observed in a non-resonantly injected condensate by Lagoudakis *et al* [72] where they were detected by interfering condensate emission with a reference beam with homogeneous phase. A fork dislocation with $m$ arms was seen in the resulting fringes which was attributed to phase winding around the vortex core (see Fig 2.7). As expected theoretically, the emission had a dark spot at the position of the vortex whose radius was in good agreement with the healing length.

Vortices have also been investigated in condensates generated by an optical parametric oscillator (OPO) configuration (see §2.2.1) where the pump at k $\sim 1.5$ μm$^{-1}$ generated a macroscopically occupied state at k $\sim$0. A weak pulsed probe was then applied in resonance with the signal state to imprint some angular momentum and the resulting dynamics were monitored [52]. Vortices were again seen with a characteristic fork-like dislocation, which persisted for 70 times the duration of the triggering pulse, indicating a persistent current in the condensate characteristic of superfluid behaviour. It has been shown [73] that a vortex in the signal state can also be generated by imprinting an anti-vortex (vortex rotating in the opposite direction) in the idler state due to the conservation of angular momentum

requirement in the OPO scattering process. The dependence of the width of the vortex core on the superfluid healing length was also demonstrated.

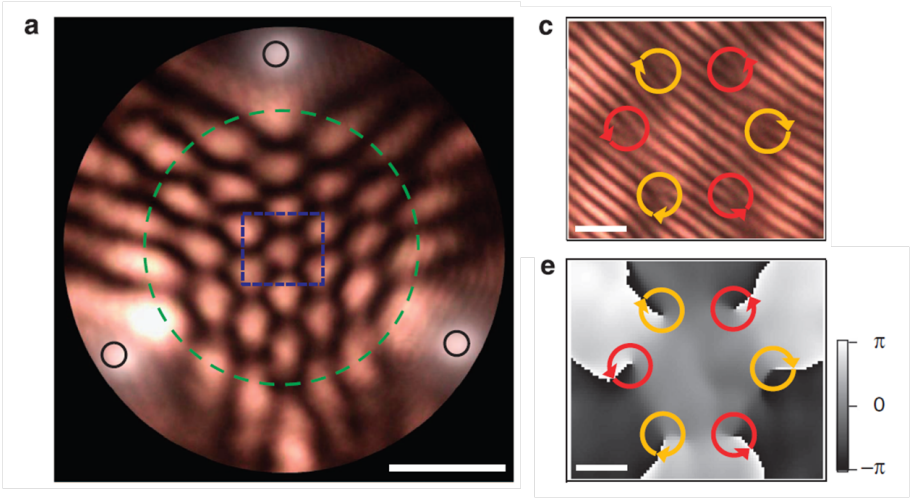


**Figure 2.7: Observation of vortices.(a)** Emission intensity distribution of a honeycomb vortex lattice. **(c)** Interference image of the region marked by the blue dashed rectangle in (a). Vortex (anti-vortex) positions revealed by fork-like dislocations in the fringe pattern are highlighted with red (yellow) circles. **(e)** Phase map of the region marked by the blue dashed rectangle in (a) showing winding of the phase around the vortex centres. Note that intensity minima in (a) correspond to the vortex positions extracted in (c,e).
Adapted by permission from Macmillan Publishers Ltd: Nature Communications [Tosi *et al*, Nature Commun., **3**, 1243 (2012)], copyright 2012.

Pattern formation has been investigated, initially by looking at the behaviour of bound pairs consisting of a vortex and an anti-vortex triggered by phase fluctuations across the inhomogeneous pump profile [74]. The formation of vortex lattices has also been studied, investigating the roles played by the shape of the pump spot [19] and the polariton-polariton interactions [20] in determining the shape of the lattice.

For superfluids which can support different polarisations, such as a polariton condensate, it is also possible to form half-vortices [75]. A closed path around a half vortex gains a phase shift of $m\pi$ as well as a polarization shift of $n\pi$, where $m$ and $n$ can take integer values. The spin degree of freedom in a polariton system makes it ideal for the investigation of more exotic polarisation patterns, such as skyrmions [76] and spin vortices [77].

In the experimental work of Amo *et al* [54, 69], polaritons were resonantly injected near the bottom of the lower polariton branch at a low in-plane k vector (k $\sim$0.5 $\mu m^{-1}$). Flow of a condensate generated in this configuration past a defect has been investigated theoretically by Pigeon *et al* [78] (see Fig 2.8). Propagating polaritons were excited by a continuous wave pump spot positioned close to a defect. By varying the flow rate compared to the speed of sound at the defect, the polariton fluid moved from a superfluid regime (low flow, no extra pattern forming around defect, Fig 2.8a) to one where vortices were generated in the wake of the defect (Fig 2.8b). By increasing the flow rate further, dark solitons were instead generated in the wake of the defect (Fig 2.8d), a phenomenon which was later observed experimentally [55] (§2.4.2).

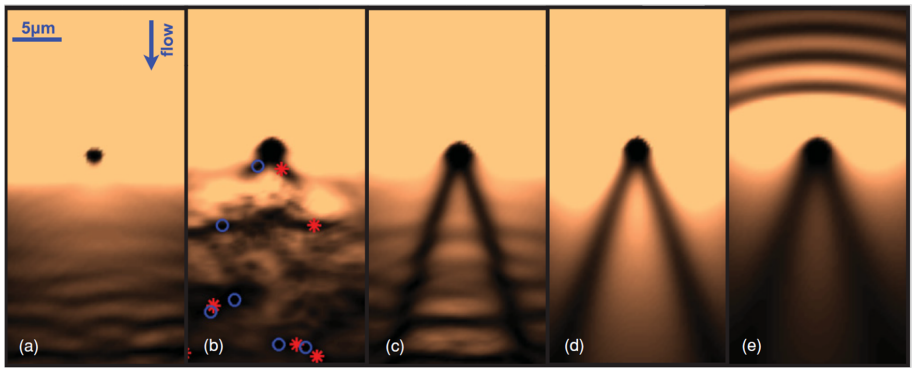


**Figure 2.8: Superfluid flow past a defect.** Normalised realspace intensity profiles. The ratio between the polariton flow rate and the speed of sound within the superfluid is increased between each panel. Effectively, the flow rate is lower than the speed of sound for panel **(a)** where the polariton fluid smoothly surrounds the defect. As the flow rate approaches the speed of sound, vortices form in the wake of the defect **(b)**. As the flow rate exceeds the speed of sound, dark solitons form in the wake of the defect **(d)**.
Reprinted Figure 1 with permission from [Pigeon *et al*, Phys Rev B, **83**, 144513 (2011)]. Copyright (2011) by the American Physical Society

### 2.2.5 Condensates in Periodic Potentials

There is currently interest in the properties of polariton condensates in tuneable periodic potentials as they provide a useful system in which to study coherent transport through an array of spatially separated condensates. The degree of coupling between the condensates can be controlled by varying the amplitude of the modulation in the potential.

#### Static potential

The static periodic case has been studied with potentials modulated in one [42] and two [79] dimensions. In both cases, the periodic potential is applied to the sample by patterning thin metallic films onto the sample surface. The condensate is spatially modulated with the period of the applied potential, separating into an array of condensate wires (for 1D modulation) or dots (for 2D modulation).

Imaging the far-field (k space) emission for the 1D case revealed an interference pattern arising from the array of wires: the visibility of this pattern demonstrated coherence between the condensate wires [42]. In the 2D case [79], the far-field images and simulations showed that condensates formed at different points on the Brillouin zone depending on the polariton density (see Fig 2.9a). This was attributed to the fact that different states have different associated symmetries. When the 2D periodic potential is applied, states with S, P and D symmetry are all available. As the excitation power is varied, the most energetically favourable state could change to one with a different symmetry (see Fig 2.9b,c) so that it was possible to select the desired k space emission pattern by tuning the pump power.

#### Dynamic potential

In experiments where the potential was generated with a surface acoustic wave (SAW, see §3.1.1), the potential at a given position on the sample changed dynamically as the SAW propagated across the sample. However, as the timescale over which the potential changed

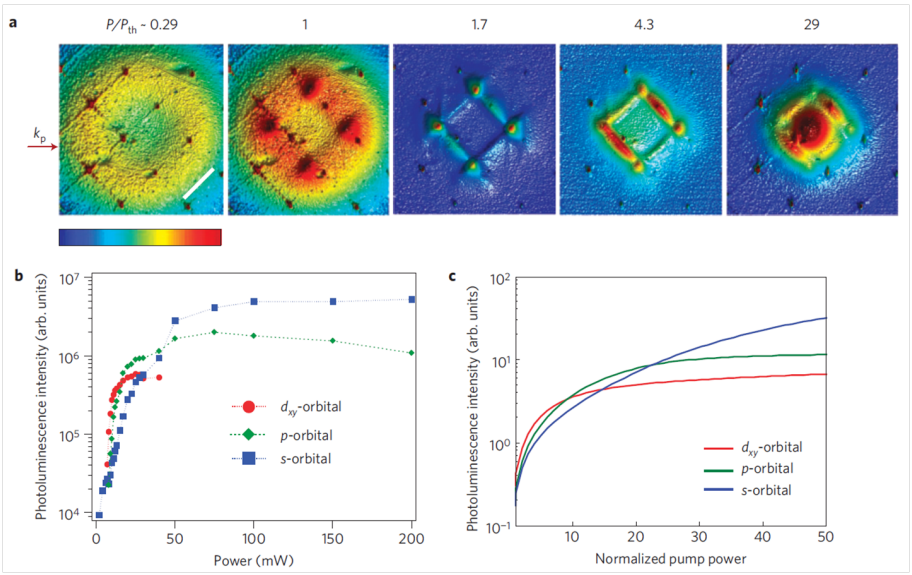


**Figure 2.9: Power dependence of k space intensity distribution, (a)** Emission intensity in reciprocal space for increasing excitation power, where $P_{th}$ is the condensation threshold power. **(b,c)** Experimental (b) and simulated (c) populations of orbitals with *s, p* and $d_{xy}$ symmetry as a function of pump power. As the relative populations of the different symmetry states change, the emission intensity distribution in (a) is also modified.
Adapted by permission from Macmillan Publishers Ltd: Nature Physics [Kim *et al*, Nature Phys., **9**, 681 (2011)], copyright 2011.

was long compared to the lifetime of the polaritons, they actually experience a quasi-static potential. Here, a condensate was generated using an OPO configuration (see §2.2.1)

Above the condensation threshold, the realspace modulation of the condensate observed in a static potential can be replicated in dynamic potentials with SAWs applied in one [41] or two [43] dimensions. However as the potential moves, the condensate lattice also moves across the sample so the realspace modulation cannot be directly observed in time integrated measurements. With one SAW, the condensate modulation was deduced by looking at the second order intensity autocorrelation function $g^{(2)}(\delta y, \delta t) = \langle I_{PL}(0,0), I_{PL}(\delta y, \delta t)\rangle$ of two spots separated by $\delta$y. Oscillations were seen in $g^{(2)}$ and as $\delta y$ was changed between 0 and $\lambda_{SAW}$, the phase of these oscillations at a given time varied between 0 and $2\pi$. The interpretation of these results was that the condensate wires were moved across the detection spots by the SAW with a velocity equal to that of the SAW. With 2D modulation, the two SAWs add to give a resultant wave propagating in one direction. The condensate dots moved with the wave, appearing as lines in a time integrated measurement. In some cases a dot lattice was seen in the time integrated measurement although it was unclear why this is visible.

With one SAW, the coherence between and along condensate wires has been extensively measured [80]. The coherence in both directions was found to decrease with increasing SAW power. The reduction in coherence between the wires was attributed to the decrease in tunnelling as the potential barriers are higher, while the reduction in coherence along the wires could be due to increased fluctuations as the dimensionality of the system is reduced from 2D to 1D.

With two large amplitude SAWs, the coherence between condensate dots can become very low. In a uniform potential, the density is fairly uniform across the condensate even if the exciting beam is gaussian as the repulsive polariton-polariton interactions redistribute the polaritons from high density to low density regions. In a uniform potential, the polaritons would be free to move within the 2D plane; with one SAW they can still move along a 1D line but with two SAWs they are confined in all three dimensions so the density profile of the condensate remains similar to that of the pump. Due to polariton-polariton interactions, the condensate energy is density dependent so neighbouring condensate dots have different energies. This limits the coherence length to the dot size. The transition from a uniform potential to this dot lattice has been investigated by gradually tuning the SAW amplitude [43]. Further work on this system has revealed the formation of gap solitons [81], which are further described in §2.4.3.

## 2.3 Solitons

Solitons are shape-maintaining wavepackets which are usually stabilised by some non-linear process. They can be found in nonlinear media, where the presence of the wavepacket modifies the medium, which in turn influences the wavepacket propagation (see §2.3.1). With the right conditions, this self action can compensate spreading induced by diffraction and dispersion, stabilising the wavepacket shape to form a soliton. Wavepacket propagation can be described theoretically by a Non-linear Schrödinger Equation (see §2.5). Shape-maintaining wavepackets can be found by looking for steady state solutions, which typically include plane waves and fundamental solitonic wavepackets with a $\text{sech}^2$ intensity profile. Higher order solutions can be found for high amplitude input waves: the width of these will tend to oscillate during propagation and they can split into several fundamental soliton modes (see §2.3.4). The Non-linear Schrödinger Equation can be modified to include perturbations such as losses to better investigate solitons in real systems [3].

Spatial solitons form when diffraction is exactly compensated by self-focussing due to the nonlinear refractive index (see §2.3.1). Similarly, when dispersive spreading is balanced by nonlinear effects, temporal solitons form [3]. These have been extensively studied in optical fibers (see §2.3.2) but have also been seen in matter systems, such as atomic Bose-Einstein condensates (see §2.3.6), and hybrid light-matter systems (see §2.4). The first recorded observation of a solitonic wave was a water wave seen by Russell in 1845 [82]. Since then, a variety of physical systems from strain waves propagating in geological rock formations [83] to bio-energy transport along protein molecules [84, 85] have been shown to exhibit solitonic behaviour.

### 2.3.1 Non-linear Media

Nonlinear optical effects are seen in media whose response (induced polarisation as a function of time, P(t)) to an electric field E(t) depends on higher orders of the polynomial expansion of the field (equation 2.4).

$$P(t) = \epsilon_0[\chi^{(1)}E(t) + \chi^{(2)}E^2(t) + \chi^{(3)}E^3(t) + ...] \tag{2.4}$$

where $\epsilon_0$ is the permittivity of free space, $\chi^{(n)}$ are the $n$th order terms of the susceptibility of the medium and $t$ is time.

The second order $\chi^{(2)}$ term gives rise to processes such as second harmonic generation and parametric amplification (see chapter 2 in Boyd [2] for more details). The third order $\chi^{(3)}$ term results in a contribution $n^{(2)}$ to the refractive index of the medium (n) which is proportional to the intensity of the applied field, so $n = n^{(0)} + n^{(2)}|E(t)|^2$ (see chapter 4 in [2]). This intensity dependent refractive index gives rise to self-action phenomena such as those described below. Media with a non-negligible $\chi^{(3)}$ are known as Kerr media while the dependence of their refractive index on the light intensity is known as the Kerr effect.

In optical fibers, the $\chi^{(3)}$ nonlinearity comes from the interaction of the electric field component of propagating light with the polarisable fiber medium [2]. This effect is small, giving typical values of $n^{(2)} \sim 10^{-20}$ $m^2W^{-1}$ [86]. While the Kerr effect normally refers to observations in optical media, analagous results are seen in other systems exhibiting a $\chi^{(3)}$-like nonlinearity. In weakly coupled microcavities such as Vertical Cavity Surface Emitting Lasers (VCSELs), the nonlinearity is stronger due to a contribution from photo-excited excitons in the quantum wells which interact with each other through Coulomb interactions [5]. Moving to a strongly coupled regime typically increases the nonlinearity by 2-3 orders of magnitude [87, 88, 89]. In polariton systems, the $\chi^{(3)}$ nonlinearity is dominated by interactions between polaritons and interactions with the uncoupled exciton reservoir (see §2.1.1). The result is a much stronger non-linearity of the order $n^{(2)} \sim 10^{-14}$ $m^2W^{-1}$ [89].

#### Self action

Self action refers to the effect on an object of a change in its environment caused by the presence of that object, such as a beam of light propagating through a medium with an intensity dependent refractive index. If the beam of light has a non-uniform spatial intensity profile, such as a gaussian, the refractive index change will vary across the wavefront. The resulting inhomogeneous medium acts as a lens and will focus or defocus a gaussian beam depending on the sign of $n^{(2)}$. Media with a positive $n^{(2)}$, such as optical fiber cores, will shrink the beam width and are said to have a focussing nonlinearity while media with a negative $n^{(2)}$ are said to be defocussing and will broaden the beam. A narrowing of the beam width due to the nonlinear refractive index is known as self-focussing [2].

#### Self-phase modulation

Self-action effects can also occur in the time domain for pulses of light. Here the light intensity, and hence the refractive index change, varies over the temporal duration of the pulse rather than over its spatial profile (see Figure 2.10). A consequence of this is self-phase moduation (SPM) [2], which results in the evolution of a frequency chirp across the pulse profile as explained below.

A photonic plane wave $\psi \propto e^{-i(kx-\omega t)}$ propagating through a medium with refractive index $n$ has phase

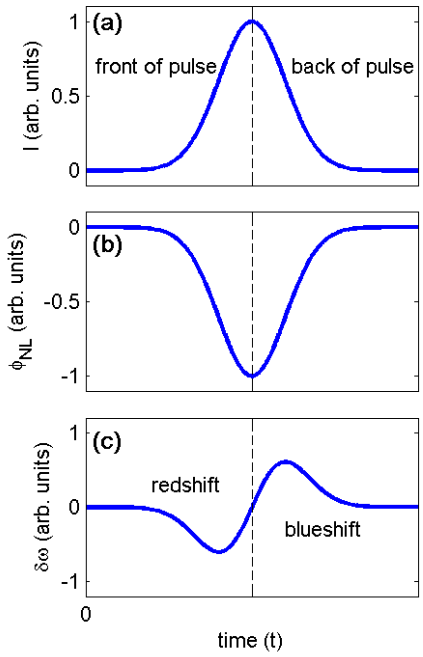


**Figure 2.10: Self-phase modulation. (a)** Gaussian intensity profile of a pulse of light **(b)** Phase $\phi_{NL}(t)$ of the pulse illustrated in (a) as it is transmitted through the medium. **(c)** Change in frequency across the pulse profile due to variations in $\phi_{NL}(t)$.

$$\begin{aligned}\phi(x,t) &= \omega t - kx \\ &= \omega t - n\omega x/c\end{aligned} \tag{2.5}$$

where $k$ is the wavevector of the light, $\omega$ is the frequency of oscillation ($= \partial\phi/\partial t$), and $c$ is the speed of light. A pulse of light has a phase term $\phi(t)$ with similar contributions, but properties such as the refractive index and frequency can now vary as a function of temporal position within the pulse. If the medium has an intensity dependant refractive index, $\phi(t)$ may include a nonlinear component $\phi_{NL}(t) \propto -n^{(2)}|E(t)|^2$. Note that in this case the phase profile will vary over the pulse duration as the field intensity $|E(t)|^2$ is not constant (see Figure 2.10). The frequency of light across the pulse can be described by $\omega(t) = \omega_0 + \delta\omega(t)$, where the change in frequency at a point $t$ in the pulse profile is given by the rate of change in $\phi_{NL}(t)$,

$$\delta\omega(t) = \frac{d}{dt}\phi_{NL} \tag{2.6}$$

As illustrated in Figure 2.10c, this redshifts the frequency at the start of the pulse and blueshifts the frequency at the end of the pulse.

### 2.3.2 Temporal Optical Solitons

Temporal optical solitons are found when the effects of self-phase modulation (SPM) and group velocity dispersion (GVD) exactly cancel out. GVD describes the frequency depen-

dence of the group propagation velocity and is proportional to the second derivative of the E-k spectrum (see Fig 2.2 in §2.1). Self-phase modulation (SPM) results in the evolution of a frequency chirp due to the varying intensity profile over a wavepacket [2] (see §2.3.1 for more details). For an optical fiber with anomalous dispersion, the group propagation velocity increases with frequency so that light at the end of the pulse which has been blueshifted by the SPM starts to catch up with the light at the start of the pulse which has been redshifted by the SPM. If the blue light approaches the leading edge of the pulse, it will in turn be redshifted by the SPM and subsequently slowed down by the GVD. The interplay between GVD and SPM therefore stabilises the shape of the wavepacket to form a soliton.

Temporal optical solitons have been generated in optical fibers at wavelengths suitable for telecommunciations ($\sim$ 1.5 μm) as early as 1980 [90] and their use in communications applications has continued to be investigated [91]. Modification of the fiber dispersion, for example by patterning air holes into the cladding to make a photonic crystal fiber [92] or tapering the fiber [93], enables the excitation of solitons at visible wavelengths.

Optical fibers have spectral regions with normal dispersion and regions with anomalous dispersion (see §2.1). Exciting solitons near the boundary between these regions can result in some interesting behaviour. The evolution of the wavepacket as it propagates is described by the E-**k** dispersion and its derivatives in the same way as for a polaritonic system (see Fig 2.2). In most cases, the first derivative (describing group velocity) and second derivative (related to GVD, see §2.1) will dominate the response and higher order terms can be neglected. However at the zero GVD point, the second derivative falls to zero and for a spectrally broad pulse, the higher order terms can contribute significantly. A similar situation arises in the polariton system and has been investigated theoretically by Egorov *et al* [94] (see Figure 2.11),

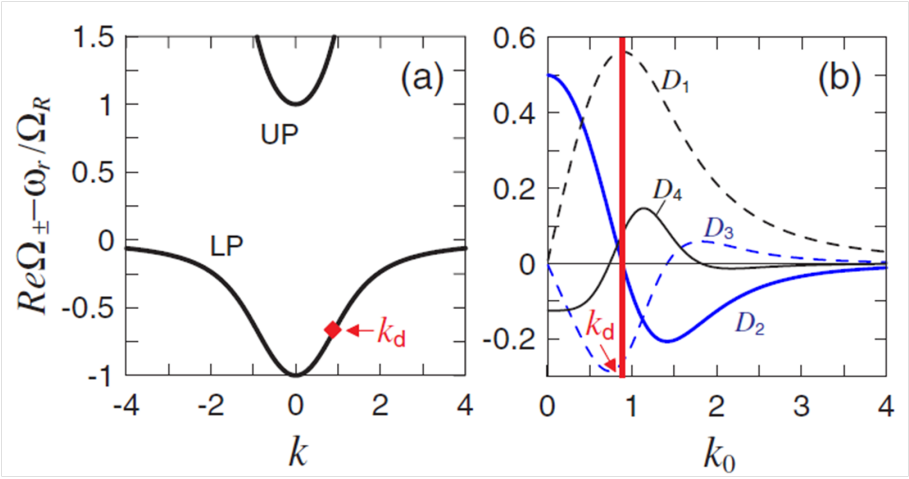


**Figure 2.11: Contribution of terms to the polariton dispersion. (a)** Polariton dispersion. Here, $k$ is the in-plane polariton wavevector, $\Omega_\pm$ are the upper and lower polariton frequencies, $\omega_r$ is the resonant frequency of both the exciton and the photon, $\Omega_r$ is the Rabi frequency and $k_d$ marks the point of inflection were $D_2$ vanishes. **(b)** Coefficients $D_n \propto \partial_k^n \Omega_-|_{k_0}$ of the nth order contributions to the lower polariton branch dispersion as a function of wavevector $k_0$. There is a significant contribution from higher order terms $D_3$ and $D_4$.
Reprinted Figure 1 with permission from [Egorov *et al*, Phys Rev Lett, **102**, 153904 (2009)]. Copyright (2009) by the American Physical Society

It has been found [95, 96] that perturbations from the third order term result in radiation from solitons, which appears at a specific frequency in the normally dispersive region and therefore corresponds to a dispersive wavepacket. However, the central frequency of the combined soliton and wavepacket is expected to be conserved, so as the dispersive wavepacket is generated in the normally dispersive region, the soliton is shifted further into the anomalous region. As the soliton spectrum moves away from that of its radiation, the amplitude of the radiation drops and the soliton frequency becomes stabilised.

Another effect which can alter the soliton frequency is a Raman interaction with the glass of the fiber medium [3]. Here, photons from the high frequency side of the soliton spectrum are converted to photons with lower frequency as some of their energy is absorbed by the fiber. If the spectrum is broad enough that there is already light at this lower frequency, stimulated Raman scattering results in a transfer of energy to the lower energy states, so that the soliton spectrum becomes centred at a lower frequency [93]. These high order effects becomes more dominant for shorter pulses (∼50 fs) where the fiber dispersion varies more within the spectral width of the pulse.

### 2.3.3 Soliton Arrays

Spatial (temporal) optical solitons will form in a beam (pulse) at a certain power $P_{sol}$ when diffraction (dispersion) is exactly compensated by a power dependent refractive index. Theoretically, a soliton with power $P_{sol}$ is a solution to the nonlinear Schrödinger equation (NLSE), but higher order solutions can also be found for powers much larger than $P_{sol}$ [2]. These can take the form of periodic multi-peak structures where adjacent peaks can have a relative phase difference of $\pi$ [97]. If the power is much larger than $P_{sol}$, the beam (pulse) can break up into several filaments each containing an optical power of $P_{sol}$ [2].

Perturbations in the system can split up this multi-peak solution into several fundamental solitons containing power $P_{sol}$. Studies of temporal solitons have shown that these individual solitons may be centred at different frequencies [98] (more detail on the causes of the frequency shift is given in §2.3.2). Similar beam break-up has been observed in a continuous wave regime where a central bright peak separated into multiple peaks, generating a regular honeycomb pattern [99]. While the authors made no claim that these peaks were solitons, they were found to exhibit soliton-like behaviour.

In addition to considering the multipeak structure of high power solutions to the NLSE, there has been interest in studying the interactions between individual solitons which are brought close together. These arrays with an arbitrary soliton separation are not necessarily exact solutions of the NLSE even though their constituent elements are [3]. There was strong motivation for these studies from an applications point of view: using solitons for the transmission of data enables a higher repetition rate as neighbouring wavepackets will not spread out and interfere during propagation, unlike dispersive wavepackets. However, interactions between neighbouring solitons which change their separation could introduce errors in reading out the data stream if they are not considered [3].

This problem was investigated theoretically for the case of two temporal optical solitons [100]. It was found that the solitons appeared to pass through one another although they were also found to interact when their wavefunctions overlap. Solitons injected with similar

amplitudes and the same phase were found to attract one another but rather than coalescing into a single peak, they would move together and apart in an oscillatory motion; it was noted that this attraction corresponds to an unstable solution. If the solitons were $\pi$ out of phase with one another, they would repel and gradually move apart. These interactions are illustrated in Figure 2.12, showing a simulation taken from [101]. The strength of the interaction decreased exponentially with separation.

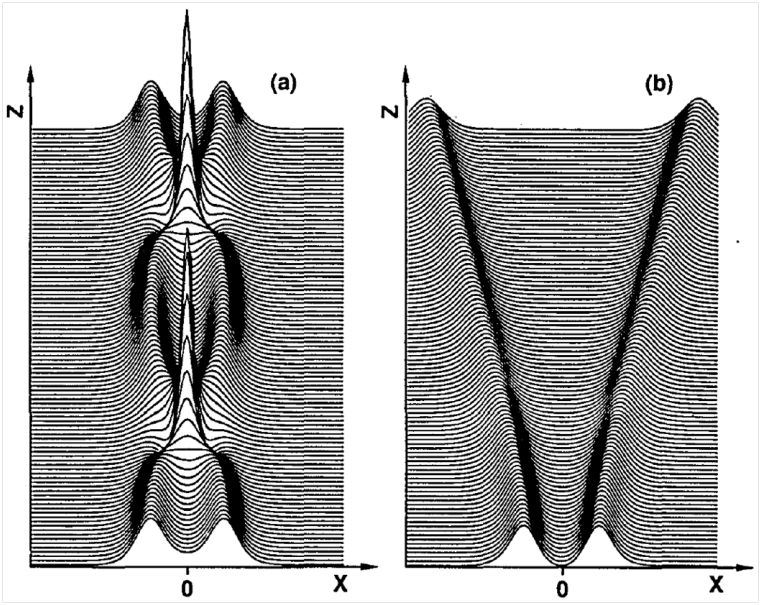


**Figure 2.12: Soliton-soliton interactions.** This simulation shows the spatial intensity profile across a pair of fundamental solitons as they propagate along z. The solitons in (a) have a relative phase of zero while those in (b) have a relative phase of $\pi$.
Reprinted with permission from the Optical Society of America from [Aitchison *et al*, Optics Letters, **16**, 15 (1991)]

Interactions between temporal soliton pairs were investigated experimentally in optical fibers a few years later [102], reproducing the predicted repulsion between solitons with opposing phases. Separated solitons with identical phases were found to attract one another, although the predicted oscillation in separation as the solitons met was not reproduced. Instead, the interactions between solitons with identical phases were found to change from attractive to repulsive once their paths crossed. This was attributed to a shift in the relative phase caused as the wavefunction of one soliton acted as a perturbation on the second, enhanced by the predicted instability of the identical phase state. Phase dependent soliton-soliton interactions have also been seen for spatial optical solitons [101]. By tuning the relative phase between two spatial solitons propagating side by side to $\pi/2$, it has also been shown that energy can be transferred from one to the other [103].

Soliton arrays have also been observed experimentally in atomic condensates [104], where repulsive interactions between the solitons were observed despite the fact that interactions between the atoms within them were attractive. The relative phase of the solitons was not measured experimentally but a change in phase between neighbouring peaks was inferred by comparing the dynamics with theoretical simulations of arrays with and without a phase jump of $\pi$ between solitons [105].

Recently, soliton-soliton interactions in an atomic condensate have been investigated more directly by deliberating colliding solitons together [106] . Here the condensate was in a harmonic trap so that the solitons were pushed together in the bottom of the trap and their separation oscillated with time. In some cases, the solitons briefly overlapped as they collided while in other cases they never met at the centre; these situations were attributed to differences in the relative phases of the solitons. The relative phase between solitons was again inferred by comparison with simulations as it could not be measured directly. By exciting the solitons with different intensities so that they were distinguishable, the solitons were observed to pass through one another, although the authors acknowledge that it is possible that atoms are transferred from one soliton to the other as they collide.

### 2.3.4 Supercontinuum Generation

In the year 2000, experiments in optical fibers revealed a large spectral broadening of input pulses with an initial width of ∼30 nm to populate a spectrum with a width of 500 nm [92]. This broadband spectrum became known as a supercontinuum. Very high excitation powers were needed for these observations with the peak power of the input pulse reaching 1.6 kW. These initial observations were seen in photonic crystal fibers, where air holes were patterned into the fiber cladding in order to modify the dispersion, shifting the zero group velocity dispersion point to visible wavelengths. Similar results were later seen in tapered fibers [107] where ordinary fibers used for telecommunications could be quickly modified to enhance their nonlinearity.

Over the next couple of years, the mechanisms behind supercontinuum generation were investigated. Theoretical simulations reproduced the broadening and showed that the extent of it could not be explained purely by self-phase modulation [108] (explained in §2.3.2). Instead, simulations showed that supercontinuum generation was linked to the fission of higher order solitons. These are solutions to the Nonlinear Schrödinger Equation where the pulse amplitude is high enough to produce multiple solitons (§2.3). These peaks propagate at the same velocity, appearing as a bound state. However, the bound state is unstable as there is no binding energy associated with the structure, which is therefore susceptible to small perturbations.

Perturbations from higher order dispersion terms can shift the frequency of the soliton peaks, changing their relative velocities and separating the high order soliton into several individual, spectrally separated, solitons [98]. The variation in frequency shifts of the individual solitons broadens the spectrum in the anomalous dispersion region, but each soliton can also emit radiation at frequencies in the normal dispersion region (§2.3.2), thus broadening the spectrum in both directions. The simulations showing this state evolving into a supercontinuum [108] were later replicated experimentally [109], justifying the conclusion that soliton fission was the dominant process leading to supercontinuum generation.

### 2.3.5 Spatial Solitons in Planar Waveguides

While temporal optical solitons have been observed in one dimensional structures such as optical fibers (§2.3.2), these devices cannot be used to look at spatial solitons where the

beam shape perpendicular to the propagation direction is stabilised. Instead, these spatial solitons can be observed in two-dimensional planar waveguides [110].

#### Glass slab waveguides

Early observations of spatial solitons were made in a single-mode glass slab waveguide [110]. Laser light was injected into one of the end facets of the slab and propagated through the waveguide to the output facet where it was imaged. The spatial intensity profile of the beam at the output (along a line perpendicular to the propagation direction) was compared to that of the input beam for a range of laser powers. For low input powers, the beam at the output facet was found to have diffracted, spreading to a width more than 4 times that of the input beam. As the input power was increased the output beam narrowed, becoming only slightly wider than the input beam for an input power of 400 kW. When the input power was further increased to 1.25 MW, the beam broke up into an array of three peaks with a larger separation than that which would be expected for a higher order soliton (§2.3.3).

Planar waveguides have been used not only to demonstrate the formation of spatial optical solitons, but also to study the interactions between solitons [101]. Two solitons were injected so that they initially propagated parallel to each other, subsequently moved together or apart depending on whether the interaction between them was attractive or repulsive. This was found to depend on the relative phase of the two solitons, as expected from observations in other soliton systems §2.3.3.

#### Semiconductor waveguides

The propagation of optical wavepackets has also been studied in semiconductor waveguide structures such as a set of InGaAs quantum wells [111] or an undoped GaAs layer [112] sandwiched between an n-doped substrate and a p-doped capping layer. Electrical contacts on the top and bottom of the sample can be used to inject electron and hole carriers. While light propagating through glass only interacts weakly with the medium, photons propagating through these doped semiconductor structures can interact strongly with free electron and hole carriers in the material. Optically exciting the sample can generate electron-hole pairs, but the presence of the optical field will also stimulate photon emission and cause the electron-hole pairs to recombine. If there is a surplus of free carriers compared with the ground state of bound electron-hole pairs (known as population inversion), the stimulated emission will be stronger than the absorption, amplifying the applied optical field.

The refractive index of these structures decreases with an increasing free carrier density [113]. Injecting light into a certain area of an electrically pumped device will locally deplete the carrier density, resulting in an intensity dependant refractive index suitable for soliton formation. The propagation of a laser beam through such a waveguide structure with embedded quantum wells has been studied by Khitrova *et al* [111] by comparing the intensity profile at the input and output of the waveguide. Low intensity beams were found to diffract while at a higher intensity, the beam shape was similar at the input and output. This is consistent with the formation of a fundamental soliton. At even higher intensities, the central peak narrowed further with lower intensity secondary peaks forming on either side, a profile which was consistent with that of a second order soliton.

Similar experiments were carried out in a waveguide structure with an embedded undoped GaAs layer where the formation of a fundamental soliton as the excitation power is increased was replicated [112]. As the power was increased to around 5 times the power needed to excite a soliton, a multi-peak structure was seen. Here, this was attributed to excess intensity around the main soliton beam which also begins to self-focus, rather than being caused by the excitation of a higher order soliton. The nonlinear refractive index coefficient of this semiconductor waveguide was estimated at $n^{(2)} = 2.8 \times 10^{-10}$ cm$^2$W$^{-1}$, several orders of magnitude higher than that of the glass slab waveguides ($n^{(2)} = 3.4 \times 10^{-16}$ cm$^2$W$^{-1}$ or $n^{(2)} = 4 \times 10^{-15}$ cm$^2$W$^{-1}$ [110]).

Later work has shown that the soliton stability may be improved in these structures by alternating regions of gain (where carriers are electrically injected via gold electrodes patterned on the sample surface) with regions of loss (no pumping, optical losses due to photons being absorbed by the medium) [114]. The shape or intensity of the resulting soliton no longer strongly depends on the input beam, provided that the beam power is above a certain threshold. Instead, the soliton intensity increases with the applied current, i.e. with increasing gain. Meanwhile the output beam width remains around 21 μm as the input beam width is varied between 15 μm and 35 μm. This behaviour is similar to the case of the dissipative polariton solitons studied by Sich *et al*, where the soliton width and intensity was determined by that of the CW pump that provided gain to the lossy microcavity (see §2.4.1).

### 2.3.6 Matter-wave Solitons

In atomic systems, bright solitons have been observed in a BEC of lithium-7 atoms by Khaykovich *et al* [115]. The BEC is trapped in two dimensions but is free to propagate in the third dimension where the energy-momentum distribution is parabolic. The large curvature of the parabolic dispersion would lead to broadening of a condensate wavepacket consisting of non-interacting particles. In optical fibers, this spreading can be compensated due to a nonlinear interaction with the fiber medium; in an atomic condensate the spreading can instead be halted by attractive interactions between the atoms.

Interactions between atoms are usually repulsive, so when they collide they will scatter apart. The scattering length for a two-atom collision can be tuned using a magnetic field and has Feshbach-like resonance features (at a Feshbach resonance, the kinetic energy of the two colliding particles equals the attractive potential energy of a bound state) in which the scattering length becomes negative [116]. The result of this is that the inter-atom interactions can be tuned continuously from their usual repulsive nature to an attractive interaction,which balances the dispersive spreading.

These matter-wave solitons were generated starting from a BEC of atoms in a trap which were then expelled into a one-dimensional waveguide. The wavepacket profile with attractive interactions was then compared to one for a gas of non-interacting particles by tuning the inter-atom interaction to zero. In both cases, the gas drifted along the wire but the resulting wavepacket remained very small (resolution limited) for the attractive gas while it broadened for the non-interacting gas. The attractive gas wavepacket was termed a soliton and it neither dispersed nor decayed as it propagated.

### 2.3.7 Dissipative Solitons

In systems such as optical fibers and atomic condensates, losses are low so the number of particles in a wavepacket stays roughly constant. These are known as "conservative" systems and can support soliton formation provided that the particle population decays over a longer timescale than the characteristic time of dispersive spreading [117]. Solitons forming in these environments (see §2.3.2 and §2.3.6) have a well defined width which can be found theoretically by equating energy terms in a similar manner to establishing the healing length of a superfluid (§2.2.4). This width will, in general, depend on the number of particles in the wavepacket (see for example Equation 2.7 in §2.4.1 defining the half width of a bright polariton soliton) so should remain constant for a conservative system. Note that losses will lead to a broadening in the expected soliton width.

For systems with high losses where the particle number drops too quickly to observe soliton formation, the particle population can be maintained using an external pump (see Figure 5.1 in §5.1 for an example setup). Solitons generated in this configuration are termed "dissipative". Dissipative spatial solitons have been observed in weakly coupled microcavities such as Vertical Cavity Surface Emitting Laser (VCSEL) structures. Properties of these semiconductor devices, such as the refractive index, vary with light intensity so that the system can be tuned into resonance with the cavity photon mode by varying the optical excitation power. The result is a bistable system in which a large area can be initialised in a low density state by a driving field and a localised region can then be excited to a high density state using a writing pulse. This region remains at high intensity once the writing pulse is switched off, maintaining its characteristic soliton size over time [118]. This bright soliton can be switched on and off by changing the phase of the writing pulse [119].

Patterns of solitons can also form where the bright peaks can be independently switched on and off by the writing pulse [120]. This property has led to the suggestion that arrays of these switchable solitons could be used for information processing [121]. While in a homogeneous sample these solitons would be stationary, they will start to drift along gradients in parameters such as phase. The ability to control this functionality by tilting the angle of the driving field to introduce a phase gradient could enable these soliton arrays to be used as an optical delay line or information buffer [122].

The first observation of a bright polariton soliton was made in a strongly coupled planar microcavity, which was a dissipative system [7]. Observations of conservative polariton solitons have recently been made in a waveguide polariton system [89]. Polariton solitons will be discussed further in §2.4

## 2.4 Polariton Solitons

Solitons are non-dispersive wavepackets which are useful for information processing and signalling as they can propagate over long distances without distortion. They can be localised in the time domain (temporal solitons) or in the spatial domain (spatial solitons). Solitons can be described as bright, where the soliton peak is an intensity maximum; or dark, when the soliton "peak" is an intensity minimum in a bright background. Solitons have been widely studied in low-loss (conservative) systems such as optical fibers (§2.3.2), although

dissipative solitons can also form in lossy systems supported by an external pump such as weakly coupled microcavities (§2.3.7).

There clearly exists a rich variety of solitons, many of which can be studied in a polariton system. While microcavity structures are associated with large photonic losses, they can be pumped to generate dissipative solitons in a similar manner to the method used in VCSELs (§2.3.7). The leakage of photons from the DBRs has its advantages, as the emitted photons can be detected, thereby continuously observing the system as it evolves in space and time.

The lower polariton branch (LPB) is strongly curved, showing regions of positive effective mass, corresponding to "anomalous dispersion" in an optical fiber; and negative effective mass, corresponding to "normal dispersion" (see Figure 2.2 and §2.1). In a similar manner to atomic condensates (§2.3.6), nonlinearity in the polariton system comes from polariton-polariton interactions (§2.1.1). In systems with repulsive (attractive) interactions, bright solitons will be stable in regions of normal (anomalous) dispersion. As repulsive interactions dominate the polariton system, a negative effective mass is required to stabilise bright solitons. Bright (§2.4.1, [7, 123]) and dark (§2.4.2, [55]) polariton solitons have both been observed experimentally.

**Theoretical work**

The behaviour of polariton condensates is often modelled using the Gross-Pitaevskii equation, which is a version of the Nonlinear Schrödinger Equation describing the evolution of a state in a mean-field approximation [124]. The same equation has been used to simulate the behaviour of gap solitons (see §2.4.3, [81]) and dark solitons (see §2.4.2, [78]) in a polariton system. This equation predicts the evolution of the shape of a solitonic wavepacket by considering the effect of energy terms such as potential energy from polariton-polariton interactions and kinetic energy, which is proportional to the second derivative of the wavefunction. Simulations using this equation give good agreement with experimental results for dark solitons, which occupy E-**k** states in the region where the E-**k** dispersion is approximately parabolic.

One dimensional bright dissipative polariton solitons are excited in states with a non-parabolic E-k dispersion by a seed pulse. These were numerically simulated by Egorov *et al* using coupled equations which separately consider the excitonic and photonic parts of the polariton. They considered solitons propagating over a continuously pumped background and found that this background needed to be in a bistable regime (see §2.2.3 for more on bistability) in order to observe solitonic solutions. These solitons were found to have an asymmetric intensity profile with a bright peak on the leading edge and a lower density tail on the trailing edge, illustrated in Figure 2.13. The dynamics of these solitons can also be described with an equation which included higher derivatives (up to fourth order) of the polaritonic wavefunction (see Fig 2.11) in order to establish the effects of these different terms.

The continuously pumped background can also act as a pump state in an OPO process (§2.2.1) generating additional signal and idler states. It was found that the transfer of polaritons between these three states could stabilise the soliton size in both the positive and negative effective mass directions so that propagating two-dimensional bright solitons could

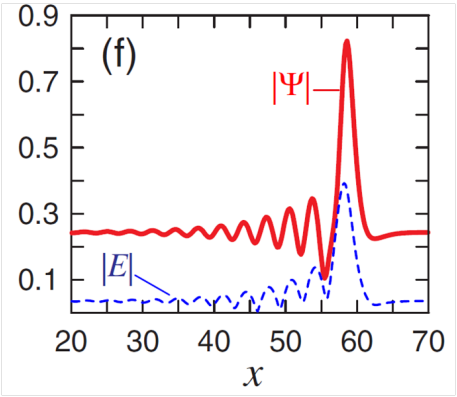


**Figure 2.13: Soliton profile.** Numerically calculated amplitude profile of the photonic $\Psi$ and excitonic $E$ components of a soliton wavepacket excited at a k vector of 1.57 $\mu m^{-1}$.
Reprinted Figure 2f with permission from [Egorov *et al*, Phys Rev Lett, **102**, 153904 (2009)]. Copyright (2009) by the American Physical Society

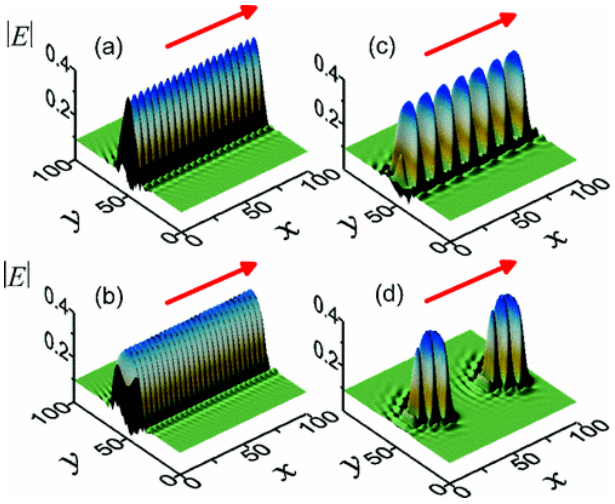


**Figure 2.14: Soliton trains.** Examples of different propagating patterns which can be excited by tuning the amplitude of the continuously pumped background and the k-vector of the seed pulse.
Reprinted Figure 5 with permission from [Egorov *et al*, Phys Rev B, **84**, 165305 (2011)]. Copyright 2011 by the American Physical Society

be excited [125], as discussed in §2.4.1. By elongating the seed pulse along the propagation direction and giving it a sufficiently long lifetime, soliton trains (multi-peak arrays of solitonic pulses) can be generated. The pattern of soliton pulses (e.g. peak separation) within these trains can be modified by tuning the amplitude of the continuously pumped background and the k-vector of the seed pulse (see Figure 2.14).

### 2.4.1 Bright Solitons

Bright dissipative solitons (described in §2.3.7) have been experimentally observed in microcavity polariton systems [7, 123]. Solitons can be excited with the continous wave (CW) pump in a bistable regime because the associated parametric instability (see §2.2.3) promotes scattering out of the pump state to populate a broad soliton spectrum. The soliton can be considered as locally exciting the pump spot from the low density state to the high density state on the bistability curve [7].

Sich *et al* experimentally observed soliton formation, triggering a wavepacket with a pulsed writing beam (WB) of diameter $\sim$ 10 μm. The wavepacket evolved into a soliton which propagated across a pump spot of length $\sim$ 70 μm. The size and shape of the solitons were found to be independent of the shape of the writing beam and were instead determined by the pump and cavity parameters. The mechanism for localisation along the propagation direction is similar to that for the formation of temporal optical solitons (§2.3.2), arising in the polariton case from the interplay between repulsive polariton-polariton interactions and the negative effective mass [94]. Spatial localisation in the direction orthogonal to the pump is not well understood but may occur due to a parametric nonlinearity which can cause the wavepacket to spread, collapse or maintain a constant size depending on the pump amplitude [125]; this mechanism is thus only valid for dissipative solitons.

As the soliton is spatially localised, it must have a correspondingly broad momentum space profile, which has been observed both in simulations [94] and experiments [7]. The measured energy-momentum relationship is linear which is in agreement with what is expected for a non-spreading wavepacket as the components at different k vectors have the same group velocity (proportional to the first derivative of the dispersion).

Recently, polariton solitons have been generated in a semiconductor waveguide [89] where photons are confined within the structure by total internal reflection [22]. The polariton lifetime is much longer so the CW pump is not required and these solitons are termed "conservative" rather than "dissipative". Polaritons are injected in the negative effective mass region, generating bright temporal solitons, localised along the direction of propagation. By introducing a modulation in intensity and phase in the transverse direction of the trigger, a dark spatial soliton can form within the temporally bright propagating wavefront. This demonstrates the potential for generating polariton devices in novel structures, however in this thesis I will focus on the microcavity system.

#### Localisation in the propagation direction

Polariton-polariton interactions (see §2.1.1) contribute a repulsive potential with energy U = gN where g is the interaction coefficient and N is the number of polaritons, favouring a spreading wavepacket. In a similar manner to optical solitons, the nonlinear shape of the

polariton dispersion can also influence the evolution of the wavepacket intensity profile. The polariton propagation velocity, given by the gradient of the E-$k_x$ dispersion (see Equation 2.1), varies with $k_x$ leading to a change in shape of the spectrally broad wavepacket, such as a broadening in realspace. The kinetic energy (K) associated with the broadening of a wavepacket of width $2\xi$ is given by $K = \frac{\hbar^2}{2m^*\xi^2}$ where $m^*$ is the polariton effective mass (see Equation 2.2). At high $k_x$ vectors, the value of $m^*$ is negative, which is analogous to the normal dispersion sometimes seen in optical fibers (see §2.1). Note that the kinetic energy term becomes negative for a negative $m^*$, describing a shrinking wavepacket.

A soliton can form in the region of normal dispersion as the spreading induced by the repulsive polariton-polariton interactions is compensated by the negative kinetic energy term (note that for optical solitons, an anomalous dispersion is required as the nonlinearity is attractive in that case). The full soliton width is $2\xi$ where $\xi$ is the healing length of the polariton fluid, found here by equating the K and U terms:

$$\xi = \frac{\hbar}{\sqrt{2m^*gN}} \tag{2.7}$$

This is similar to the method used to estimate the width of vortex excitations in a superfluid (see §2.2.4)

#### Localisation perpendicular to the propagation direction

Localisation perpendicular to the propagation direction is less well understood as $k_y \sim 0$ so the effective mass is positive. If parametric scattering is not included, bright solitons for a positive effective mass and repulsive interactions are unstable [87]. One proposed localisation mechanism [126] includes parametric scattering from the pump state ($k_x = k_p, k_y = 0$) to a pair of signal ($k_x = 0, k_y = 0$) and idler ($k_x = 2k_p, k_y = 0$) states (see §2.2.1). The overall photonic E and excitonic $\psi$ fields are a sum of the interacting pump, signal and idler states which are all at different detunings, so have different exciton fractions and effective masses. Above some threshold, the pump-only state becomes unstable, triggering scattering from the pump to the signal and idler, reducing the pump population. This local depletion of the pump population modifies the effective potential of the system in a similar manner to the intensity dependent refractive index seen in optical fibers (see §2.3.1), which limits the spread of the wavepacket. Simulations have shown that the signal and idler states can further stabilise the soliton resulting in self-focussing into bright solitons even with the positive effective mass [125]. It should be noted that this localisation mechanism is only valid for dissipative solitons as it relies on the external CW pump, which is not present for the conservative case (see §2.3.7).

#### Polarisation properties of solitons

Just as the polariton eigenmodes are circularly polarised, stable soliton solutions with a dominant σ+ or σ– polarisation have been found [123]. Experimentally, solitons were most easily excited when the pump and WB were co-circularly polarised: in this situation the soliton polarisation matched that of the WB and pump. For a linearly polarised pump, a stable circularly polarised soliton was still excited by a WB of the same circular polarisation.

This system could be used as a polarisation switch as there is a range of pump polarisations (with degree of circular polarisation ranging from about -0.25 to 0.25) for which either σ+ or σ– solitons could be reliably triggered with an appropriate WB. Recent theoretical work by Fu *et al* [127] suggests that a dark soliton with the opposing circular polarisation may also be triggered under these conditions, although this has not been verified experimentally. If the pump and WB were cross-circularly polarised, no soliton was excited: this could be used to extinguish solitons which propagated to a certain region and could be implemented in a logic gate.

If both the pump and WB are linearly polarised, excitation is harder as there are no stable solutions for linearly polarised solitons. For the case where the pump and WB polarisation are orthogonal, theory predicts that either σ+ or σ– solitons will be generated with equal probability. Experimentally this corresponded to an apparently unpolarised soliton as the polarisation changed randomly from pulse to pulse and each measurement integrates over many pulses. If the pump and WB have parallel polarisation, the excitation of a double hump soliton is predicted with each hump having a different circular polarisation. This structure would be difficult to see experimentally due to the limited resolution of the setup, and in fact solitons were not reliably excited in this configuration [123].

Similar proposals for using the polarisation degree of freedom as a spin switch [88] or a logic gate in a polariton based circuit [128] have been made for polariton condensates. The bistability described in §2.2.3 can extend to multistability when the spin degree of freedom is considered due to the spin dependence of polariton-polariton interactions: polaritons with like spins strongly repel while those with opposite spin can weakly attract [129]. If, for example, the population of σ+ polarised polaritons is larger than that of σ- polarised polaritons, the σ+ polaritons will experience a large blueshift due to the stronger repulsion from polaritons with the same spin. The two populations would blueshift into resonance at different laser powers, giving multiple bistability thresholds.

There has been much theoretical [130, 129] and experimental work looking into the multistability of polaritons in planar cavities [131, 88], traps [132, 133, 134], and magnetic fields [135]. Such systems could be used as switches in a polaritonic circuit [136]. A spatial variation in intensity, such as for a gaussian pump spot, coupled with spin multistability can result in spatial spin patterns such as spin rings [137].

#### Polariton solitons in microwires

There has been much recent interest in microcavity polariton systems confined in one dimension [39]. This can be realised experimentally by etching areas of the top DBR around a wire structure so that photons are confined to the region where the full cavity remains. Systems such as this could be used to make elements for circuit applications, including transistor switches [138], Mach Zehnder interferometers [139] and logic gates [140]. Much of this previous work has been implemented with polariton condensates in which a single state is macroscopically occupied. In contrast, in the soliton system a broad spectrum of states is populated, giving solitonic wavepackets with a well defined size and amplitude. These solitons can be considered as carriers of information bits in all optical signal processing device based on polaritons [141].

### 2.4.2 Dark Solitons

Dark solitons consist of a low density wavepacket propagating through a high density background. In contrast to bright solitons, polaritons with repulsive interactions form stable dark solitons in the region of anomalous dispersion, such as in a condensate at the bottom of the lower polariton branch [87].

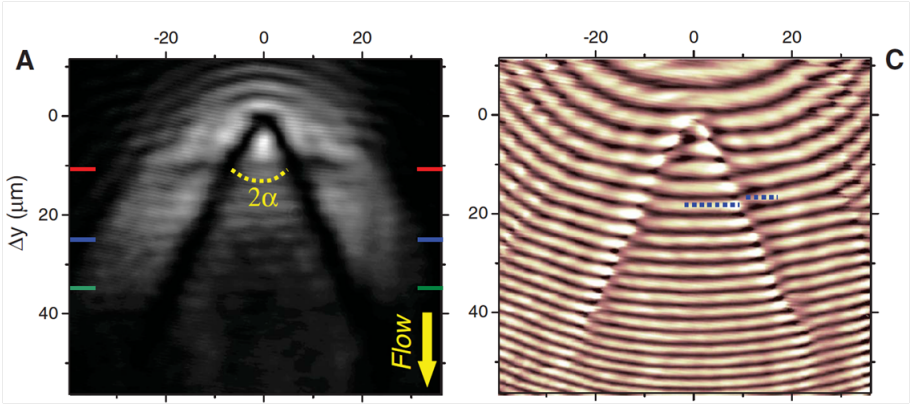


**Figure 2.15: Dark polariton solitons** experimental observation. **A** shows a two-dimensional image of the realspace emission. The condensate flows past a defect located at the origin forming dark solitons in the wake of the defect. **C** Interference of the soliton emission with a constant-phase reference beam, revealing phase jumps at the centres of the solitons.
From [Amo *et al*, Science, **332**, 1167 (2011)]. Reprinted with permission from AAAS.

The formation of conservative dark polariton solitons in a condensate was observed by Amo *et al* [55], looking at the flow of a condensate past an obstacle . When the flow rate was low, superfluid behaviour was seen where scattering was suppressed, as evidenced by the lack of density modulation which would have been induced by interference with back-scattered particles (see §2.2.4). As the flow rate increased, vortices began to form in the wake of the obstacle and as the speed increased further these evolved into a pair of dark oblique solitons (reprinted in Fig 2.15A). This replicated the numerical simulations of Pigeon *et al* [78] which are reprinted in Figure 2.8.

In the experiment, the solitons formed when the flow rate was around 0.6 of the speed of sound through the condensate. A phase jump of up to $\pi$ was observed across the soliton; a feature which is characteristic of solitons in condensates (reprinted in Fig 2.15C). A pair of soliton doublets was also observed by increasing the obstacle size and flow momentum. There have been suggestions in the literature that these observations can be described by linear wave dynamics [142], however further analysis by Amo *et al* supports the original claim that these results correspond to dark solitons [143]. There has been a theoretical proposal by Pinsker and Flayac for generating dark soliton trains (soliton arrays with peaks separated in time) in a one-dimensional wire [144]. Here, a polariton condensate flows through a step potential in the wire, generating a sequence of peaks whose separation can be tuned by varying the height of the potential step.

In analogy to half vortices, spin polarised half solitons have been observed [145, 146]. Theoretical work by Flayac *et al* shows that for a half soliton, a phase jump of up to $\pi/2$ and a rotation of the polarisation of up to $\pi/2$ would be expected across the soliton when measured in a linearly polarized basis. Measurements taken in a circularly polarised basis should reveal

a phase jump of up to $\pi$ in one circularly polarised component only. This behaviour was observed experimentally in work by Hivet *et al* [146], where the condensate was excited with linear polarisation parallel to the flow direction. The resulting dark solitons were observed with polarisation dependent detection. When detected in circular polarisation, each soliton was only visible in either $\sigma+$ or $\sigma-$ detection; this was the case for both the intensity maps and the phase maps that were measured. In the phase maps, a phase jump of around $0.85\pi$ was observed. When the detection was linear and diagonal, both the $\sigma+$ and $\sigma-$ solitons were visible and showed phase shifts approximately half that seen in circularly polarized detection. The expected polarisation shift across the soliton was also visible using linearly polarised detection. The half solitons had different trajectories as an effective magnetic field within the cavity accelerated solitons of opposite spin in different directions.

### 2.4.3 Gap Solitons

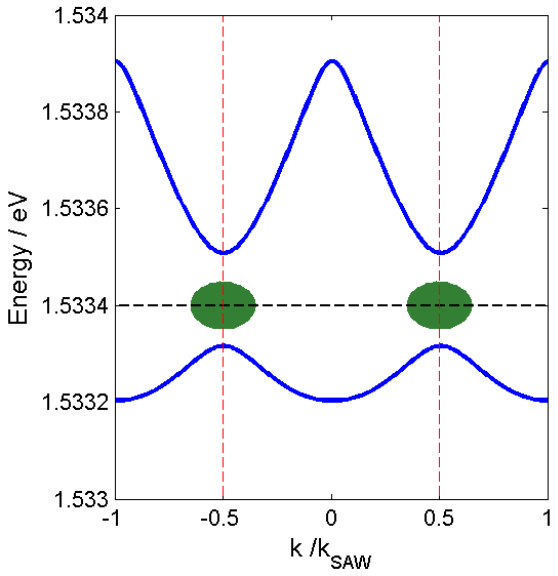


**Figure 2.16: Gap soliton states.** Blue lines show a polariton dispersion in a periodic potential (see Fig 2.4 in §2.1.3) which has a band gap at the energy indicated by the black dotted line. Red dotted lines indicate the edges of the mini-brillouin zone where the lowest energy mode has a strong negative curvature. Green circles indicate the positions at which gap solitons would form.

Gap solitons are localised wavepackets whose E-k dispersion lies in a bandgap (see Fig 2.16). The effect of a periodic potential on the polariton dispersion is discussed in §2.1.3, but the significant feature here is a band gap which opens up where two modes anti-cross (see Fig 2.16). The gap soliton forms when polaritons condense in the band gap at the anticrossing points where the negative curvature of the dispersion can be interpreted as a negative effective mass (see discussion in §2.1). These condensates are localised in realspace due to the interplay between polariton-polariton repulsion and an effective attraction arising from the polaritons' negative effective mass [147].

Gap solitons have been observed in several systems with periodic potentials including atomic [148] and photonic systems [149] as well as polaritonic devices with a potential

modulated in one [150] or two [81] dimensions. The two-dimensional modulation was applied using a surface acoustic wave (SAW, see §3.1.1 for details on applying the SAW as well as §2.1.3 and §2.2.5 for a discussion of the resulting behaviour of polaritons at low and high densities). These observations of gap solitons was made by Cerda-Mendez *et al* using the same sample used for the experiments presented in Chapter 4 of this thesis.

In this experiment, the size of the gap soliton was determined by the coherence length in realspace. This was typically smaller than the total size of the emission area but larger than the period of the potential modulation. The coherence length decreased with increasing SAW amplitude, which was attributed to a change in the energy balance determining the size of the gap soliton: the polariton effective mass increased with SAW amplitude (described in their supplementary material) so the magnitude of the kinetic energy term was larger. The repulsive term did not change as the polariton number was constant, so that balancing the energy terms resulted in a decreasing soliton size with increasing SAW amplitude. The decrease in coherence length was accompanied by a broadening of the k space peaks as expected for fourier-related variables. The experimental observations were well replicated by numerical simulations looking for gap soliton solutions.

## 2.5 Quantum Effects

While many observations can be explained using a classical wave description of light, certain behaviours can only be understood when the quantum nature of light is considered [151, 152]. The quantum properties of light can be revealed through the intensity fluctuations of a light source (§2.5.2) or by measuring correlations between pairs of emitted photons (§2.5.3).

In a quantum mechanical description of a system, there is a discrete set of outcomes that can be observed in a measurement of the system. For example, one observation of an electron in a hydrogen atom might show it is in the ground state with energy -13.6 eV while a second measurement might find it in the first excited state with energy -3.4 eV. However the electron will never be measured between these states with some intermediate energy. These observable states and energies are known as the eigenstates $\psi_i$ and eigenvalues $E_i$ of the particle and can be found by solving the time-independent Schrödinger equation

$$\hat{H}\psi_i = E_i\psi_i \tag{2.8}$$

where $\hat{H}$ is the Hamiltonian describing the environment, including terms such as potential energy in the background, the kinetic energy of the particle and interactions with neighbouring particles. While the particle can only be observed in an eigenstate, the unobserved system is described by a wavefunction $\psi = \sum_i c_i\psi_i$, where $|c_i|^2$ gives the probability of measuring the system in eigenstate $\psi_i$. $\psi$ evolves in time according to the time-dependent Schrödinger equation.

$$i\hbar\frac{\partial}{\partial t}\psi(\mathbf{r},t) = \hat{H}\psi(\mathbf{r},t) \tag{2.9}$$

where $\psi(\mathbf{r},t)$ describes the wavefunction at position $\mathbf{r}$ and time $t$. The Nonlinear Schrödinger Equation used to describe solitons (§2.3) has the same form but nonlinear terms, such as

those proportional to $|\psi(\mathbf{r}, t)|^2$, are included in the Hamiltonian.

Properties of the particle states can be measured, however due to Heisenberg's Uncertainty Principle, there is a limit to how precisely one can know the value of certain pairs of complementary variables, such as position and momentum. For example in the hydrogen atom, the energy of the electron in the atom can be measured but its precise location relative to the nucleus is unknown. Measurements of parameters with these uncertainties therefore have a certain amount of noise associated with them so that the measured value fluctuates. This noise can be reduced for a given parameter (at the expense of increasing the fluctuations of its complementary parameter) by generating "squeezed" states, which will be further discussed in §2.5.1.

### 2.5.1 Squeezed States

As mentioned previously, there is an inherent uncertainty in the measurement of complementary parameters of a system. These might describe properties which evolve sinusoidally, but have a relative phase difference of $\pi/2$. For example in a classical harmonic oscillator, such as a mass on a spring, the mass will oscillate sinusoidally about a centre position $x_0$. Its velocity will be at a maximum at $x_0$ and at a minimum at the position of largest displacement ($x - x_0$) where the mass changes its propagation direction. For a particle in the ground state of a quantum harmonic oscillator, the position and momentum jointly have a minimum uncertainty

$$\Delta x \Delta p \geq \frac{\hbar}{2} \tag{2.10}$$

where $\hbar$ is Planck's constant divided by $2\pi$, $\Delta x$ is the uncertainty in the position $x$ and $\Delta p$ is the uncertainty in the momentum $p$. Successive measurements of properties $x$ and $p$ will give different values, fluctuating about the mean (given by an eigenvalue) within the range $\Delta x$ or $\Delta p$ to give a noisy measurement.

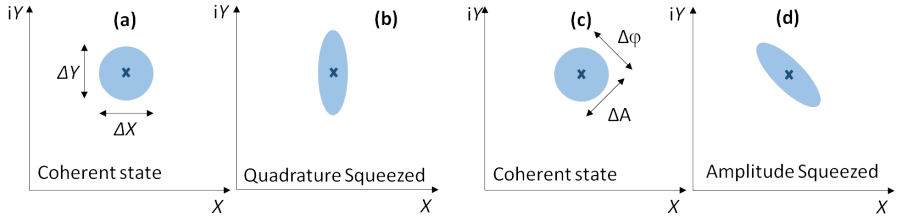


**Figure 2.17: Coherent and squeezed states**. **(a)** Coherent state: fluctuations in parameters $X$ and $Y$ have similar magnitudes. **(b)** Quadrature squeezed state: fluctuations are reduced in quadrature $X$ but simultaneously increased in quadrature $Y$ **(c)** Coherent state: fluctuations in amplitude A and phase $\phi$ have similar magnitudes. **(d)** Amplitude squeezed states: fluctuations in amplitude are reduced while those in phase are increased.

A more general system may have properties $X$ and $Y$ which again oscillate out of phase and have a similar uncertainty relation; these properties are called "quadratures". Measurements of these values can be represented in the complex plane with a phasor diagram. Classically, the least noisy state is a coherent state, which has similar fluctuations in $X$ and $Y$ (see Figure 2.17a). However in a quantum system, so-called "squeezed states" can be

generated where the fluctuations are decreased along one axis in the phasor diagram at the expense of being increased along the perpendicular axis. The squeezing can occur in one of the quadratures $X$ or $Y$, which is known as a "quadrature squeezed" state (see Figure 2.17b). Alternatively, the fluctuations in the combined amplitude of $X$ and $Y$ can be squeezed while increasing the fluctuations in the phase relation between $X$ and $Y$, which is known as an "amplitude squeezed" state (see Figure 2.17d).

It has been predicted theoretically that quadrature squeezing of light fields can be achieved in a beam propagating through a medium with a non-linear refractive index (Kerr nonlinearity), with the strongest squeezing occurring at the boundary of the bistable region [153]. As discussed in §2.3.1, the polariton system has a strong Kerr-like nonlinearity and squeezing was first observed in such a system by Karr *et al* [154]. More recent theoretical work showed that squeezing could be enhanced in a more confined system [155]. Accordingly, further experimental work was carried out in micropillar samples (micrcavities etched into circular pillars a few μm in diameter) by Boulier *et al* [156] where they were able to measure squeezing of 20.3% (thought to be 35.8% after corrections).

Quadrature squeezed states are used in quantum information systems based on continuous variables, such as position [157], where they can be used to produce entangled states. These states are expected to be easier to generate than their counterparts based on discrete variables such as photon number, although the quality of the entanglement would not be as good.

### 2.5.2 Emission Statistics

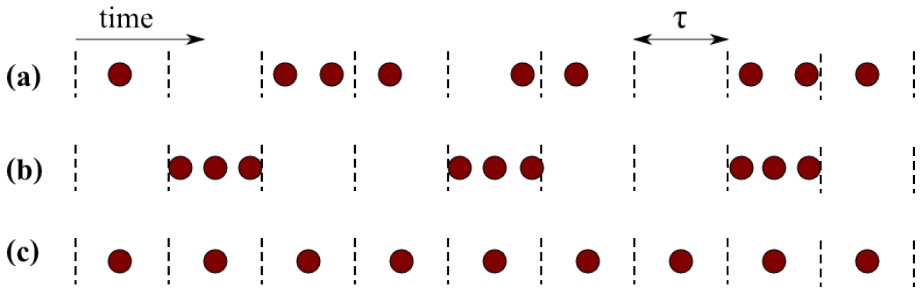


**Figure 2.18: Types of light**. **(a)** Coherent light (poissonian statistics). This could be a laser beam with constant intensity. **(b)** Bunched light (super-Poissonian statistics). This could be a laser beam with a random intensity fluctuation, or a thermal light source. **(c)** Anti-bunched light (sub-Poissonian statistics). This example shows a single photon source. Sub-Poissonian statistics and anti-bunched correlations (§2.5.3) can only be explained using a quantum description of light, while classical analogues can be found for coherent and bunched light.

A stream of photons can be detected by a detector which counts the number of photons arriving in a certain time interval $\tau$ (see Figure 2.18a). First, consider a stream of photons with constant intensity, then the mean number of counts per interval will be $\bar{n} = \Phi\tau$ where $\Phi$ is the photon flux. If $\tau$ becomes sufficiently small, $\bar{n}$ becomes fractional but fractional photons cannot be detected. Instead, a photon will be detected in a fraction $\bar{n}$ of all intervals while no photons will be detected in (1-$\bar{n}$) intervals, so even with a perfectly constant photon flux, the count rate varies randomly from one time interval to the next. It can be shown

theoretically [151] that the ratio between the variance (fluctuations) in count rate ($\Delta n^2$) and $\bar{n}$ is one, which corresponds to a Poissonian probability distribution.

If the intensity of the photon stream now has fluctuations in time (see Figure 2.18b), the photon flux $\Phi(t)$ can be expressed as the sum of a constant flux $\phi_0$ and a time varying fluctuation $\phi(t)$, so $\Phi(t) = \phi_0 + \phi(t)$ . The fluctuations about the mean value average to zero ($\overline{\phi(t)} = 0$) so the mean count rate $\bar{n}$ is unchanged by $\phi(t)$, but the fluctuations between the count rates in different time bins will be increased. The ratio of variance to mean will therefore clearly be increased to values greater than 1 ($\Delta n^2/\bar{n} > 1$), corresponding to what is known as a "Super-Poissonian" probability distribution. Most classical light sources are expected to shown super-Poissonian statistics, tending to Poissonian statistics in the limit of a perfectly constant photon flux. In order to cross to the regime of "Sub-Poissonian" statistics ($\Delta n^2/\bar{n} < 1$), a quantum mechanical description is needed.

For the Poissonian light described above, the photons are randomly distributed between the time intervals. For the situation where photons are evenly spaced with separations of time T, the statistics can be very different (see Figure 2.18c). If the time interval over which the photons are counted ($\tau$) is equal to T, there will always be exactly one photon counted so the variance in count rate drops to zero. If $\tau \neq$T, the variance becomes non-zero but remains less than the mean unless $\tau \ll$T, where it once again tends to the mean value to approach Poissonian statistics. This variation in the measured $\Delta n^2/\bar{n}$ is simulated in Figure 2.19 where the cases of Poissonian light and regularly spaced single photons are compared.

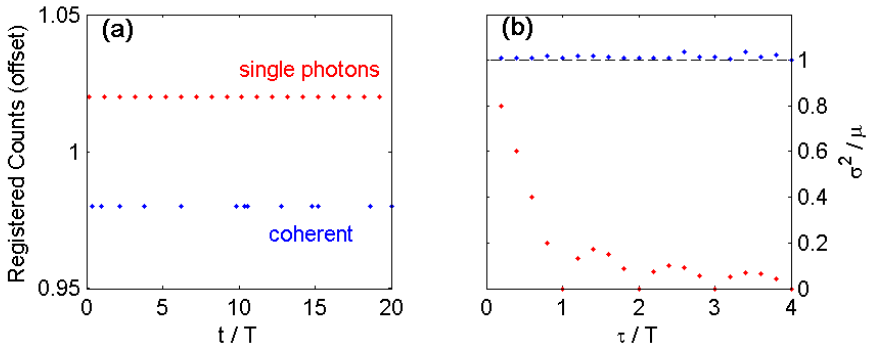


**Figure 2.19: Photon Statistics**. **(a)** Shows two beams of light. The blue (lower) dots show photon counts over time t for a coherent beam of light where the photons are on average separated by a time interval T. The red (upper) dots illustrate the counts registered for a stream of single photons emitted at regular intervals of T. The counts are slightly offset to help distinguish the two light beams. **(b)** Ratio between the variance and mean in the count rate (number of photons arriving in time interval $\tau$) for the photon beams illustrated in (a) as a function of the width of the time interval $\tau$. The black dashed line indicates a ratio of 1 corresponding to Poissonian statistics.

The single photon source shown in Figure 2.18c is an example of a "photon number state" (with photon number 1), where the photons are counted exactly but their phase is completely undefined. These in turn are extreme examples of amplitude squeezed states (see §2.5.1). Photon number states with multiple photons would give sub-Poissonian statistics in the same way as the single photon state: if the number of photons in the measured time interval is well defined, the variance between measurements will be dramatically reduced.

The measurement of sub-Poissonian statistics is severely hampered by low detection

efficiencies as the low efficiency randomly removes photons from the beam. This is illustrated in Fig. 2.20 for the case of regularly spaced single photons separated by time T. The photons are counted in time intervals of $\tau$=T, which should result in a variance of 0 as discussed in Fig 2.19. However, as the efficiency is reduced, the ratio of variance to mean rapidly approaches 1, for example with an efficiency of 3% (comparable to the streak camera used in this thesis) the measured ratio of variance to mean is $\sim 0.97$ instead of 0.

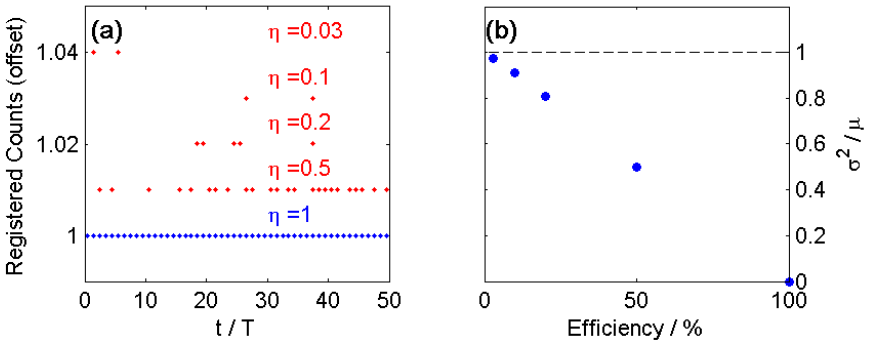


**Figure 2.20: Effect of detector efficiency.** **(a)** Shows the photons detected by detectors of different efficiencies $\eta$ when the incoming photon beam is a stream of single photons separated by time T. The count rates are offset so that the beams can be distinguished. **(b)** Ratio between the variance and mean in the count rate (number of photons arriving in time interval $\tau$ = T) for the photon beams illustrated in (a). The black dashed line indicates a ratio of 1 corresponding to Poissonian statistics.

The detection efficiency $\eta$ modifies the mean and variance $(\mu, \sigma^2)$ according to equations 2.11 and 2.12 so that values $(\mu_m, \sigma_m^2)$ are measured instead [151, 152].

$$\mu_m = \eta\mu \tag{2.11}$$

$$\sigma_m^2 = \eta^2\sigma^2 + \eta(1-\eta)\mu \tag{2.12}$$

### 2.5.3 Pair Correlations

In addition to measuring the photon statistics in a beam of light, the correlations between photon pairs can also be studied. This looks at how the detection of one photon influences the probability of detecting a second photon. Pair correlations can be quantified by looking at the second order autocorrelation $g^{(2)}(\tau)$ defined as

$$g^{(2)}(\tau) = \frac{\langle I(t)\ I(t+\tau)\rangle}{\langle I(t)\rangle\ \langle I(t+\tau)\rangle} \tag{2.13}$$

where $I(t)$ is the measured intensity in time interval $t$ and $I(t+\tau)$ is the measured intensity in time interval $(t+\tau)$, while the brackets $\langle ...\rangle$ indicate an average over many time intervals [151].

In a coherent light beam (see Figure 2.18a), the photons are randomly distributed; the detection of one photon has no effect on the probability of detecting a second. The photons are uncorrelated, giving a normalised value of $g^{(2)}(\tau) = 1$ for all $\tau$ (see Figure 2.21a).

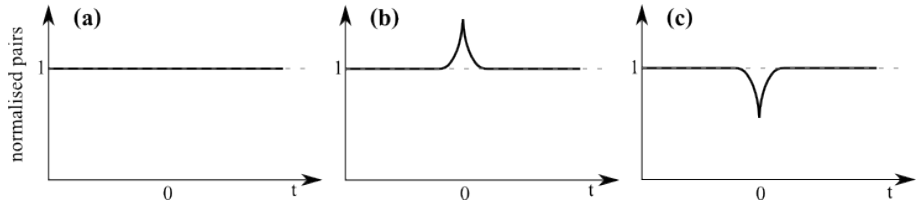


**Figure 2.21: Schematic $g^{(2)}(\tau)$ functions** for **(a)** coherent light, **(b)** bunched light and **(c)** anti-bunched light

In a bunched light beam (see Figure 2.18b), such as a beam with varying intensity, the detection of one photon increases the likelihood of detecting a second at the same time, as both photons are more likely to be detected when the beam intensity is at a maximum. Here, $g^{(2)}(0) > 1$, although for sufficiently large $\tau$ the photons will no longer be correlated due to their large temporal separation, so that $g^{(2)}(\tau \gg 0) \sim 1$ (see Figure 2.21b). Bunched light can be generated, for example, by spectrally filtering a laser beam which has a constant intensity but whose lasing frequency drifts over time, as the spectral filter then imposes a time varying intensity on the light which it transmits.

For amplitude squeezed photon sources where there are always $n$ photons in a given time interval $\tau$, $g^{(2)}(0) < 1$ as the detection of one photon reduces the number of photons remaining in the time interval to *n-1*. For a perfect single photon source (see Figure 2.18c), the detection of one photon means there is zero probability of detecting a second photon at the same time as there is never a second photon present. This gives the result $g^{(2)}(0) = 0$. Once again, $g^{(2)}(\tau \gg 0) \sim 1$ as photons in well separated time bins are uncorrelated (see Figure 2.21c).

## 2.6 Polaritonic Devices

Polariton systems are very versatile, exhibiting phenomena such as long range coherence (§2.2), bistability (§2.2.3) and soliton formation (§2.4). They have a strong nonlinearity due to polariton-polariton interactions, which is several orders of magnitude larger than that in optical fibers, so nonlinear effects can be observed at much lower excitation powers. The nonlinearity in polariton systems is typically 2-3 orders of magnitude higher than that in weakly coupled structures (discussed in §2.3.1). In addition, the response time of the strongly coupled system is enhanced by 2-3 orders of magnitude compared with weakly coupled devices due to the increased influence of the photonic component compared with the carrier dynamics [87].

The need to cryogenically cool the well-studied GaAs based polariton systems could be seen as a barrier to the wide-spread application of polariton systems, however progress is being made towards achieving similar functionality in newer materials which can operate at room temperature such as ZnO [25], GaN [26] and organic polymers [27]. Several proposals for polaritonic devices use polariton condensates: as noted in §2.2, these macroscopically coherent phases appear at much higher temperatures in a GaAs based polariton system (of the order of a few Kelvin) than in an atomic system, where μK temperatures are required. The combination of these factors makes polariton systems a promising platform for the

development of all-optical devices.

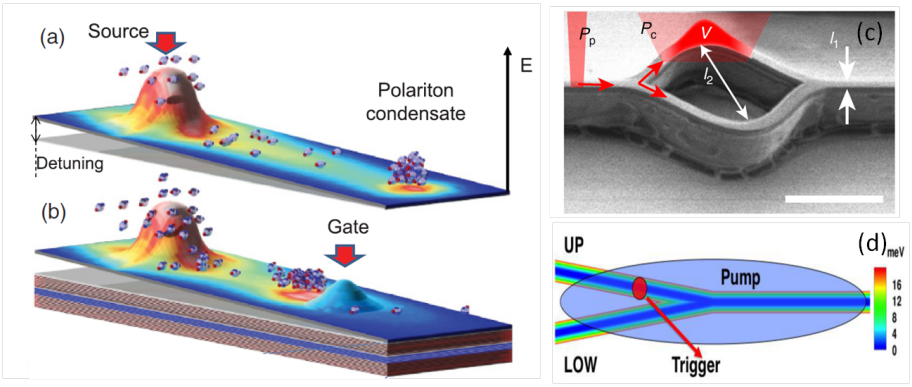


**Figure 2.22: Polariton Devices (a,b)** Polariton transistor demonstrated by Gao *et al.* (a) shows the transistor in the "on" state where a condensate forms at the collector while (b) shows the "off" position where the polariton flow is stopped by a gate.
Reprinted Figure 1 with permission from [Gao *et al*, Phys Rev B, **85**, 235102 (2012)]. Copyright (2012) by the American Physical Society
**(c)** Mach-Zehnder interferometer investigated by Sturm *et al* for modulating the intensity and polarisation of polaritons at the output (right hand side).
Reprinted from [Sturm *et al*, Nature Commun., **5**, 3278 (2015)] under a Creative Commons Licence.)
**(d)** Y-splitter structure for a soliton-based logic gate investigated by Cancellieri *et al.*
Reprinted from [Cancellieri *et al*, Phys Rev B, **92**, 174528 (2015)] .

### Transistors and logic gates

One device which has been proposed is a transistor switch, where the flow of polaritons into a certain area (the "collector") is controlled by modifying the potential landscape [138, 158]. This structure is illustrated in Figure 2.22(a,b). Here, polaritons are ejected from a condensate due to repulsive polariton-polariton interactions in the high density regions. They propagate along a potential gradient towards the collector located at the end of a mesa, where they accumulate to form a second condensate: in this case the transistor is "on". The flow of polaritons to the collector position can be gated by using a second laser beam to locally excite polaritons which blueshift the polariton dispersion, thus creating a barrier. Due to the short polariton lifetime (18ps), the polariton density at the collector will then decay, turning the transistor "off".

A different transistor device has been demonstrated which shows a sharper threshold-like behaviour by exciting a state (the "Address" state) with the laser slightly blueshifted from the lower polariton branch (LPB) so that as the polariton density increases, the LPB will blueshift into resonance with the laser and become highly populated [159]. A small polariton population injected into a second state (the "Control"), excited in resonance with the LPB, which can be used to switch the high intensity address state on and off. The amplification of the Address state compared with the Control state opens the possibility for cascadability, where polaritons ejected from the Address state can be used to switch the state of a neighbouring device. This can be further extended by using two transistors to switch the state of a third; a configuration which can be modified into an AND gate (where the third transistor only switches on if both of the inputs are on) or an OR gate (where either input will switch on the third transistor).

An alternative logic gate architecture has been proposed which uses bright dissipative solitons propagating at $\sim 0.7\mu m\ ps^{-1}$ [141]. A Y-splitter configuration (see Figure 2.22d) is simulated where a logical "1" is taken to be the arrival of a soliton with a given circular polarisation at the output (bottom of Y, right hand side of Fig. 2.22d). In the OR gate configuration, a soliton in either of the input arms at the top of the Y can propagate to the output to give a logical 1. The wire parameters (or pump parameters) can be modified so that solitons arriving simultaneously at both inputs are required to generate a soliton in the output branch, thereby creating an AND gate. It is estimated that these devices could work with repetition rates of up to 100 GHz. It is also shown that if solitons with opposite polarisations arrive from the two inputs, these will annihilate due to the attractive interaction between polaritons with opposite spins (see §2.1.1).

**Intensity and polarisation modulation**

The interference of polariton fluids has been studied experimentally in a Mach Zehnder interferometer device [139]. Here, a polariton fluid is injected into an input wire which splits into two arms. These later recombine in an output wire as shown in Figure 2.22c. A phase shift can be introduced into one of the arms by using a weak laser field to generate a small potential barrier which slows the flow of polaritons. By tuning the phase shift, the output intensity can be modulated by constructive or destructive interference.

The wire mesas have a splitting between modes polarised along the wire (x direction) and those polarised across the wire (y direction). This splitting results in an effective magnetic field which rotates the polarisation of the injected polaritons as they propagate through the device. Polaritons are injected into the input wire polarised along the horizontal axis of the sample, corresponding to the x direction of the input and output wires. In the interferometer arms, the wire bends away from the horizontal axis. Here the injected horizontal polarisation is no longer aligned with the x direction, so contains contributions from x and y polarised components. The energy splitting between the x and y contributions gives an effective magnetic field, resulting in precession of the polariton polarisation. The direction of spin precession depends on the sign of the angle between the x component in the wire at a given position and the horizontal axis, so the spin precesses in opposite directions in the two arms, introducing a $\pi$ phase shift in the vertical component of the two arms. The vertically polarised component will interfere destructively while the horizontal component interferes constructively, so that polarisation at the output can be modulated along with the intensity.

Experiments passing an atomic BEC through a Mach-Zehnder interometer have revealed the generation of non-classical (number-squeezed) states [160], something which may be replicated in future experiments on polaritonic devices.

**Spin switching**

Experimental work has shown that under certain conditions, a polariton device can be initialised into a multistable regime, where a high density state with $\sigma_+$ or $\sigma_-$ circular polarisation can be excited from a linearly polarised low density state using a $\sigma_+$ or $\sigma_-$ polarised trigger [88], a functionality which could be used to develop memory elements [134]. There has been a theoretical suggestion [128] of creating a propagating signal by switching

on consecutive multistable regions in a wire structure (a so-called "polariton neuron") and using this system to create AND and OR gates. However, the soliton approach suggested by Cancellieri *et al* [141] (described earlier in this section) has an advantage over this system as the solitonic device effectively resets after the soliton passes, enabling a high pulse repetition rate. Bright dissipative solitons with either circular polarisation can be triggered by a writing beam with matching polarisation and will propagate over a linearly polarised continuous wave pump spot, as has been demonstrated experimentally [123].

#### "NOT" functionality

While suggestions have been made for the construction of AND and OR gates, many computation algorithms also require a NOT-type gate, which inverts the input (so that a logical 1 at the input gives a logical 0 at the output, and vice versa).

A theoretical suggestion has been made for generating a network of AND and NOT gates, consisting of micropillar nodes connected by quasi-1D channels whose polarisation splitting induces a spin precession in any polaritons propagating through them [136]. The logical states are again encoded in the circular polarisation state of the polaritons. The micropillar nodes are initialised using a continuous wave laser in a low density state but can be switched to a high density state with either $\sigma+$ or $\sigma-$ polarisation by a low density signal of the same polarisation entering the node through one of the microwires. This amplifies the polarisation signal: a functionality which is important for cascadability (i.e. using the output of one node as the input to the next, allowing many operations to be carried out).

The "NOT" functionality comes from the spin precession in the microwire. It is then possible for a $\sigma+$ polarised node to eject polaritons into a channel whose spin precesses as they propagate, so that they excite the next node in a $\sigma-$ polarised state, thus the logical state is inverted between nodes. An AND gate can be constructed by introducing a slight polarisation bias into the continuous wave pump in the nodes, so that the $\sigma+$ will be excited in the output node unless both input nodes have $\sigma-$ polarisation.

Solnyshkov *et al* propose a similar structure consisting of two microwire sections at an angle of 45° separated by a micropillar, but now with controlled-NOT (CNOT) functionality [161]. This gate consists of two bits: the control and the target. If the control bit is set to 1, the target bit is inverted while setting the control bit to 0 leaves the target bit unaltered. Here, the target bit propagates through the microwire sections, interacting with the control bit localised in the micropillar which can rotate the polarisation of the target bit if required. Realisation of this two-bit gate would be an important step towards implementing quantum algorithms on a polaritonic chip.

#### Soliton arrays for memory

A related approach for constructing memory elements could involve using solitons. In weakly coupled cavities (VCSELs), arrays of solitons were optically excited where each peak could be individually switched on and off by an optical control beam [121]. Polariton systems have a much stronger nonlinearity so should show similar behaviour at lower optical powers. There have also been suggestions for using gap solitons (§2.4.3) in photonic crystals for all-optical memory, where the memory bit consists of a trapped soliton which can be released for

readout by a second control pulse when required [162]. Similar functionality was suggested in the polariton system by Tanese *et al* when they observed gap solitons in a 1D periodic potential [150].

# Chapter 3

# Methods

This chapter explains the experimental methods used for the work in this thesis. Details of the samples are given in §3.1 while the cryogenic cooling is described in §3.2. The optical setups used to excite the sample and image the emission are described in §3.3. More details of certain measurement techniques, such as the measurement of the phase profile over the emission, are given in §3.4.

## 3.1 Samples

All experimental work presented in this thesis was carried out on microcavity samples containing quantum wells. The wafers were grown by Molecular Beam Epitaxy (MBE). Some experiments (Chapter 5) were carried out on a section of the wafer with no further processing while in others, the wafers were modified either by patterning structures onto the top surface (Chapter 4) or by etching sections of the top DBR to define mesas in which the polaritons were confined (Chapter 6).

### 3.1.1 Sample for Surface Acoustic Wave Experiments

A dynamic periodic potential can be generated using a Surface Acoustic Wave (SAW). This strain wave periodically compresses and extends the sample thickness along the growth direction, modulating the width, and hence the bandgap, of the quantum wells.

The SAW is applied via interdigitated transducers patterned onto ZnO islands on top of the microcavity (see figure 3.1). The islands are necessary because if the SAW were to propagate along a piezoelectric axis of the GaAs sample surface, the field would dissociate the excitons [163, 164], so this must be avoided. By placing the transducers on piezoelectric ZnO islands, the IDTs convert the electrical signal to a mechanical strain along the piezoelectric axis of the ZnO and then the ZnO transfers the strain wave to the GaAs. The resulting surface acoustic wave can then be applied along any GaAs axis by changing the orientation of the ZnO island.

This technique was developed by Rudolph *et al* for use on an excitonic system [163]. In that case, the periodic strain field from the SAW induced a modulation in the band gap of the quantum well at the frequency of the SAW, trapping the excitons in the minima of

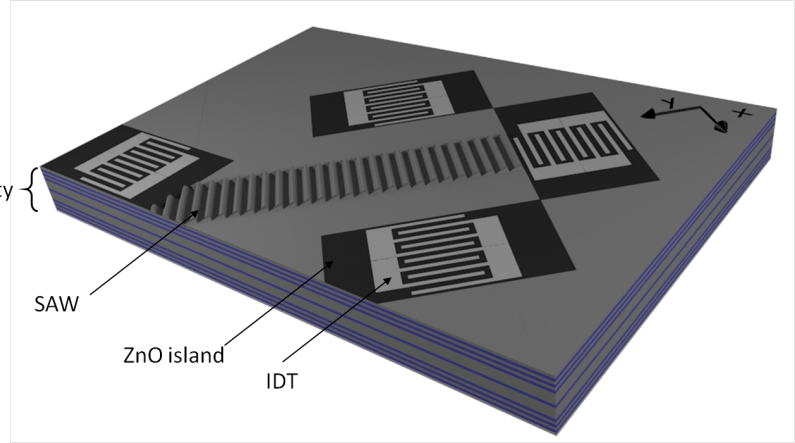


**Figure 3.1: Surface Acoustic Wave:** A surface acoustic wave (SAW) is applied to the surface of the microcavity wafer using interdigitated transducers (IDTs) patterned onto ZnO islands on the sample.

the potential. Here, the microcavity resonance is simultaneously modulated by compression and extension of the cavity and the refractive index of the material is also modified by the strain field [44]. Both the excitonic and photonic components are therefore subjected to a modulated potential due to the SAW which is inherited by the polariton [41].

The sample used was a GaAs/AlGaAs microcavity consisting of two DBRs surrounding a $\frac{\lambda}{2}$ cavity. Three pairs of 15 nm thick quantum wells were embedded in the cavity. The Q factor of the cavity was $\sim 2000$ with a Rabi splitting of $\sim 6$ meV and the cavity mode was detuned from the exciton by $\sim -2$ meV. SAWs of frequency 374 MHz with a corresponding wavelength of $\sim 8\mu$m were applied to the sample surface.

### 3.1.2 Sample for Bright Dissipative Soliton Patterns

The sample used to study patterns of bright dissipative solitons in Chapter 5 is a GaAs based λ microcavity with 6 GaAs quantum wells (15nm thick). The exciton emission is at ∼806.3 nm (∼1.5377 eV) which is above the bandgap of the GaAs substrate (∼818 nm, ∼1.52 meV [165]). This sample could only be studied in a reflection configuration as its emission would be absorbed by the substrate. The Rabi splitting was ∼5.0 meV. The bottom of the LPB was at ∼808.7 nm (1.5331 eV), corresponding to a cavity mode at ∼807.9 nm (1.5346 eV) and a cavity-exciton detuning of ∼-3.1meV. With these parameters, the point of inflection of the E-$k_x$ dispersion is expected to be at around $k_x = 1.7\ \mu m^{-1}$. The cavity mode varied across the wafer, allowing the selection of a particular value for the exciton-photon detuning. The polariton lifetime in this wafer was $\sim 5$ ps.

### 3.1.3 Sample for Nonlinear Wavepackets in Microwires

Experiments on nonlinear wavepackets in microwire structures (Chapter 6) were carried out in a transmission configuration. For this, a new wafer was grown with the exciton emission at an energy (∼1.492 eV, 831±1 nm) below the bandgap of the GaAs substrate (∼818 nm, ∼1.52 meV [165]). The large uncertainty in the position of the exciton emission is due to

the fact that it is not measured directly but is found by fitting to the measured polariton dispersion. As the Rabi splitting is another free parameter in this fitting, a small range of values can be found which fit the measured dispersion. The wafer is a $\frac{3\lambda}{2}$ microcavity with 3 InGaAs quantum wells (10nm thick, 4% Indium). The DBRs are GaAs/AlGaAs (85% Al) with 23 and 26 repeats for the top and bottom DBRs respectively, resulting in a polariton lifetime of $\sim$ 15 ps. The Rabi splitting was $\sim$5.0 $\pm$ 1 meV. By design, the energy of the cavity mode varied across the wafer, allowing the selection of a particular value for the exciton-photon detuning between -9meV and -4meV.

The planar cavity used in §6.7 has a detuning of -7 meV; the short wire sample used in §6.6 had a detuning of -8 meV; and the long wire sample used for most measurements in Chapter 6 had a detuning of -5 meV (Figure 6.3). These parameters give an expected point of inflection in the lower polariton branch at $k_x = 2.0\ \mu m^{-1}$ for the long wire sample, $k_x = 2.3\ \mu m^{-1}$ in the short wire sample and $k_x = 2.2\ \mu m^{-1}$ in the planar sample.

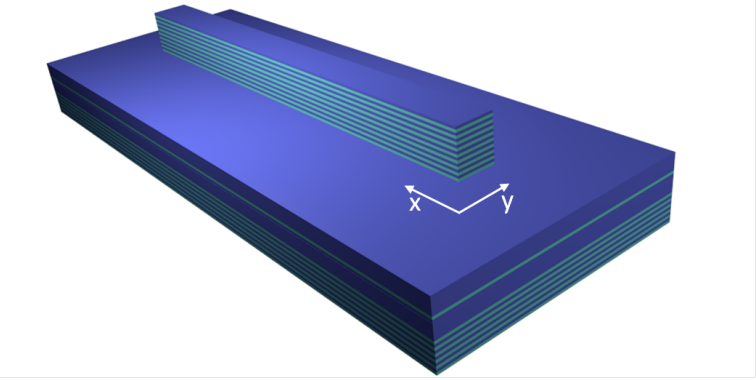


**Figure 3.2: Microwires:** the top DBR on a planar microcavity is etched away in all but a few regions. Photons are still trapped in the cavity, but only in these remaining mesas. The polaritons excited in the sample are similarly confined to these mesas.

Wire-shaped mesas (see Figure 3.2) were then defined by etching the top DBR using Electron Beam Lithography (EBL). The top DBR was only partially etched to avoid damaging the quantum wells and broadening the exciton. Sufficient confinement of the photonic mode was achieved by partial etching to generate discrete energy levels in the mesa, as can be seen from the far-field emission at low excitation power shown in Figure 6.3 in §6.1. Wires with widths varying between 4 and 8 µm were measured. The wire length was either 1000 µm ("long wires", used in most of Chapter 6) or 100 µm ("short wires", used in §6.6).

## 3.2 Sample cooling

The samples used for all experiments were cooled with liquid helium to temperatures between 4 K and 20 K. In most experiments, a continuous flow cold finger cryostat was used. In this system, liquid helium is continuously pumped through the cryostat where it vaporises, cooling the finger and the sample. Vibrations from the pump and the continous flow of helium introduced noise by vibrating the sample during experiments, however as the amplitude of the movement was on the order of 1 µm this did not inhibit the observation of nonlinear wavepackets where the smallest features were $\sim$ 4 µm wide (this was the width of

the narrowest wire used in Chapter 6). It may however have resulted in an overall broadening of the measurement emission in realspace as the measurements were integrated over the oscillation period. The large windows on this cryostat gave good optical access to the sample from both the front and back, enabling measurements to be carried out in either a reflection or a transmission configuration (§3.3.1).

For the experiments involving surface acoustic waves (Chapter 4), a bath cryostat was used to cool the sample. The higher cooling efficiency of this system was advantageous as the application of the SAW could otherwise heat the sample, inhibiting the formation of excitons. Use of this cryostat does however limit the duration of an experiment as the helium supply would run out 4-5 hours after the cryostat was filled, so it was not used for all experiments.

## 3.3 Optical Setups

For the experiments in this thesis, the cryogenically cooled samples (§3.1) are optically excited by a tunable continuous wave (CW) laser (chapter 4), a tunable pulsed laser (chapter 6), or both of these lasers (chapter 5). Components were added to the CW excitation path to control the size, shape (circular or elliptical) and polarisation of the laser beam (§3.3.2). The component of the wavevector in the plane of the quantum wells could also be controlled by changing the angle at which the incoming laser light hit the top DBR. The pulsed laser excitation path had similar functionality, but a pulse shaper was also added to fine-tune the pulse duration and energy (§3.3.3). For some sample characterisation measurements, the sample was pumped non-resonantly through the top DBR using a CW HeNe laser at normal incidence. The overall setup is illustrated in Figure 3.3 with a block diagram.

Emission from the sample could be collected from the top DBR in a reflection configuration (the sample is excited through the top DBR) or from the bottom DBR in a transmission configuration, provided that the emission was at a lower energy than the bandgap of the GaAs substrate (§3.3.1). The collection path (§3.3.4) could be configured to image the near-field (realspace) or far-field (k space) emission onto the entrance slit of the spectrometer. The emission could pass unaltered through the spectrometer to the detectors, or could be spectrally resolved using the spectrometer gratings (§3.3.6).

Throughout the experimental chapters, references are made to $x$ and $y$ directions. These refer to the in-plane axes on the sample and are aligned with sample features such as the trajectories of applied surface acoustic waves (Chapter 4) and the long ($x$) and short (y) axes of etched microwires (Chapter 6). The samples are mounted so that the $x$ axis corresponds to the *horizontal* direction in the laboratory frame (parallel to the optical bench) while the $y$ axis corresponds to the *vertical* direction in the laboratory frame (perpendicular to the optical bench). These axes are illustrated in Figure 3.4.

### 3.3.1 Transmission and Reflection configurations

Figure 3.3 shows an optical setup using a transmission configuration, where the excitation and collection paths use separate objective lenses on opposite sides of the sample. In this configuration, the sample is excited through the top DBR and the emission is collected from

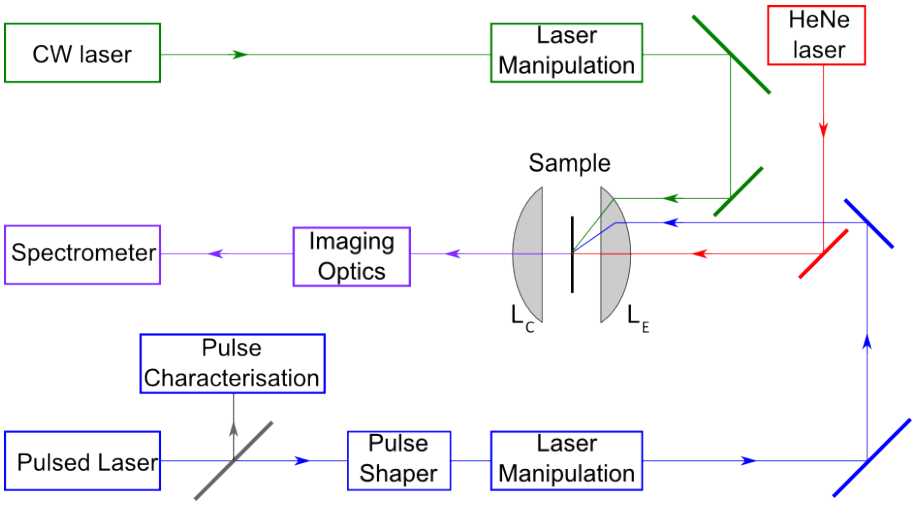


**Figure 3.3: Optical setup block diagram**. This diagram shows how the excitation and collection paths used for most experiments were laid out. Here, a transmission configuration is shown for clarity, but a reflection configuration was used for experiments in Chapters 4 and 5 where the excitation and imaging of the sample were done through the same objective lens (see §3.3.1). Here, lens $L_E$ is the objective lens used for excitation while lens $L_C$ is the objective lens used for collection. The sample is mounted in a cryostat as discussed in §3.2. The HeNe excitation path (red) is used to non-resonantly excite the sample while the CW and Pulsed laser paths (green and blue) are used to resonantly excite the sample. The "Laser Manipulation" blocks include components to control the size, shape, power and polarisation of the laser beam as shown in Figure 3.6. The "Pulse Characterisation" and "Pulse Shaper" blocks are shown in Figures 3.7 and 3.8 respectively. More details on the imaging optics (purple) are shown in Figure 3.10.

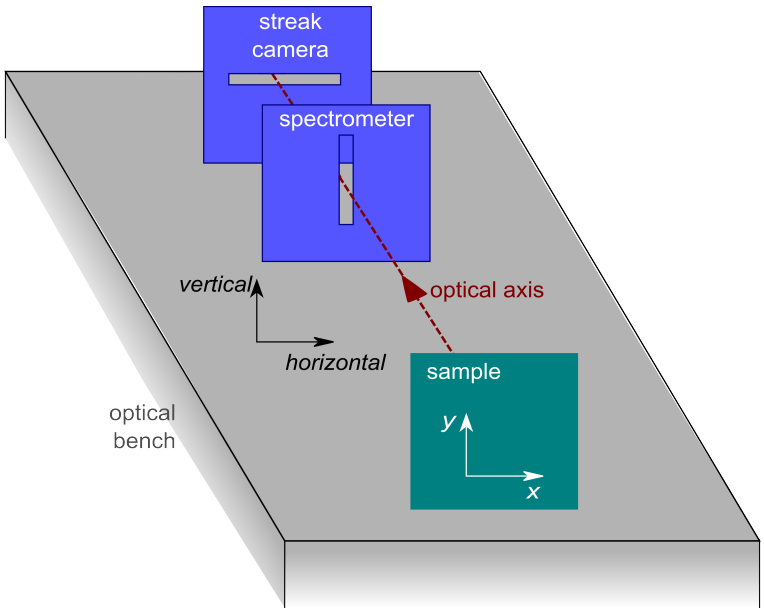


**Figure 3.4: Schemetic of Sample Orientation** showing the relationship between the $x$ and $y$ sample axes and the *horiontal* and *vertical* laboratory axes. The vertical slit on the entrance to the spectrometer and the horizontal slit on the entrance to the streak camera are also illustrated.

the bottom DBR through the GaAs wafer substrate. This setup requires the emission to be at a lower energy than the bandgap of the GaAs substrate (∼818 nm, ∼1.52 meV [165]) in order to be transmitted through, rather than absorbed by, the substrate.

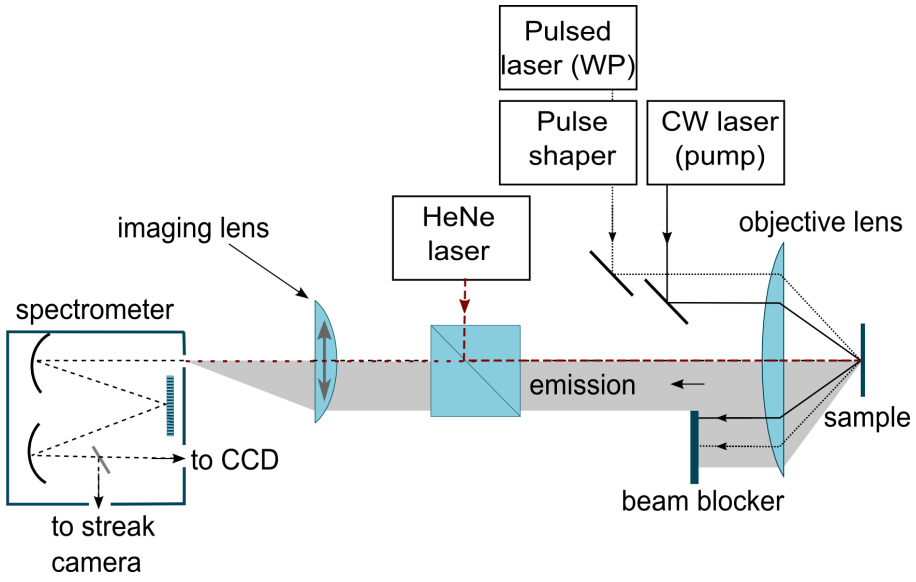


**Figure 3.5: Reflection Configuration.** The excitation and collection paths share the same objective lens. A beam blocker is used to block the resonant laser reflections so that they do not saturate the detectors.

Samples whose emission is at a higher energy than the GaAs bandgap can however be studied using a reflection configuration (Figure 3.5), where both the excitation and collection are done through the top DBR. The down-side to this configuration is that strong reflection of the excitation lasers from the sample surface can saturate and damage the detectors, so these must be reduced in the imaging path. A non-resonant laser reflection (such as that from the HeNe laser) can be filtered out using a long-pass filter which blocks light above a certain energy. This approach does not work with resonant excitation as the laser wavelength is too close to the emission wavelength. However, as the experiments presented in this thesis use resonant excitation at a high k vector, the laser reflection is offset from the main optical axis of the emission so can be blocked with a beam blocker as shown in Figure 3.5. This approach reduces the detectable range of k-space when compared to the transmission configuration but is still sufficient for many experiments, such as those presented in Chapters 4 and 5.

### 3.3.2 Continuous wave excitation

Continuous wave excitation of the sample is done with a Ti:Sapphire tunable laser (Coherent MBR-110). It can be tuned into resonance with the lower polariton branch and was used at wavelengths between 805 nm and 835 nm. The laser emits vertically polarised light, but the polarisation can be manipulated by using a half-wave plate to rotate the plane of linear polarisation, or by using a quarter-wave plate angled at 45° to the linear polarisation direction to convert to circularly polarised light. A linear polariser can be inserted before the wave-plates in order to clean the polarisation, as this could be distorted by optical elements in the setup; it is therefore desirable to place the polarisation control block as close to the

sample as possible. The excitation power is controlled using ND filters. The CW excitation path is illustrated in Figure 3.6.

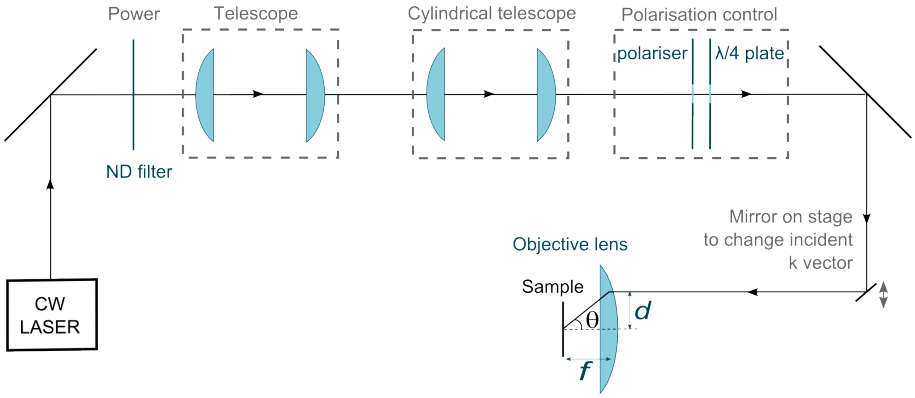


**Figure 3.6: Continuous Wave Excitation** including components to control the power, size, shape, polarisation and in-plane k vector of the laser beam hitting the sample. $f$ is the focal length of the objective lens while $d$ is the distance of the incident beam path from the optical axis of the lens.

The size and shape of the beam are controlled using two telescope blocks: the first magnifies the size of the laser spot on the sample while the second uses cylindrical lenses to compress the spot along the vertical axis, generating an elliptical spot elongated along the horizontal axis when required (this was used for experiments in §5.2) The component of the wavevector in the plane of the quantum wells can be controlled by changing the angle at which the incoming laser light hits the top DBR. All light beams which are incident on the objective lens parallel to the optical axis will be focussed to the same focal point on the optical axis, so light beams coming from a position away from the centre of the lens will arrive at the focal point with some angle $\theta$ given by $tan(\theta) = d/f$ where $d$ is the distance from the centre of the lens and $f$ is the focal length of the lens. The in-plane wavevector is then given by

$$k_{inplane} = \frac{2\pi}{\lambda} \sin\theta \tag{3.1}$$

where $\lambda$ is the wavelength of the laser light.

### 3.3.3 Pulsed excitation

Pulsed excitation of the sample is done using a pulsed Ti:Sapphire tunable laser (Spectra-Physics Tsunami). The laser can be set up to emit pulses with durations of $\sim$ 300 fs or $\sim$ 3 ps and the centre wavelength of these pulses can be tuned. A small portion of the laser light can be removed from the main path using a glass wedge or beam splitter: part of this is spectrally analysed to check the centre wavelength of the emitted pulse while part acts as a trigger for the streak camera measurement. With the laser in the ps regime, part of this light is also sent to an autocorrelator in order to check the pulse duration (see Figure 3.7).

For the experiments presented in this thesis, the laser pulses were passed through a pulse shaper in order to increase the pulse duration to $\sim$ 5 ps (see Figure 3.8). The pulse shaper works by using a slit to select a small region of energies out of the broadband laser emission,

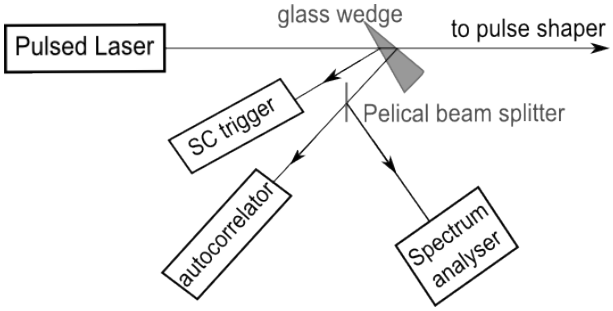


**Figure 3.7: Pulse characterisation**. A portion of the laser pulse is used to trigger the streak camera measurement. A second portion goes to the autocorrelator, which is used to measure the pulse duration in the ps regime. A third portion is sent to a spectral analyser which is used to check the approximate wavelength of the laser pulses. The rest of the laser beam goes on to the pulse shaper and the rest of the excitation path.

so the centre energy of the output pulse can be changed by moving the slit. The output pulse duration can be increased by narrowing the slit, as energy and time are conjugate variables (related by a fourier transform), so a decrease in the energy width corresponds to an increase in the pulse duration. For the experiments presented in Chapter 5, the laser was set up to emit 300 fs pulses, allowing significant tuning of the energy using the pulse shaper. Unless otherwise stated, the experiments in Chapter 6 were conducted with the laser emitting 3 ps pulses, increasing the laser power through the pulse shaper as more of the laser pulse is allowed through (see Figure 3.9). The laser beam can be split into multiple parts at other stages in the setup as required, for example to use one part as a reference beam in a phase measurement (§3.4.2) or to have two trigger pulses to inject two polariton wavepackets into the system (as for experiments in §6.3.3).

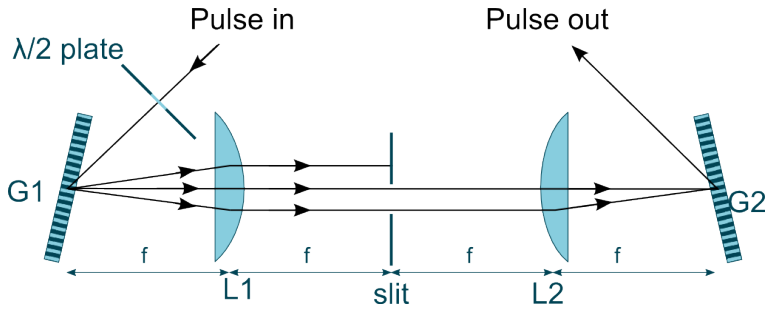


**Figure 3.8: Pulse shaper**. The $\frac{\lambda}{2}$ plate optimises the linear polarisation angle of the input pulse for the diffraction gratings. The laser is incident on grating G1 and the first diffraction maximum from the grating is sent along the pulse shaper. The beam is now split into energy components which are collimated by lens L1. The slit selects a small range of energies, lengthening the pulse: both the width and position of the slit can be adjusted to select the bandwidth and centre energy of the pulse. Lens L2 focusses the filtered laser onto grating G2 which recombines the energy components into a collimated output laser beam. The input pulse length was ∼300 fs (or ∼3 ps) while the output pulses are ∼5ps. f = 50 cm is the focal length of lenses L1 and L2.

The power, polarisation, size and in-plane wavevector of the pulsed excitation can be controlled in the same way as the continuous wave excitation (§3.3.2). The laser powers quoted in the experimental chapters are average powers $P_{av}$: the peak power in the pulse $P_{peak}$ can be found using $P_{peak} = P_{av}/(F\tau)$ where $\tau$ is the pulse duration (∼ 5 ps after the

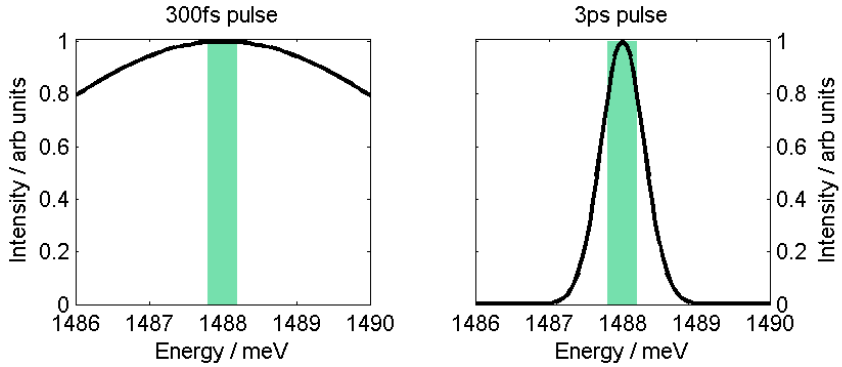


**Figure 3.9: Laser pulse profiles**. Intensity vs energy distribution for gaussian laser pulses of length 300 fs (left image) and 3ps (right image). The shaded rectangle indicates the energy range selected by the pulse shaper (∼0.4 meV) for a 5 ps WB pulse.

pulse shaper) and $F$ is the pulse repetition frequency of the laser (82 MHz). However, it is not known how much of the laser power reaches the cavity as some power is lost in the optical elements and some is reflected from the sample surface, so the quoted laser powers should not be taken as a measure of the absolute number of polaritons excited in the sample.

### 3.3.4 Imaging Optics

The near-field (realspace) and far-field (k-space) emission can be collected and focussed on the spectrometer slit using the setups shown in Figure 3.10. The image can be spectrally filtered by introducing components such as beam blockers at the focal plane of the objective lens while spatial filtering can be applied in a magnification stage as shown in Fig 3.10b. In a reflection configuration, one objective lens is used for both excitation and imaging while in a transmission configuration, separate objectives are used on each side of the sample (§3.3.1). In most experiments, the emission is recorded using a CCD or streak camera, although in some cases Avalanche Photo-Diodes were used in a Hanbury-Brown and Twiss setup (see §3.4.1).

### 3.3.5 Two-dimensional imaging

The streak camera images intensity as a function of time and horizontal position $x$. It can however be helpful to measure the intensity in two spatial dimensions as well as time (see, for example, the figures in §5.3). This can be done by taking a series of measurements, scanning the vertical position of the imaging lens between each one. This effectively moves the emission image over the horizontal slit at the entrance to the streak camera, measuring intensity along $x$ for each $y$. The two dimensional intensity profiles can then be reconstructed from this series of traces (Fig 3.11).

Intensity profiles (either along a line or integrated over some region) can be taken and gaussian peaks can be fitted in order to extract parameters such as the width of a wavepacket or the separation of several soliton peaks in a pattern, as in Chapter 5. For realspace imaging, the spectrometer slit can be widened to image an area $\sim 60$ μm wide. While this is sufficient for the measurements presented in Chapters 4 and 5, the nonlinear wavepackets observed

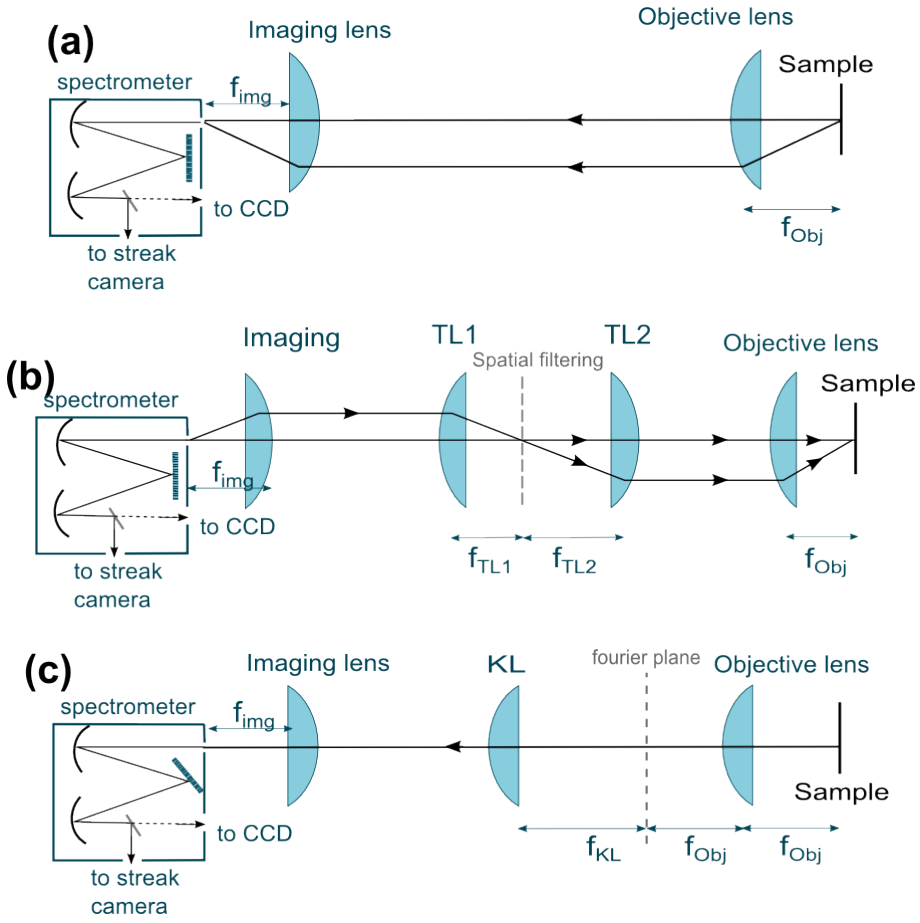


**Figure 3.10: Imaging optics**. **(a)** The sample emission is collected using the objective lens and focussed onto the spectrometer slit using the imaging lens. This pair of lenses images the realspace (near-field) intensity profile of the sample emission. **(b)** The image can be magnified using a telescope block (lenses TL1, TL2) and spatial filtering can be applied at the focal plane in the middle of the telescope. **(c)** the k-space (far-field) intensity profile can be imaged by adding an extra lens (KL) focussed on the fourier plane of the objective lens. $f_{img}$, $f_{Obj}$, $f_{TL1}$, $f_{TL2}$ and $f_{KL}$ are the focal lengths of the imaging lens, the objective lens and lenses TL1, TL2 and KL.

in Chapter 6 propagate for $\sim 200$ µm. In order to observe the whole propagation path, the imaging lens can again be moved, directing a different portion of the emission to the streak camera.

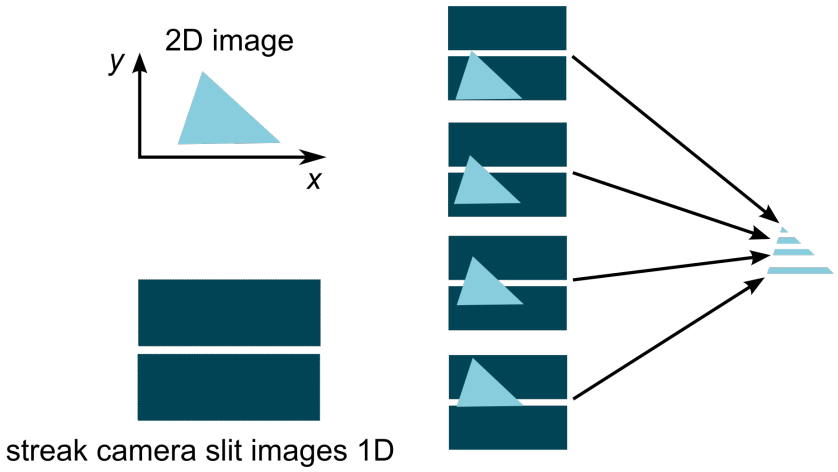


**Figure 3.11: Reconstructing images:** A two-dimensional spatial image can be recorded using a detector which only measures one spatial dimension. The image can be scanned over the detector slit so that a different section is selected in each measurement. The recorded data can be then be reconstructed from the recorded images.

A similar method can be used to measure energy dispersions as a function of $k_x$ and $k_y$ (in-plane wavevectors in the $x$ and $y$ directions). At the entrance to the spectrometer is a vertical slit. For spectrally resolved measurements, this is normally set to be narrow (0.1 mm wide) in order to select emission in a small range of $k_x$. The emission is diffracted from the grating so that components at different energies appear at different horizontal positions. This image can be directed towards the CCD to record the emission intensity as a function of energy (along the horizontal axis) and $k_y$ (vertical axis) for a given value of $k_x$. The imaging lens can again be scanned, changing the selected value of $k_x$ to generate a series of spectra from which an image of intensity as a function of energy and $k_x$ can be reconstructed.

The imaging lens was mounted onto automated translation stages. A LabVIEW program was used to scan the stages and record a series of measurements using the CCD or streak camera. Plots of intensity as a function of two parameters were reconstructed from this data set using Matlab. An example of this reconstruction is shown in Figure 3.12 where an E-$k_x$ spectrum is measured. The intensity versus energy at this $k_x$ for a particular $k_y$ (usually $k_y$=0) is extracted from the E-$k_y$ image recorded on the CCD (Fig 3.12a). This is repeated for many $k_x$ and the profiles are combined to form an image (Fig 3.12b). From this image, the positions of intensity maxima can be extracted to which a pair of polariton modes can be fitted to characterise the sample at this position.

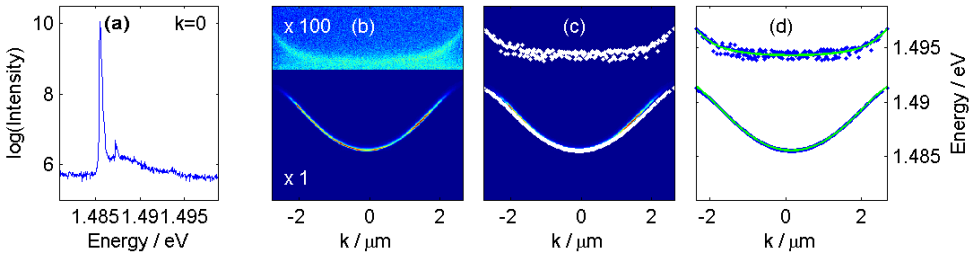


**Figure 3.12: Data processing example:** measurement of an E-$k_x$ spectrum. **(a)** Intensity as a function of energy at a given $k_x$ and $k_y$. **(b)** Combination of profiles (as shown in (a)) for different values of $k_x$ to form an E-$k_x$ spectrum. The upper part of the image has been magnified so that both polariton branches are visible. **(c)** Intensity peaks are extracted from the two dimensional image. **(d)** Polariton modes are fitted to the extracted peaks in order to characterise the polariton modes in this sample.

### 3.3.6 Detectors

The collected emission is focussed onto the input slit of a Horiba Triax320 monochromator/spectrometer. The spectrometer is used with a 1200 groove/mm grating to give a spectral resolution of 0.06nm (source: Horiba Triax320 data sheet). Real-space images can also be obtained by opening the spectrometer slit to its maximum value of 7 mm and using the grating at zero order. The spectrometer has two exit ports, so the emission can be directed either towards a Princeton Instruments Pixis 1024 CCD on one port or a Hamamatsu streak camera (model C5680) with a time resolution of 2 ps (source: Hamamatsu C5680 data sheet) on the other port in order to take time integrated or time resolved measurements (see Figure 3.10).

#### Streak camera operation

The operation of the streak camera is illustrated in Figure 3.13. The measurement is triggered by the laser pulse: a small portion of the laser light is detected using a PIN diode positioned after the laser as shown in Figure 3.7. The emission to be measured passes through a horizontal slit to a photocathode, which converts the photonic signal into an electrical one. The electrons are accelerated and swept vertically, so that photons arriving at different times are converted to electrons arriving at different vertical positions. A phosphor screen converts the electronic signal back to a photonic signal and the two-dimensional image is recorded. A time window of $\sim 120$ ps can be recorded with a resolution of 2 ps, while time windows of up to 2 ns can be recorded at a reduced resolution.

#### Photon counting mode

In normal operation, images recorded on the streak camera are integrated over many laser pulses: during a typical exposure time of 120 ms, emission excited by 10,000,000 laser pulses is recorded. In order to measure quantum properties, such as emission statistics and photon correlations (see §2.5), one needs to know which photons come from the same laser pulse. This information can be obtained using the streak camera's "photon counting" mode.

In this mode, one vertical sweep records the emitted photons from one laser pulse only. A second delay unit can be used on the streak camera to sweep the emission horizontally, so

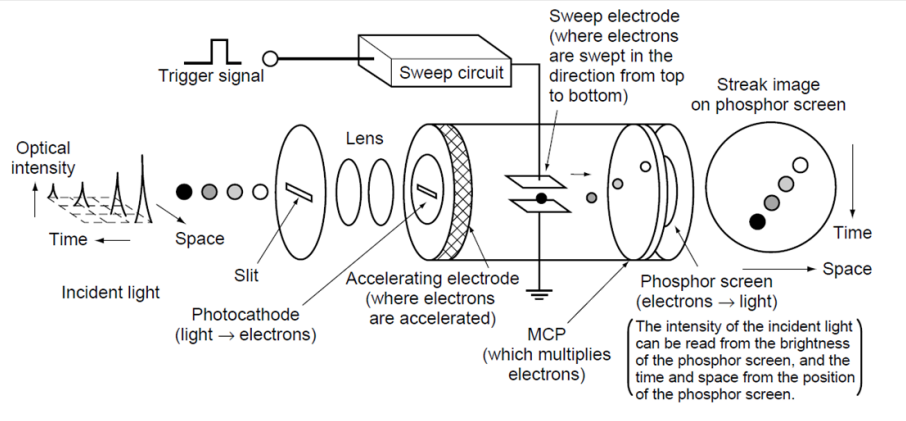


**Figure 3.13: Operating Principle of the Streak Camera**. Source: Hamamatsu C5680 data sheet

that emission from consecutive laser pulses appear at different horizontal positions on the detector. In the measurements presented in §6.5, the horizontal axis covers 200 ns while the vertical axis covers 110 ps. The horizontal sweep allows the separate detection of 15 laser pulses, each forming a different vertical streak. This increases the number of pulses which can be recorded. Many frames, typically 200000 in my measurements, are recorded in this way. The separation between each recorded frame is determined by the frame rate of the camera, which is this case is 6 ms. Any emission between the end of the nth frame and the start of the (n+1)th frame is lost, so this method of collecting emission is inefficient.

### Streak camera broadening

Traces measured on the streak camera can appear broader than they actually are due to the limited sampling rate and time resolution of the detector. The time resolution of the streak camera is about 2 ps, but for a wavepacket moving at $\sim 1\%$ of the speed of light, this can be a significant limitation. The solitons in this experiment typically move at 2-4 μm $ps^{-1}$: as illustrated in Figure 3.14, integrating the emission from a narrow wavepacket over a 2 ps time window can easily double the measured width.

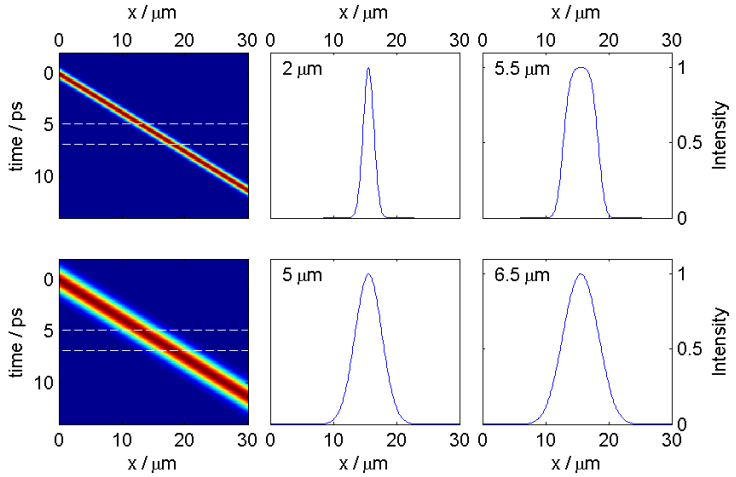


**Figure 3.14: Streak Camera Broadening. Left column:** Simulated streak camera image for a wavepacket propagating at a velocity of 3 μm ps$^{-1}$. White dashed lines show the boundaries of a 2 ps time window, corresponding to the resolution of the streak camera. **Middle column:** intensity profile of the "real" wavepacket with the width specified in the label. **Right column:** "measured" intensity profile, integrated over the 2 ps window. The "measured" width (FWHM) (see label on the image) appears broader the "real" wavepacket due to the limited resolution of the streak camera. The two rows show data for wavepackets of different widths. The broadening effect is more significant for narrower wavepackets.

## 3.4 Measurement Techniques

### 3.4.1 Hanbury Brown and Twiss

In a Hanbury Brown and Twiss setup, the emission is passed through a 50:50 beam splitter and the resulting 2 signals are each sent to an avalanche photodiode (APD) as illustrated in Figure 3.15. One APD acts as a trigger, so when a photon hits it a timer is started. When a photon hits the second detector, the timer is stopped and a count is recorded. In this way, the relative time of arrival of the 2 photons can be recorded. Once enough counts have accumulated, this trace can be used, for example, to look at the probability of the 2 photons arriving at the same time. This method can be used to measure the 2nd order autocorrleation function $g^{(2)}(\delta y, \delta t) = \langle I_{PL}(0,0), I_{PL}(\delta y, \delta t)\rangle$ to reveal bunching or antibunching behaviour (see §2.5.3).

In this work, an HBT setup is used in the SAW experiments (Chapter 4) to measure the dynamics of the emission intensity over time. While the streak camera reveals time resolved behaviour on the picosecond timescale (§3.3.6), this HBT setup records the behaviour on the nanosecond timescale. The HBT setup can be used to study the dynamics over a period of 50 ns, while the maximum time window for the streak camera is 2 ns.

The emission spot can be magnified so that only photons emitted from a small region are detected by each APD. The APDs can be made to focus on the same region by spatially filtering the emission image: inserting a pinhole at the focal plane of a telescope setup (see Figure 3.10) selects a small region of the realspace image. If this is comparable to the size of the APD detectors, they can be aligned to image the same spot by maximising the signal from the spatially filtered emission. The pinhole can be removed for measurements of the

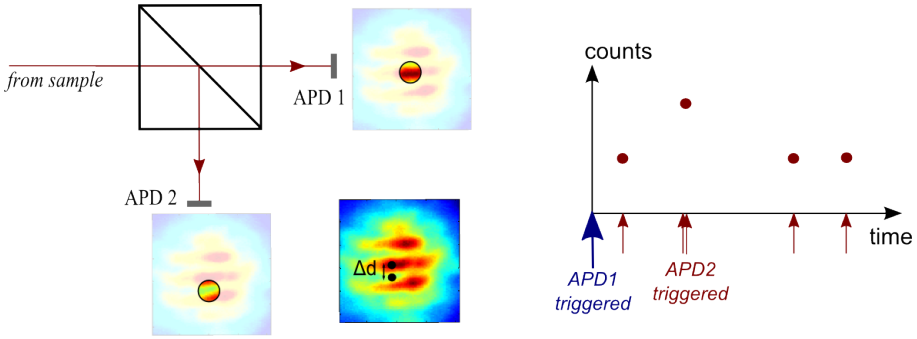


**Figure 3.15: Hanbury Brown and Twiss setup.** A beam splitter directs half of the emission to APD1 and half to APD2. A measurement is started when a photon arrives at APD1, then stopped when a photon arrives at APD2; the recorded count shows the time difference between the arrival of photons at the two detectors. The emission spot can be magnified so that only photons emitted from a small region are focussed onto each APD, allowing the correlations between photons emitted from different spatial positions (separated by $\Delta$d) to be measured.

correlations between photons emitted from different spatial positions on the sample.

### 3.4.2 Measurement of phase

Changes in phase across a realspace intensity profile can be measured by interfering the emission with a reference beam, ideally with a flat phase profile. Variations in the fringe pattern reveal changes in the relative phase between the emission and the reference beam. The period of the interference fringes can be reduced by introducing a difference in k vector between the emission and the reference beam: the higher number of fringes makes it easier to observe phase discontinuities, such as the fork-like dislocations which are characteristic of vortex-like behaviour [72] (see §2.2.4).

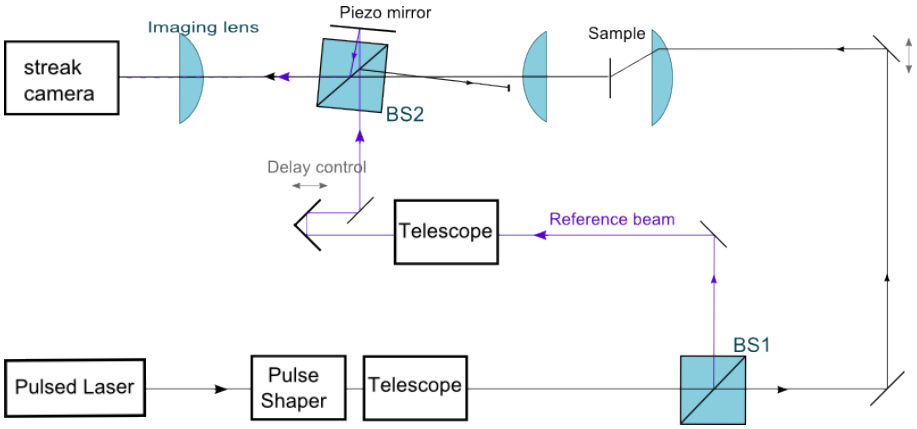


**Figure 3.16: Setup used for phase measurement.** The pulsed laser beam is split into two parts with beamsplitter BS1. One is directed to the sample as before while the other is used as a reference beam. This is expanded and recombined with the sample emission using beamsplitter BS2. The delay control stage is used to make sure the reference beam arrives at the same time as the emission from the sample. The piezo mirror provides a much finer delay stage used to scan the phase difference between the reference beam and the sample emission.

The reference beam and emission should have the same energy and be mutually coherent in order to observe a clear fringe pattern. This can be achieved by dividing the emission into

two parts using a beam splitter and using one part as the reference beam. The reference portion should be inverted, for example using a retroreflector, so that the phase profile across the two beams is not identical as the relative phase between the emission and the reference would then be the same at each spatial position. This method can be useful for revealing localised discontinuities such as vortices [72], although it may be harder to see more extended phase variations using this method.

An ideal reference beam will have a constant phase over its spatial profile, making it clear that changes in relative phase come from the emission rather than the reference. For the phase measurements presented in §6.4, the pulsed writing beam (WB) is split into two parts: one is used for excitation while the second is used as the reference. The reference beam was expanded by a factor of 6 in order to reduce the gradient of any phase changes across the spatial profile. The emission from the sample and the reference beam were recombined as they were focussed onto the streak camera as illustrated in Fig 3.16.

The interference fringe pattern can be made clearer by subtracting a background which consists of the overall intensity profile of the wavepacket emission and reference beam. This background profile can be found by summing over several streak camera traces where the relative phase between the wavepacket emission and reference beam is changed. This effectively averages out the interference pattern. Due to timing jitter in recording the streak camera images, the intensity profile across the wavepacket is a little smeared out compared to the single streak camera images, however the contrast between the interference fringes and the background intensity profile is significantly improved. This processing is illustrated in Figure 3.17.

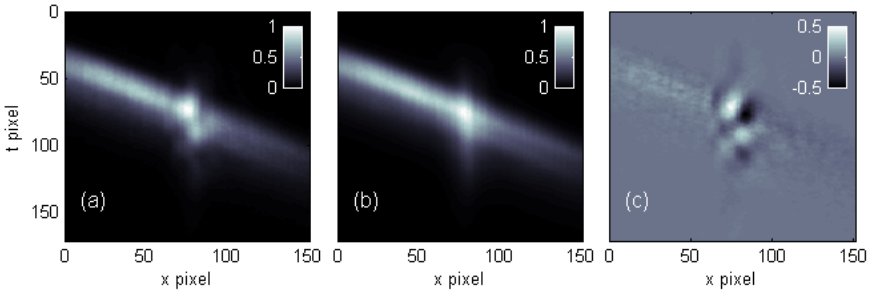


**Figure 3.17: Phase measurement: background subtraction.** **(a)** Streak camera image showing the interference of wavepacket emission with a reference beam. **(b)** Background, found by averaging over 101 streak camera traces where the relative phase of the emission and reference beam was steadily increased between traces. **(c)** Result of subtracting the backgroud in (b) from the streak camera trace in (a).

### 3.4.3 Measurement of $g^{(2)}$ using streak camera

Correlations between pairs of photons can be observed by measuring the time dependent second order correlation function $g^{(2)}$ as discussed in §2.5.3. The $g^{(2)}$ function is often measured using an HBT setup (see §3.4.1), however the nanosecond resolution of this setup makes it inappropriate for measuring the nonlinear wavepackets investigated in Chapter 6 of this thesis, which exist and evolve over a timescale of ∼100 ps. The streak camera provides an alternative method for measuring $g^{(2)}$ and its picosecond resolution enables the

measurement of the evolution of $g^{(2)}$ over 100 ps (results presented in §6.5).

As explained in §3.3.6, the streak camera can be used in "photon counting mode" where emission from different laser pulses is recorded separately. Correlations can then be measured within a given laser pulse. As the arrival time of each photon is recorded, this method can also be used to measure the emission statistics by finding the ratio between the variance of count rates in different time intervals and the mean count rate: a ratio of less than one is known as sub-Poissonian statistics and is an indication of non-classical behaviour as discussed in §2.5.2.

The $g^{(2)}$ function of the wavepacket emission was measured using the streak camera, following the method used by Aßmann *et al* [166]. Using the photon counting mode of the streak camera, emission triggered from 15 consecutive laser pulses is recorded in each exposure where each pulse appears in a different horizontal position within the recorded frame. In a single measurement, typically 200,000 frames are taken.

In order to claim an observation of, for example, antibunching behaviour, one needs to demonstrate both that $g^{(2)}(0) < 1$ and that $g^{(2)}(0) < g^{(2)}(t \gg 0)$. In order to check the second condition, correlations between photons emitted in the time window of interest and those emitted at some later time must be measured. Due to the limited field of view in the experiment, emission from the same wavepacket at a later time could not be recorded. Instead, correlations were measured between photons in neighbouring pulses (separated by $\sim 12$ ns) to check that these uncorrelated photons gave a normalised $g^{(2)}(t \gg 0) \sim 1$.

The measured second order correlation function will be referred to as $g^{(2)}(p)$ to emphasise that it measures correlations between different laser pulses. This is calculated as

$$g^{(2)}(p=0) = \frac{\langle n_{p1}\ (n_{p1}-1)\rangle}{\langle n_{p1}\rangle^2}$$
$$g^{(2)}(p\neq 0) = \frac{\langle n_{p1}\ n_p\rangle}{\langle n_{p1}\rangle\ \langle n_p\rangle} \tag{3.2}$$

where $n_{p1}$ is the number of photons recorded in pulse $p_1$ and $n_p$ is the number of photons recorded in pulse $p$. As will be described below, initially $g_s^{(2)}(p_1, p_1 - p)$ is calculated over a subset $s$ of the total number of exposures F. This is averaged over the subsets $s$ and the pulses $p_1$ to find $g^{(2)}(p)$ .

For each frame *f*, a time bin of 13 ps for each laser pulse is selected, excluding any photons detected outside this range (see Fig. 3.18). The photons pairs between pulse ($p_1$) and pulse ($p_1 - p$) for $1 \leqslant p_1 \leqslant 5$ and $-5 \leqslant p \leqslant 5$ are counted, as well as the number of photons $n_{f,p}$ for each pulse in the frame. The pair count and photon count are summed over F frames to get a value for $g_s^{(2)}(p_1, p_1 - p)$ as shown in Equation 3.3. For the case where $p_1 = p$, the pair count is doubled in the calculation of $g_s^{(2)}(p_1, 0)$ [166].

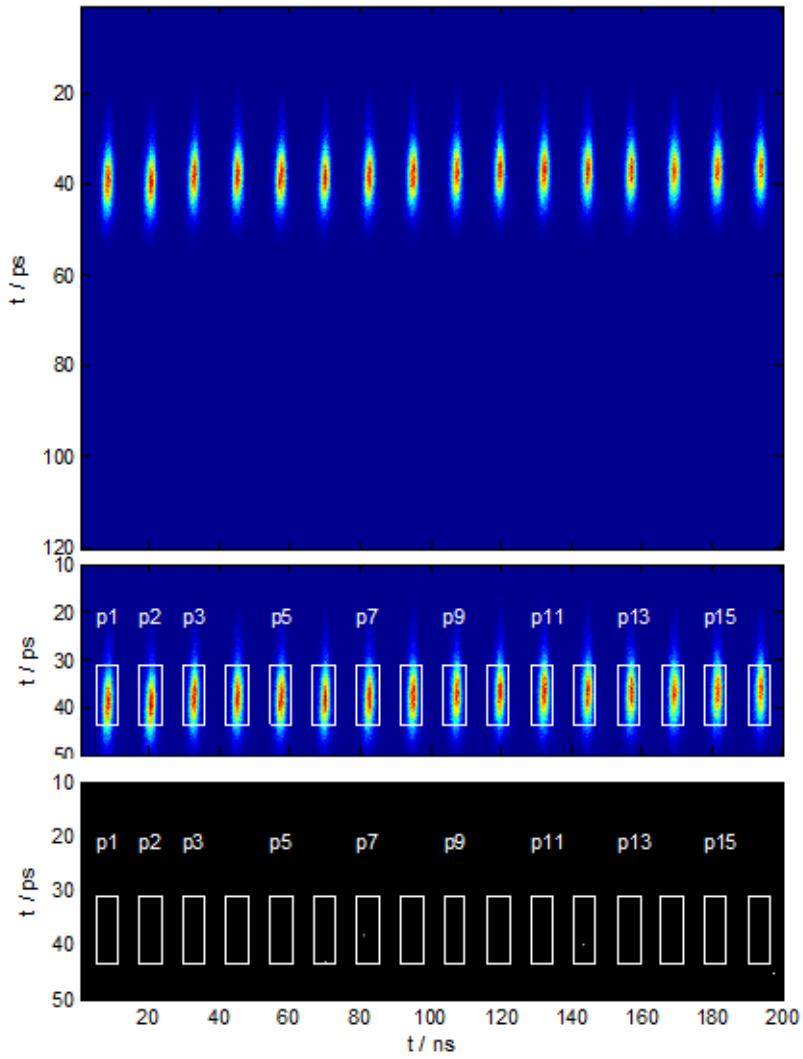


**Figure 3.18: $g^{(2)}(p)$ processing: selection of pulses. Top:** counts from all frames. The pulses at different horizontal positions correspond to different laser pulses. **Middle:** Selection of regions of interest. **Bottom:** a typical single frame. Photons outside of the marked regions of interest are not considered.

$$g_s^{(2)}(p_1, p_1 - p) = \begin{cases} \dfrac{\sum_{f=(s-1)F+1}^{sF} (n_{f,p1})(n_{f,p1} - 1)}{\frac{1}{F}\left(\sum_{f=(s-1)F+1}^{F} n_{f,p1}\right)^2} & \text{if } p_1 = p \\ \dfrac{\sum_{(s-1)F+1}^{sF} (n_{f,p1})(n_{f,p})}{\frac{1}{F}\left(\sum_{f=(s-1)F+1}^{F} n_{f,p1}\right)\left(\sum_{f=1}^{F} n_{f,p}\right)} & \text{if } p_1 \neq p \end{cases} \tag{3.3}$$

Initially, F was taken to be the total number of exposures, however in some cases the measured value of $g^{(2)}(p \gg p_1)$ was higher than 1. Further investigation revealed that in these measurements, a significant slow variation in the photon count rate (attributed to a drift in the laser intensity) meant that the $g^{(2)}(p)$ function was incorrectly normalised, resulting in an increase in the measured value. A more reliable calculation could be made by averaging over subsets of frames $s$ with a constant count rate. For this reason, a value of F = 5000 was used to calculate $g_s^{(2)}(p_1, p_1 - p)$ for each subset s. In the plots shown in Fig. 6.19, an average is taken over 40 subsets s and 5 streaks p1 to get $g^{(2)}(p)$.

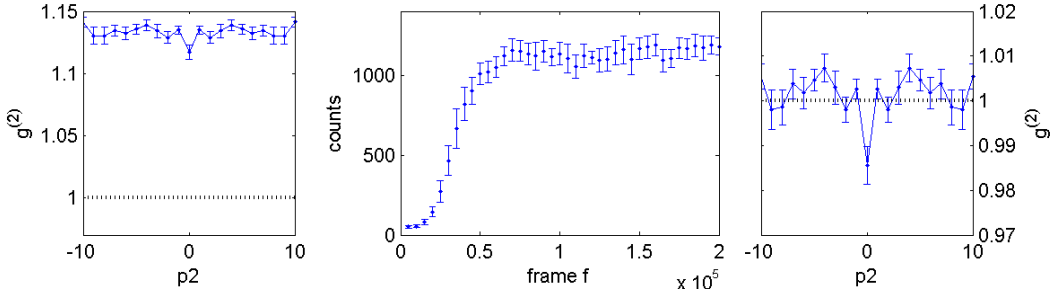


**Figure 3.19: Effect of varying count rate**. **Left image:** $g^{(2)}(p)$ where F was taken to be the total number of exposures (200,000). The high value of $g^{(2)}(|p| \gg 0)$ shows that there is some problem with normalisation. **Middle image:** variation in count rate during the acquisition of 200,000 frames. **Right image:** $g^{(2)}(p)$ where F was taken to be 5000. Here, $g^{(2)}(p)$ is an average of 40 values of $g_s^{(2)}(p)$ taken for each subset s of 5000 frames.

As can be seen from Figure 3.18, emission from many pulses is recorded in each streak camera frame, so only a narrow portion of the emission along the horizontal direction can be collected. These measurements were therefore taken by detecting the far-field (k space) emission (Figure 3.10c), which was narrow along the horizontal direction. Telescope elements were introduced in order to shrink the image so that as much emission as possible was passed through the streak camera slit in each measurement.

# Chapter 4

# Phonon-Assisted Scattering in Gap Soliton Formation

There has been much interest in the behaviour of polariton OPO condensates in periodic potentials [44, 42, 79, 41, 43, 167] (see §2.2.5), more recently in the context of gap solitons [81, 150] (see §2.4.3 for more on gap solitons). Rather than forming at k=0 (an S state) as in the case of a planar cavity with no potential modulation, the condensate instead forms at multiple non-zero k vectors (S' states) defined by the period of the potential modulation. Several mechanisms for this have been proposed (see §4.2.4), however these do not necessarily explain all of the observations reported in the literature.

Cerda-Mendez *et al* have done considerable work using a Surface Acoustic Wave (SAW) to generate a periodic potential in one [41] and two [43, 81] dimensions. In this case, the periodic potential moved across the sample as the SAW propagated (see §3.1.1). Time resolved measurements have shown an oscillation in the polariton density at a given spatial position over time [41]. This was attributed to the fact that the condensate density was modulated into "wires" by the potential, which were pulled across the detection spot by the propagating SAW.

An alternative description of this modulation is that it arises from the interference of two plane wave states $\psi_a = Ae^{i(\boldsymbol{k_a}\cdot\boldsymbol{r}-\omega_a t+\phi_a)}$ and $\psi_b = Be^{i(\boldsymbol{k_b}\cdot\boldsymbol{r}-\omega_b t+\phi_b)}$. The resulting intensity pattern is $I = |\psi_a + \psi_b|^2$, giving:

$$I = A^2 + B^2 + 2AB\cos(\Delta\boldsymbol{k}\cdot\boldsymbol{r} - \Delta\omega t + \Delta\phi) \tag{4.1}$$

where $\hbar\Delta\omega$ is the energy difference, $\hbar\Delta\boldsymbol{k}$ is the in-plane momentum difference and $\Delta\phi$ is the phase difference between the states. This describes a modulation in $\mathbf{r}$ with period $2\pi/\Delta\boldsymbol{k}$ and an oscillation in time with frequency $\Delta\boldsymbol{\omega}$. For waves with equal amplitude ($A = B$), the minima in the modulation go down to zero while for waves with different amplitude ($A \neq B$) the modulation appears on top of a finite background. While several proposed mechanisms give explanations for the choice of k vectors of the condensate states, an energy difference between them is not explained. In addition, the modulation will be averaged out unless the two states have a fixed phase difference $\Delta\phi$; they should be mutually coherent for a visible pattern. SAWs have been investigated in other systems for their uses in applications

including single electron transport [168, 169], control of magnetisation properties [170, 171] and chemical sensing [172, 173]

In this chapter, I investigate the role played by the phonons constituting the SAW in selecting the states in which the condensate forms. Once the setup is tested (§4.1), the work done by Cerda-Mendez *et al* is built on by carrying out investigations of the interference between the S' states with a SAW applied in the y direction (y-SAW) (§4.2.1). It is proposed that the energy separation between the S' states as well as the mutual coherence between them may be explained by a mechanism of phonon-assisted scattering (§4.2.2) and the predictions of this theory are tested by taking measurements when a SAW in the x direction (x-SAW) is applied in addition to the y-SAW (§4.2.3). Further observations reveal additional modulation patterns (§4.3), which are attributed to a contribution to the phonon assisted scattering process from a reflection of the SAW from features on the sample surface. The influence of the small reflected SAW demonstrates the possibility of creating a stationary spatial modulation in the condensate population by combining the applied SAW with one which is reflected from structures on the sample surface.

## 4.1 Application of a SAW

In order to test that the experimental setup worked as expected, a SAW was applied in one dimension to a low polariton population and the far-field emission was recorded and compared to observations seen in the literature. A 50 μm wide spot on the sample was optically excited with a continuous wave (CW) pump laser with a power of 2 mW. The pump laser energy was 1.5386 eV (2.3 meV higher than the lower polariton branch (LPB) at $\mathbf{k}$=0) and was tuned into resonance with the LPB at a k vector of around ($k_x$,$k_y$) = (2.4,0) $\mu m^{-1}$. A SAW was applied in the y direction (y-SAW) and the (E, $k_y$) spectrum for emission at $k_x$=0 was recorded.

#### Low excitation power

The initial experiment was carried out on a low density polariton population where a range of states on the LPB is populated. As the SAW power is increased from zero, the spectrum changes from the usual LPB as the dispersion becomes folded (Figure 4.1). The low energy branches are redshifted compared to the case with no SAW while energy gaps appear at $k_y \sim \pm\frac{k_{SAW}}{2}$. The positions of the dispersion peaks as the SAW amplitude is increased are shown in Figure 4.1a. The dispersions remain unchanged for low SAW powers, but above a threshold the energy gap between the two states at the edge of the mini brillouin zone (MBZ, see §2.1.3) increases linearly with SAW amplitude at a rate of 0.04 meV $mW^{-\frac{1}{2}}$ (Fig 4.1c). The initial flat response indicates that there may be an offset between the power reading on the RF generator that drives the SAW and the power output from the generator. By design, $\lambda_{SAW}$ is 8μm [41], corresponding to a k value of $k_{SAW} = \frac{2\pi}{\lambda}_{SAW} = 0.8\mu m^{-1}$. Gaps should therefore appear at around $k_y = \pm$ 0.4 $\mu m^{-1}$, which is consistent with the experimental observations (Figure 4.1f). The low energy branches appear flattened compared to the case with no SAW, indicating localisation of the polaritons. Modelling the SAW as a population of coherent phonons, as done by De Lima *et al* [44], predicts the redshift of the LPB. Here,

the k=0 peak redshifts with increasing SAW amplitude at a rate of 0.03 meV $mW^{-\frac{1}{2}}$ as shown in Fig 4.1b .

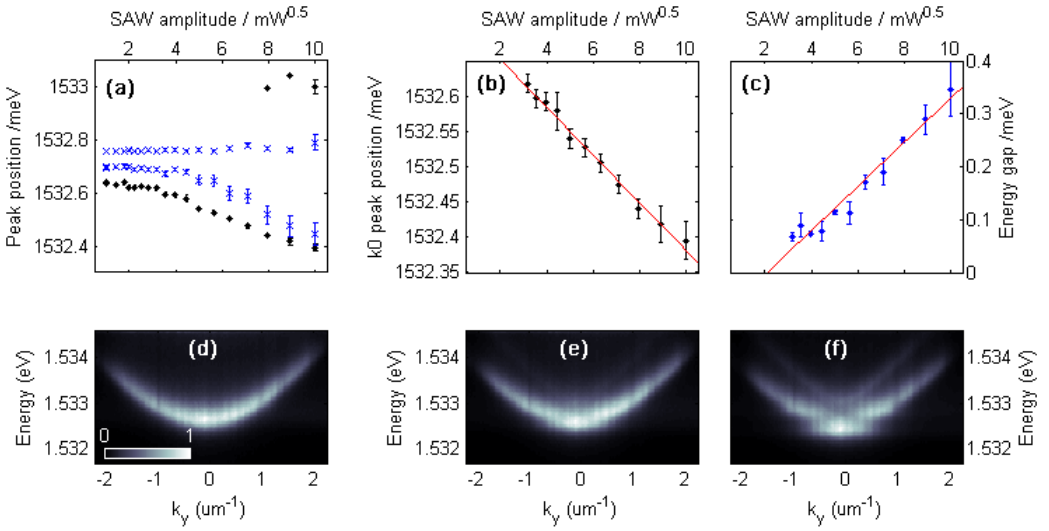


**Figure 4.1: Dispersion, increase SAW power:** Effect on dispersion with low optical excitation power as SAW power is increased. **(a)** Energies of the main peaks with increasing SAW amplitude. Black dots show the energies of emission integrated over $-0.1 \leq k_y \leq 0.1$ while blue crosses show the energy peaks integrated over $-0.55 \leq k_y \leq -0.35$, $0.35 \leq k_y \leq 0.55$. **(b)** Energy of the peak at $-0.1 \leq k_y \leq 0.1$, showing redshift at a rate of 0.03 meV $mW^{-\frac{1}{2}}$. **(c)** Width of energy gap between two peaks at the edges of the MBZ ($-0.55 \leq k_y \leq -0.35$, $0.35 \leq k_y \leq 0.55$) increasing at a rate of 0.04 meV $mW^{-\frac{1}{2}}$. **(d-f)** Example dispersions with SAW amplitudes of 0 $mW^{\frac{1}{2}}$ , 4 $mW^{\frac{1}{2}}$ and 8 $mW^{\frac{1}{2}}$

Each branch of the folded dispersion actually corresponds to a 2-dimensional E-**k** spectrum, leading to multiple LPB branches in the transverse direction. If the SAW is instead applied in the x-direction (x-SAW), the (E, $k_y$) spectrum therefore shows LPB curves appearing at different energies, but crossing and dispersion folding is not seen (Figure 4.2c).

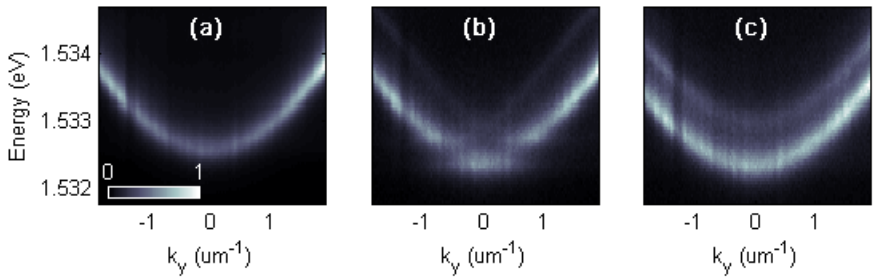


**Figure 4.2:** E-$k_y$ dispersion under low power excitation with (a) no applied SAW, (b) a y-SAW and (c) and x-SAW. Dispersion folding is seen in the dimension parallel to the SAW propagation (i.e. for the y-SAW) while the dispersion perpendicular to the SAW propagation (i.e. for the x-SAW) shows multiple shifted LPBs.

### High excitation power

The experiment with a y-SAW was repeated on a high density polariton population where the polaritons are condensed at ($k_x$, $k_y$) = (0,0) when no SAW is applied. Here, the optical excitation power is increased to 200 mW and $k_x$ is reduced to 1.9 $\mu m^{-1}$. As the SAW power is increased, high density states form instead at $k_y \sim \pm\frac{k_{SAW}}{2}$; these are termed S' states. As the SAW power is increased further, the polaritons start to spread over the bottom of the LPB instead of being concentrated in well defined states (Fig 4.3, left column). This has been seen previously [41] and can be explained by the increasing level of confinement in realspace: increasing localisation in realspace gives a broader spectrum in k space due to the fourier relationship between the two properties (see Appendix A).

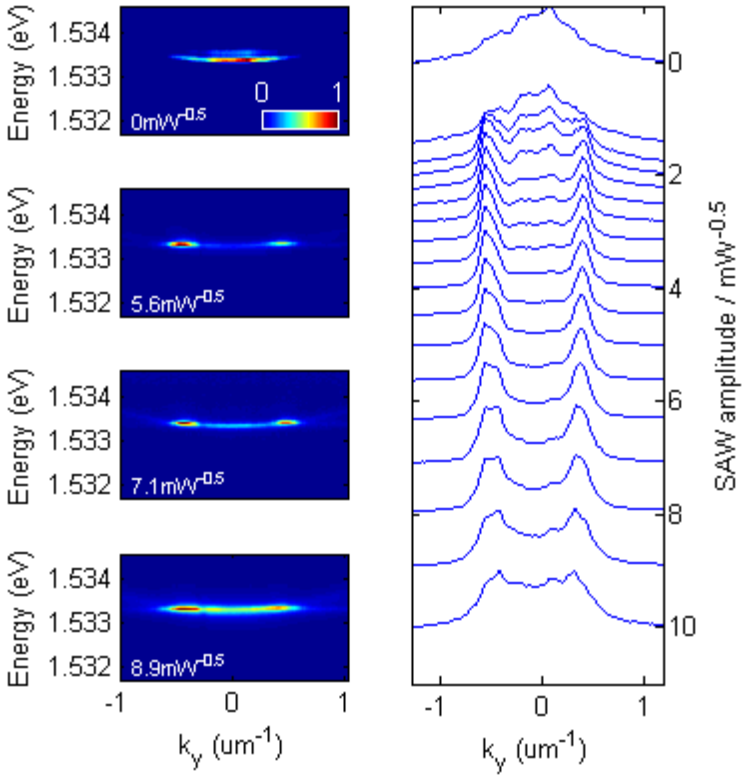


**Figure 4.3: Condensate states, increasing SAW power. Left column:** Intensity distribution over $k_y$ and energy at $k_x$=0. White labels show the amplitude of the SAW for each measurement. **Right column:** Intensity as a function of $k_y$ as a function of SAW amplitude, integrated over energy.

At high SAW powers, it appears that the k vector of the S' state can decrease slightly (Fig 4.3, right column). This effect has been observed by Cerda-Mendez *et al* [81] where it was used to support their claim that the k-space configuration of the states is determined by the polariton density distribution and the SAW amplitude rather than by interactions between the main pump state and its replicas. A discussion of different mechanisms for the formation of S' states will be given in §4.2.4

In addition to measurements of the (E,$k_y$) spectrum, k-maps showing the polariton density at different ($k_x$,$k_y$) states were also recorded for different SAW configurations. With

no SAW, the condensate forms at ($k_x$,$k_y$)= **0** (Fig. 4.4a). With 1 SAW, the condensate forms at ($k_x$,$k_y$)= ($\pm\frac{k_{SAW}}{2}$,0) or ($k_x$,$k_y$)= (0,$\pm\frac{k_{SAW}}{2}$) for an applied x-SAW and y-SAW respectively (Fig. 4.4(c,b)).

With both SAWs on, the condensate states can form either in these positions or at ($k_x$,$k_y$)= ($\pm\frac{k_{SAW}}{2}$,$\pm\frac{k_{SAW}}{2}$) i.e. at the corners of the MBZ (Fig. 4.4(d-f)). The position at which they form seems to depend on the optical pump power, although the power dependence was not explicitly measured. A similar effect has been seen in a static case where it was shown that at different pump powers, states with different symmetries (which appear with different k distributions) become favourable [79] (see §2.2.5). The formation of the states in the corners (Fig. 4.4f) suggests that two phonons are involved: one from the x-SAW and one from the y-SAW. Each of these can be either emitted or absorbed. An alternative process is that only one phonon is absorbed (or emitted) which is a superposition of an x-SAW phonon and a y-SAW phonon. States created in this way would form a circle in k space, which is visible in Fig. 4.4e. As expected, the corner states in which two phonons were absorbed have a larger $|\mathbf{k}|$ so fall outside this circle.

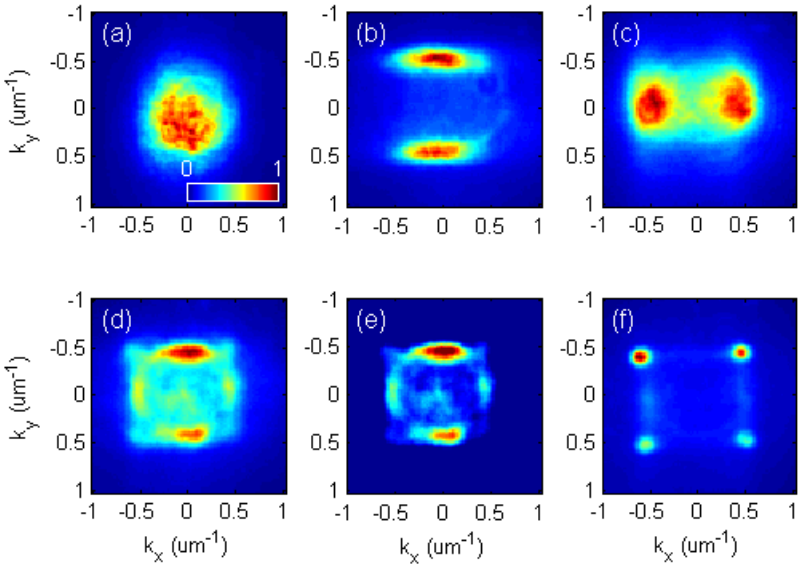


**Figure 4.4: 2D k space maps** with high power optical excitation. **(a)** No SAW is applied. **(b)** A y-SAW is applied with amplitude 4.0 $mW^{\frac{1}{2}}$ **(c)** an x-SAW is applied with amplitude 4.5 $mW^{\frac{1}{2}}$. **(d-f)** Both an x-SAW and a y-SAW are applied with amplitude 5.0 $mW^{\frac{1}{2}}$. (d) and (e) show the same data, but in (e) the image is renormalised to highlight the pattern at the edges.

Another factor which could have an effect on the **k** at which the condensate states form with two SAWs is screening of the potential by the polariton population. This has previously been shown to have a significant effect at high optical pump power [167]. The SAW generates a periodic potential and the polaritons accumulate at the lowest energy points, but the higher polariton density then increases the energy at those points due to polariton-polariton repulsion. The SAW potential is thus screened as the polariton population essentially generates a second periodic potential in antiphase with the SAW potential. In the 2-SAW experiment, there is a small region where the x-SAW and y-SAW overlap to generate the

2D lattice potential and it is here where the excitation spot is centred. The overlap region then has the highest polariton population and the largest degree of screening. Around the edges of the excitation spot, only one SAW will have a significant amplitude. Emission from these regions could dominate the position of the S' states as the lower polariton population would mean that the periodic potential was stronger here. If the power is reduced slightly, the screening effect is weaker so the polaritons condense in the corner states.

If this mechanism was active, the polaritons at the centre of the excitation spot would be expected to emit either in the corner states (if the potential is not screened) or around k=0 (where the potential is screened). This emission should have a higher intensity than the states at the edges of the MBZ which would come from the edges of the excitation spot. In the case of Fig. 4.4e, the highest emission intensity is from the states at the edge of MBZ suggesting that these states form at the point with highest polariton density. On the other hand, as can be seen in Fig. 4.4d, there is emission around $\mathbf{k}$=0 and the corner states (Fig. 4.4d). The integrated emission intensity for all these states is $\sim 70\%$ of the emission intensity integrated over the edge states. This suggests that for Fig 4.4(d,e), there are states which have absorbed 0 phonons, 1 phonon and 2 phonons while in Fig 4.4f the emission is dominate by states which have absorbed 2 phonons. It is not clear how the k states are selected, although it is possible that screening could play some role.

## 4.2 Intensity Correlations

Time resolved oscillations in the polariton density at a point have been observed in previous experiments in the high density regime [41]. Here, these results are replicated by recording all emission at angles of up to 15° when a y-SAW is applied. An alternative mechanism is proposed and its predictions are tested with measurements when both an x-SAW and a y-SAW are applied simultaneously.

### 4.2.1 Measurements with a y-SAW

In order to compare the phase of the spatial modulation induced by the SAW at different positions within the condensate, a Hanbury Brown and Twiss setup (§3.4.1) was used to measure the classical second order intensity auto-correlation function $<I(y,t)\, I(y+\delta y, t+\delta t)>$ between two small spots separated by $\Delta$d (see Figure 3.15) [41]. Measurements were initially taken with both detectors pointing at the same 2μm spot ($\Delta$d=0) to observe temporal oscillations in emission intensity. By comparing the phases of traces as $\Delta$d was gradually increased from 0-12 μm along y, it was possible to observe the propagation of high polariton density regions across the sample. Fig. 4.5a shows temporal oscillation at $\omega_{\mathrm{SAW}}$ while the change in oscillation phase as $\Delta$d is increased shows spatial modulation with period $\lambda_{\mathrm{SAW}}$ (Figure 4.5b).

The measurements in Figure 4.5 replicate previous observations by Cerda-Mendez *et al* [41], showing a modulation in polariton density with the period and frequency of the SAW which propagates across the sample at the velocity of the SAW (3000 $\mathrm{ms}^{-1}$[41]). Cerda-Mendez *et al* [41], describe this as condensate "wires" being pulled across the sample as they are localised in the propagating potential minima induced by the SAW. These observations

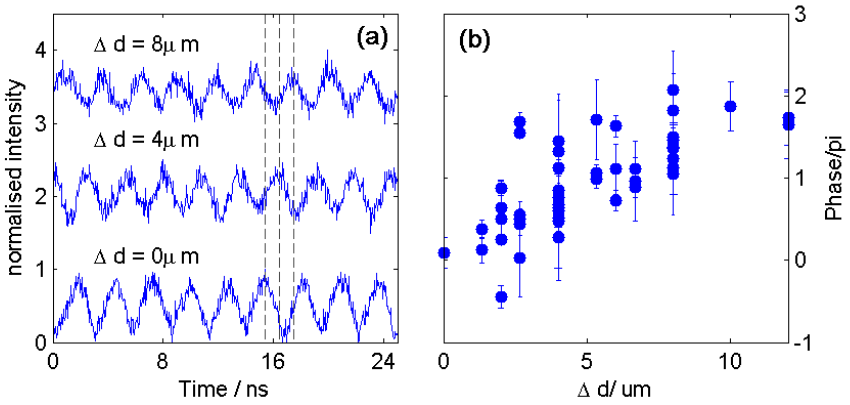


**Figure 4.5: Time resolved oscillations. (a)** Time resolved intensity oscillations at a given point on the sample for three values of the relative detector position, $\Delta$d. Grey dashed lines are a guide to the eye, indicating the position of an intensity maximum for each trace. **(b)** Change in the phase of the modulation at time t=0 as $\Delta$d is increased.

can also be described as interference between 2 states separated by energy $\hbar\omega_{SAW}$ and k vector $k_{SAW}$ (see Equation 4.1 at the beginning of this Chapter). This leads me to consider a new mechanism in which phonons are absorbed during an OPO scattering process (see §4.2.2).

In such a phonon-assisted scattering process, the SAW acts as a reservoir of coherent phonons which can be absorbed or emitted during the OPO scattering process. This mechanism results in the state at $+\frac{k_{SAW}}{2}$ gaining an energy of $\frac{\hbar\omega_{SAW}}{2}$ compared to the case with no SAW while the state at $-\frac{k_{SAW}}{2}$ loses $\frac{\hbar\omega_{SAW}}{2}$. The resulting states thus have ($k_y$,$\Delta$E) = ($+\frac{k_{SAW}}{2}$,$\frac{\hbar\omega_{SAW}}{2}$ ) and ($-\frac{k_{SAW}}{2}$,$-\frac{\hbar\omega_{SAW}}{2}$) where $\Delta$E is the increase in the energy of a state due to the application of the SAW. Phonon-assisted scattering could also account for mutual coherence between the S' states as each of them is linked to both idler states.

### 4.2.2 Phonon assisted scattering

The condensate is generated by Optical Parametric Oscillation (OPO, see §2.2.1): a pump is applied with $\mathbf{k_P}(k_x, k_y) = (k_p, 0)$ on resonance with the LPB generating a reservoir of polaritons at the pump k vector where x and y are the in plane axes. With no SAW, pairs of polaritons scatter parametrically to a signal state with $\mathbf{k_S} = (0, 0)$ and an idler state with $\mathbf{k_I} = (2k_p, 0)$. In this event, the energy, momentum and phase of the pump polaritons are conserved as they scatter to the signal and idler states.

When 1 SAW is applied, it acts as a reservoir of coherent phonons with energy $\hbar\omega_{SAW}$ and momentum $\hbar\mathbf{k_{SAW}}$. For ease of illustration, consider first the case where the SAW is applied in the y direction, so $\mathbf{k_{SAW}} = (0, k_{SAW})$. A schematic of the process is shown in Figure 4.6.

During the parametric scattering event, a phonon can be absorbed from the reservoir, so now the energy and momentum of two pump polaritons plus a phonon must be shared between the resulting signal and idler polaritons. A possible resulting signal-idler pair would have $\mathbf{k_{S2}}, = (0, +\frac{k_{SAW}}{2})$ and $\mathbf{k_{I2}}, = (2k_p, +\frac{k_{SAW}}{2})$. Both the signal and idler polaritons would also gain energy $\frac{\hbar\omega_{SAW}}{2}$ compared to the case with no SAW. Equally, there can be stimulated

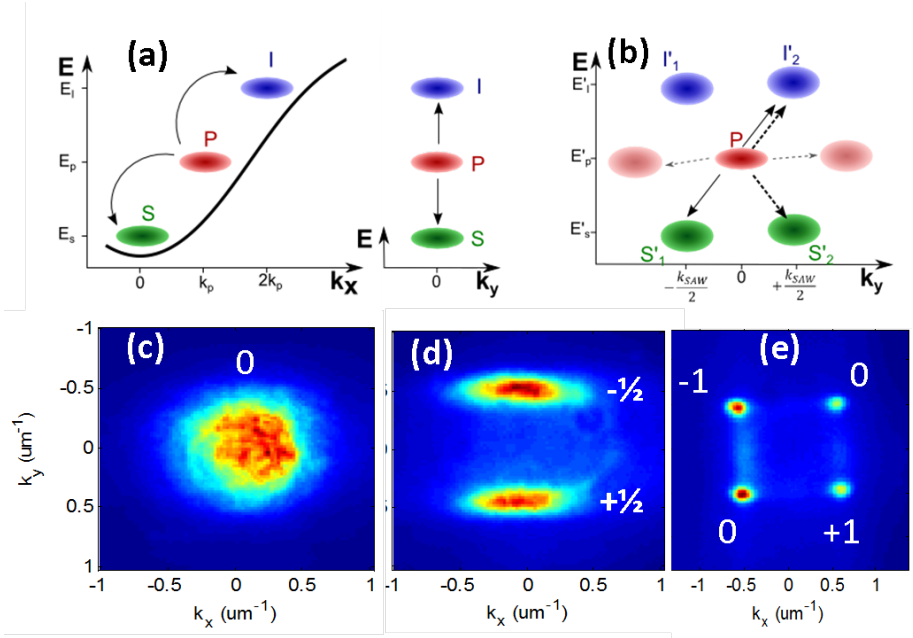


**Figure 4.6: Phonon-assisted scattering:** OPO with **(a)** no SAW and **(b)** a y SAW applied. In case (b), the black dashed arrows indicate an event in which a phonon is absorbed while the solid black arrows show an event in which there is no phonon absorption. The presence of both paths explains how the S' states can be coherent: they are parametrically linked via the common I' state. Grey dashed arrows show the pump states that would form due to phonon absorption if there was no OPO event. **(c-e):** k maps of the signal states when (c) no SAW (d) a y-SAW and (e) an x-SAW and a y-SAW are applied simultaneously. The white numbers indicate the expected change in energy of each state compared to the case when no SAW is present in units of $\hbar\omega_{\mathrm{SAW}}$.

emission of a phonon into the reservoir generated by the SAW and a corresponding pair of signal and idler states with $\mathbf{k_{S1}}, = (0, -\frac{k_{SAW}}{2})$ and $\mathbf{k_{I1}}, = (2k_p, -\frac{k_{SAW}}{2})$. Both the signal and idler polaritons would also lose energy $\frac{\hbar\omega_{SAW}}{2}$ compared to the case with no SAW. Thus, signal states form at the edges of the MBZ and have an energy separation of $\hbar\omega_{SAW}$. Once the polariton population begins to build up at these k vectors, further emission is stimulated. It is not entirely understood why the states at the edge of the MBZ are preferred; there may be multiple mechanisms contributing to this, some of which will be described in §4.2.4.

When 2 SAWs are applied in perpendicular directions, 2 phonons can be absorbed. This results in 4 signal states with k vectors $\mathbf{k_S}, = (\pm\frac{k_{SAW}}{2}, \pm\frac{k_{SAW}}{2})$ i.e. at the corners of the MBZ. These states have different energies as indicated in Figure 4.6e. A test of the phonon assisted scattering theory would be to measure the time resolved interference between the states with $\mathbf{k_S}, = (+\frac{k_{SAW}}{2},+\frac{k_{SAW}}{2})$ and $\mathbf{k_S}, = (-\frac{k_{SAW}}{2},-\frac{k_{SAW}}{2})$. The theory predicts that the energy separation of these two states would be $2\hbar\omega_{SAW}$, so temporal oscillations at frequency $2\omega_{SAW}$ should be seen. This was checked and the results are presented in §4.2.3.

### 4.2.3 Measurements of Interference with 2 SAWs

In order to test the hypothesis of phonon-assisted scattering (§4.2.2), time resolved measurements were taken using the same setup as in §4.2.1 but with both an x-SAW and a y-SAW applied simultaneously. The SAWs are driven by the same frequency generator so are mutually coherent. The absorption of two phonons during the OPO scattering process could alter the energies of the final signal states by 0, $+\hbar\omega_{SAW}$ or $-\hbar\omega_{SAW}$ as illustrated in Figure 4.6e.

For some measurements, the emission was spectrally filtered to select only two out of the four condensate states so that the energy difference between a particular pair of states could be determined from the observed oscillation period. The experimental results are shown in Figure 4.7, where (a-c) show how the k space states were filtered and (d-f) show the temporal oscillations. (g-i) show the frequency distribution, found by fourier transforming the temporal oscillations in (d-f). In case (b,e,h), the oscillations have a frequency of $\sim$735$\pm$17 MHz corresponding to $2f_{SAW} = \sim$750MHz as predicted by the theory, where $f_{SAW} = \frac{\omega_{SAW}}{2\pi}$. In case (c,f,i), no oscillations are expected as the states should have the same energy, however there may be additional states formed by the contribution of the reflected SAWs in the phonon assisted scattering process as will be described in §4.3.3, resulting in the observed oscillation at $\sim$370 MHz, corresponding to $f_{SAW} = \sim$374MHz. In case (a,d,g), components oscillating at both $f_{SAW}$ and $2f_{SAW}$ are seen, which is consistent with the fact that there are some pairs of states with an energy difference of $\hbar\omega_{SAW}$ and one pair with a difference of $2\hbar\omega_{SAW}$.

### 4.2.4 Alternatives for S' state formation

There are several proposed mechanisms in the literature for why the condensate subjected to a SAW forms at the edges of the MBZ. It is possible that multiple mechanisms contribute to this, resulting in the edge states being preferred compared to the lowest energy state at $\mathbf{k}$=0.

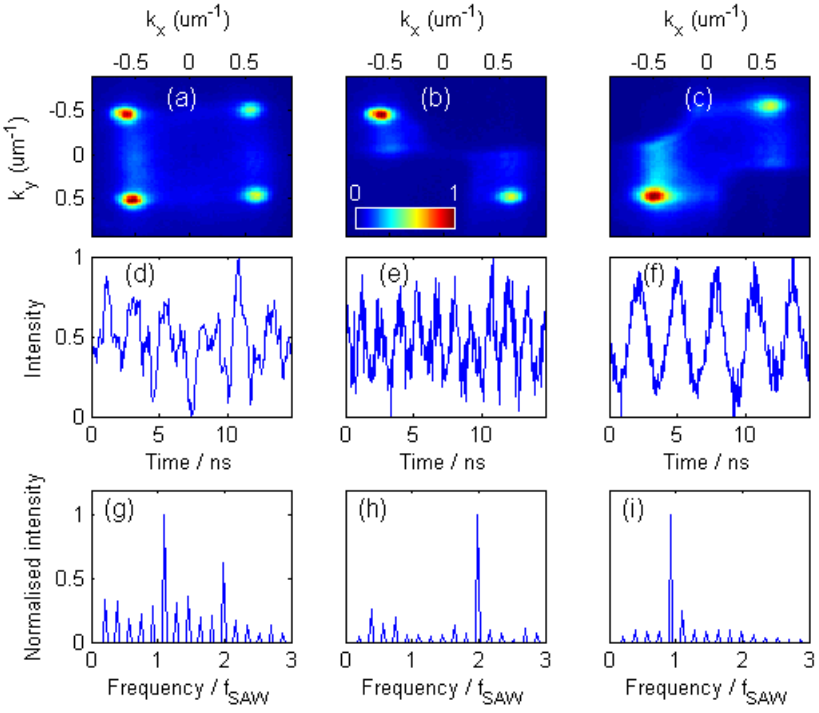


**Figure 4.7: Intensity correlations, two SAWs** **(a)** 2-dimensional k-map at high power showing the positions in k space where polaritons are condensed. **(b,c)** show how the emission can be filtered to select diagonal or off-diagonal states. **(d-f)** show the corresponding time resolved realspace oscillations measured using an HBT setup where both detectors point at the same spot ($\Delta$d = 0), **(g-i)** Normalised Fourier transforms of the traces in (d-f). The frequency is normalised to that of the applied SAW ($f_{SAW}$ = 375 MHz).

**Gap solitons: negative effective mass point**

It has been shown [81] that the states generated at the corners of the MBZ with two perpendicular SAWs correspond to 2D gap solitons. While it hasn't been explicitly shown that the states with one SAW correspond to 1D gap solitons, the mechanisms involved with separate and combined SAWs are likely to be similar. These states may also be gap solitons similar to those which have been seen in a 1D static potential [150].

For gap solitons, spatial localisation is stabilised by the interplay between polariton-polariton repulsion and the negative effective mass of the polaritons at the edge (corner with 2 SAWs) of the MBZ. As a degree of confinement is imposed by the SAW, the negative effective mass polaritons at the edge (corner) of the MBZ are favoured as they give an attractive kinetic energy term which compensates the repulsive coulomb interaction term, which in turn favours a more localised distribution.

**Symmetry of states**

Kim *et al* [79] suggest a theory where the position on the MBZ at which the condensate forms depends on the symmetry of the condensate. This depends on both the symmetry of the system and the power of the pump laser (see Figure 2.9, reproduced from Kim *et al* [79]). With no potential modulation, a condensate with S symmetry forms; with a 1D modulation (corresponding to 1 SAW), the condensate may have S or P symmetry; with a 2D modulation (corresponding to 2 SAWs), the condensate may have S, P or D symmetry. Condensates with S symmetry are most likely to form at $\mathbf{k} = 0$ (the $\Gamma$ point); condensates with P symmetry at the X points (edges of a square MBZ); while condensates with D symmetry are most likely to form at the M points (corner of a square MBZ). The expected condensate symmetry depends on the pump power. For a 2D potential modulation, as the pump power increases, the symmetry of the condensate is expected to change from D to P and then to S. This describes the results shown in Figure 4.4 where the condensate forms at different points on the Brillouin zone with 2 SAWs. In the paper by Kim *et al*, the potential modulation is static and is applied from patterning of metal strips on the sample.

**Scattering with pump diffraction replicas**

In previous work, Cerda-Mendez *et al* [41] suggested that the spatial modulation of the condensate density resulted in the formation of diffraction replicas of the pump polariton state with k vectors of $\pm k_{SAW}$. These scattered with the normal pump polaritons to generate the same signal and idler states shown in 4.6. This mechanism, however, does not account for any energy difference between the states. In addition, later measurements by the same group show that the k positions of the S' states can change with SAW power [81] (replicated here in §4.1, Fig 4.3). This suggests that the k-space configuration of the states is determined by the polariton density distribution and the SAW amplitude rather than by interactions between the main pump state and its diffraction replicas as the latter mechanism should result in states with a fixed k vector.

This would also appear to contradict the proposed mechanism of phonon-assisted scattering as this should also give S' states at fixed k vectors which should not change with SAW power as the SAW k vector remains the same. However, there are other factors to be taken

into account. At high SAW powers, the pump state is less well defined as it is broadened in k space due to the realspace confinement of the pump polaritons. The resulting states generated by OPO would then also be poorly defined, resulting in a broadening of the S' states with SAW power, something which is seen in both [81] and §4.1. When the SAW power is very high, the polaritons spread all along the bottom of the LPB, which looks more like a thermal relaxation rather than a stimulated OPO process. There is still clearly a maximum near the edge of the MBZ at the highest power shown in Figure 4.3 so the process cannot be entirely thermal, but there could be an increase in scattering from thermal phonons leading to a relaxation of S' states towards k=0 as a high SAW power heats the sample.

Another possibility is that the momentum of the absorbed SAW phonon is not shared evenly between the signal and idler states in the OPO process. As long as the I' state forms with $\mathbf{k_I}, \geq (2k_p, + \frac{k_{SAW}}{2})$, the S' state can have $\mathbf{k_S}, \leq (0, + \frac{k_{SAW}}{2})$. This situation may become more favourable at higher optical pump powers as the Coulomb interactions from the increased polariton density blueshift the LPB, bringing states with lower k vectors into resonance with the energy of the S' state.

## 4.3 Additional Interference Patterns

Further investigations revealed modulations in both the temporal and spatial domains which are not explained by the interference between the two S' states formed by the phonon assisted scattering mechanism (§4.2.2). This data is presented in §4.3.1.

### 4.3.1 Observations

Time integrated measurements showing real space intensity maps covering the whole excitation spot were taken by directing the emission to the CCD. When one SAW is applied, a spatial modulation is clearly visible as shown in Figure 4.8b. The orientation of the pattern changes with the SAW direction such that the fringes appear parallel to the SAW wavefront (Figure 4.8b,k). The pattern appears as the SAW is applied, then becomes smeared out as the SAW power is increased in a similar manner to the S' states as illustrated in Figure 4.8(a-c). The period of the modulation is $\sim \lambda_{SAW}$: in Fig. 4.8(b) it is 8.0 ± 0.6 μm, in (c) it is 7.8 ± 0.7μm and in (k) it is 7.9 ± 1.1μm . This is consistent with the expected period of the SAW, $\lambda_{SAW} = 8\mu m$, driven at 374 MHz with an acoustic speed of ∼3000 μm $s^{-1}$ [41].

When emission from only one S' state is observed , the spatial intensity modulation observed in time integrated measurements disappears (Fig. 4.8d). However, time resolved measurements reveal that some temporal oscillations persist (Fig. 4.8i). Unlike the unfiltered case, there is no phase change as the relative detector position Δd is increased. This means that different areas on the sample oscillate with the same phase, indicating that this modulation is stationary (Fig. 4.8j). The temporal oscillations observed in the spectrally filtered measurements suggest the presence of states with energies separated by $\hbar\omega_{SAW}$ but with the same k vector (although an alternative explanation is presented in §4.3.4). This energy separation of ≈ 1.5 μeV is beyond the resolution of the spectrometer.

Spatially resolved luminescence measurements were also taken with both an x-SAW and a y-SAW applied simultaneously. When two perpendicular SAWs are applied, the

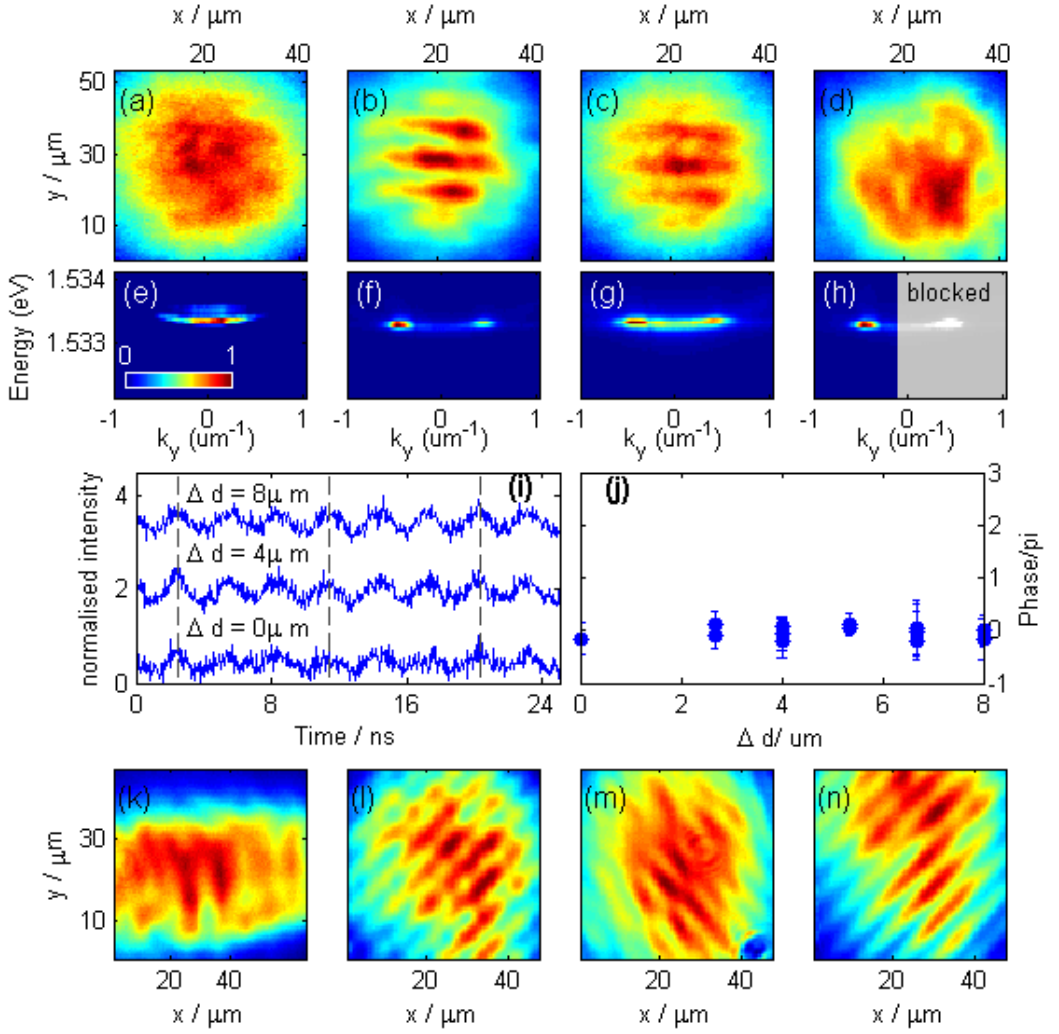


**Figure 4.8: Additional Interference Patterns (a-d)** Real space time-integrated patterns under high power excitation when a condensate forms. The amplitude of the applied y-SAW is 0.0 $mW^{\frac{1}{2}}$ in (a), 5.6 $mW^{\frac{1}{2}}$ in (b) and 8.9 $mW^{\frac{1}{2}}$ in (c). In (d), the emission is spectrally filtered as shown in (h), with a SAW amplitude of 5.6 $mW^{\frac{1}{2}}$. The corresponding energy-$k_y$ dispersions are shown in **(e-h)** (also see Figure 4.3). (h): Spectral filtering where greyed out areas were blocked. The experiments shown in Fig 4.5 were repeated while spectrally filtering the emission as in (h). Results are presented here in **(i,j)**. **(k)** shows a time-integrated real space intensity map when a x-SAW is applied with amplitude 5.6 $mW^{\frac{1}{2}}$. **(l-n)** show time-integrated real space intensity maps when an x-SAW and y-SAW are applied simultaneously with amplitude 5.6 $mW^{\frac{1}{2}}$. In (l), all emission is recorded while (m,n) show the pattern when only two states are selected, as in Fig 4.7(b,c)

condensate is expected to form a dot lattice, mirroring the potential induced by the two SAWs. This would be moved diagonally across the sample by the resultant wave when the two SAWs are superposed, so should show diagonal lines in a time integrated measurement. By changing the relative amplitude of the x-SAW and y-SAW, the direction of propagation of the condensate dot lattice should be tunable, although this additional degree of freedom was not investigated here.

These lines along the leading diagonal are visible in the unfiltered signal as shown in Figure 4.8l although there is some additional intensity variation along the line. Figure 4.8(m,n) shows the resulting pattern when the off-diagonal or diagonal states on the k map are filtered out as shown in Figure 4.7. Figure 4.8n shows the expected pattern: the two unfiltered states have different k vectors and the same energy so superpose giving a static pattern. However, Figure 4.8m would be expected to show no modulation as the unfiltered states have different energy. Qualitatively, it can be seen that Fig. 4.8l is some combination of Fig. 4.8(m) and (n). The periods of the fringes in Figure 4.8 (l,m,n) are 6.0 ± 0.1 μm, 5.6 ± 0.3 μm and 6.2 ± 0.1 μm. The expected period for Figure 4.8(l,n) is $\frac{\lambda_{SAW}}{\sqrt{2}} = 5.66$ μm.

### 4.3.2 Discussion

In time integrated measurements of the condensate with 1 SAW applied, the intensity profile should be a Gaussian spot with no visible spatial modulation: modulation induced by the SAW should be smeared out as it moves across the sample over a much shorter timescale than the integration time (∼20ns vs 1s). However, a stationary modulation replicating the expected SAW wavefront is clearly visible. The pattern is well defined at SAW powers where the S' states are well defined, has a period corresponding to the difference in k between the S' states (i.e. $k_{SAW}$) and it disappears when one S' state is filtered out. All these factors suggest that the pattern relates to interference between the S' states, although temporal oscillations due to their energy difference should smear out the pattern. Time resolved measurements have also revealed a stationary intensity oscillation with frequency $\omega = \omega_{SAW}$ when emission at either $+\frac{k_{SAW}}{2}$ or $-\frac{k_{SAW}}{2}$ is filtered out.

These observations could be explained by considering the possibility that the SAW may be reflected from the sample edge or from another transducer (see Fig 4.9). The observed spatial pattern with period $\lambda_{SAW}$ is not consistent with the accumulation of polaritons in the nodes or antinodes of a standing wave generated from back reflection of the SAW as this would generate a pattern with a period of $\frac{\lambda_{SAW}}{2}$. However, if the reflected SAW is treated as a second reservoir of coherent phonons with an equal and opposite k vector to the original SAW, phonon-assisted scattering with the second reservoir would generate additional states with $(k_y,\Delta E) = (+\frac{k_{SAW}}{2},-\frac{\hbar\omega_{SAW}}{2})$ and $(-\frac{k_{SAW}}{2},+\frac{\hbar\omega_{SAW}}{2})$ as explained in §4.3.3. The spatial modulation can arise from the presence of some states with opposite k but the same energy. This mechanism also explains the stationary temporal oscillation as there are now two states in the filtered emission with different energies but the same k vector. It should be noted that the contrast of the fringes is poor as would be expected if the modulation arises from only some of the occupied states (see Table 4.2).

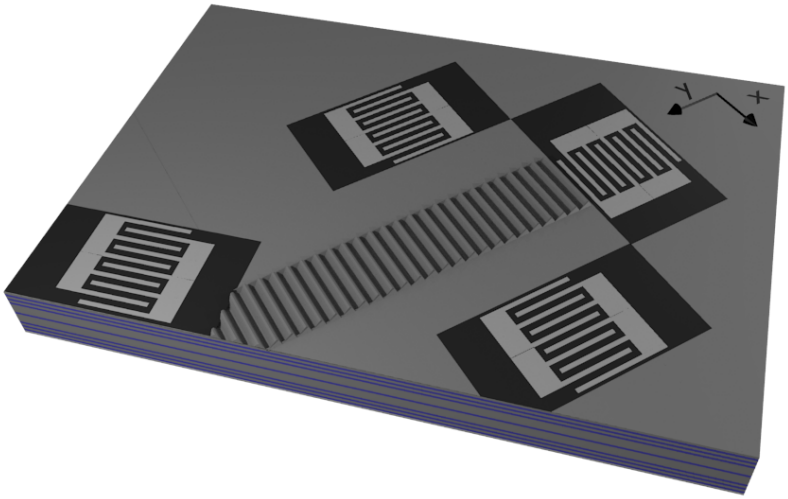


**Figure 4.9: Transducer positions:** Three transducers form three sides of a square. SAWs propagating in the x direction can be reflected from the opposite transducer. The fourth transducer is at an angle, but the edge of the transducer combined with the edge of the sample forms a retro-reflector structure which could reflect SAWs propagating in the y direction.

### 4.3.3 SAW Reflection

This section describes a mechanism which would explain the temporal oscillations with no accompanying spatial modulation seen in time resolved measurements. Additionally, it is consistent with the observation of spatial modulation in time integrated measurements. The theory was formulated for 1 SAW, then the case of 2 perpendicular SAWs was simulated.

§4.2.2 describes how condensates could form with different k vectors and energies by absorbing phonons from the SAW. In this situation, all the phonons had the same k vector i.e. were propagating in the same direction. However, if there was some back reflection of the SAW from the edge of the sample or from the opposite transducer (see Fig 4.9), there would be some phonon population with a k vector of opposite sign. If one of these phonons was absorbed during the scattering event, the resulting signal state would still gain energy $\frac{\hbar\omega_{SAW}}{2}$ compared to the case with no SAW, but would have k vector $\mathbf{k_s} = (0, -\frac{k_{SAW}}{2})$. Similarly, the emission of a phonon into the reflected SAW reservoir would generate a state which had lost $\frac{\hbar\omega_{SAW}}{2}$ but appeared at $k_y = +\frac{k_{SAW}}{2}$. With this mechanism, there are effectively 4 S' states as described in Table 4.1.

The observation of unexpected oscillations can be explained by the presence of extra states induced by the SAW reflection. Even when states at either + or $-k_S$ were filtered out, states with an energy difference of $\hbar\omega_{SAW}$ were present, giving rise to temporal oscillations (Fig 4.8i,j). As there was only one k vector present, there was no spatial pattern so no phase shift was observed in the oscillations as the detector separation $\Delta$d was increased. Similarly, states with the same energy but different k vectors lead to a stationary interference pattern generating a spatial modulation of the condensate population as seen in Fig 4.8. The fringe contrast is not 1 in any of the measurements (see Table 4.2): poor contrast can be explained by the fact that the interfering waves have different amplitudes, as shown in Equation 4.1. In addition in the time integrated measurements, pairs of states with different energy provide a quasi constant background.

**Table 4.1: S' states.** Comparison of the energies and k vectors of the states formed when phonons are emitted or absorbed. The phonons can either be part of the SAW applied by the transducer, or could be reflected from a structure on the sample surface with a reflection coefficient of r.

| State | k vector | energy gain | amplitude | generation |
|---|---|---|---|---|
| 1 | $+\frac{k_{SAW}}{2}$ | $+\frac{\hbar\omega_{SAW}}{2}$ | 1 | absorb applied |
| 2 | $-\frac{k_{SAW}}{2}$ | $-\frac{\hbar\omega_{SAW}}{2}$ | 1 | emit applied |
| 3 | $-\frac{k_{SAW}}{2}$ | $+\frac{\hbar\omega_{SAW}}{2}$ | r | absorb reflected |
| 4 | $+\frac{k_{SAW}}{2}$ | $-\frac{\hbar\omega_{SAW}}{2}$ | r | emit reflected |

#### Simulation

In order to check that this mechanism describes the experimental observations, the expected interference patterns with different reflection coefficients (r) of the SAW were simulated. In the case of 1 SAW, the resulting fringe contrast was calculated and compared to the contrast of experimental results with x or y SAWs in order to determine the value of r. The fringes with the y SAW had contrasts of 9 ± 5% corresponding to r = 1-4% while the x SAW fringes had contrasts of 10 ± 3% corresponding to r = 2-4%.

With 2 SAWs, the situation is more complicated. Using a value for r of 3%, the contrast between the maxima and minima of the whole interference pattern was calculated both when the signal is unfiltered, and when only a subset of the total states are selected, as in Figure 4.7b,c: these values however did not match those measured in the data. What was particularly unexpected was that the experimental data for emission filtered as in Figure 4.7b showed a much better contrast that the predicted value (13 ± 5% vs 2%).

For the case of an unfiltered signal, the contrast of the pattern along a "bright diagonal fringe" (black box in Figure 4.10b) was also calculated and was found to be a closer match to equivalent fringes in the experimental data: for a 3% reflection, this simulated contrast is 20% while the data shows contrasts of up to 20%. The images of the expected pattern (shown in Figure 4.10) also qualitatively match the measured data and suggest that the value of r is 1-3%. The calculated and measured contrasts are summarised in Table 4.2. Overall, the results from different data sets and different SAW configurations are mostly consistent both with each other and with the simulations.

### 4.3.4 Further Discussion

#### Effects of a SAW reflection

The SAW reflection could be expected to contribute to the emission intensity distribution in two ways. Firstly, the phonons making up the reflected SAW can be absorbed by the polaritons as they scatter to signal states and interfere as described in §4.3.3. Only the contributions from polaritons in signal states are seen in the experimental observations as emission from higher k states (pump, idler) is not collected. Any interference between pump polaritons which have absorbed a phonon but have not scattered to signal and idler states (which might result in modulation with wavelength $\frac{\lambda_{SAW}}{2}$) is therefore not observed.

**Table 4.2: Fringe Contrasts.** The contrast is the amplitude of the intensity modulation compared to the background i.e. contrast = (max(I)-min(I))/min(I) where I is the intensity profile. The contrasts measured with different experimental conditions are compared with simulated values where each state is considered as a plane wave and the "observed states" are combined to calculate an interference fringe pattern.

| **SAW Applied** | **States Observed** | **Measured Contrast/%** | **Simulated Contrast/%** | **Value of r/%** |
|---|---|---|---|---|
| x | all | 7-13 | 4, 8, 11, 15 | 1, 2, 3, 4 |
| y | all | 4-14 | | |
| x,y | all | 11-21 | 71 | 3 |
| x,y | diagonal | 8-17 | 2 | 3 |
| x,y | off diagonal | 16-30 | 97 | 3 |
| | | Contrast along bright diagonal fringe | | |
| x,y | all | up to 20% | 10 | 1 |
| | | | 20 | 3 |
| | | | 30 | 5 |

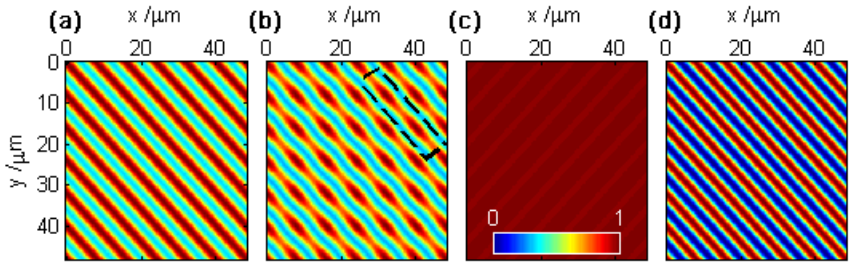


**Figure 4.10: SAW reflection simulation, 2 SAW** (a) shows the expected realspace pattern for a time integrated measurement if there was no SAW reflection while (b) shows the pattern for a 3% reflection. The black dashed box shows what is meant by a "bright diagonal fringe" (Table 4.2). (c) and (d) show the pattern for 3% reflection when the k space is filtered to select a subset of states, as illustrated in Fig 4.7.

In fact, two separate interference patterns each with period $\lambda_{SAW}$ can be generated from the S' states: one from the interference of states 1 and 3 and the second from states 2 and 4 (see table 4.1). The combination of these would only give regular fringes spaced by $\lambda_{SAW}$ if the patterns were in phase. The phases of states 1 and 2 should be linked as they are generated from the same reservoir of coherent phonons: the same applies to states 3 and 4. This could provide a link between the phases of the two interference patterns, as required to account for the experimental observations.

The second effect that might be expected for a reflected SAW is that it would combine with the applied SAW to make a standing wave with period $\frac{\lambda_{SAW}}{2}$. This modulation in the strain field on the cavity translates to a modulation in the potential felt by the polaritons, so polaritons might accumulate in the potential minima. As explained in §4.1, this potential can be screened by the polariton population. Note that polaritons in all states, including the high intensity pump state whose emission is not recorded in the experimental observations, can contribute to screening and reduce the effect of the standing wave potential on the density distribution in the signal states. This could explain why the experimentally observed intensity modulation appears to be dominated by the interference mechanism rather than the standing wave mechanism, resulting in modulation with wavelength $\lambda_{SAW}$.

### Alternative sources of oscillation

There are alternative explanations for the observations of time resolved intensity oscillations with one S' state filtered (Figure 4.8)(i,j). Indeed, multiple mechanisms may contribute at any one time.

Previous observations of intensity oscillations (no filtering, similar to the results presented in Figure 4.5) described them as the effect of condensate wires being moved across a sample [41]. In this picture, any observed oscillations would be expected to correspond to a propagating wave, but the oscillations shown in Figure 4.8, where emission from only one S' state is collected, correspond to a stationary wave. This could arise from the fact that the spatial resolution in the detection is lost when an S' state is blocked so that emission is collected from the whole excitation spot rather than a small region defined by the pinhole (see §3.4.1 for optical setup). Temporal oscillations could then arise from the finite size of the excitation spot and the fact that as the condensate wires are moved through it, the number of intensity maxima in the spot can oscillate in time, as illustrated in Figure 4.11.

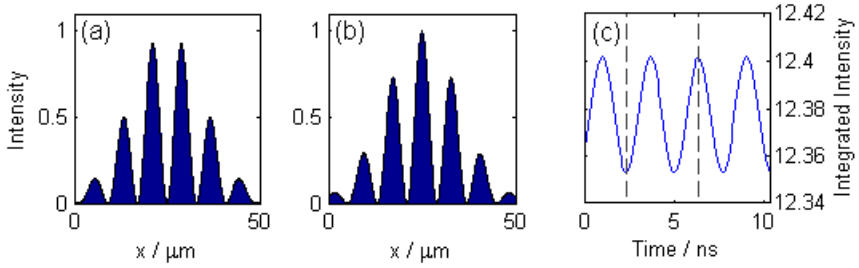


**Figure 4.11: Intensity oscillation:** the total polariton density within the pump spot oscillates in time as maxima move in and out of the pumped region. **(a)** Spatial intensity distribution at 2.3 ns, **(b)** spatial intensity distribution at 6.4 ns. **(c)** Intensity integrated over the spatial pattern as a function of time: grey dashed lines indicate the times at which patterns (a) and (b) are shown.

## 4.4 Conclusions

Experimental observations of temporal intensity oscillations suggest that S' states have different energies as well as different k vectors and are coherent with each other. While there are several suggestions in the literature for mechanisms generating states with different k vectors, neither the energy difference nor the mutual coherence between the states were well understood. A mechanism of phonon-assisted scattering can explain both of these phenomena and is consistent with all experimental observations of interference if it is assumed that the SAW can reflect back across the sample.

Further experiments carried out by Cerda-Mendez *et al* on the case with two perpendicular SAWs have shown that the generated states are gap soliton states [81]. As the same method is used to generate the 1D potential modulation with 1 SAW and gap soliton states have been observed with a 1D potential modulation [150], I believe it is reasonable to suggest that the S' states investigated here may correspond to 1D gap soliton states, although experiments to prove this were not explicitly carried out. There have been suggestions for using gap solitons in photonic crystals for all-optical memory, where the memory bit consists of a trapped soliton which can be released for readout by a second control pulse when required [162]. Similar functionality was suggested in the polariton system by Tanese *et al* when they observed gap solitons in a 1D periodic potential [150] and could also be applied to the system presented here.

Detailed observations of the interference pattern between the resulting signal states revealed a strong influence on the pattern from a reflected SAW. By adding new structures to the sample surface with a higher reflection coefficient, this could lead to the fabrication of a SAW resonator structure. Such a device could be used to apply a stationary spatial modulation of the potential landscape with a tunable period ($\propto 1/\omega_{\mathrm{SAW}}$), amplitude ($\propto$ SAW amplitude) and orientation ($\propto$ ratio of x-SAW and y-SAW amplitudes) to a system.

# Chapter 5

# Formation of Soliton Patterns in a Dissipative System

Bright dissipative polariton solitons were first observed by Sich *et al* in 2012 [7]. In this chapter, this work is extended so that instead of exciting a single soliton with each laser pulse, a soliton array can be triggered. This enables the study of the interactions between neighbouring solitons, opening up the possibility of continuously generating solitonic pulses using CW excitation, a setup which could be used as a clocking device in a polaritonic circuit. A fast clock rate of ∼100 GHz could be achieved as the minimum soliton separation would no longer be limited by the laser repetition rate (82 MHz). The solitons studied in this chapter are dissipative, meaning that losses due the short polariton lifetime are compensated by a CW pump with a k vector above the point of inflection of the lower polariton branch (LPB). The soliton velocity is determined by the k vector of the CW pump.

One dimensional arrays of up to four solitons arranged along the direction of propagation are investigated. Two regimes of these arrays are studied, termed "soliton trains" (§5.2.1) or "x-arrays" (§5.2.3) depending on their characteristics. The Energy vs k vector (E-$k_x$) spectra of these arrays are examined and observations are made to show how the excited regime can be influenced by the position of the writing beam (WB) relative to the pump spot. It is shown that the soliton separation in arrays can be tuned by varying excitation conditions such as the WB power (§5.2.2), which could be used to tune the clock rate of a polariton device. Observations of arrays of solitons perpendicular to the direction of propagation are also presented (§5.3).

Here, I define some terminology which will be used to describe different soliton patterns in this chapter:

- **X direction** - This is the in-plane axis along which wavepackets and solitons propagate.
- **Y direction** - This is the in-plane axis perpendicular to the direction of propagation.
- **Soliton train:** 1D array where solitons are arranged along the x direction. The E-$k_x$ spectrum of this ensemble is a single straight line and the train is believed to be a single bound state known as a multi hump soliton.

- **X-array:** 1D array where solitons are arranged along the x direction. The E-$k_x$ spectrum does not form a single straight line and the ensemble is thought to be an array of separate solitons rather than a single bound state.
- **Y-array:** 1D array where solitons are arranged along the y direction.

## 5.1 Setup

In order to excite a single dissipative soliton, a continous wave (CW) laser generates a pump spot of size $\sim$ 70µm which acts as a reservoir of polaritons: this is necessary to maintain the polariton population due to the short photonic lifetime of the microcavity. The reservoir is in a bistable regime so that high and low density states can exist in neighbouring regions of the spot. The pump initialises the system in the low density state. A soliton can be generated by a pulsed writing beam (WB) of size $\sim$ 8µm which excites a localised region of the bistable pump spot into the high density state. This wavepacket propagates across the spot, self-focussing into a soliton [7].

In order to excite an x-array or a soliton train, a similar setup is used but the WB is elongated along the propagation direction. The injected wavepacket breaks up into multiple solitons whose width is again determined by the healing length (see Equation 2.7 in §2.4.1). Soliton trains can be generated when the WB is outside the bistable region so that the excited wavepacket propagates for $\sim$20 µm before hitting the bistable pump spot, while x-arrays are excited when the WB overlaps with the bistable region of the pump spot. A y-array can be excited by elongating the WB perpendicular to the propagation direction. It should be noted that the pump and WB never have the same k vector in these experiments (see §3.3 for details of the setup).

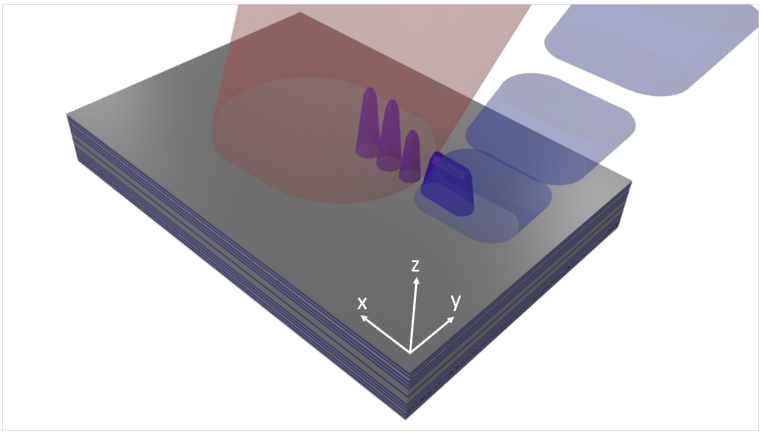


**Figure 5.1: Setup:** Following the method used by Sich *et al* [7], a continuous wave pump (red) is used to maintain a reservoir of polaritons, compensating photonic losses due to a short cavity lifetime. A wavepacket is injected by a pulsed writing beam (blue) and interacts with the pump polaritons to form a soliton. Here, the writing beam is elongated along the propagation direction (x) to trigger multiple peaks.

It has been shown that the polarisations of the pump and WB influence that of the excited solitons [123] (see §2.4.1). Stable solitons have circular polarisation and can be triggered using a circularly polarised WB as long as the pump is either co-circularly polarised

with the WB or has linear polarisation (in which case some component will be co-circularly polarised). Here, all experiments were carried out with the pump and WB co-circularly polarised to generate the most stable structures and suppress the polarisation degree of freedom. Unless stated otherwise, these experiments were carried out in a reflection configuration (see §3.3.1).

## 5.2 Multi-peak Patterns Along X

In this section, I describe observations of multi-peak states where bright peaks form a line along the propagation direction, travelling across the pump one after the other. They were generated by elongating the WB along the direction of propagation of the soliton (Fig. 5.1). Multi-peak patterns with different characteristics were generated by changing the relative position of the pump and the WB and optimising parameters such as the WB energy.

### 5.2.1 Soliton Trains

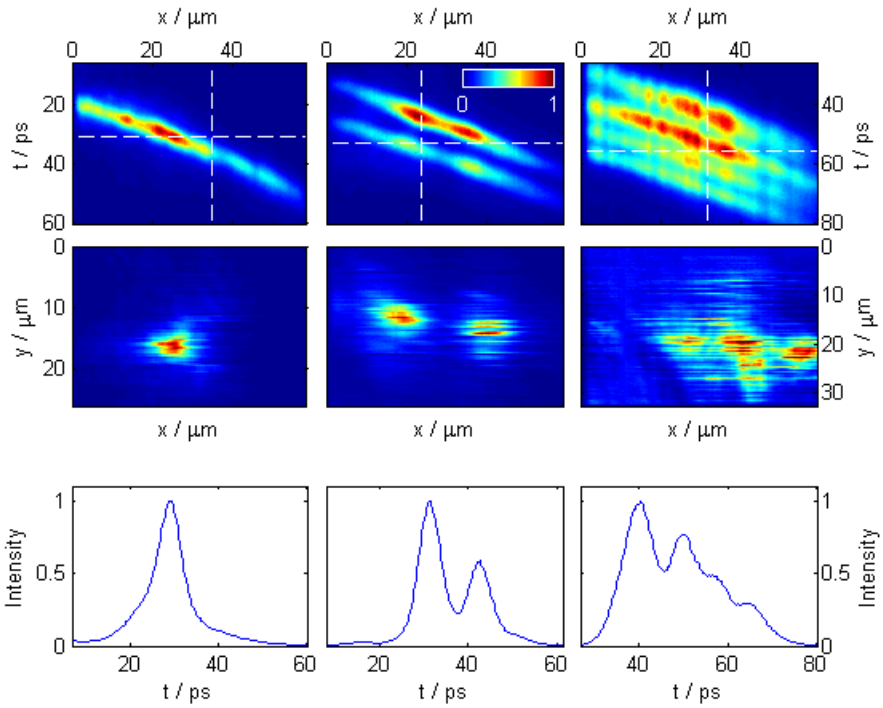


**Figure 5.2: Soliton train, realspace** Here, the realspace intensity profiles for a single soliton (left column), a 2-peak soliton train (middle column) and a 4-peak soliton train (right column) are presented. **Top row:** Streak camera traces showing intensity as a function of time and position. The horizontal dashed line indicates the time at which the images in the second row are taken while the vertical dashed line shows the position at which the profile in the bottom row is taken. **Second row:** Two-dimensional spatial intensity map, taken at the time indicated in the top row. **Bottom row:** Intensity as a function of time at the x position shown in the top row, integrated over y.

Here, the generation of trains of up to four solitons by varying the WB size is demonstrated. It is further shown that the E-$k_x$ spectrum of a parametric soliton train is similar to that of a single soliton, consisting of a single straight line albeit with a different intensity

profile. Soliton trains were excited by placing the WB $\sim 20$ μm outside the bistable region of the pump spot. The pump laser energy was set to 807.0 nm (1.5364 eV, 3.3 meV higher than the LPB at **k=0**) at a power of 300 mW. For a single soliton, the pump $k_x$ vector was set at $k_p = 2.3$ $\mu m^{-1}$. The pump k vector was optimised for different soliton patterns, taking values between 2.0-2.4 $\mu m^{-1}$ and ensuring that the pump spot was in the bistable regime in all cases. The WB energy, $k_x$ vector and power were also optimised for each soliton train, although the $k_x$ vector of the WB was higher than that of the pump for all measurements, typically by $\sim 0.3 \mu m^{-1}$. In these multi-peak patterns, the solitons propagate at the same velocity, maintaining the same regular spacing over the propagation path as illustrated in the streak camera traces in the top row of Figure 5.2.

Previous observations of bright solitons show localisation in both the x and y directions [7]. This result is replicated for soliton trains, where streak camera traces of the intensity as a function of x and t (top row) are taken at different positions of y. These images are combined to reconstruct the two dimensional realspace images shown in the second row of Figure 5.2 ( see §3.3.5). Two dimensional spatial images demonstrate localisation along y, however for larger soliton trains the total x-width of the train is wider than the detection window so not all peaks are visible. An alternative way of viewing the propagating array is to look at the intensity as a function of time at a given x position: successive solitons passing that position give intensity maxima in the temporal profile. As this is no longer limited by the width of the detection window, all peaks in the train can be seen in a single image. Intensity profiles over time at x = 30 μm and integrated over y are shown in the bottom row of Figure 5.2, illustrating the formation of patterns containing up to four solitonic peaks.

### Spectra of soliton trains

Further evidence that solitons in a train are bound together comes from the E-$k_x$ dispersions shown in Figure 5.3, where (e-h) show the spectra corresponding to the arrays in (a-d). All four spectra exhibit linear dispersion of the soliton emission at all $k_x$-vectors down to zero in strong contrast to the dispersion of the lower polariton branch, which is parabolic at $k \approx 0$. The single line E-$k_x$ spectrum indicates that all solitons in the train have the same energy and k distribution, so could be bound.

The intensity profiles show two main peaks at around 1.5335 eV and 1.5352 eV. It should be noted that energies higher than this are cut out as the emission is filtered in k space to block the pump and WB laser reflections (see §3.3.5), but it is expected that there would be a full peak near the pump state as well as an additional idler peak at a higher k vector. For the two-soliton train, the spectral filtering may have cut a little more as the high energy peak is not visible here.

### Spectral narrowing vs number of solitons

The lower energy spectral peak becomes narrower and more pronounced with an increasing number of solitons (Figure 5.3i), which has been predicted theoretically [125]. In observations of the transition to an OPO condensate, similar spectral narrowing was seen and was attributed to the appearance of macroscopic coherence [58]. Similarly, this narrowing of peaks in energy-momentum space for soliton trains is an indication of the onset of

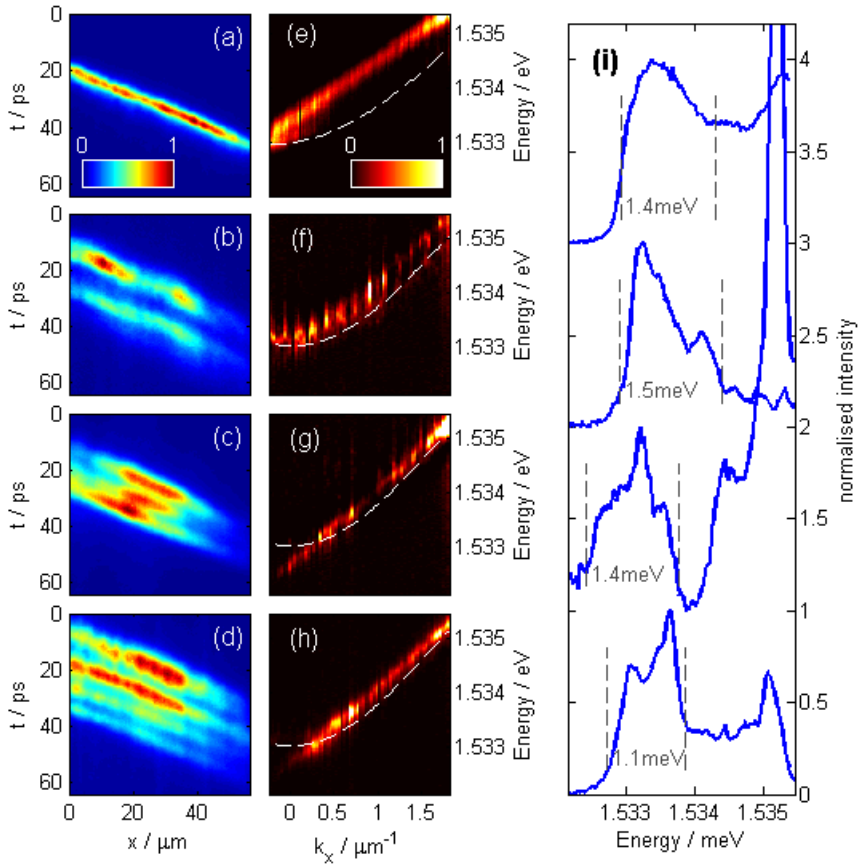


**Figure 5.3: Soliton train dispersions. (a-d)** Streak camera traces in realspace showing (a) a single soliton and (b-d) soliton trains of 2-4 peaks. **(e-h)** Intensity in E-$k_x$ space at $\sim$ 30 ps taken at $k_y$=0 within $\Delta k_y = 0.1$ μm$^{-1}$ for the soliton structures shown in (a-d). The white dashed line shows the approximate position of the LPB. **(i)** Normalised intensity profiles as a function of energy, integrated over $k_x$, so $I(E) = \int_0^{2\mu m^{-1}} I(E, k_x) dk_x$. The top trace shows the profile for a single soliton (a, e), the second is for the two peak structure (b,f), the third is the 3 peak structure (c,g) and the bottom trace is the 4 peak structure (d,h). Grey dashed lines and text show the approximate width of the low energy peak.

spatio-temporal coherence across the soliton train, which could be caused by phase-locking of spectral harmonics of adjacent solitons. This matches what would be expected theoretically as the system moves towards a regime of continuous generation of solitonic pulses: the spectrum for an infinite array of solitons should be delta-function like peaks at the pump, signal and idler states [125, 126]. Phase-locking could occur between neighbouring peaks because the tails of solitons overlap in real-space, so polaritons residing at different k-vectors in one soliton could stimulate parametric scattering to spectral harmonics of adjacent solitons.

Due to the sequential nature of the data acquisition, intensity fluctuations could appear between data points at different k vectors. It is possible that the intensity modulation observed in the energy spectrum is caused by these environmental fluctuations, however these should be averaged out as the intensity versus energy profiles are integrated over many measurements. As an extra check that the observed intensity modulation was a real feature of the soliton emission, a lower resolution data set was taken (Fig. 5.4). As fewer steps

were required, this measurement was four times faster than the data shown in Fig 5.3(e-h), reducing the effect of a drift in the environmental conditions. Nevertheless, a similar trend is seen where the spectral peaks narrow with an increasing number of solitons in an array, providing firmer evidence that this is a real feature of the emission.

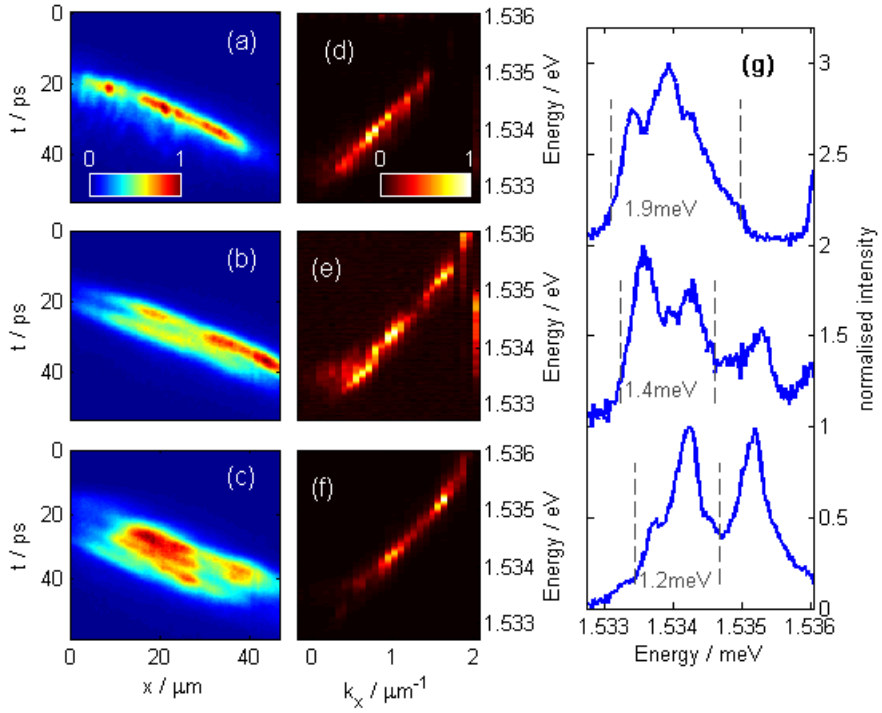


**Figure 5.4: Soliton train dispersions, low resolution (a-c)** Streak camera traces in realspace showing (a) a single soliton and (b-c) soliton trains of multipeak structures. **(d-f)** Intensity in E-$k_x$ space for the soliton structures shown in (a-c). **(g)** Normalised intensity profiles as a function of energy, integrated over $k_x$. The top trace shows the profile for a single soliton (a,d), the middle one is for the two-peak train (b,e) and the bottom trace is for the structure in (c,f). Grey dashed lines and text show the approximate width of the low energy peak.

### Spectral width vs spatio-temporal width

For single solitons, such as the one shown in Figure 5.3(a,e), the temporal width $\Delta t$ of the peak should be inversely proportional to the energy width $\Delta E$ of the spectral peak due to the fourier relationship between these two quantities. Similarly, the spatial width $\Delta x$ should be inversely proportional to the breadth of populated k vectors $\Delta k$, again due to a fourier relationship. For gaussian intensity profiles, the peak widths are related by

$$\begin{aligned} \Delta x \Delta k &= 4ln2 \\ \Delta E \Delta t &= \hbar\ 4ln2 \end{aligned} \tag{5.1}$$

(see Appendix A).

The spectrum shown in Figure 5.3e covers an energy range $\Delta E \approx 2$ meV and a k range $\Delta k \approx 1.5\ \mu\text{m}^{-1}$. While the spectral intensity profile shown in Figure 5.3e is clearly not

gaussian, Equation 5.1 can still be used to give a rough estimate of the expected relationships. This spectrum should correspond to a wavepacket with a temporal width of $\Delta t \approx 1$ ps and a spatial width of $\Delta x \approx 2$ μm. Note that the value of $\Delta x$ matches the theoretical soliton width calculated previously for a bright dissipative soliton [7]: this was estimated from cavity parameters for a sample from the same wafer as the one used in this chapter.

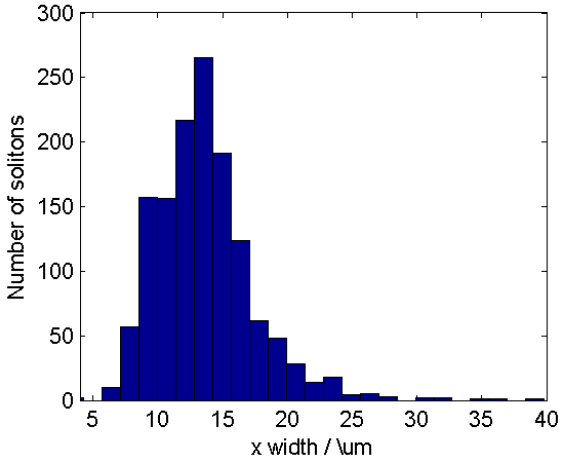


**Figure 5.5: Soliton widths:** Histogram showing the fitted widths of all soliton peaks recorded in the data set for Fig 5.6.

However, the recorded soliton trace shown in Figure 5.3a is ∼5 times broader that these calculated values, having a temporal width of 5.0 ± 0.3 ps and a spatial width of 10 ± 1 μm. These wide peaks are typical of the solitons observed experimentally, both for single solitons and soliton arrays, as illustrated by the histogram in Figure 5.5. This broadening could be due to the limited resolution of the detection optics, in particular the 2 ps time resolution of the streak camera (see §3.3.6). In addition, there may be errors introduced by fitting the soliton intensity profile with a gaussian to find the width: the soliton's spatial intensity profile is expected to have an asymmetric shape with a low density tail (see Figure 2.13 in §2.4).

An alternative explanation is that a multi-hump soliton is excited, which would consist of multiple narrow peaks that cannot be resolved in this experimental setup. Stable multi-hump solutions have been found in numerical simulations published alongside these experimental results [8] and reproduced in Figure B.1 in §B.1. Previous simulations by Egorov *et al* have shown that it may be possible to excite more complex structures by optimising the excitation conditions. For example, one solution was found where groups of 3 closely spaced solitons are separated by a distance of the same order as the width of the group rather than the width of the soliton (reproduced in Figure 2.14d). As the individual soliton peaks would be too narrow to resolve, such a structure would look like an array of wider peaks in an experimental observation.

### 5.2.2 Power Dependence of Peak Positions

If the WB is elongated along the x direction and its power is gradually increased, the number of solitons in the train increases. However, a systematic study reveals that the

spacing between bright peaks is not fixed, but instead varies with WB power. For the data set presented in Figure 5.6, all experimental parameters were kept constant apart from the WB power.

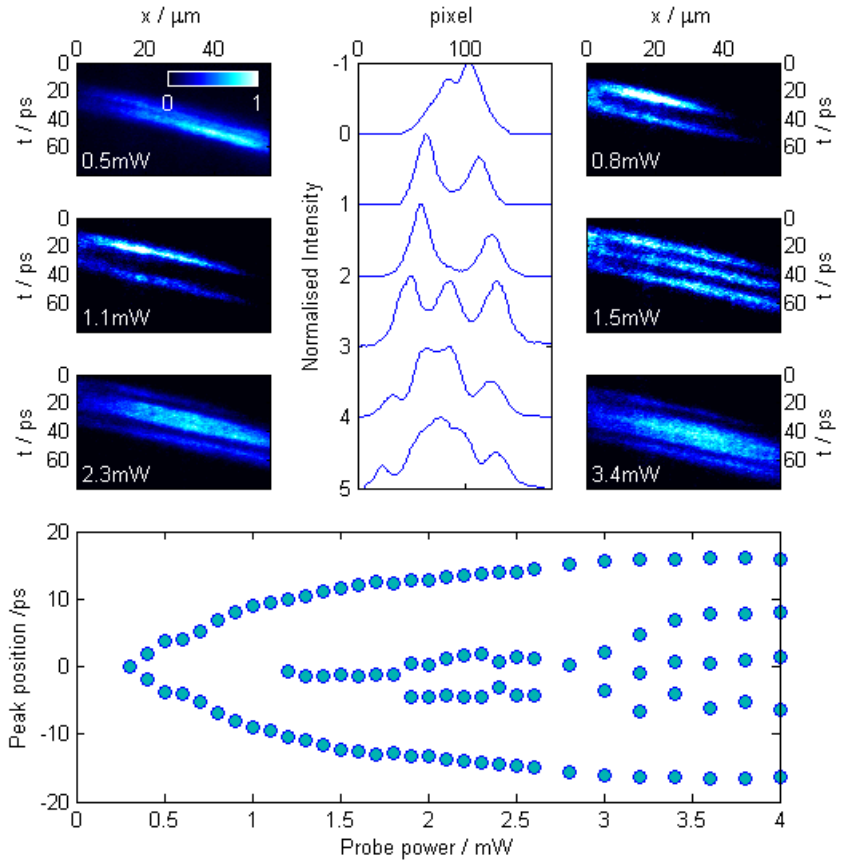


**Figure 5.6: Soliton train, power dependence. Outer columns:** streak camera traces showing the emission intensity as a function of x position and time as the WB power is increased. **Middle column:** Line plots showing the intensity profile across the soliton wavefront for the traces in the outer columns. The intensity profiles are integrated over the soliton trajectory as illustrated in Figure 5.7 and explained towards the end of §5.2.2. **Bottom:** positions of the peak centres in the soliton array as a function of WB power, taken from plots of the intensity profile across the soliton wave-front.

Figure 5.6 illustrates the behaviour of a soliton train as a function of WB power. At the lowest power, only one soliton is excited but as the power is increased, this separates into two peaks which then spread apart. Further peaks appear in between the original two as the power is increased further. A selection of patterns are shown in the outer columns of Fig 5.6 as streak camera traces. During this measurement, fluctuations in laser intensity on the timescale of ∼1s broadened the measured soliton traces and could start to obscure the observed peak pattern. Clearer peak patterns could be obtained using a shorter integration time, although this reduced the signal to noise ratio.

As shown in the outer columns of Figure 5.6, the solitons in the train propagated at a constant velocity of $v \approx 2.2$ μm ps$^{-1}$ and maintained a constant separation over the whole propagation path, indicating the formation of stable soliton patterns. This meant that

instead of selecting one horizontal position and looking at the intensity profile, the intensity profile could be integrated over the whole propagation path, thus increasing the signal to noise ratio. The resulting profiles are shown in the middle column of Figure 5.6 for the x-t traces in the outer columns. This data processing is illustrated in Figure 5.7.

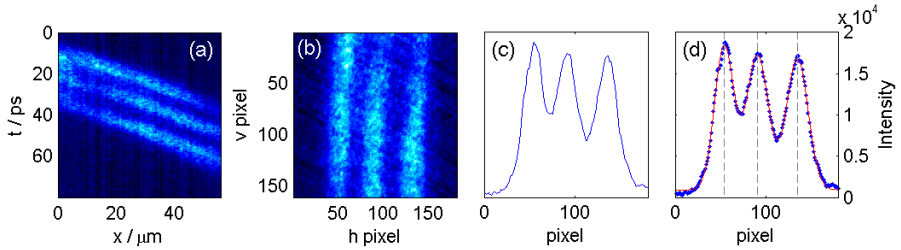


**Figure 5.7: Integration over soliton path.** **(a)** Example of a soliton trace, taken from Fig 5.6. **(b)** Soliton trace is rotated by an angle $\theta = 63°$, aligning the propagation trajectory with the matix columns. **(c)** The emission in (b) is integrated over the matrix rows to give an intensity profile. **(d)** An array of gaussians is fitted to the intensity profile in (c). Peak centres are marked by grey dashed lines. Peak separations in pixels $\Delta$p can be converted to separations in micrometers $\Delta$x or picoseconds $\Delta$t using ($\Delta$x,$\Delta$t)=( ($\Delta$p/cos$\theta$)*X, ($\Delta$p/sin$\theta$)*T) where X and T are the scale factors to convert streak camera pixels to μm or ps.

Figure 5.6 shows the power dependence of the positions of soliton peaks relative to the middle of the corresponding soliton patterns. The positions of soliton peaks are defined as $x = 1/T \int_0^T (x(t) - x_0(t))dt$ (this integration is illustrated in Figure 5.7), where $x(t)$ is the trace of the soliton peak of interest. $x_0(t)$ is the middle between the two outer solitons $x_1(t)$, $x_2(t)$ in each pattern, i.e $x_0(t)$ fits $1/2(x_1(t) + x_2(t))$. The soliton velocity $v \approx 2.2$ $\mu$m/ps and $T$ is the propagation time of each soliton within the observation window. While it would have been preferable to define the pattern relative to some fixed reference, this was not possible as no reference was visible: the WB emission was blocked (see §3.3.1) and it was later established that a systematic temporal drift between measurements at different powers meant that the position of the soliton trace within the detection window could also not be used as a reference.

The peak separation could also be tuned by varying other excitation parameters. In Figure 5.8, the $k_x$ vector of the WB is increased leading to an increasing temporal separation between the solitons in the array. Here, all experimental parameters were kept constant apart from the WB k vector. It may be that optimising the WB excitation in this way results in a more efficient injection of polaritons into the microcavity, increasing the effective area of the WB.

### 5.2.3 X-Arrays

In contrast to soliton trains, x-arrays were excited when the WB overlapped with the bistable region of the pump spot. The formation of multi-peak patterns is illustrated by the spatio-temporal traces shown in Figure 5.9(a-c). There is a clear separation between peaks, however the array appears to be less stable than the soliton trains presented in §5.2.1. Solitons in some of these structures are seen to move at slightly different speeds, so they can approach one another and merge (e.g. Figs. 5.9c). This could be because the presence of the WB within the pump spot significantly modifies the intensity distribution, making the potential

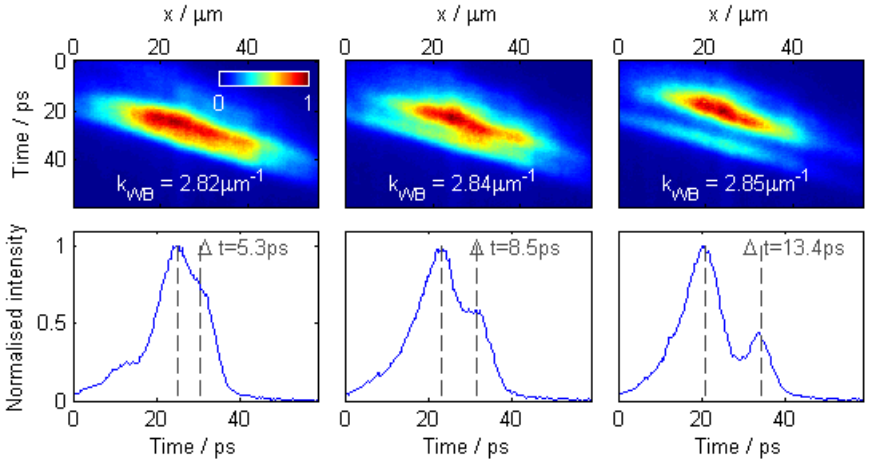


**Figure 5.8: Peak separation, change $k_{WB}$.** Top row: spatio-temporal traces of a multi-peak array as the $k_x$ vector of the WB is increased (indicated in white text). Bottom row: intensity as a function of time at x=30 µm. The temporal separation of the peaks is indicated by grey dashed lines and text.

within the pump spot less uniform while the WB pulse is present. Solitons generated at the high intensity centre of the gaussian WB could have a stronger initial acceleration than those generated at the lower intensity edges due to increased polariton-polariton repulsion.

### Comparison with Trains

A comparison of the E-$k_x$ dispersion of these x-arrays with that of a single soliton and that of the LPB can give further insight. In the case of a single soliton (Figure 5.10a) or a soliton train (Figure 5.10b), a straight line dispersion is seen extending from the k vector of the WB ($k_{WB}$) to k=0 while in arrays (Fig. 5.10 (c,d)) the spectrum tends to consist of several shorter lines which may appear over different k vector ranges and can have different energies. The sections still appear more linear than the LPB, suggesting that the peaks maintain a solitonic character, but as they have different gradients this can result in the solitons propagating at different speeds.

In realspace, the trains look similar to the x-arrays, although they now all travel at the same speed and the soliton trajectory tends to be straighter, indicating that the pattern is less influenced by sample inhomogeneities. One explanation for this is that in the train the soliton peaks are bound, sharing a wavefunction which covers a larger spatial area compared to that occupied by an unbound soliton in an x-array. The wavefunction may be influenced by the average potential background over this area, effectively smoothing the effects of defects. This is similar to the motional narrowing (see §4.4.5 in [5]) of a quantum particle moving through a disordered medium. The disorder creates some variation in the background potential giving it some broad linewidth, but the particle linewidth is narrower than this as it is influenced by the potential averaged over its path rather than the absolute potential at each point along its path.

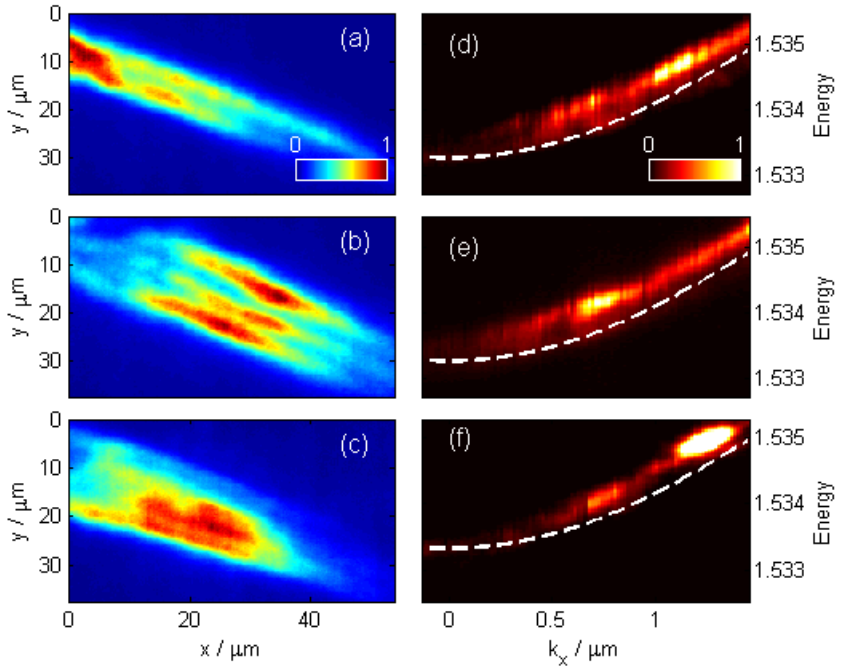


**Figure 5.9: X-arrays. Left column:** spatio-temporal traces from the streak camera. **Right column:** corresponding E-$k_x$ dispersion. The number of solitons in an array increases in each row.

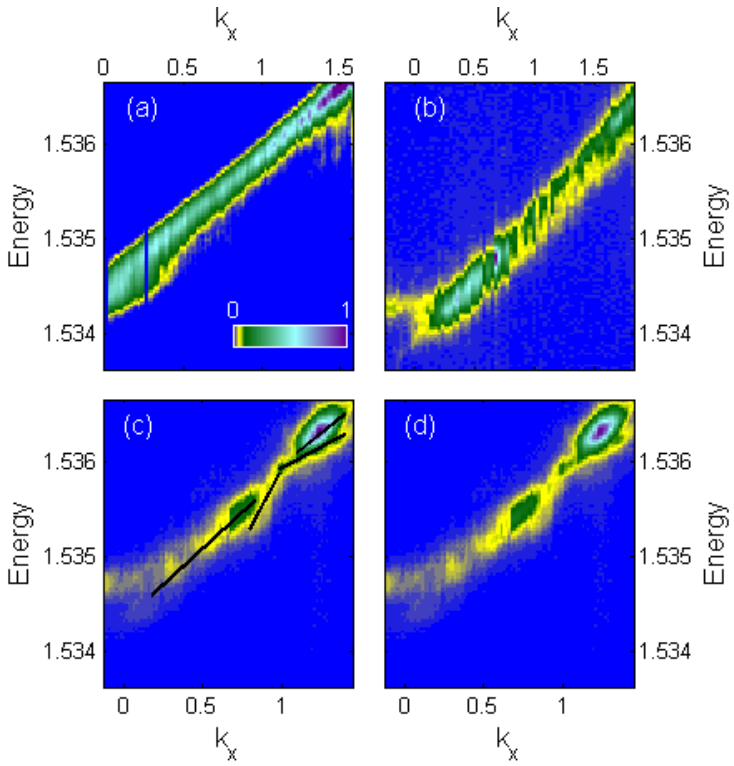


**Figure 5.10: Comparison of dispersions** Energy-$k_x$ spectra for (a) a single soliton (b) a soliton train and (c,d) a horizontal soliton array. (c) and (d) show the same data, but on (c) lines have been added as a guide to the eye showing that this spectrum may be constructed from several line segments with different gradients.

### 5.2.4 Nucleation of Arrays

In most of the data sets presented in this chapter, the evolution of a smooth wavepacket excited by the WB into a multi-peak pattern along x was not recorded due to the limited field of view of the detection optics. However, in some observations of x-arrays, this break-up is visible as the initial wavepacket was excited very close to the edge of the detection window, which imaged the bistability region of the pump. In Figure 5.11(a,b), streak camera images of two-peak x-soliton arrays where the nucleation of solitons is visible are shown. As these are taken from different data sets, several experimental parameters (laser powers, detuning of lasers from LPB etc) will have changed between them which could be why the soliton widths are different in the two cases. Note that separate soliton peaks form at different times out of the broad polariton background around the edge of the bistability region. In Fig. 5.11a the second soliton appears within $\sim$ 7 ps after the emergence of the first one, while on Fig. 5.11b the second soliton is created $\sim$ 20 ps after the first one.

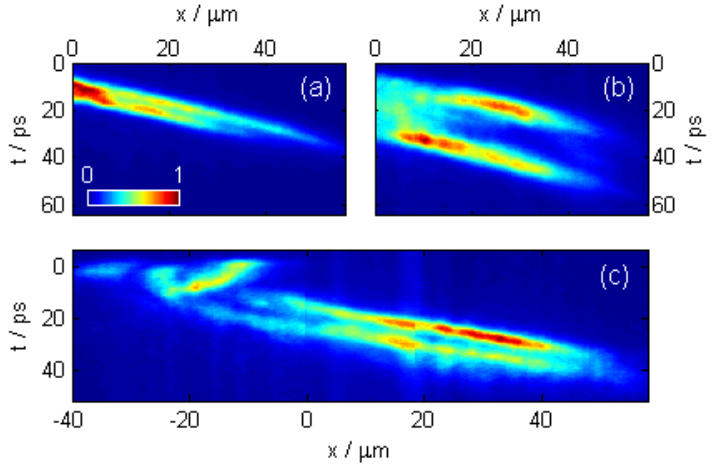


**Figure 5.11: Nucleation of Arrays** Streak camera traces of an x-soliton array (a,b) or train (c) imaged at different positions. $x \sim 30$ μm is the centre of the pump beam, $t = 0 \pm 5$ ps is the approximate time of arrival of the WB. The traces were taken for different WB powers: (a) at $P_{wb} = 2P_0$ and (b) at $P_{wb} = 7P_0$, where $P_0 = 0.1\ mW$ is the threshold for single soliton formation. (c) A blended streak camera trace of an x-soliton array, composed of two streak camera traces offset 35 μm along the $x$-axis and the same position along $y$, taken with WB power $P_{wb} = 3P_0$.

Figure 5.11c shows the evolution of a soliton train, where the WB was positioned ∼20 μm from the edge of the bistability region. Here, a second image was recorded where the imaging window was moved by 35 μm to observe the emission at earlier time including the time of WB arrival. In this case, dim emission at the point of the WB excitation can be seen, even though the WB is blocked (see Figure 3.5), due to scattering of the laser beam. It should be noted that all real-space images are formed only from a portion of the emission with k-vectors below 2 $\mu m^{-1}$, since higher k-vectors are blocked to avoid saturation of the detectors by the pump and WB reflections. Therefore polaritons resonantly injected by the pump and WB are not detected, but only polaritons which scatter to lower k-vectors are observable experimentally.

Surprisingly, the break-up of the WB pulse starts to occur before it reaches the bista-

bility zone, however similar behaviour has also been observed in numerical simulations (see Appendix B Fig. B.2). It is believed that the break-up occurs due to a combination of two factors. Firstly, the difference in the k-vectors of the pump and WB leads to interference of the two beams, hence modulating the excitation power along the $x$-axis. Secondly, polaritons injected by the WB outside the bistability region but still within the pump spot may induce the onset of polariton-polariton scattering from the pump state to the soliton harmonics, causing break-up before the wavepacket reaches the bistability area as in Fig. 5.11c, or right at the beginning of the bistability area, as in Fig. 5.11(a, b).

### 5.2.5 Nonlinear Wavepackets in Microwires

Similar behaviour was observed in a new sample (§3.1.3) designed for use in a transmission configuration (see Methods §3.3). The microcavity was modified by etching the top DBR to form wire-shapes mesas, as for Chapter 6. Measurements of self-focussing wavepackets supported by the CW pump were repeated in a wire of width 4 µm and length 100 µm. Here, the WB k vector was again higher than the pump but the WB energy was much higher than the energy of the LPB, instead being closer in energy to the exciton reservoir (Figure 5.12c). With these parameters, wavepackets could be excited which would only propagate significant distances when the CW pump spot was present. The propagation length here is significantly extended due to the long cavity lifetime, resulting in reflections of the wavepacket from the ends of the 100 µm wire (Figure 5.12).

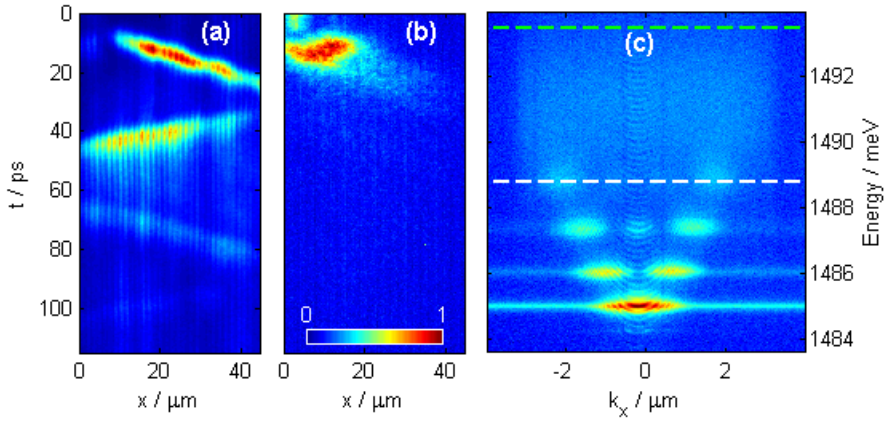


**Figure 5.12: Nonlinear wavepackets measured in a wire: (a,b)** Streak camera trace showing emission intensity as a function of position and time. In (a), both the pulsed WB and the CW pump are present while in (b), only the pulsed WB is used. **(c)** E-$k_y$ spectrum of a wire aligned with long axis along x. The energy of the CW pump is marked with a white dashed line while the energy of the pulsed WB is marked with a green dashed line.

When the WB was quasi-resonant with the LPB as for most results presented in this chapter, the emission was dominated by wavepackets that would propagate regardless of whether or not a pump was used due to the higher Q factor of this new sample. These non-linear wavepackets are studied in great detail in Chapter 6.

It would be expected that a dissipative soliton should not propagate with the opposite k

vector to the CW pump, but in Figure 5.12 the reflected wavepacket propagates unhindered. The emission intensity also drops over time, which appears to be due to photonic losses from the cavity and potentially inelastic collisions with the end of the wire. While this would be expected for nonlinear wavepackets with no pump as presented in Chapter 6, for the dissipative solitons presented in the rest of this chapter, the soliton intensity should be maintained by the pump [7]. Once excited, the wavepacket in Figure 5.12 thus behaves more like those investigated in Chapter 6, suggesting that the role played by the CW pump is less significant at later times.

It could be that this experiment represents an alternative method for exciting the self-focussing wavepackets investigated in Chapter 6 using a non-resonant pulse WB to trigger a wavepacket in the CW resonant pump, rather than using a resonant pulsed WB with no CW pump. This alternative excitation was not investigated here, but could be pursued in future experiments as relaxing the requirements for the pulsed WB may make the excitation scheme easier to realise in a polariton device.

## 5.3 Y-Arrays

It has previously been observed [7] that the soliton size in the y direction (perpendicular to the propagation direction) is independent of the size of the WB. In previous observations [7], the WB diameter was 7 μm but the excited wavepacket was seen to shrink to 5 μm in the y direction, a size which was maintained during further propagation. This behaviour is similar to that seen in the x (propagation) direction, although the mechanisms of formation are different in the two directions (see §2.4.1). Previously in this chapter I have shown that if the WB is elongated along the x direction to more than double the soliton size, the excited wavepacket breaks up into a soliton train or x-array. In this section, I explore the effects of elongating the WB in the y direction.

### Observation

If the WB is extended to $\sim 30$ μm along the $y$-axis and $\sim 7$ μm along the $x$-axis, the beam profile can be made to break into an array of localised wavepackets, forming a y-array. As the WB power is gradually increased, the number of wavepackets in the pattern increases (Figure 5.13). The number of peaks created depends, as for the soliton trains (§5.2.1), on the effective spot size of the WB. Peaks are spaced by $\sim 8$ μm, are of the size (FWHM) of $\sim 7$ μm and travel along the $x$ direction within the pump bistability area. The number of solitons can also be tuned by adjusting the WB energy, where the system appears to move through some resonance (Fig. 5.14).

Due to the instability of the system (small fluctuations in laser intensity could trigger the entire pump spot into the high density state on the bistability curve), fast measurements of the variation along the y-axis were preferable. In order to quickly determine the pattern, images of the intensity as a function of y position and time were recorded on the streak camera. To do this, the emission had to be rotated so that the y axis was aligned with the horizontal streak camera slit (see Figure 3.4). This was done by adding a Dove prism before the imaging lens in the setup at the expense of potentially introducing some distortion in

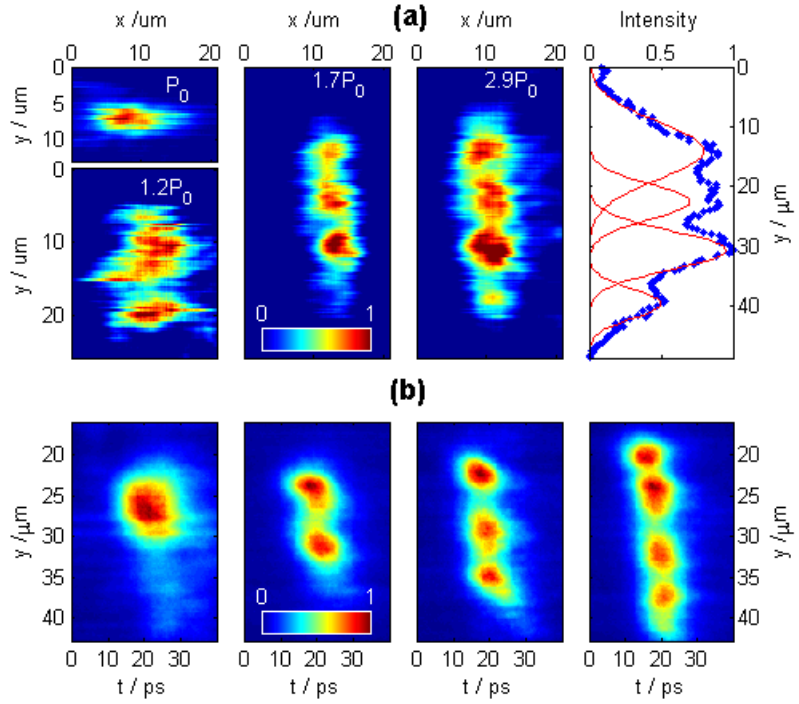


**Figure 5.13: Y-arrays.** **(a)** 2D images of one- to four-peak arrays obtained for different WB powers $P_0$, $1.2P_0$, $1.7P_0$ and $2.9P_0$ where $P_0 = 230\ \mu$W, at time $t = 20$ ps after the WB pulse. These images are reconstructed by combining streak camera traces showing the intensity as a function of x and time, taken at different positions along y as explained in §3.3.5. The right hand image is the profile of the four-peak array along the $y$ axis, integrated over x. **(b)** Intensity as a function of y and t. Each image is only one streak camera trace, taken by rotating the emission using a Dove prism to align the y-axis on the sample with the horizontal slit on the streak camera. Examples are shown of arrays containing one to four peaks.

the imaging. Several data sets were taken with this rotated configuration, including those shown in Figures 5.13b, 5.14, 5.15 and 5.16.

### Dynamics

By recording emission from different points along the soliton propagation path, the dynamics of array formation can be studied. In Figure 5.15, the WB power and energy were optimised to generate y-arrays of one to four solitons, as shown in the bottom row. For each array, the intensity profile along y integrated over x is shown as a function of time. The apparent propagation along the y direction over time is an experimental artifact indicating that the emission was not fully rotated by the Dove prism to align the y axis with the horizontal slit.

The intensity profile evolves over time: both the three and four soliton arrays start off as a single bright peak with a broader background, which then evolves into multiple peaks of comparable intensities. Once a pattern is formed, it continues to evolve with some peaks merging (for example, Fig 5.15c, at (y,t) = (20 µm, 30 ps)) and others separating (for example Fig 5.15b, a new peak emerges at (y,t) = (35 µm, 35 ps)). These y-arrays are therefore less stable than the soliton trains presented in §5.2.1 in which the peak separation remains constant over the propagation path.

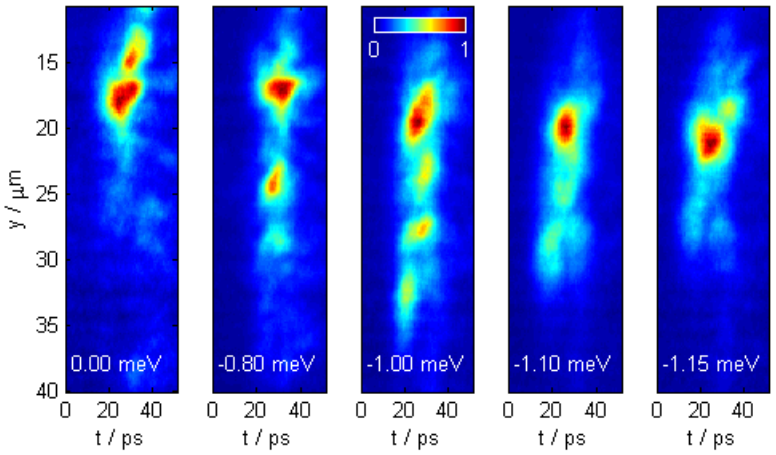


**Figure 5.14: Y-arrays, decrease WB energy**. Intensity vs y and t traces are recorded. The emission is rotated to align the y-axis with the detection slit so that the presence of a pattern in this direction can be deduced from a single trace. White text shows how the WB energy was changed between each measurement.

### Independence of pattern and sample disorder

The initial shape of the y-array depends strongly on that of the WB, with additional peaks being created on the "sides" of the WB as the excitation power is increased. In order to check that the pattern was induced by the WB shape rather than disorder on the sample, the array pattern was recorded firstly as the WB was kept stationary and the sample was moved and secondly as the WB was moved over the sample (Figure 5.16). In these experiments the slice along y which was imaged on the streak camera was fixed relative to the centre of the pump excitation spot, which was also fixed in the laboratory frame. This data provides direct comparisons between soliton array profiles for different positions of the WB and sample without the need to conduct scans along the $y$ axis as for Fig 5.13.

In the first experiment, the array stayed in the same position relative to the pump and detection window while the pattern was not significantly altered as the sample was moved, indicating that the shape of the array does not depend on localised defects on the sample. In the second experiment, the pattern was translated as the WB was moved across the sample and detection window, showing that it is determined by the WB.

The break-up of the wavepacket into a y-array has been investigated numerically by Andrey Gorbach and Dmitry Skryabin (presented in [8], reproduced in §B.2 in Appendix B). It is shown that in a Gaussian wavepacket the curvature of the wavefront is different at different spatial positions leading to a variation in the front velocity across the wavepacket. This can result in the break-up of an initially smooth beam profile, an effect which is amplified when there is a difference in k vector between the pump and WB, which is the case in these experiments (see Figure 3.5). An alternative mechanism for y-array formation could be laser-beam filamentation, described in §5.4.1.

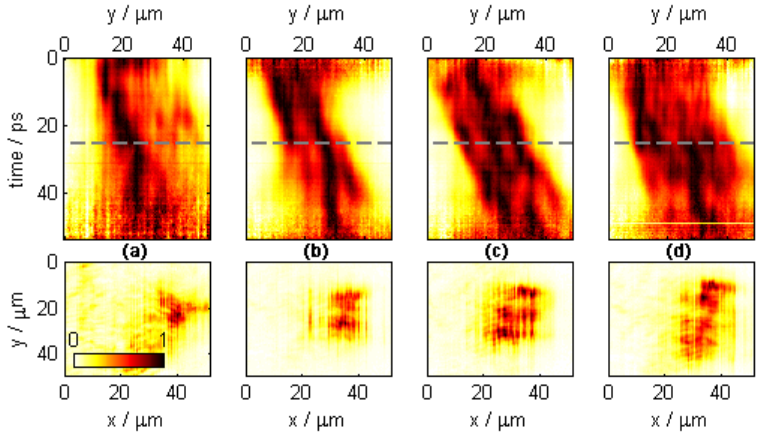


**Figure 5.15: Dynamics of y-arrays**. Intensity vs y and t traces are recorded for different positions along x. The WB power and energy are optimised to generate y soliton arrays with (a) one (b) two (c) three and (d) four peaks. **Top row:** emission intensity as a function of y-position and time, integrated over x. Each row is separately normalised to make the pattern more visible. **Bottom row:** emission intensity as a function of x and y at 25ps (marked by grey dashed line)

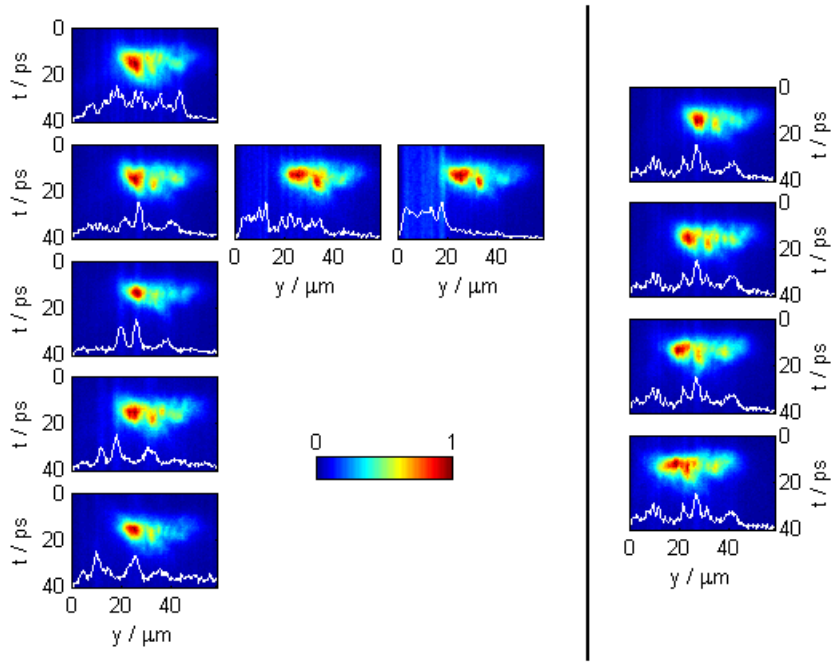


**Figure 5.16: Independence of Pattern and Sample:** Intensity vs y and t traces are recorded with the emission rotated to align the y-axis with the detection slit. White lines show intensity vs y position integrated over 70 <t< 110ps: here there is only emission from the CW pump spot whose intensity distribution matches any disorder over the sample. Changes in the sample position can therefore be deduced from changes in this background intensity profile. Note that the horizontal axis in these images corresponds to the y axis on the sample. **Left:** WB position is kept constant while the sample position is moved vertically and horizontally. The position of each trace in the figure maps the position of the sample when each trace was taken. The sample is moved by $\sim 10$ µm between each image. **Right:** The sample position is kept constant while the WB position is moved vertically by $\sim 10$ µm.

## 5.4 Discussion

### 5.4.1 Soliton Separation

As shown in §5.2.2, the separation between solitons in an x-array or train can be tuned by optimising the excitation conditions, particularly the WB power. It might be expected that the solitons in a train should have a well defined, uniform spacing; this would be the case for most of the parametric trains proposed by Egorov *et al* [126]. However, it is shown in that paper that adjusting the system parameters can result in more complex behaviours, for instance a structure is shown where groups of 3 closely spaced solitons are separated by a distance similar to the width of the group rather than the width of the soliton (reproduced in Figure 2.14d).

Another factor which could be involved in wavepacket break-up is phase matching. When the first part of the WB wavepacket hits the pump spot, the first soliton starts to form and its phase is set. As the next part of the wavepacket approaches and the second soliton starts to form, its phase could be influenced by that of the first soliton due to overlap with the tail in its wavefunction. The phase of the first soliton may inhibit the formation of further solitons if the phase difference is too large, so there is a gap where no solitons form due to destructive interference. This could result in the observation of soliton groups.

Numerical modelling has shown ([8], reproduced in Appendix B) that the irregular soliton spacing as well as the increasing separation with power can be replicated if an angle is introduced between the pump and the WB, suggesting some interference effect. In this experiment, there is always a finite angle between the two laser beams as the mirror used to direct the pump to the sample would block the WB if the angle were the same (see Figure 3.5 in §3.3.1). These simulations were carried out by collaborators A. Gorbach and D. Skryabin.

#### Analogies with other soliton systems

In general, soliton solutions can be found analytically by solving the Non-linear Schrödinger Equation (see §2.3). So-called "fundamental" solitons have a single peak with a sech amplitude profile, however higher order solutions can be found if the injected intensity is increased. At higher powers, these high-order solitons can split into several fundamental solitons in a process known as "soliton fission" (see §2.3.3, §2.3.4). For arrays produced in this way, neighbouring solitons can have different energies, something which has been observed previously in optical fibers. It is possible that the polariton soliton arrays presented here are analogous to these structures: the soliton trains (§5.2.1) may be examples of higher order solitons sharing a single line E-k spectrum; while x-arrays (§5.2.3) could occur as a result of soliton fission, where neighbouring solitons can have different spectra.

In optical systems with a nonlinear refractive index, laser break-up or filamentation can be seen when the laser power exceeds the expected power for soliton formation [2]. In experiments by Bennink *et al* [99] where a laser beam is passed through an atomic vapour, laser break-up resulted in the formation of a pattern of three spots. As the laser power was increased from zero, the initial spot broke into three peaks which moved apart. At the highest powers, new spots appeared at the centre point of the pattern. In their paper, they show that this behaviour matches simulations based on non-linear self-action effects. While

this system is very different from the microcavity soliton system discussed in this thesis, it shows similar behaviour to what is seen here. In particular, the increasing separation of solitons in a train as the WB power is increased (§5.2.2) is replicated. This supports the suggestion that the nonlinearity leading to soliton formation could also cause the breakup of a wavepacket at high excitation powers.

### 5.4.2 Relationship of Pump and WB

It is believed that localisation of these solitons in the y direction arises from some interaction of the triggered wavepacket with the pump (§2.4.1), a result which will be verified in §6.7. The results in this chapter reveal further effects arising from this interaction.

The experimental setup used here has the limitation that the pump and the WB cannot have the same k vector. Simulations have shown that even a small angle between the two laser can account for some of the results presented here. Y-arrays (§5.3) can arise from a break-up of the propagating wavefront due to the inhomogenous intensity profile of the triggering WB, a process which is enhanced if the laser beams have different k vectors. In addition, the increasing separation between solitons in a train with WB power can be replicated in numerical simulations by introducing a similar relative angle of around 3°. By contrast, if the pump and WB were parallel, the number of peaks in a soliton train would increase with WB power, but the separation between them would remain the same. These simulations, carried out by Andrey Gorbach and Dmitry Skryabin, are published in [8] and reproduced in Appendix B.

If adjacent solitons in an x-array have different energies, the relative phase between them will evolve over time. However for a soliton train, the single line dispersion whose peaks narrow with an increasing number of soliton peaks suggests that the whole array may be coherent with a constant phase relation between adjacent peaks. Experimentally, the relative position of the writing beam and pump spot were found to determine whether an excited soliton pattern would evolve into a soliton train (single dispersion line, §5.2.1) or an x-array (multiple line segments in the dispersion, §5.2.3). However, moving the WB by a few microns in the pump spot did not affect the pattern that was formed along the y axis (Fig. 5.16). This could be because the distance moved was too small to affect it, especially as the WB was only moved around within the pump spot rather than being moved to some distance away from it.

The writing beam hits the sample at an angle, so that photons from one side of the extended WB arrive at the sample surface before those at the other side. There is therefore a phase gradient across the writing beam and as a result, there is a phase gradient imprinted across the excited wavepackets (so the first one is phase shifted compared to the last one). If the WB is positioned outside the bistability region of the pump, adjacent wavepackets can interact (the soliton wavefunction has a tail as illustrated in Figure 2.13 in §2.4, so the tail of the first will overlap with the peak of the second) and can lock their phases with each other. This is effectively a bound state of wavepackets which is excited into a multi-hump soliton when it hits the bistability region. If, however, the WB is positioned within the bistable region of the pump, there is no time for interactions and phase-locking to occur between wavepackets, so individual solitons may be excited rather than one multi-hump

bound state. There is no requirement for the individual solitons to have the same energy, resulting in different spectral lines.

### 5.4.3 Mechanisms for Soliton Formation

As discussed previously (§2.4.1), the final soliton size is determined by the interplay between the coulomb repulsion due to polariton-polariton interactions and the attraction arising from the polaritons' negative effective mass. However, there are other aspects to consider, for example the observed soliton spectrum extends to k vectors close to zero where the polariton effective mass is positive, calling into question how much the negative effective mass will contribute once the soliton has formed and continues to propagate. This situation contrasts with that of gap solitons (Chapter 4, [81]) where only states with negative effective mass are populated.

Before an attempt is made to trigger a soliton, the system is initialised with a continuous wave pump quasi-resonant with the LPB at a high k vector, where the polariton efffective mass is negative. The pump power is tuned so that the system is in a bistable regime where the polariton density can be high or low. When the WB trigger pulse arrives, it injects polaritons quasi-resonant with a slightly different point on the lower polariton branch. In realspace, this injected wavepacket triggers a small region of the bistable pump spot into the high density state: this is the wavepacket which is observed to evolve into a soliton.

Looking at the E-$k_x$ spectrum, the polariton population injected by the WB can start to stimulate the scattering of polaritons out of the pump state and into the WB states (the WB has a broader linewidth so excites a few polariton states). This is a parametric process (see §2.2.1 for more details), so as the WB states are populated, states with an equal and opposite energy and k separation from the pump spot also become populated. In this way, the linear soliton spectrum starts to form. The triggered wavepacket evolves into a soliton with a well defined size: this often meant that the wavepacket shrank in experiments as the WB size was chosen to be larger than the expected soliton size. Both the interplay of negative effective mass and coulomb repulsion and the fact that parametric scattering broadens the k space spectrum can contribute to the initial shrinking of the soliton.

Because the soliton spectrum is linear, once the soliton forms it will maintain its shape as the curvative of the dispersion tends to zero so that components at different energies propagate at the same speed. Linearisation of the spectrum also increases the effective mass, which is inversely proportional to the curvature, making it harder to change the propagation speed of each component. The rate of scattering between polaritons in different states should be much lower than scattering between polaritons in the same state due to the reduced spectral overlap between them. This could inhibit fast relaxation of the polaritons to the curved lower polariton branch, helping to maintain the linear spectrum.

It is clear that the linear spectrum helps the soliton to maintain its size, although it is less clear why this spectrum is chosen in the first place. The triggered OPO process that is thought to populate the spectrum is probably largely responsible, combined with the fact that the broad linear spectrum stabilises the shape-maintaining soliton favoured by balancing the energy terms. However, there are also parallels to be drawn with superfluid behaviour, where excitations of the superfluid have a linear dispersion known as a Bogoliubov spectrum

(see §2.2.4). Similar linearisation of the spectrum has previously been seen in a propagating polariton condensate excited by a triggered OPO (TOPO) process [69]. As my system also starts with a system primed to trigger an OPO induced condensate but then uses TOPO to populate states away from k=0, there could be a preference for exciting a linear Bogoliubov like dispersion.

## 5.5 Conclusions

In this chapter, I have build on previous studies of bright polariton solitons [7, 123] to generate multi-peak soliton patterns. Arrays of solitons can be triggered both along and perpendicular to the direction of propagation by elongating the WB along the x and y directions respectively. Increasing the effective area of the WB by changing its power increases the number of peaks in the excited array.

Y-soliton arrays (peaks arranged perpendicular to the propagation direction) can form despite the polaritons' positive effective mass in this direction. The pattern is not determined by disorder in the sample. Simulations presented in [8] (reproduced in Appendix B) offer a possible explanation, where variations in velocity over the array wavefront lead to break-up into several localised peaks. This effect is enhanced when the CW pump and pulsed WB have different k vectors, as is the case in my experimental setup.

In the x direction (peaks arranged along the propagation direction), two regimes of patterns can form. X-arrays have multiple peaks but these can have different widths and move at different velocities, resulting in an irregular pattern with spectra consisting of several distinct linear components. By contrast, soliton trains form regular patterns where each soliton moves with the same velocity. The E-$k_x$ spectrum of a soliton train is linear, with spectral peaks which narrow as the number of solitons is increased, suggesting that the solitons form a bound, coherent state. As it is possible to move between these two regimes simply by changing the relative position of the pump and WB, the variation in behaviour is attributed to a difference in the interactions within the triggered wavepacket before and after it encounters the CW pump spot.

The peak separation in x-arrays and trains is not fixed, but can be tuned by optimising the WB power and energy. This tunability of the soliton repetition rate could make soliton arrays an attractive candidate for providing a clock signal on a polariton device, capable of operating with 100GHz repetition rate. This could be particularly useful if soliton arrays could be triggered using only continuous wave sources. The current work of generating multiple solitons with each laser pulse could be built on to generate solitons in a CW environment as suggested in §7.1.4.

# Chapter 6

# Nonlinear Wavepackets in Microwires

In this chapter, observations of nonlinear polariton wavepackets in quasi one-dimensional microcavity structures (microwires) are presented. While in Chapter 5 polaritons lost from the system are replaced by a continuous wave pump, in this set of experiments only the pulsed writing beam (WB) is used. These observations of dynamics with no CW pump are made possible by the longer lifetime of the polaritons in the sample used in this chapter (up to ∼30 ps instead of ∼5 ps) due to the increased photonic lifetime. Once a wavepacket is triggered, the polariton number decreases exponentially over the propagation path as photons escape from the cavity.

The dynamics of these wavepackets are investigated, looking at changes in energy, real-space size and k-space distribution over the propagation path §6.2. With the right excitation conditions, the wavepackets initially shrink in real-space; this self-focussing is an indication of soliton-like behaviour. The self-focussing is seen with excitation at k vectors above the point of inflection of the lower polariton branch (LPB) where the injected polaritons have negative effective mass. This matches the conditions which would be required for bright soliton formation (see §2.4).

Wavepacket arrays (§6.3) can be generated by increasing the excitation power in a similar manner to the generation of soliton arrays (Chapter 5). The phase across the array is studied (§6.4), revealing the evolution of phase discontinuities between peaks during propagation as higher excitation powers are used. Photon counting statistics and pair correlations in the wavepacket emission are measured, revealing that the occupied states exhibit non-classical behaviour which may correspond to amplitude squeezing (§6.5).

Similar dynamics are seen in "short" wires, where the wavepacket reflects from the end of a wire during propagation (§6.6). In a planar cavity, self-focussing is observed along the propagation direction but the wavepacket spreads in the perpendicular direction (§6.7), supporting the theory that the mechanism for localisation in the perpendicular direction for dissipative solitons (§2.4.1) involves interactions with the continuous wave pump.

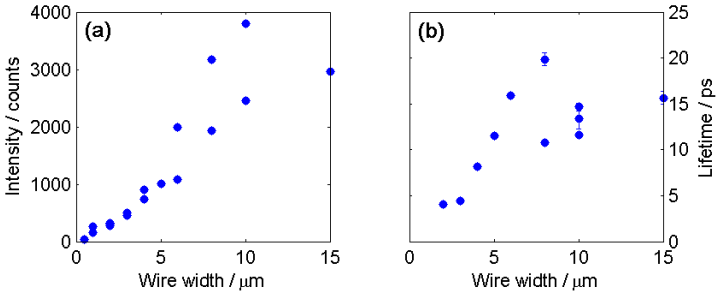


**Figure 6.1: Effect of wire width** (a) Intensity of wire emission as a function of wire width. (b) Polariton lifetime in wires of different widths.

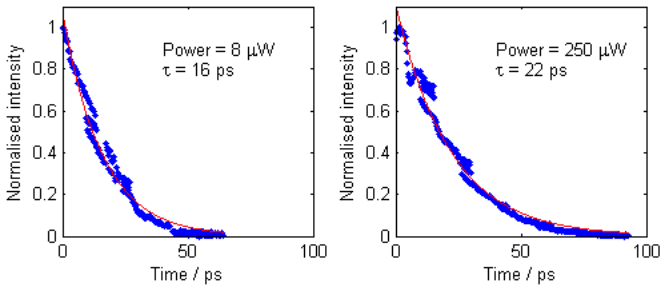


**Figure 6.2: Sample Lifetime:** Two data sets showing emission intensity as a function of time. Here, the polariton lifetime $\tau$ appears to change as a function of WB power. The sample is excited with a WB at a k vector above the point of inflection (these are the data sets at powers $P_0$ and $P_3$ shown in §6.3)

## 6.1 Sample characterisation

The samples used in this chapter are quasi-1D structures. These are made by taking a planar cavity and partially etching the top DBR to define mesas (see §3.1.3). The wires used here are typically a few microns wide and either 1000 μm ("long wires", used for most of this chapter) or 100 μm ("short wires", used in §6.6) long. All of the "long wires" used in this chapter had a width of 5 μm. These are multi-mode structures but while decreasing the wire width increases the mode spacing and so decreases the number of occupied modes, if the wire width is too small the observed emission becomes dim and the polariton lifetime drops (see Fig 6.1). This could be due to increased losses from the side walls as surface roughness on the walls becomes more significant as the wire width decreases. The case of narrow wires is similar to the case of small micropillars where non-radiative relaxation can occur on the walls of the pillar. This is particularly significant if the pillar is smaller than the diffusion length of the carriers (typically micrometers) [5]. The polariton lifetime ranges between ∼15-30 ps as the excitation conditions, such as the WB power, are varied (see, for example, Figure 6.2).

Details of the wafer are given in §3.1.3, while Energy-k spectra for the different samples used in this chapter are illustrated in Figure 6.3. In these measurements, the wire was excited non-resonantly with a HeNe laser. When required, energy as a function of both $k_x$ and $k_y$ could be measured by moving the imaging lens to select different values of $k_x$, then reconstructing the full spectrum from a series of measurements (§3.3.5). The samples used

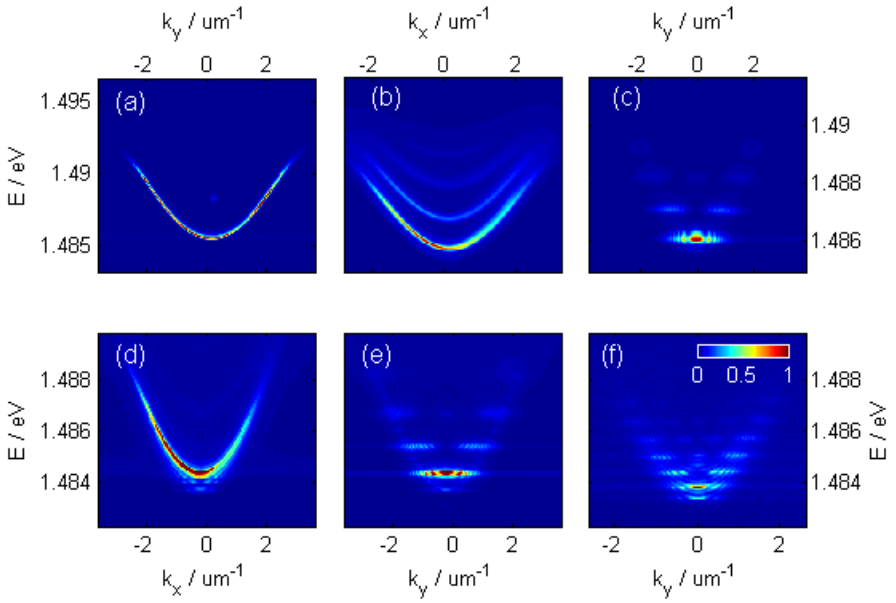


**Figure 6.3: E-k spectra of samples (a)** Dispersion for planar cavity. **(b,c)** Dispersions for 1 mm long, 5 µm wide wires along the length (b) and across the width (c) of the wire. **(d-f)** Dispersions for 100 µm long wires. (d) shows the dispersion along the length of a 4 µm wide wire while (e) is taken across the width of a 4 µm wide wire. (f) is the dispersion across the width of an 8 µm wide wire.

in this chapter are all taken from the same wafer, but have different detunings and mesa shapes as explained in §3.1.3.

## 6.2 Dynamics of Self-focussing Wavepackets

In this section, I look at how the shape, E-$k_x$ spectrum and **k** distribution of a wavepacket changes as it is injected in the non-linear regime, propagates along a wire and finally collapses to a dispersive wavepacket in the linear regime. The cases where only the lowest confined mode of the wire is excited (§6.2.1) and when two wire modes are excited (§6.2.2) are both investigated. These non-linear wavepackets are found to show soliton-like behaviour; in particular, when excited with a beam of large area, they are seen to self-focus during their initial propagation. This contrasts with the case where polaritons are injected in the linear (low power) regime, where the wavepackets never shrink, but instead spread slightly as they propagate as shown in Figure 6.4.

The expected full width of a soliton $w$ can be approximated by doubling the healing length of a quantum fluid. This can be found by equating the kinetic energy due to dispersion with the potential energy due to polariton-polariton interactions and the resulting soliton width is given by $w(t) = 2\hbar(\sqrt{2MgN(t)})^{-1}$ where $M$ is the effective mass of the polariton, $g$ is the interaction coefficient for the polariton-polariton interaction and $N(t)$ is the polariton density at a given time $t$ [7]. The width of a soliton would therefore be determined by its environment ($M$ from polariton dispersion, $gN(t)$ from polariton-polariton interactions) rather than the size of the WB that triggers it. In the experiments presented in this chapter, $N(t)$ decreases exponentially with time as photons escape the cavity, reducing the overall

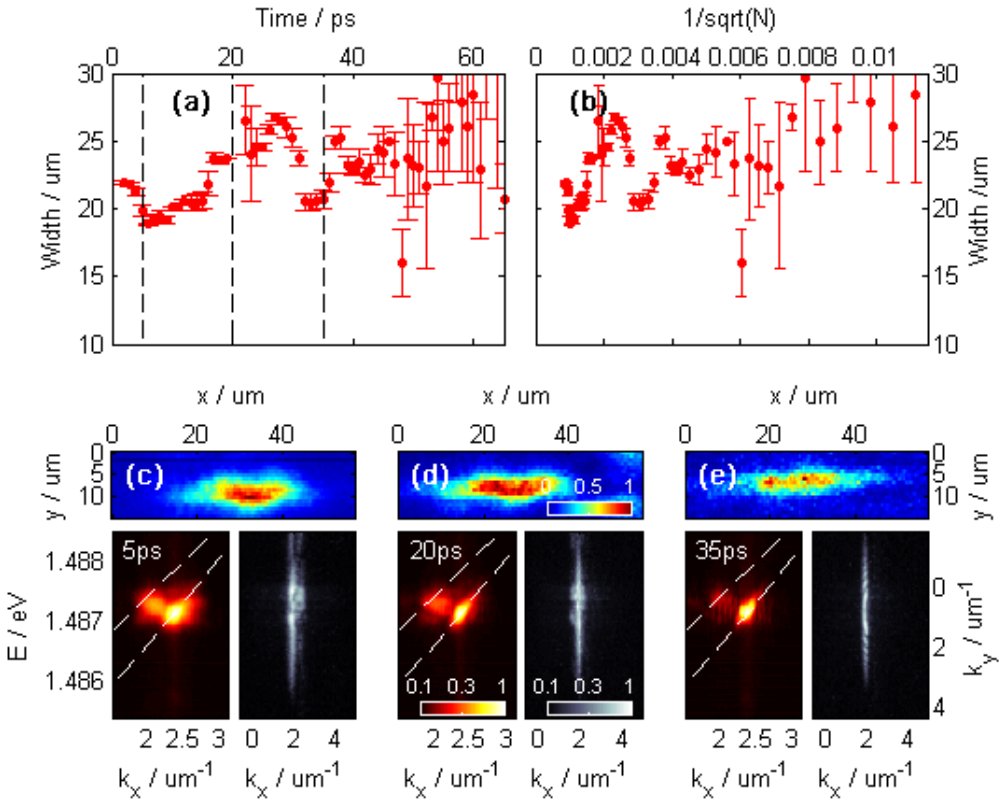


**Figure 6.4: Dynamics, linear regime**. **(a)** Wavepacket width (FWHM) vs time. Black dashed lines indicate the times at which (c-e) are recorded. **(b)** Wavepacket width vs $1/\sqrt{N}$ where $N = \int_t^{120ps} I(t)dt$ and $I$ is the emission intensity (measured in counts registered on the streak camera. Note that this is proportional to rather than equal to the number of photons emitted from the sample due to gain in the streak camera in normal operation). **(c-e)** realspace images, E-$k_x$ dispersions and k-maps at different times during the wavepacket's propagation. The white dashed lines show the position of the lower polariton modes and the dispersions are shown here with a logarithmic colour scale

polariton population and changing $w$. If a wavepacket is excited by a WB with a width larger than $w$, it could be said to exhibit soliton-like behaviour if it initially shrinks, but then subsequently expands in proportion to $1/\sqrt{N(t)}$.

### 6.2.1 Single mode

The lowest order wire mode was resonantly excited using a WB at $k_x = 2.22$ μm$^{-1}$ with an excitation power of 200 μW. An initially broad wavepacket with a width of $\sim 20$ μm is injected as shown in Fig. 6.5c. The evolution of the size of the wavepacket as it propagates is shown in Fig. 6.5a. The wavepacket initially shrinks in size, reaching a FWHM of 9 μm after 50 ps before growing to a width of 13 μm. The approximately linear increase in size with $\frac{1}{\sqrt{(N(t))}}$ in the range $0.0015 < \frac{1}{\sqrt{(N(t))}} < 0.005$ is consistent with soliton-like behaviour, as explained in the introduction to this section. At later times (t > 100 ps) and lower emission intensities $\frac{1}{\sqrt{(N(t))}} > 0.005$, the wavepacket size stays roughly constant. The change in relationship between the wavepacket size and $\frac{1}{\sqrt{(N(t))}}$ indicates that the wavepacket is no longer in the non-linear (soliton-like) regime and a dispersive wavepacket is formed instead. At these low polariton densities, the Coulomb repulsion is low, reducing the expected spread of the wavepacket.

In Fig 6.5(c-e), two-dimensional realspace images of the wavepacket at different times are compared with the E-$k_x$ spectra measured at the same points after excitation. The realspace images show the shrinking and subsequent expansion of the wavepacket already described. As the wavepacket shrinks in realspace, the range of states occupied on the E-$k_x$ spectrum broadens. The blueshift in energies at early times compared to the marked lower polariton branch is due to the Coulomb interactions between the polaritons injected at high densities. The marked LPB was measured using non-resonant excitation. At later times, the polariton density drops, redshifting the spectrum back towards the marked LPB.

Plotting the emission intensity for the E-$k_x$ spectra on a logarithmic colour scale reveals that the polariton density is modulated along the spectrum, as emphasised in the intensity profile superposed on Figure 6.5d. Five peaks are visible with an average separation of $0.27 \pm 0.02$ μm$^{-1}$. This modulation could arise from the parametric scattering mechanism which is believed to be what populates the soliton-like spectrum, which will be further discussed in §6.2.5. A series of delta function peaks with this spacing corresponds to a realspace modulated pattern with peaks of width $9 \pm 1$μm separated by $23 \pm 1$ μm (see Appendix A). Although an extra peak was not observed in realspace, there could a contribution to the dispersion from a dim tail propagating behind the main self-focussing peak.

### 6.2.2 Multi mode

As the WB is broad in k space, it can be tuned into resonance with multiple modes of the wire to resonantly excite a multimode wavepacket. This can be done by decreasing the k vector compared to the single mode case while keeping the WB energy constant. The results are shown in Fig. 6.6 where the WB was at $k_x = 2.11$ μm$^{-1}$ and had an excitation power of 100 μW.

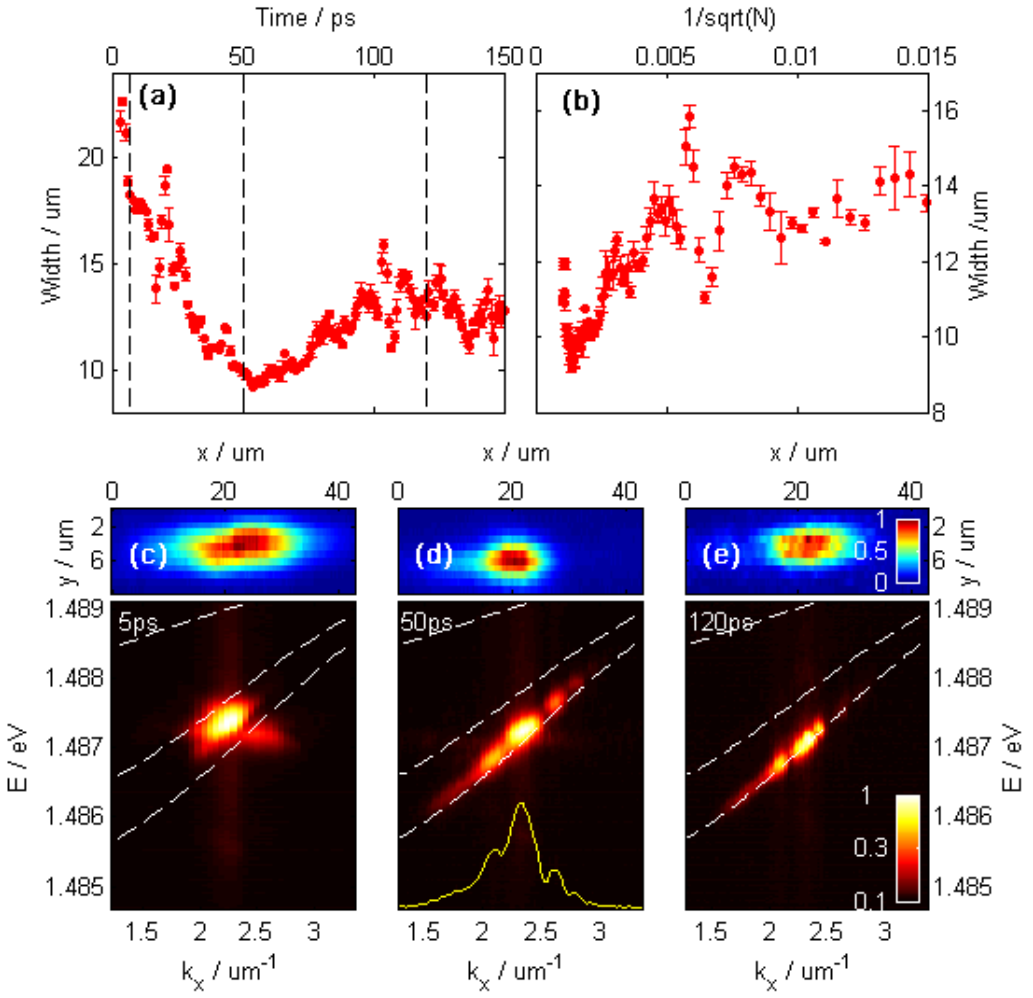


**Figure 6.5: Dynamics, single mode wavepacket**. **(a)** Wavepacket width (FWHM) vs time. Black dashed lines indicate the times at which (c-e) are recorded. **(b)** Wavepacket width vs $1/\sqrt{N}$ where $N = \int_t^{120ps} I(t)dt$ and $I$ is the emission intensity. Very low intensity (t>90ps) data is excluded as this would otherwise dominate the plot, obscuring the nonlinear region of interest. **(c-e)** realspace images and E-$k_x$ dispersions at different times during the wavepacket's propagation. The white dashed lines show the position of the lower polariton modes and the dispersions are shown here with a logarithmic colour scale. The yellow line in (d) shows the intensity profile of the E-$k_x$ spectrum along $k_x$, integrated over energy.

Initially, a broad wavepacket (width $\sim$ 30 μm) is excited by the pulsed writing beam (WB) with emission coming from multiple wire modes as can be seen in the dispersion and k-maps at early times. As for the single mode case §6.2.1, the dispersion is blueshifted due to Coulomb repulsion between the polaritons. Due to this multi-mode excitation, the wavepacket appears to "snake" between the walls of the wire (y direction) as it propagates in the x direction. During the first ∼40 ps after the arrival of the WB, the excited wavepacket shrinks in size as would be expected for a soliton.

The wavepacket shrinks to a minimum width of $\sim$ 12 μm (note that while the main peak looks $\sim$ 8 μm wide, the width shown here is the FWHM which may appear extended due to the lower density tail). The emission is now concentrated in the lowest energy mode of the wire and the range of occupied energy states in this mode is slightly extended. The "snaking" between the wire walls is reduced. It is thought that the evolution from a multi-mode structure to a single-mode structure is due to an initially higher density in the lower mode, which stimulates scattering from the higher mode to the lower mode. Between 40 and 80 ps, the wavepacket size increases (Fig 6.6a). This corresponds to the linear section of Fig 6.6b and is consistent with solitonic behaviour, where the soliton width would be proportional to $\frac{1}{\sqrt{\langle N(t)\rangle}}$.

At later times (t > 80ps), the wavepacket continues to spread but this no longer has the same relationship with N(t) (Fig 6.6a,b). This indicates that the polariton population is now too low to be in the non-linear soliton-like regime and a dispersive wavepacket is formed instead. The E-$k_x$ spectrum narrows and occupies states on the lower polariton branch.

### 6.2.3 Excitation Conditions

The nonlinearity in this system comes from polariton-polariton interactions (see §2.1.1), so nonlinear effects will be stronger with higher excitation powers as these will inject higher polariton densities. The self-focussing illustrated in §6.2.1 and §6.2.2 may have a similar origin to the self-focussing seen in the formation of bright dissipative polariton solitons §2.4.1. If this is the case, this should only be seen when the polaritons are injected at high k vectors where they have negative effective mass.

The change in wavepacket size over the first 40 ps is measured as a function of k vector and power (Fig. 6.7(a-c)). First, the power is fixed at 60 μW and the excitation k vector is varied (Fig. 6.7a). At high k vectors, the wavepacket initially shrinks after it is excited,(Fig. 6.7d) but at low k vectors the wavepacket size stays roughly constant, or even spreads slightly (Fig. 6.7e). The change between a spreading and a self-focussing wavepacket occurs when the excitation k vector goes above $\sim$ 2 $\mu m^{-1}$, which is approximately the point of inflection of the lower polariton branch.

In order to verify the change in behaviour as the point of inflection is crossed, the wavepacket spread as a function of power was measured for two k vectors, one on either side of the point of inflection. For the low k vector (Fig. 6.7b), the spread increases with excitation power as might be expected due to the increase in polariton-polariton repulsion. At the high k vector (Fig. 6.7c), for all powers apart from the very lowest (linear regime, non-linear effects are negligible), the spread is negative i.e. the wavepacket shrinks. The jump in width between 85 μW and 250 μW is attributed to the presence of an extra peak

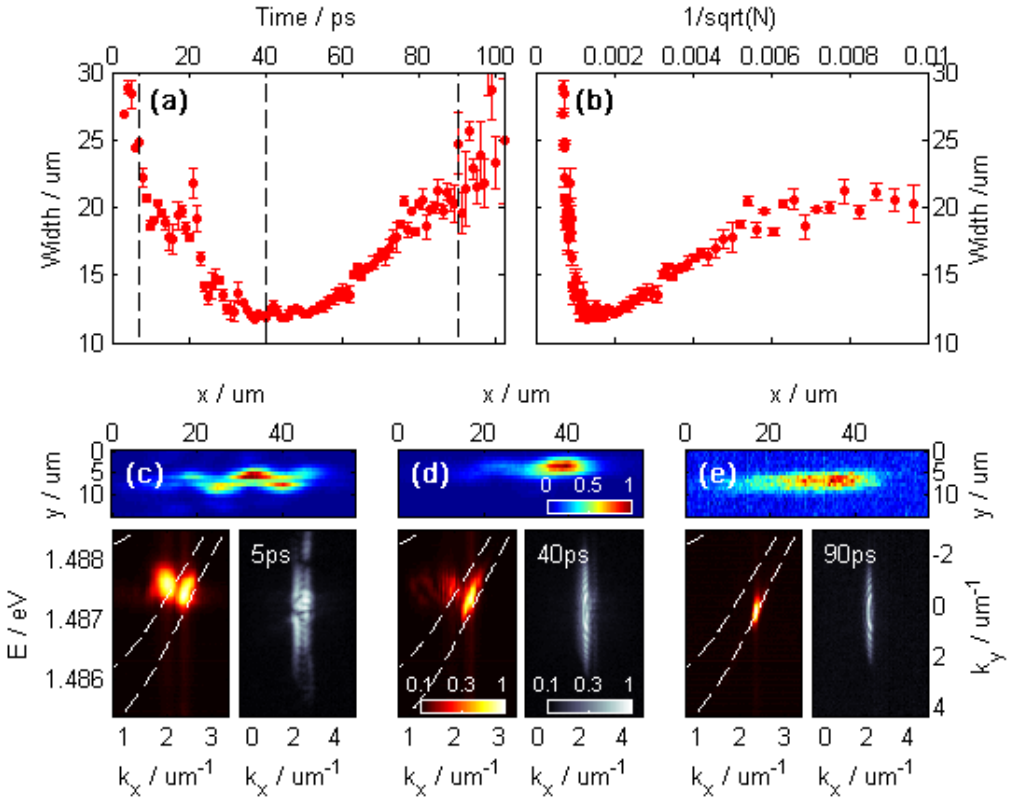


**Figure 6.6: Dynamics, multimode wavepacket**. **(a)** Wavepacket width (FWHM) vs time. Black dashed lines indicate the times at which (c-e) are recorded. **(b)** Wavepacket width vs $1/\sqrt{N}$ where $N = \int_t^{120ps} I(t)dt$ and $I$ is the emission intensity. Very low intensity (t>90ps) data is excluded as this would otherwise dominate the plot, obscuring the nonlinear region of interest. **(c-e)** realspace, k-space and E-$k_x$ dispersion at different times during the wavepacket's propagation. The white lines show the position of the lower polariton branches corresponding to the wire modes. The dispersions are shown here with a logarithmic colour scale

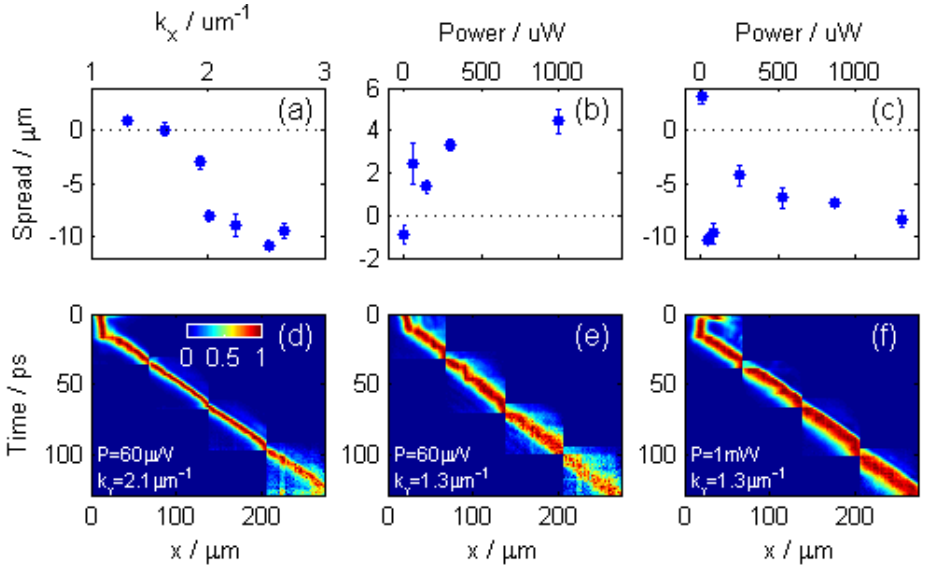


**Figure 6.7: Power and k dependence (a)** Wavepacket spread (width at 40 ps minus width at 0 ps) vs excitation k at a fixed power of 60 µW. The negative spread at high k vector corresponds to a shrinking wavepacket. **(b)** Wavepacket spread as a function of power at k = 1.6 $\mu m^{-1}$. **(c)** Wavepacket spread as a function of power at k = 2.2 $\mu m^{-1}$. **(d-f)** Intensity vs x and time, integrated over y. Each row is individually normalised so the shape of the intensity profiles at different times can be compared rather than the relative intensity, which decays exponentially with time. Note that these images are constructed from four measurements as only emission from a limited window could be recorded in each measurement. This results in discontinuities in the resulting image, but the overall behaviour can be observed. (d) Excitation at high k vector, self-focussing wavepacket. (e,f) Excitation at low k vector giving a spreading wavepacket, both when the excitation power is the same as in case (d) and when it is much higher.

as a wavepacket array is formed, increasing the FWHM which is measured across the entire structure. These multi-peak structures will be investigated further in §6.3.

### 6.2.4 Dynamics of E-k profiles

In order to get a better picture of the energy changes as the wavepacket evolves, the intensity profiles of the dispersions over time were plotted in Figure 6.8. A smooth drop in energy is observed over the propagation path for both single mode and multimode excitation. This drop in energy could arise from the redshift of the energy states as the polariton density decreases resulting in a drop in Coulomb repulsion. Surface roughness along the walls of the wire could also play a role as polaritons could scatter inelastically from the edges (see §6.3.2). Looking at the intensity vs $k_x$ profile, it can be seen that for multi-mode excitation, the higher k (lower order) wire mode maintains the same central k vector over all time. The second mode is quickly depopulated, although it could play a role in the subsequent broadening of the k spectrum at around 50 ps by providing an alternative relaxation path.

For the single mode case, the central k vector appears to shift to a higher k vector at later times. This is a little unexpected: as will be shown in §6.3, at higher powers the k spectrum will tend to shift towards lower k vectors. As the shift observed here corresponds to a change in the measurement position, it could be an artifact of the experiment, although the smoothness of the transition in the intensity vs energy profile suggests that this is not

the case. A shift to higher k vectors can occur due to the redshift of the LPB as the polariton density drops. While here the polariton energy is seen to drop, if it is falling slower than the LPB (for example, due to getting trapped at the bottleneck region), the LPB states which the polaritons are resonant with start to shift to higher k vector. A similar shift has been observed in polariton condensates in the literature [36], where it enhances the acceleration of polaritons away from a high density pump spot, see §2.2.2.

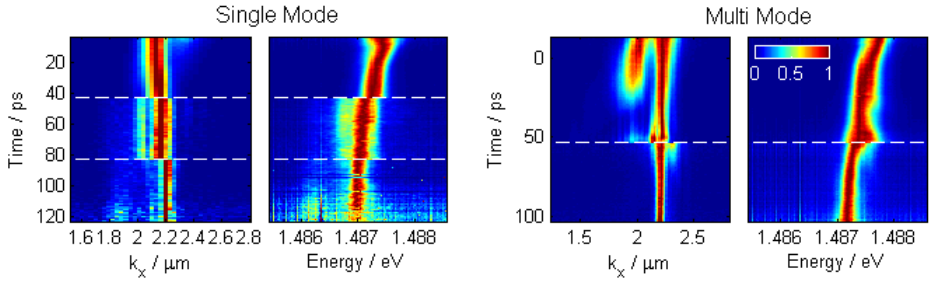


**Figure 6.8: Dispersion profiles, long wires**. At each time, the E-$k_x$ dispersion is constructed as a 2D image. The emission intensity is then integrated over all recorded $k_x$ vectors to find the intensity vs energy profile, or integrated over all energies to get the intensity vs $k_x$ profile. The profiles are then normalised. This was repeated at each time to show the continuous evolution of the dispersion. Here, data is shown for long wires for single mode (corresponding to the data in §6.2.1) and multimode (§6.2.2) excitation. As the wavepacket propagation distance is larger than the field of view of the imaging optics, the measurement was taken in three stages looking at different points along the propagation length. For this reason, there are discontinuities along the time axis where the data sets are joined, indicated by white dashed lines.

### 6.2.5 Secondary parametric scattering

It is thought that the extended wavepacket spectrum is populated by the parametric scattering (§2.2.1) of polaritons from a high density pump state to a series of signal and idler states [7]. Further scattering from the signal and idler states could broaden the spectrum, however the more excitonic polaritons at high energy have higher losses, for example due to inhomogeneous broadening of the exciton component by disorder in the quantum wells. The losses in the higher k idler states may be too great to allow time for further scattering events, although these might be possible at lower k vectors where the polariton lifetime is longer. This could lead to a migration of the emission to lower E-$k_x$ states over time, as illustrated in Fig 6.9.

This cascade of parametric scattering events could lead to a regular modulation in k, particularly if the original pump state acts as the idler for a secondary scattering event. Such modulation has been seen in some of the experimental data in both long wires (presented in Fig 6.5d) and short wires (will be presented in Fig 6.26).

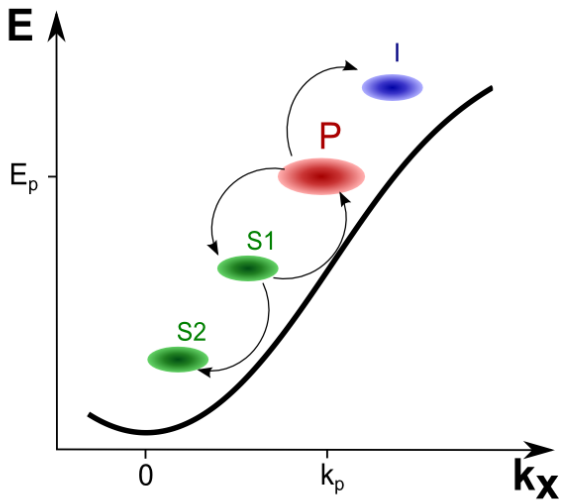


**Figure 6.9: Secondary parametric scattering:** schematic diagram. Calling the WB state P, an OPO process can populate states S1 and I by scattering two polaritons out of state P. State I has a short lifetime, so loses polaritons quickly. State S1 has a long lifetime and can act as a second pump state for a further OPO event. Two polaritons in S1 can then scatter to populate S2 at a lower k vector and I2 at a higher k vector (I2 could correspond to P).

## 6.3 Wavepacket Arrays

By steadily increasing the WB power, more peaks can be generated with each laser pulse (see I(x,t) traces in Fig. 6.10) in a similar manner to the soliton trains and horizontal arrays presented in Chapter 5. Stable arrays of two and sometimes three peaks travelling at the same speed can be excited. As the power increases, the spread in occupied E-$k_x$ states also increases (Fig. 6.11). The extended spectrum appears to be linear for all but the highest powers, indicating that all spectral components propagate at the same speed, as is required for a non-dispersive wavepacket. As multiple peaks appear in the realspace slices, a corresponding modulation appears in the intensity profile of the E-$k_x$ spectrum. For power $P_3$, the broad peaks in k space (more obvious in the 2D kmap images) are separated by $0.8 \pm 0.1$ $\mu m^{-1}$, corresponding to a peak separation in realspace of $8 \pm 1$ $\mu m$.

At very high excitation powers, the regular wavepacket array structure breaks down. E-$k_x$ states on the LPB are populated rather than states on a linear dispersion, resulting in realspace peaks propagating at different velocities and forming spreading structures. Rather than being evenly distributed around the WB state, the emission tends to relax to the low energy, low k side of the WB.

The drop to lower energies could have several contributions. It is already known that increased polariton-polariton scattering at high densities aids relaxation to low k vectors, for example by enabling polaritons to relax past the bottleneck region where they can become trapped at low densities. Inelastic scattering with the rough sidewalls of the microwire could play a role: it will be shown in §6.6.1 that reflection of a wavepacket from the end of a wire can be an inelastic process, so it is reasonable to suggest that interactions with the side walls can also result in a loss of energy. It is believed that parametric scattering of polaritons out

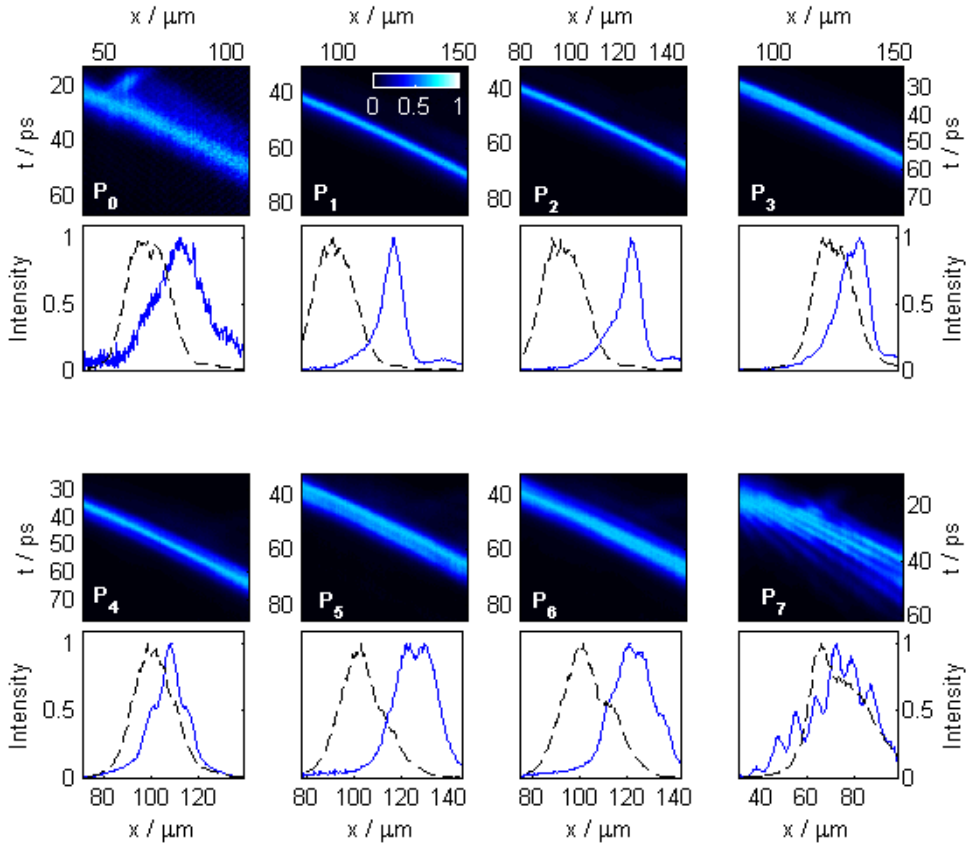


**Figure 6.10: Arrays, increase power, realspace.** The 2D images show the intensity as a function of position x and time t, integrated over the width y of the wire . Each row is separately normalised in order to emphasise the intensity profile at each time rather than the relative intensities at different times. In the line plots, the solid blue line shows the intensity profile over x at a time in the middle of the 2D plots (∼50 ps in most cases) while the black dashed line shows the intensity profile a few ps after the arrival of the triggering WB for comparison. The powers used were: $P_0 = 8$ µW, $P_1 = 50$ µW, $P_2 = 85$ µW, $P_3 = 250$ µW, $P_4 = 530$ µW, $P_5 = 870$ µW, $P_6 = 1.3$ mW, $P_7 = 28$ mW.

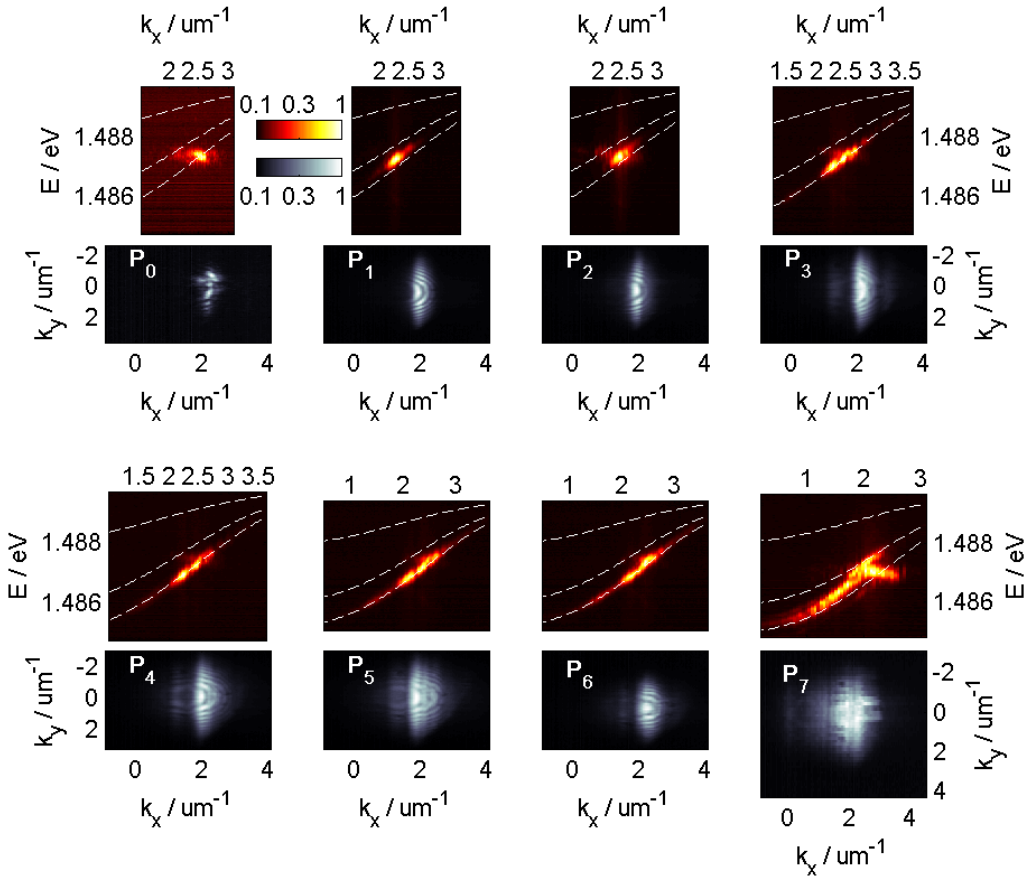


**Figure 6.11: Arrays, increase power, k-space** For each power, the top image shows the intensity as a function of energy and $k_x$ while the bottom image shows the emission intensity as a function of the 2-dimensional in-plane k vector. All plots use a logarithmic colour scale. The powers used are the same as those in Fig 6.10

of the WB state contributes to the broadening of the E-$k_x$ spectrum. Secondary scattering events from highly occupied states combined with longer polariton lifetimes at lower k vectors could also result in a shift to lower energies as discussed in §6.2.5.

### 6.3.1 Array dynamics

The formation of a wavepacket array triggered by a single WB pulse is illustrated in Fig 6.12. As for the case of a single self-focussing wavepacket, the initially broad injected wavepacket shrinks in size while the range of occupied k states broadens slightly. For this data set, the excitation conditions are the same as for the data set presented in §6.2.2 except that the excitation power was increased from 100 μW to 150 μW.

With the larger polariton number, a second peak starts to form in the tail after around 35 ps. As this happens, the energy-$k_x$ dispersion broadens to cover a k range of $\sim 2$ $\mu m^{-1}$, modulated into three peaks: this can be seen in both the E-$k_x$ dispersion images and the 2-dimensional k space images. Over time, the second realspace peak becomes brighter than the first. Eventually the first peak disappears, becoming part of the spreading background surrounding the central peak. In k space, the high $k_x$ peak disappears or becomes too faint to detect.

The dynamics of the E-k dispersions as the power is increased (Fig 6.13) could give some insight into the mechanisms involved. It should be noted that the states with high populations dominate these plots, which have a linear intensity scale. Fig 6.11 shows that there is dim emission over a larger energy range which is not examined here. The cases of powers $P_0$ (linear wavepacket), $P_1$ and $P_2$ (single self-focussing wavepackets) are similar to those discussed in §6.2.4. The drift to lower energies over time could be due to the redshift of the lower polariton branch as the polarition density drops.

As the power is increased to $P_3$ and beyond, some new behaviour emerges. During the main nonlinear region (middle section, $\sim 40-80$ ps), the range of occupied energies increases while the centre energy drops. The intensity profile over energy is not smoothly varying but instead forms three peaks for powers $P_3$-$P_5$ and two peaks for $P_6$. It appears that polaritons are transferred from the highest energy state to the lower energy states as only the lowest energy peak remains at later times.

The regular intensity modulation over energy could be due to the fact that there are now multiple wavepackets passing through the imaged area at different times: the fourier transform of an array of temporally separated peaks should give an array of peaks separated in energy. For power $P_5$, the energy peaks are separated by $\sim 0.3$ meV, corresponding to a separation in time of 14 ps. The high intensity wavepacket peaks observed in Fig 6.10 are only separated by $\sim 5$ ps, however there are some dim additional peaks seen $\sim 12$ ps before the main peaks which could be the cause of this modulation in the energy-intensity profile. Looking at the occupied k vectors, the k range broadens and the intensity profile becomes modulated in the middle section but maintains a similar central k vector over time. At the highest power $P_7$, the emission broadens and drops to lower energies and lower k vectors, moving to states in the positive effective mass region of the lower polariton branch.

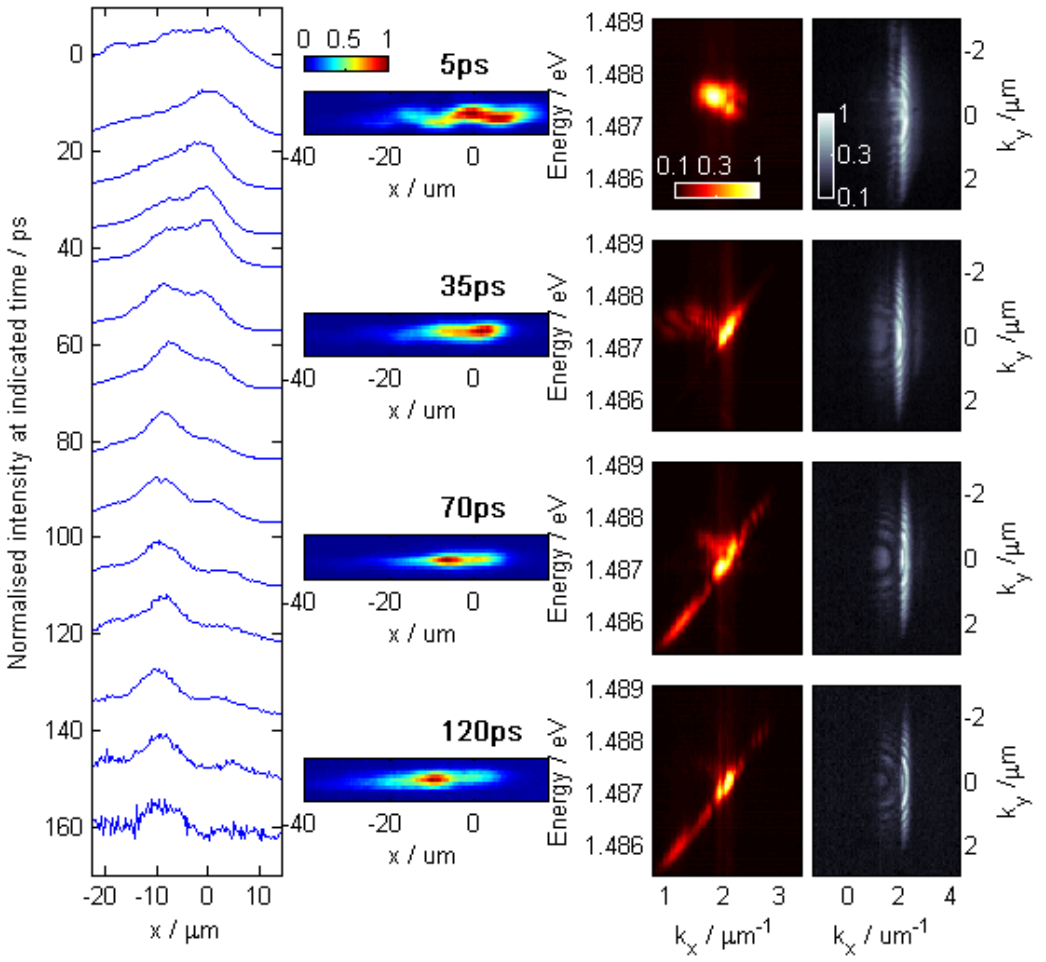


**Figure 6.12: Dynamics of wavepacket arrays: Left column:** normalised intensity profiles (along x, integrated over the wire width y) at different times after the arrival of the trigger WB. **Rows:** 2D images showing the emission intensity distribution in real space, energy and $k_x$, and in-plane k space. Each row corresponds to a different time as indicated by the label above the realspace image. The E-$k_x$ and **k** plots are shown with logarithmic colour scales.

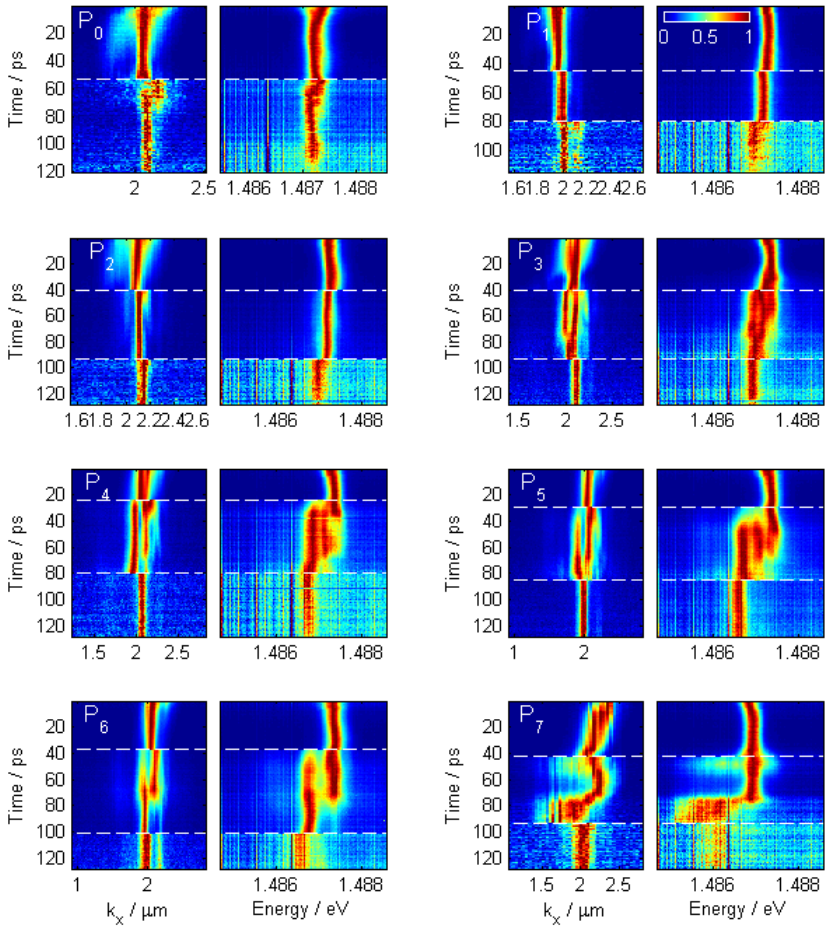


**Figure 6.13: Dispersion profiles** - these are plotted in the same way as those presented in §6.8. The intensity profile at each time pixel is individually normalised in order to keep the pattern visible as the emission intensity drops. White dashed lines show where data sets are joined. The dispersions are the same as those presented in Fig. 6.11.

### 6.3.2 Continuum

In optical fibres, the formation of high order solitons using large excitation powers has been linked to the population of a supercontinuum (see §2.3.4), where the spectral width of the input pulse can be broadened by a factor of up to 15 [92]. This observation was seen when the input pulse was excited close to the boundary between spectral regions with normal dispersion and those with anomalous dispersion. Mechanisms contributing to this were found to include perturbation by high order dispersion terms (particularly the third order term) and Raman scattering processes where energy was transferred to the fibre medium [174].

Similarities can be found with the self-focussing polariton wavepackets investigated here. The wavepacket is injected just above the point of inflection which marks the boundary between normal dispersion (where the curvature of the E-**k** spectrum is negative) and anomalous dispersion (where the curvature of the E-**k** spectrum is positive). High order terms are thought to dominate the polariton dispersion at this point (see Figure 2.11b, reproduced from [94]) . Energy losses could be introduced by the roughness of the microwire sidewalls, introducing localised defects and opening up new scattering channels compared with the ideal case [38].

The observations of a supercontinuum in optical fiber systems can be compared with the broadening seen at high power ($P_7$) in Figures 6.11 and 6.13. While the pulse in fiber systems can be broadened by a factor of 15 to cover $\sim$ 500 nm, in this polariton system the broadening is limited by the spectral extent of the lower polariton branch: it can be see in Fig 6.11 that at the highest powers, the lowest available states are occupied so further spreading is inhibited. Similarly, there would be a boundary at the high energy side as lower polariton branch states cannot exceed the exciton energy. Nevertheless, significant broadening of the injected wavepacket spectrum by a factor of $\sim$5 is seen in this polariton system at high power.

Aside from the difference in the extent of spectral broadening, other aspects of the behaviour of the high power polariton system and the fiber supercontinuum system are more closely linked. In both cases, the width of the populated spectrum increases with power. The spread across the boundary between regions with normal and anomalous dispersion results in radiation of a dispersive wavepacket [95, 96] which appears as a broad background peak in the realspace streak camera images presented here (see, for example, Fig 6.21) or a tail as seen by an asymmetric peak in the intensity profile (see, for example, powers $P_1$ and $P_2$ in Fig 6.10). Interactions between the solitonic and dispersive wavepackets are thought to contribute to the supercontinuum formation in a fiber system [174].

A precursor to the supercontinuum regime is expected to be soliton fission, where each spatially separated soliton occupies a different region of the dispersion. While this was not explicitly measured here, the variation in velocity of the wavepackets shown for power $P_7$ in Fig 6.10) suggests that each one may populate a different part of the spectrum (Fig. 6.11) as the changing gradient of the E-k curve represents a changing group velocity between different spectral regions. The clear analogy between observations in optical fibers and the results presented in §6.3 suggest that at high powers, the system could be moving from a soliton-like regime into a continuum-like regime.

### 6.3.3 Wavepacket collision

It might be expected that these soliton-like wavepackets could be made to collide by injecting two wavepackets propagating in opposite directions using two writing beams. This was attempted, but the colliding wavepackets appear to have no effect on each others' speed or trajectory (Fig. 6.14a). This could be because the interaction time between them is only a few picoseconds while the time taken for the wavepacket to fully self-focus is $\sim$ 30ps (see §6.2 Dynamics). This suggests that the interaction time may be too short to significantly influence the shape of the wavepacket, as the mechanisms which determine this are much slower.

Experiments in the literature of collisions between cold atom solitons [106] showed that while the solitons passed through one another, they were seen to interact as they collided. A single density minimum was seen when the solitons had a phase difference of $\pi$, indicated that they never overlap due to repulsion. A density maximum was seen for solitons which were in-phase, which are expected to have attractive interactions so can occupy the same spatial position (see §2.3.3).

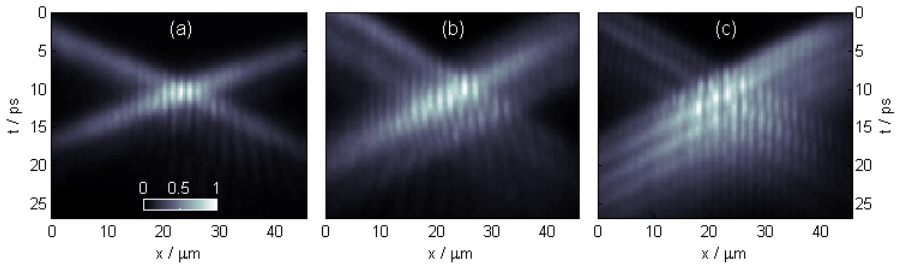


**Figure 6.14: Wavepacket collisions.** (a) Collisions between single self-focussing wavepackets. (b,c) Interference of wavepacket arrays.

Here, although the soliton-like wavepackets are not seen to collide as particles, interference patterns can be seen where they overlap. In the case of a single wavepacket, interference fringes are seen with modulation along the x direction but no modulation along the time direction (Fig. 6.14a). When wavepacket arrays collide, more complex fringe patterns emerge (Fig. 6.14(b,c)) where some of the fringes appear to be shifted across the gap between the peaks in a manner which looks like a fork-like dislocation, reminiscent of the signature of vortices in polariton condensates [72, 52, 175]. While these phase structures appear complex at first glance, it is thought that they can arise from phase jumps between the individual peaks in at least one of the wavepacket arrays. Rather than looking at the interference of two wavepacket arrays, the phase across one wavepacket can be examined by interfering its emission with a reference beam with a constant phase across its spatial profile, as presented in §6.4.

## 6.4 Phase profiles

The phase across a wavepacket array is measured by interfering the emission with a reference beam, which should ideally have a flat phase profile. The reference beam is made by splitting off a small portion of the WB, expanding it and combining it with the emission using a beam

splitter (see §3.4.2). The relative phase between the reference beam and the emission can be scanned by moving the position of the piezo mirror.

Examples of the x vs t traces obtained for this measurement are shown in Fig. 6.15(a-d). Figure 6.15a shows the trace for a wavepacket in the linear regime, showing vertical interference fringes. A similar image is obtained for a single self-focussing wavepacket (Fig.6.15b) but for the nonlinear wavepacket arrays in Fig.6.15(c,d), the fringes are no longer uniform in the vertical direction. Instead, a checkerboard pattern starts to emerge, indicating a variation in relative phase in time as well as position. The early phase jumps appear to coincide with minima in the intensity profile (the images are less clear at later times due to the lower intensity). The fringe pattern is revealed more clearly in Figure 6.15(e-h) where a background has been subtracted as described in §3.4.2. Similar data is shown in Figure 6.15(m-p), but with a different relative phase between the emission and the reference beam.

To take a closer look at the phase profile, I look at fringe amplitudes along the x direction (Fig. 6.15(i-l)). By comparing the profiles at different time pixels, the spatial period of the fringes at different points in the wavepacket array can be compared. In the case of the linear wavepacket (Fig. 6.15, first column), neither the fringe position nor the fringe period changes at different times. For a single nonlinear wavepacket (Fig. 6.15, second column), the fringe period doesn't change over the selected lines, but the positions of the maxima and minima clearly shift over time.

For the arrays however, the apparent period of the interference fringes can be increased as the line along x crosses from one wavepacket to the next. In Fig. 6.15k, the green line has its first minimum at x$\sim$14 μm, as does the red line. However, while the red line then increases to a maximum and decreases to a second minimum (x$\sim$19 μm), the green line increases to a maximum and then stays bright until the edge of the frame. The red line covers emission from within a single wavepacket peak, while the green line crosses between wavepackets, passing through intensity maxima in both. Similarly in Fig. 6.15l, the green line has a maximum and minimum followed by a minimum and maximum while the blue and red lines, which are again mainly contained within a single wavepacket peak, show alternating maxima and minima. This suggests that there is a phase jump between the wavepacket peaks for both of these arrays. For Fig 6.15l, the phase jump seems to be $\sim \pi$ as the interference minimum in the second wavepacket lies directly below the interference maximum in the first, forming a checkerboard pattern. In Fig 6.15k, the magnitude of the phase jump appears to be lower as the minimum in the second wavepacket is offset compared to the maximum of the first.

### 6.4.1 Temporal Evolution

Figure 6.16 shows the evolution of a wavepacket array and the phase structure within it. As the reference beam is more extended in time than in space when compared to the emission, the relationship between the emission intensity profile and the phase can be seen more clearly when the fringe amplitude profile is taken along t. Each row shows the results of probing the wavepacket array at a different time after the arrival of the WB.

Figure 6.16a) shows the situation $\sim$13 ps after the arrival of the WB. The excited wavepacket is still broad and the phase over the main wavepacket is roughly constant,

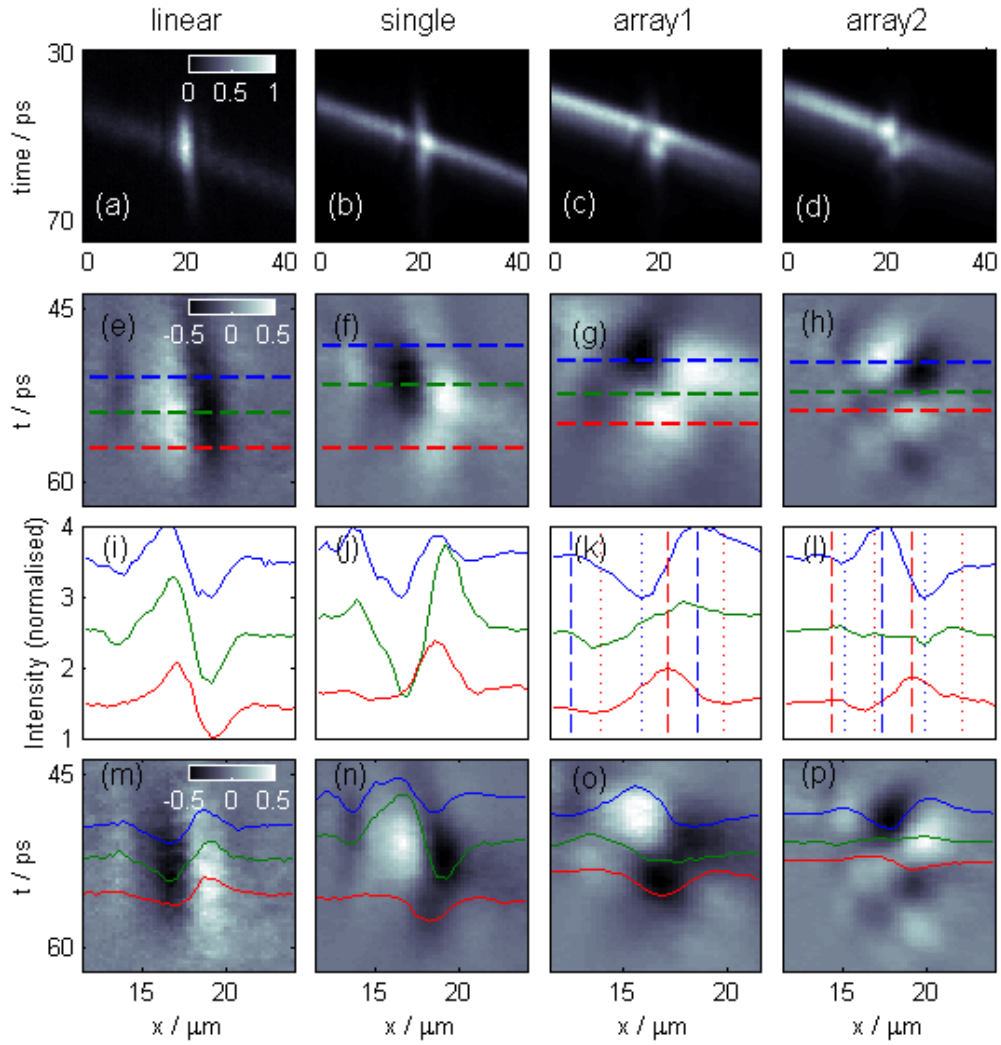


**Figure 6.15: Phase profiles**. **(a-d)** Streak camera traces showing the interference of the emission and a reference beam for (a) a linear wavepacket, (b) a single self-focussing wavepacket, and (c,d) wavepacket arrays. **(e-h)** Grey scale image: streak camera slices, zoomed into the interference region with the background subtracted. Dashed lines: these illustrate the times along which amplitude profiles are taken along x and plotted in figures **(i-l)**. Vertical dashed (dotted) lines in (k,l) highlight the maxima (minima) along the first and third profiles. **(m-p)** are similar to (e-h), but are taken with a different relative phase. Amplitude profiles are overlaid on the images.

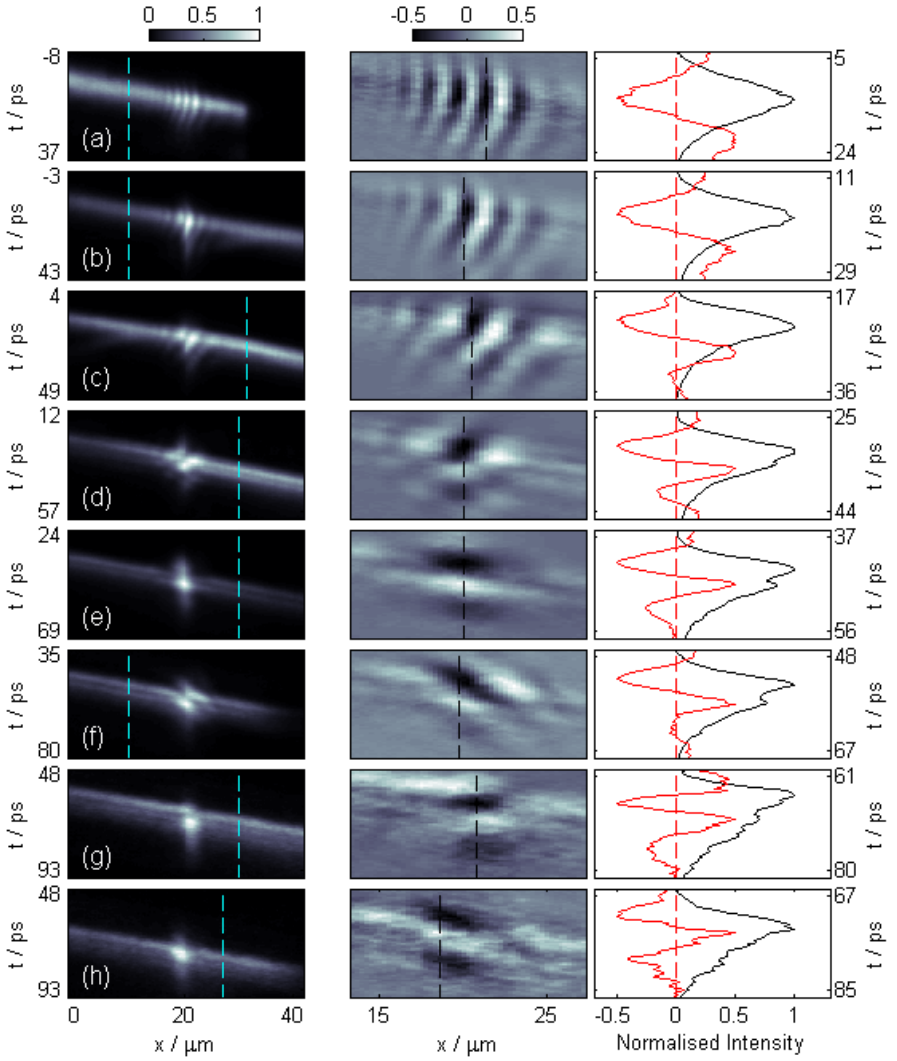


**Figure 6.16: Phase Time Dependence**. Each row shows data taken at a different time along the propagation path. The y axis here is the time in ps since the arrival of the WB at t=0. **Left column:** Streak camera trace. The dashed line indicates the x position along which the wavepacket intensity profile (black line in the right column) is taken. **Middle column:** streak camera trace zoomed into the interference region with the background subtracted as for Fig 6.15. The dashed line indicates the x position along which the fringe amplitude profile (red line in the right column) is taken. **Right column:** Intensity vs time profiles. Black line: normalised intensity profile across the wavepacket array. The profile is shifted in time to indicate the approximate profile at the position of the reference beam. Red line: normalised amplitude profile across the fringe pattern. The red dashed vertical line indicates a fringe amplitude of zero.

as can be deduced from the vertical fringes in the middle column. There is some linear phase gradient at the end of the wavepacket resulting in a kink in the fringes. In the profiles plotted in the right column, it can be seen that the peak in the black line (temporal width of the wavepacket emission) has a similar duration to that in the red line (temporal width of the interference fringe). The images in Figure 6.16(b, c) have similar features. As the emission peak narrows, so does the fringe peak, indicating that the fringe period is linked to the duration of individual wavepackets in the array. The overall phase gradient increases and in Figure 6.16(c), the interference maximum at the end of the array becomes quite pronounced: there is a clear phase difference between the main wavepacket peak and the lower density tail that follows it.

By Fig. 6.16d), which is ∼32 ps after the WB, two peaks can be resolved in the emission, indicating the formation of an array. The peak positions correspond well with extrema in the fringe profile: for this slice, the first wavepacket has a fringe minimum while the second has a fringe maximum. The low density tail again has a fringe minimum. The period of the interference fringes has clearly decreased compared to Figure 6.16a), but as the reference beam is the same, this shows that the phase profile across the emission profile has changed significantly. Figures 6.16(e,f) show similar patterns with the fringe extrema tracking the wavepacket intensity maxima as they start to spread apart.

In Fig. 6.16g, a third bright peak may be resolvable along with a fourth interference extremum. As the emission intensity drops, the features become harder to resolve with most peaks smeared out in Fig. 6.16h), however the interference fringe pattern clearly maintains the structure established at earlier times. The fringe extrema do not always exactly coincide with the intensity peaks any more. It may be that the separate wavepackets in the array have broadened and merged while maintaining a steep phase gradient.

### 6.4.2 Power dependence

The power dependence of the phase profile across a wavepacket array is presented in Fig. 6.17. The only parameter which was changed between these data sets was the excitation power, indicated in the left hand column for each row. These data sets are measured under similar conditions to those in §6.3 for powers $P_1$, $P_3$, $P_4$ and $P_5$.

For the single self-focussing wavepacket (Fig 6.17, 40μW), the phase profile is fairly uniform with maybe a small linear phase gradient. As the excitation power is increased, the phase gradient becomes steeper, covering four amplitude extrema at the highest power compared with one maximum at the lowest power. However, while the phase profile is quite different between the second and fourth rows, the array intensity profile is similar: in both cases, two peaks are resolvable, although in the fourth row they are slightly more separated. In many of the results shown so far in this section, it has been observed that sharp changes in phase tend to occur at the edges of individual wavepacket peaks, however in the second row of Fig 6.17, it can be seen that there will not always be a sharp change in phase at such a boundary. The two main peaks have similar phases while the tail has the opposite phase. Increasing the power further results in phase changes around all of the wavepacket boundaries, or an increased overall phase gradient, as observed previously. This observation suggests that these arrays can be stable both when the adjacent wavepackets are in phase

and when there is a phase jump between them.

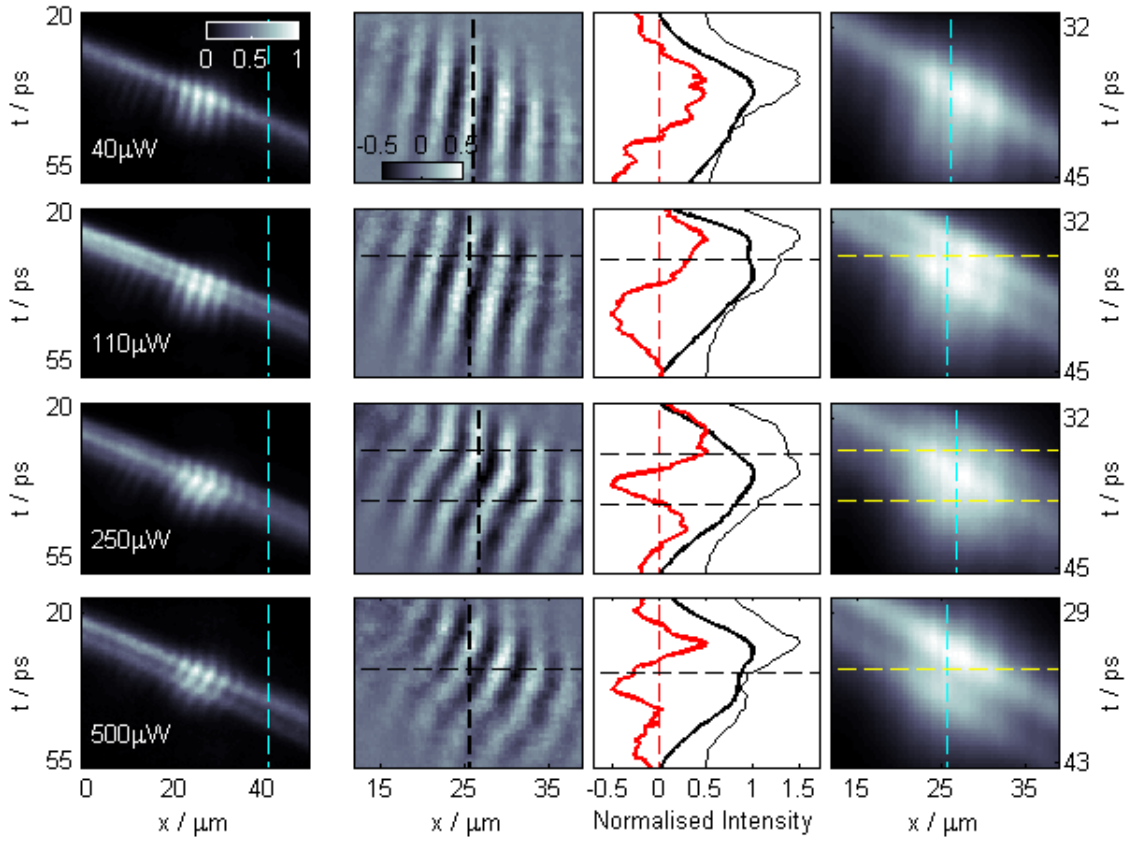


**Figure 6.17: Power dependence of phase pattern.**. The phase pattern is monitored as the excitation power is increased. Each row shows data for a different WB power as indicated in the annotation in the left column. In all columns, vertical dashed lines indicate the x position along which an intensity or amplitude profile is taken. Horizontal dashed lines indicate the positions of minima in the emission intensity profile, marking the boundaries of individual wavepackets in the array. **Left column:** streak camera trace. **Second column:** streak camera trace zoomed into the interference region with the background (right column) subtracted as for Fig 6.15. **Third column:** Intensity vs time profiles. Red line: normalised amplitude profile across the fringe pattern shown in the second column. The red dashed line indicates a fringe amplitude of zero. Thick black line: normalised intensity profile of the wavepacket array taken from the "background" image in the right column along the same line as the fringe profile is taken. Thin black line: normalised intensity profile across the wavepacket array along the line indicated in the left column. The profile is shifted in time to indicate the approximate profile at the position of the reference beam. **Right column:** Background image taken by averaging 101 phase steps (see §3.4.2).

To check that the change in power did not affect the phase profile across the reference beam or the initially excited wavepacket, the phase across the emission $\sim$ 10 ps after the arrival of the WB was measured. This is shown in Fig. 6.18. Neither the phase pattern nor the emission intensity profile changes much at this time as the excitation power is increased: as expected from §6.4.1, the phase profile evolves at later times as the wavepacket array emerges.

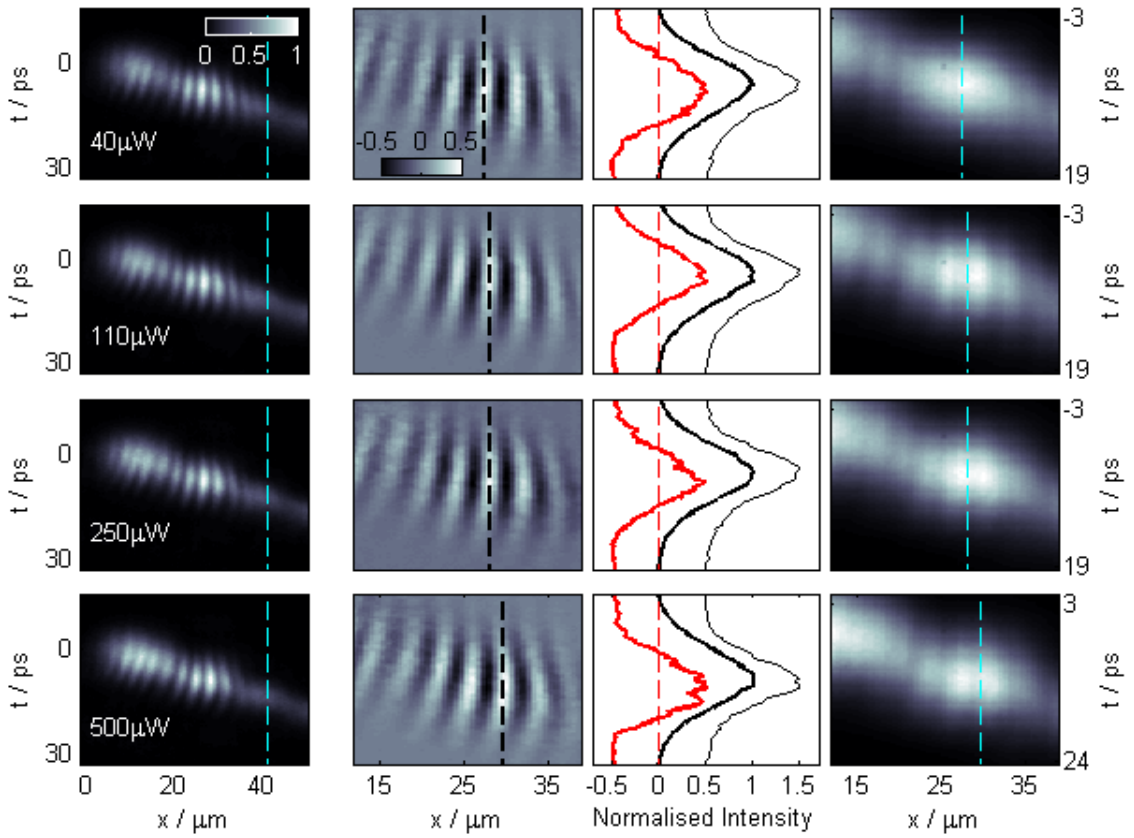


**Figure 6.18: Power dependence of phase pattern at early times.** The data in this figure is taken from the same set as that in Fig. 6.17, but the emission is measured at an earlier time, before significant self-focussing is observed.

### 6.4.3 Discussion of phase observations

As shown in Fig 6.15, a change in the phase gradient or a phase jump can be introduced at the edges of the nonlinear wavepackets which is not present for a wavepacket in the linear regime (i.e. with a low excitation power). In the case of wavepacket arrays, the phase profile can exhibit dislocations when moving from one peak to the next although as shown in Fig. 6.17, it is also possible to have multi-peak structures without a phase jump between the peaks. This suggests that two regimes of nonlinear wavepacket arrays can be generated: one in which a phase jump is seen between adjacent peaks and one in which neighbouring peaks have the same phase. The case where the phase is the same appears to occur at lower excitation power and where the peaks in the array are more closely spaced. The phase profile is not imprinted when the wavepacket is injected by the WB even at high power (§6.4.2), but evolves as the wavepacket array emerges (§6.4.1).

The arrays of non-linear wavepackets investigated here can be compared with soliton arrays, both those investigated in a dissipative polariton system (Chapter 5) and those investigated in other systems such as optical fibres (§2.3.3). It was noted in §5.4 that two regimes of soliton array appeared to be generated: one in which the solitons shared the same linear E-$k_x$ spectrum, implying coherence across the array and a second where it was suggested that neighbouring solitons may occupy different spectral regions and coherence may not be maintained across the array. It was suggested that these regimes could be analogous to structures observed in optical fibers, namely higher order solitons and arrays of fundamental solitons (§2.3.3).

Similarly, two regimes of nonlinear wavepacket arrays are seen here: one at lower power where neighbouring wavepackets are in phase and one at a higher power where a phase shift can evolve between neighbouring peaks as they propagate. Analogies can again be drawn, where the in-phase arrays may correspond to higher order soliton solutions and the out-of-phase arrays may correspond to the case of soliton fission, which is expected to occur at higher excitation powers. Theoretically, neighbouring peaks in a stable pattern of solitons are expected to be $\pi$ out of phase [97, 176, 177]. Pairs of solitons which are in-phase are expected to attract creating an unstable pattern. Phase shifts have sometimes been seen to evolve between temporal solitons which are injected into optical fibers in phase, thus stabilising the pattern [102] (see §2.3.3). There are clear similarities between these reported observations and the evolution of phase jump presented in §6.4.1

## 6.5 Quantum properties

The quantum properties of the polariton states can be examined by looking at the photon emission statistics (the ratio between the variance and the mean number of photons detected in a certain time interval) and the correlations between pairs of emitted photons, as explained in §2.5. Both of these properties can be measured using the photon counting mode of the streak camera (see §3.4.3). To look at correlations, the $g^{(2)}(p)$ function between emission excited by consecutive laser pulses $p$ (defined by Equation 3.2 in §3.4.3) are measured. This can be done with different excitation conditions, for example by changing the WB power and k vector (Figure 6.19, top row).

Once the polaritons have been injected by the WB, they continue to emit over ∼120 ps. However as the wavepacket is propagating and the detection window is limited, each measurement only records emission over an interval of ∼ 15 ps. The detected interval can be changed by moving the objective lens in order to collect emission from different points along the propagation path. This approach can be used to look for changes in the $g^{(2)}(p)$ function as the wavepacket propagates, as shown in the bottom row of Figure 6.19 and Figure 6.20. It is expected that $g^{(2)}(p \neq 0) = 1$ as the emission of polaritons triggered from different laser pulses should be independent. The deviation from 1 for this background can therefore be taken as an indication of the error in the measurement.

**Experimental observations of $g^{(2)}(p)$**

Bar plots of $g^{(2)}(p)$ for different excitation conditions are shown in the top row of Figure 6.19, while the bottom row shows the evolution of $g^{(2)}(p)$ over the propagation path of a non-linear self-focussing wavepacket. For a continuous wave (CW) laser, $g^{(2)}(p) \sim 1$ for all $p$ as expected for a coherent source. For low power excitation, $g^{(2)}(0) > 1$, so the light is bunched as expected for the thermalised emission excited in the linear regime. Bunching is often observed in signals which are spectrally filtered as the wavelength of the emission can jitter around the central value, so can be blocked by a narrow spectral filter at times when the deviation in wavelength is large. The resulting time varying intensity corresponds to bunched emission, as explained in §2.5.3. Here, the laser pulse is spectrally filtered both by the pulse shaper and by the microcavity, which transmits light much more efficiently when it is resonant with a cavity mode (photonic or polaritonic).

For high power excitation, a dip in the $g^{(2)}(p)$ value is seen at p=0. This is the case whether the wavepacket is excited at 2.2 $\mu m^{-1}$ (high k, above the point of inflection of the E-$k_x$ dispersion, self-focussing regime) or 1.6 $\mu m^{-1}$ (low k, below the point of inflection, dispersive wavepacket). For the high k case, the emission has $g^{(2)}(0) = 0.979$. This value is both less than 1 and less than the mean value of $g^{(2)}(p \neq 0)$ (mean $\mu = 1.001$, standard deviation $\sigma = 0.001$), thus meeting both conditions for antibunching (see §2.5.3). Similarly, the low k case has $g^{(2)}(0) = 0.981$ which is lower than the background of $g^{(2)}(p \neq 0)$ ( $\mu = 1.003$, $\sigma = 0.002$) so is also antibunched.

The evolution of the $g^{(2)}(p) \sim 1$ over the wavepacket propagation path is shown in the bottom row of Figure 6.19. This data set is the same as that in the top right image of Fig. 6.19 but looks at different times. In the interval 4-17 ps, some light from the WB may be collected along with the wavepacket emission (the WB pulse duration is ∼10 ps). As in the case of the CW laser, the WB is expected to have $g^{(2)}(0) = 1$ (or $g^{(2)}(0) > 1$ due to spectral filtering) so this contribution could increase the measured value of $g^{(2)}(0)$ at this time. In the time interval 25-37 ps, no contribution from the WB will be present, revealing that the wavepacket emission is antibunched (this is the high power, high k vector set described in the previous paragraph). At later times, the antibunching is no longer seen with $g^{(2)}(0) \geq 1$. At low intensities, the error in the $g^{(2)}$ is higher due to the low number of recorded counts.

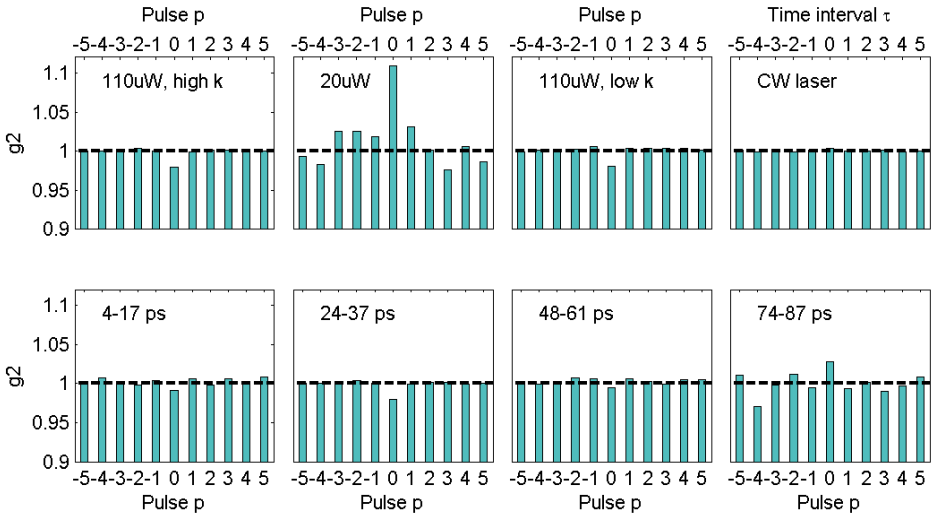


**Figure 6.19: $g^{(2)}(p)$ correlations** between photons emitted in pulses $p_1$ and $(p_1 - p)$, averaged over pulses $p_1$. The pulses $p$ have durations of ∼13 ps, and are separated by ∼12 ns. **Top row:** $g^{(2)}(p)$ for different excitation conditions for emission ∼30 ps after the arrival of the WB. The left plot shows emission from a wavepacket in the nonlinear regime (high excitation power) at a high k vector (2.2 $\mu m^{-1}$). For the second plot, the excitation power has been reduced to instead inject a wavepacket in the linear regime. In the third plot, the excitation power is high but the k vector has been reduced (to 1.6 $\mu m^{-1}$), so the wavepacket is in a non-linear regime but does not self-focus in realspace as the excited polaritons have a positive effective mass. The right plot shows the $g^{(2)}(\tau)$ for a CW laser, which is expected to be 1. The time intervals $\tau$ are ∼ 50 ps long and are separated by ∼12 ns. **Bottom row:** $g^{(2)}(p)$ for wavepacket emission collected within different time intervals after the arrival of the WB, as indicated by the labels on the plots. The wavepacket is injected at $k_x = 2.2\ \mu m^{-1}$ with an excitation power of 110 μW.

### Mechanisms for anti-bunching

In anti-bunched light, the number of photon pairs emitted simultaneously is lower than what would be expected for coherent light (such as a laser beam) of the same intensity (see §2.5.3). Experimentally, this corresponds to the case where $g^{(2)}(0) < 1$ and $g^{(2)}(0) < g^{(2)}(|p| \gg 0)$, so the detection of one photon in a given time interval makes it less likely that a second photon will be detected in the same time interval. It could be imagined that removing photons from the beam might reduce the value of $g^{(2)}(0)$ as the number of photon pairs would be reduced. Care needs to be taken as this would also reduce the normalisation factor, so that randomly removing photons from the beam (such as by having a low detection efficiency) should have no overall effect on the value of $g^{(2)}(0)$.

However, systematically selecting one photon in a pair can reduce $g^{(2)}(0)$ to give anti-bunching behaviour. This has been seen, for example, in a photonic Optical Parametric Amplifier configuration [178]. As shown in §2.2.1, in this configuration particles injected into a pump state are usually scattered into signal and idler states, stimulated by some population injected into either of the final states. By controlling the phase between the injected populations, the particles can instead be made to scatter from the signal and idler states into the central pump state. Particles in the signal state can therefore be paired with those in the idler state which have a higher energy and k vector. If the emission is spectrally filtered so that only photons from the signal state are recorded, the normalised pair count

is then reduced.

Here, as much emission as possible is collected from the microcavity and directed towards the streak camera, but some filtering is applied in k space by the detection optics. For example, the emission is spread over a broad range of k vectors in the y direction (see, for example, Figure 6.6) but the horizontal slit in front of the streak camera (see Figure 3.4) only collects emission from $\sim \frac{1}{3}$ of the occupied $k_y$ vectors, even when additional telescope lenses are added to the collection optics to shrink the k space image. In addition to filtering by the optical setup, the change in polariton character between different points on the LPB can also affect the likelihood of detecting emission from those states. For the negatively detuned sample used here, polaritons with lower energy are more photonic while those with higher energy are more excitonic. Polaritons are only detected when they emit photons from the cavity, so if a photonic polariton is paired with an excitonic one, it is less likely that the excitonic polariton will be detected at all. Photonic polaritons which are detected will then appear to be unpaired, which will reduce the value of $g^{(2)}(0)$ and correspond to an observation of antibunching.

The slight antibunching in some of the data sets indicates non-classical behaviour. One interpretation of the observation of antibunching is that the polaritons may occupy squeezed states, behaviour which has been seen before in systems with a Kerr-like non-linearity (see §2.5.1). While the measurement of quadrature squeezed states would require a new experiment using homodyne detection [151], a signature of amplitude squeezed states is sub-Poissonian statistics (see §2.5.2). As each photon detection is recorded individually by the streak camera (§3.4.3), the photon statistics (mean $\mu$ and variance $\sigma^2$) can be extracted from the data used to calculate $g^{(2)}(p)$.

### Further Observations of Non-classical behaviour

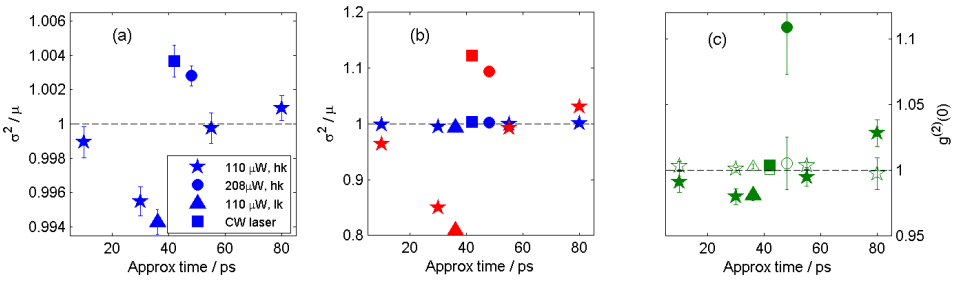


**Figure 6.20: Quantum statistics.** For all three plots, statistics and correlations relating to different excitation conditions are represented by the different marker shapes shown in the legend of (a). The star marker is for the set excited at 110 μW with a high k vector (2.2 $\mu m^{-1}$): the circle is for the set excited at high k with power 208 μW : the triangle is excited at 110 μW with a lower k vector (1.6 $\mu m^{-1}$) and the square shows data for the CW laser. $g^{(2)}(p)$ for these sets is shown in Fig. 6.19. The black dashed lines indicate unity: values less than 1 show non-classical behaviour. **(a)** Ratio between the measured variance and mean number of photons detected in each time bin. **(b)** Blue points are the same as those in (a) while red points show the ratio between the variance and mean corrected according to equations 2.11 and 2.12 in §2.5.2. **(c)** Solid markers show $g^{(2)}(0)$ values while unfilled markers shown the mean of $g^{(2)}(p \neq 0)$ with the standard deviation indicated by the error bars.

The ratio between the variance and mean for the different data sets is shown in Fig 6.20a.

The values less than 1 exhibited by the high excitation power data sets at $\sim 30$ ps have sub-Poissonian statistics (see §2.5.2), suggesting that the polariton states are indeed amplitude squeezed (see §2.5.1). Although this effect is very small, it should be noted that the statistics will be modified by a low detection efficiency as this randomly samples the emission, making it tend towards Poissonian statistics ($\mu/\sigma^2 = 1$). Figure 6.20c shows $g^{(2)}(0)$ for the same data sets, revealing that the data sets exhibiting sub-Poissonian statistics correspond to those with antibunching behaviour.

As described in §2.5.2 the measured mean and variance are modified by the detector efficiency according to equations 2.11 and 2.12. Corrected ratios are plotted in Fig 6.20b where the detection efficiency $\eta$ is taken to be 3%, the quantum efficiency of the streak camera at 830 nm (taken from the manufacturer's test report). The correction amplifies deviations of the ratio from unity but does not change the nature of the statistics (e.g. from sub-Poissonian to super-Poissonian). The actual detection efficiency will be much lower as losses through the optical setup have not been taken into account.

Another factor which can make the detected statistics tend towards the Poissonian case is if the length of the time bin $\tau$ is less that the average gap between photons T: as shown in Fig 2.19 in §2.5.2, this can lead to an increase in the ratio of variance and mean even in the case of a regular stream of single photons. The ratio $\frac{\tau}{T}$ is the mean number of photons per bin, which varied between 0.2 and 0.4 in the sub-Poissonian measurements shown here. The deviation of the statistics from the Poissonian case is likely to be significantly reduced in this measurement due to optical losses, a low detection efficiency and a short time bin.

## 6.6 Nonlinear Wavepackets in Short Wires

In order to make use of self-focussing wavepackets in different polaritonic devices, it is desirable that they can be reliably excited in a range of environments. Their robustness can be tested by attempting to excite them under slightly different conditions and observing their dynamics. In this section, I present observations of wavepackets excited in shorter wires, where they reflect multiple times from the wire ends during their propagation. More wire widths were available on this sample, so the effect of doubling the wire width was also investigated. It will be shown that the behaviour seen in long wires, such as self-focussing in realspace accompanied by broadening and linearisation of the E-$k_x$ spectrum, is replicated here.

While most experiments in this Chapter are carried out with a pulsed laser emitting pulses with a duration of $\sim 3$ ps, the results in this section and in §6.7 are carried out with a laser emitting pulses with a duration of $\sim 300$ fs. In all cases, the laser pulses are lengthened to a duration of 5-10 ps using a pulse shaper (see §3.3.3), so the laser pulse duration is not expected to significantly affect the dynamics of the injected polaritons. This assertion will be verified in §6.6.4.

### 6.6.1 Dynamics of single wavepackets

#### Self focussing

The microwire is excited on one end with a pulsed writing beam (WB) with an in-plane k vector of 2.6 $\mu m^{-1}$ in quasi-resonance with the fundamental mode of the lower polariton branch. Its subsequent spatial dynamics are illustrated in Figure 6.21. Initally, a spatially broad wavepacket is excited. This travels at a velocity of $\sim$3 $\mu m\ ps^{-1}$. As the wavepacket propagates, its size along the direction of propagation reduces from $\sim$30 $\mu$m to $\sim$10 $\mu$m while travelling a distance of $\sim$200 $\mu$m. At this time, the intensity profile is dominated by the narrow soliton-like peak, but a broader background can also be seen, which may correspond to a dispersive wavepacket as it appears to spread even at early times. The narrower peak remains visible for a further $\sim$200 $\mu$m ($\sim$ 60 ps), but is eventually dominated by the dispersive wavepacket as the intensity drops.

The polaritons appear to form two wavepackets: one with emission at k vectors above the point of inflection, corresponding to the self-focussing wavepacket; and a second with emission from the positive effective mass region at lower k vectors, corresponding to a dispersive wavepacket. The interaction between these components may contribute to further broadening in the E-k spectrum, as discussed in §6.3.2.

#### Mode occupation

As the microwires are multi-mode, the wavepacket can contain polaritons occupying several modes. In order to study this, a wider wire of width 8 $\mu$m was used in order to reduce the energy separation between the modes, enabling the simultaneous excitation of the ground state and the next few excited modes with a single WB pulse. The transition to soliton-like behaviour appears to correspond to a change in the mode occupation. When a wavepacket is excited at high power, it initially occupies multiple modes of the wire as can be seen from k-maps (Fig. 6.22). The multimode occupation can also be deduced from a "snaking" motion of the wavepacket, where it move between the edges of the wire as it propagates along the wire. In some cases, the wavepacket appears to jump from one edge to the other while the intensity in the middle of the wire remains low, suggesting that here only a higher order mode is occupied. Once the wavepacket self-focusses, the propagation path stays in the middle of the wire rather than snaking between the edges. The corresponding k map has a single maximum, indicating the occupation of a single nonlinear mode. For low power excitation, the wavepacket again initially occupies multiple low order modes of the wire but as time goes on, the higher order modes become populated. This can be deduced from patterns in the realspace emission and can also be directly observed from k-maps.

The k maps are energy-integrated 2-dimensional measurements of the far-field emission. For a cartoon picture of what the k-map shows, it is useful to consider the E-$k_x$ and E-$k_y$ dispersion relations as shown in Figure 6.23. Due to confinement by the narrow wire in the y-direction, quantised modes are seen. These have associated sinusoidal intensity distributions as indicated in Figure 6.23a. Each of these modes corresponds to a lower polariton branch with a shifted cavity mode when viewed along $k_x$ (Figure 6.23b). In this experiment, polaritons are excited at high energy and k vector as indicated by the dark red circle in Figure 6.23b. Polaritons scattering out of these initial states can scatter to other

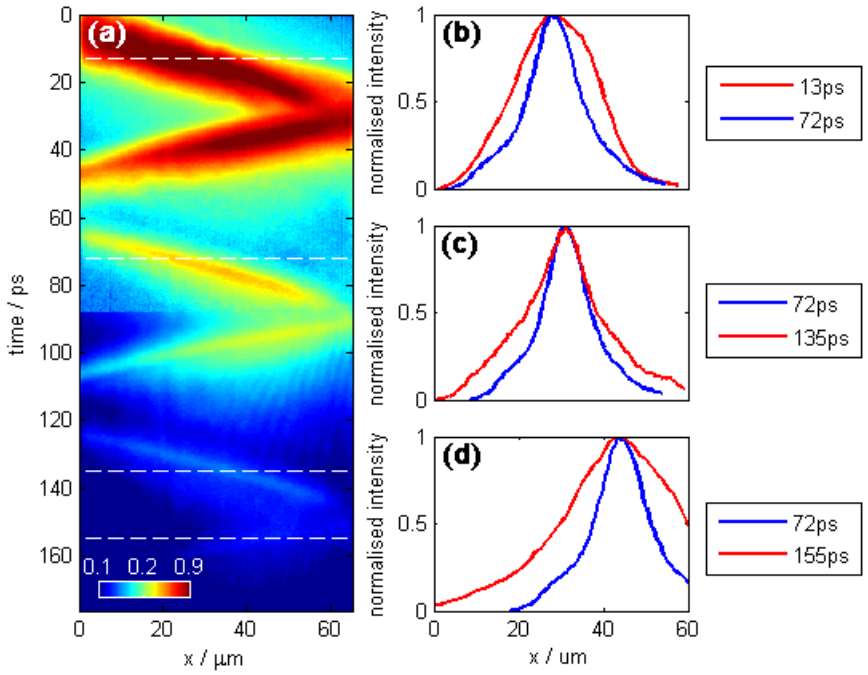


**Figure 6.21: Self focussing. (a)** Spatio-temporal trace of the self-focussing wavepacket, plotting using a logarithmic color scale. This image is constructed from two streak camera traces, each covering a time range of $\sim$ 90 ps. **(b-d)** Comparison of the wavepacket profiles at different times. The blue curve corresponds to the wavepacket intensity profile after 72 ps while the red curves show the normalised profiles at 13 ps, 135 ps and 155 ps for comparison. (b) shows a reduction in wavepacket width during the initial self-focussing period. (c) shows that a soliton-like peak persists after a further 60 ps, although there is also a broader background attributed to an additional spreading wavepacket. Finally, (d) shows the spreading wavepacket dominating the profile at later times when the intensity has dropped.

branches, maintaining their energy even as their momentum changes. In the case where a large proportion of the polariton population maintains its energy, the energy-integrated k-map measurement actually corresponds to a high energy cut of the E-**k** spectrum as indicated by the red band in (Figure 6.23b) due to the higher occupation of these states. It should be noted that in this energy band, the mode with the highest $k_x$ component corresponds to the lowest energy mode which has only 1 maximum in the y direction. Modes which are lower in $k_x$ have more intensity maxima along $k_y$.

### Dispersion

As the wavepacket self-focusses in realspace, the E-$k_x$ dispersion (Figure 6.24) broadens from a k bandwidth of $\sim$0.5 $\mu m^{-1}$ to a bandwidth of greater than 1.5 $\mu m^{-1}$ (the E-$k_x$ dispersion may extend beyond the angular range of the objective lens). The emission spectrum was compared with the lower polariton branch measured using non-resonant excitation (§6.1). Rather than following the curve of the lower polariton branch, the wavepacket spectrum is linear, indicating that the group velocity of polaritons at each k vector is the same allowing the wavepacket to hold its shape. This is most obvious for high k vectors in Figure 6.24c where the LPB is significantly curved. The intensity profile along the dispersion curve

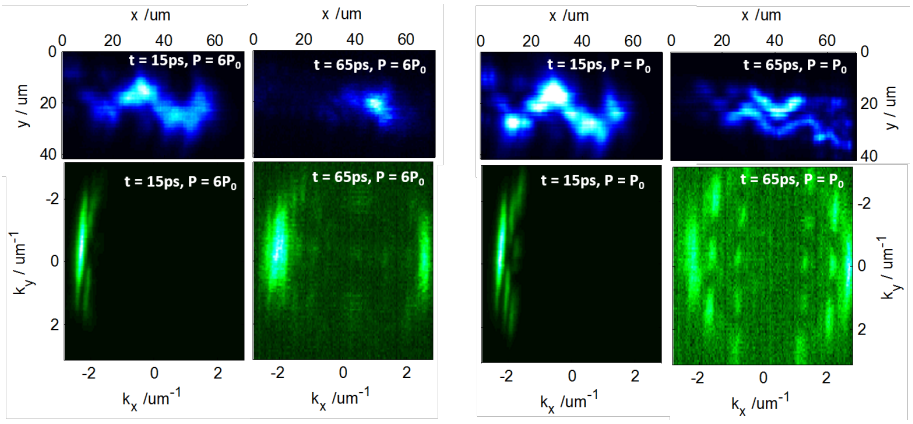


**Figure 6.22: Mode occupation.** The top row shows 2D realspace images of the wavepacket in the wire at two excitation powers and times while the bottom row shows the corresponding k maps. The left two columns show data for a high excitation power ($6P_0$) showing how an initially broad wavepacket self-focusses while polaritons accumulate mostly in a single nonlinear mode at later times despite occupying multiple modes at early times. The right two columns show data for low excitation power ($P_0 = 90$ μW) where the wavepacket remains broad and the polaritons scatter to occupy more wire modes as they propagate.

appears to have 3 broad peaks (the one at highest k vector may be partially cut off). I attribute this to the fact that the dispersion is generated by parametric scattering of the WB states into a range of signal and idler state pairs. Similar behaviour was seen in microwires 8 μm wide and 4 μm wide (only the 4 μm results are shown in Figure 6.24, but data for the 8 μm wire can be seen in Figure 6.29).

In order to get a better picture of the energy changes as the wavepacket evolves, the intensity profiles of the dispersions over time were plotted. In the case of short wires (Fig 6.25), the wavepacket reflects from the ends of the 100 μm long wire resulting in sharp change in k vector as the wavepacket changes direction. By comparing the I vs $k_x$ plots with the I vs energy plots, it can be seen that for each wavepacket reflection in the 8 μm wire and the first reflection in the 4 μm wire, a sharp loss of energy occurs. The reflection of these wavepackets from the end is therefore an inelastic collision.

For the narrower wire, sharp changes in energy are not seen for subsequent reflections although there is a smooth drop in energy over the propagation time. The change to a more elastic collision could be due to the fact that as the polaritons approach the bottleneck region of the dispersion (described in §2.2.2) they cannot easily drop to lower energy states on the LPB. For the wider wire, the wire modes are more closely spaced, so higher wire modes may provide an alternative route for polaritons to scatter to lower energies. The energy redshift could also result from a loss of polaritons, which may either escape from the wire wall or may become trapped at the end of the wire. This trapping at the end of the wire was seen more often in the case of wider wires (not shown), so would provide a plausible explanation for higher redshifts in wide wires after the point of reflection.

Here, the drop in energy over time is accompanied by a decrease in the k vector. This could be as a result of the polaritons scattering between LPB branches, particularly as the evolution in k appears to come in discrete jumps rather than a continuous shift. The interpretation of these results is complicated by the reflections from the ends of the wire

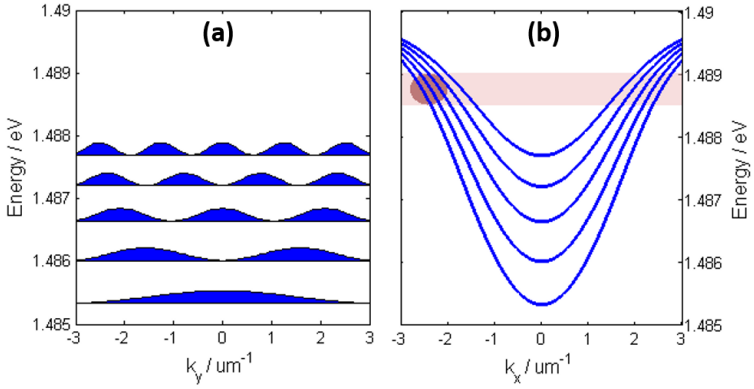


**Figure 6.23:** Cartoon E-$k_x$ and E-$k_y$ dispersion relations explaining the shape of the measured k-maps. The filled blue areas in (a) indicate the approximate intensity distribution for different modes quantised in the y direction. (b) shows multiple lower polariton branches appearing in the x direction where an energy shift is applied to the cavity mode due to quantisation in the y direction. The dark red circle indicates the approximate energy and k vector of the WB while the lighter red band indicates states with similar energies but different k vectors. It should be noted that in this energy band, the mode with the highest $k_x$ component corresponds to the lowest energy mode which has only one maximum in the y direction. Modes which are lower in $k_x$ have more intensity maxima along $k_y$.

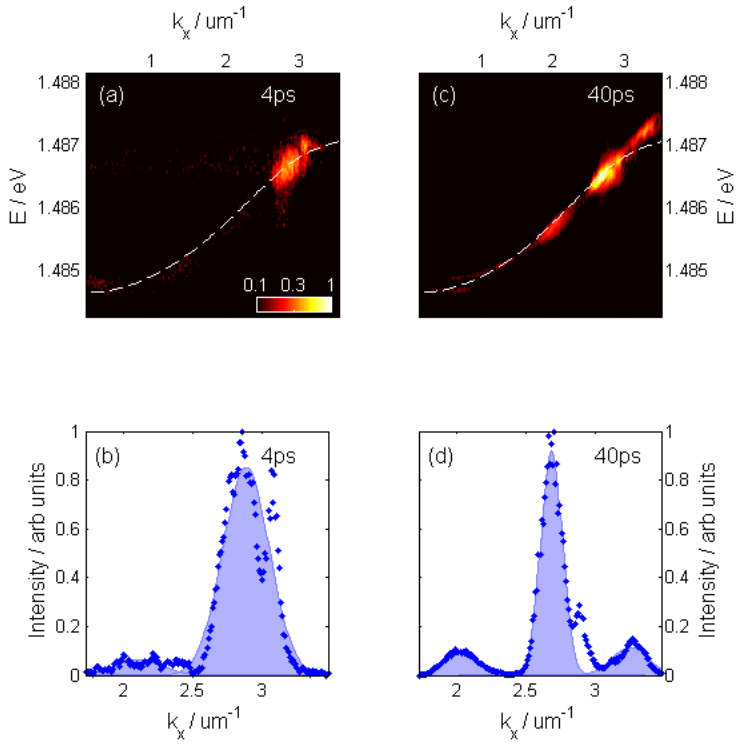


**Figure 6.24: E-$k_x$ dispersion** (a, b) show the spectrum of the polaritons injected into a 4 µm wide wire by the WB at early time while (c, d) show the spectrum of the self-focussed wavepacket. (a,c) show the intensity of the emission as a function of $k_x$ and E using a logarithmic colour scale. (b,d) show the intensity profile along the line of the dispersion as a function of $k_x$ (using a linear intensity scale). The single peak at early time centred around 2.9 $\mu m^{-1}$ in (b) is replaced at later times by 3 peaks at 2.0 $\mu m^{-1}$, 2.7 $\mu m^{-1}$ and 3.3 $\mu m^{-1}$ (d). These peaks are attributed to signal, pump and idler states in a parametric process with the asymmetry of pump-signal and pump-idler separations attributed to the truncation of the high k side of the idler peak.

as well as by the fact that the lower polariton branches change shape as their population decreases.

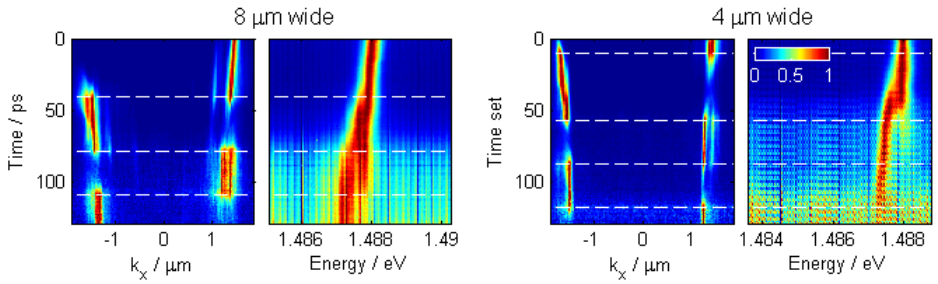


**Figure 6.25: Dispersion profiles, short wires**. At each time,the E-$k_x$ dispersion is constructed as a 2D image. The emission intensity is then integrated over all recorded $k_x$ vectors to find the intensity vs energy profile, or integrated over all energies to get the intensity vs $k_x$ profile. The profiles are then normalised. This was repeated at each time to show the continuous evolution of the dispersion. White dashed lines show the approximate times where the wavepacket is reflected from the end of the wire as a guide to the eye. Here, data is shown for short wires of two widths, where more modes are accessible for the wider wire. The sharp changes in k vector (sign change) correspond to reflections of the wavepacket from the end of the wire.

### 6.6.2 Wavepacket arrays

The generation of wavepacket arrays has been studied in long wires in §6.3. Some examples of arrays observed in short wires are shown in Figure 6.26. As for the case of a single self-focussing wavepacket in a short wire with a width of 4 μm (Fig 6.24 in §6.6.1), the dispersion is broad and linear although much of the emission is dim reducing the visibility of any intensity modulation. There does appear to be a slight modulation with peaks separated by 0.6 ± 0.1 $\mu m^{-1}$ corresponding to a peak separation in realspace of 10.5 ± 1.5 μm (see Appendix A) which is comparable to the peak separation in the images shown. For the 8 μm wire the separation between realspace peaks is clearer, particular in the 2D spatial images in Figure 6.26. Correspondingly, the intensity modulation seen along the dispersion is much stronger and more peaks are visible. This moduation has a smaller period of around 0.35 ± 0.03 $\mu m^{-1}$ corresponding to a realspace peak separation of 17.9 ± 1.7 μm. This is in agreement with the 2D realspace measurement shown, where the wavepacket separation is $\sim 18 \pm 2$ μm.

In short wires, it is hard to continuously image the propagation of the wavepacket array as there will be times when the first and last peaks in the array are propagating in opposite directions as one reflects. In addition, inelastic collisions with the end of the wire as shown in Fig 6.25 could introduce extra complications in the dynamics. Measurements made in this system do however demonstrate the robustness of the nonlinear arrays investigated in long wires with no reflection from the end (§6.3)

### 6.6.3 Excitation conditions

The k vector and energy of the WB were simultaneously varied in order to quasi-resonantly excite the same lower polariton branch mode at different k vectors as shown in Fig. 6.27a.

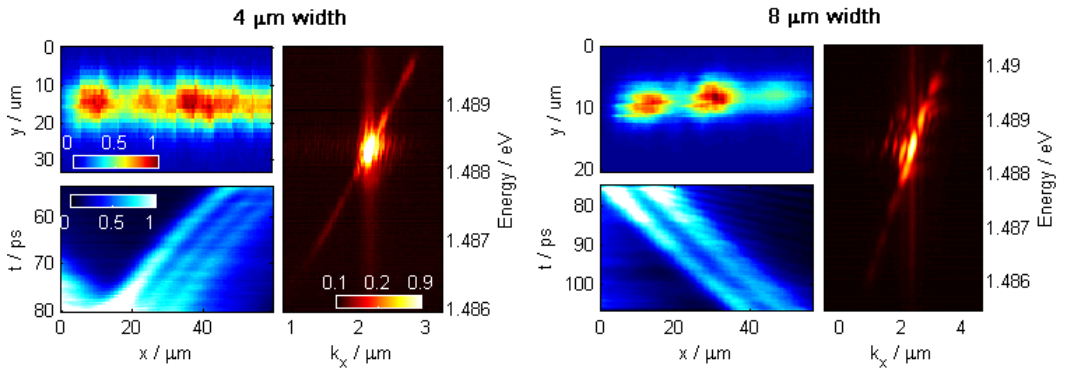


**Figure 6.26: Wavepacket arrays, short wires:** Multipeak structures in wires of two widths (4 µm and 8 µm). These are short wires, so the polaritons have reflected from the wire ends twice before these images are taken. For each wire width, the top left image shows a 2D realspace image at a time when the train is near the middle of the wire while the bottom image shows the intensity profile as a function of position x and time t, integrated over the width of the wire (i.e. this integrates over streak camera slices taken at different vertical positions). The right hand image shows the intensity as a function of energy and $k_x$ plotted using a logarithmic colour scale.

Once the k vector was selected, the energy was optimised to excite the narrowest wavepacket (not the brightest, so the laser is not actually resonant). The WB is small in realspace so it is correspondingly broad in k-space, spanning a range of ∼0.8 $\mu m^{-1}$: the quoted excitation k values correspond to the centre k vector. The WB power was 210 µW which should be sufficient to excite self-focussing wavepackets. The degree of self-focussing is assessed by measuring the minimum width reached by the wavepacket during its propagation.

The dependence of the degree of self-focussing on the excitation $k_x$ vector is shown in Figure 6.27b. The excited wavepacket remains broad at low k vectors although its width decreases slowly. Between ∼2.1 $\mu m^{-1}$ and ∼2.4 $\mu m^{-1}$ , the wavepacket width decreases rapidly before the width saturates after ∼2.4 $\mu m^{-1}$. Using the parameters measured for the planar cavity (Rabi splitting, exciton energy), the point of inflection is expected to be at ∼2.3 $\mu m^{-1}$ (green dashed line in Figure 6.27b.). This agreement between the $k_x$ vectors where self-focussing is observed and the theoretical value for the point of inflection of the E-$k_x$ dispersion is consistent with the behaviour that would be expected for a soliton, which would only form when the polaritons are injected with negative effective mass.

In addition to the initial shrinking of the wavepacket, soliton formation would be characterised by the occupation of a broad range of k vectors. Both of these parameters were measured for these wavepackets as a function of WB power and found to have non-linear dependencies as shown in Fig. 6.28. The range of occupied k vectors at different powers is shown in Fig. 6.28a. Example spectra at low (50 µW) and high (450 µW) powers are shown in Fig. 6.28(c,d). Here, the k breadth is estimated by eye by looking at the spectrum intensity vs $k_x$ integrated over energy. Instead of taking the FWHM, I look at the range over which any signal, even if it is very small, is seen.

For the lowest power, the breadth corresponds roughly to the k range of the WB spot. As the WB power is increased, more k states are occupied until there is a jump in k breadth when the measured WB power is between 250 and 300 µW. After this point, the k breadth

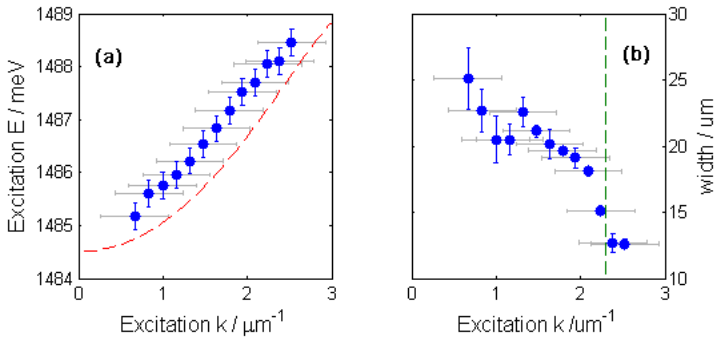


**Figure 6.27: Dependence of self-focussing on excitation k vector.** **(a)** E-$k_x$ position of the WB for each measurement (blue dots) in relation to the LPB (red dashed line). The blue error bars indicate the energy range of the WB while the grey error bars indicate the k range of the WB. **(b)** Wavepacket width vs excitation $k_x$. The wavepacket width shown here is the smallest width which the wavepacket reaches. The grey x-error bars indicate the range of k vectors which make up the WB while the y-error bars indicate errors from the fit to the wavepacket width. The green dashed line indicates the approximate k vector of the point of inflection of the LPB.

is saturated. For Fig. 6.28b, the wavepacket width shown is the smallest size that the wavepacket reached as indicated on the example streak camera traces shown in Fig. 6.28(e,f). The data point at the lowest power is similar to the size of the wavepacket triggered by the WB for all powers. As the WB power is increased, the minimum wavepacket size drops until it saturates when the WB power is $\sim 250\mu$W.

### 6.6.4 Femtosecond vs Picosecond Laser Pulses

As discussed in §3.3.3, higher excitation powers can be achieved when the pulsed laser is in the picosecond regime rather than the femtosecond regime. The femtosecond regime does also have its advantages: the range of energies which can be selected in the pulse shaper is broader for shorter laser pulses. This makes it easier to study k dependent behaviour, such as that shown in Figure 6.27, as the WB can be more easily tuned into quasi-resonance with the lower polariton branch at the different k vectors.

The laser pulse passes through a pulse shaper so the WB is 5-10ps long when it reaches the sample regardless of whether the initial laser pulse was 3 ps or 300 fs . The laser regime might therefore be expected to have a negligible effect on the end results, however this is worth verifying as the intensity distribution over the WB energies may not be the same in the two cases (see Fig. 3.9 in §3.3.3). For a femtosecond laser pulse, the pulse shaper selects $\sim 6\%$ of the laser energies so the intensity profile may be roughly a top hat. On the other hand if the laser pulse is already 3 ps long, the pulse shaper selects $\sim 50\%$ of the laser energies so the gaussian intensity distribution of the original laser pulse may persist in the WB.

The effect of changing the laser pulse duration is examined in Fig. 6.29, considering the realspace images, E vs $k_x$ spectra and intensity vs ($k_x$, $k_y$) maps. The left two columns show the broad wavepackets injected by the two laser pulses while the right two columns show the wavepackets at later times, once they have self-focussed. The same sample (an 8x100 μm wire) is used in both experiments although other experimental parameters may have changed

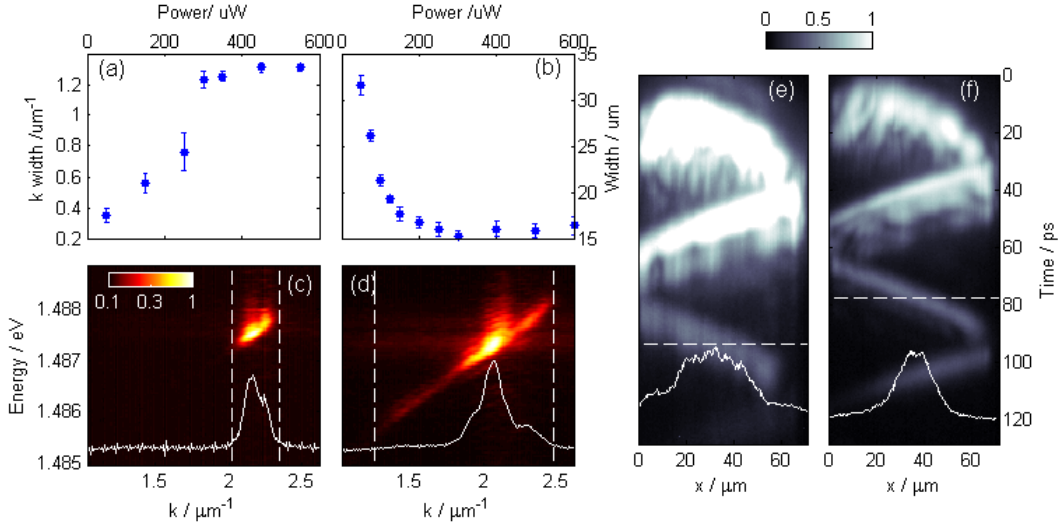


**Figure 6.28: Power dependence** of soliton-like behaviour characterised by **(a)** the widest occupied range of k vectors as a function of power and **(b)** the smallest wavepacket width as a function of power. **(c,d)** E-$k_x$ spectra at 50 µW and 450 µW. Solid lines show the intensity profile of the spectrum along $k_x$, integrated over energy. Dashed lines indicate the range of k at over which there is some signal (this may be more visible in the 2-dimensional image rather than the 1-dimensional intensity profile): this is the width plotted in (a). **(e,f)** Streak camera traces at (e) 50 µW and (f) 400 µW. Solid line shows the intensity profile over x taken at the time indicated by the dashed line. The widths in (b) are found by fitting a gaussian to these profiles. Logarithmic colour scales are used in (c-f) to increase the visibility of dim emission.

slightly as the two data sets were taken at different times. For example, the k maps in Fig. 6.29(j,l) are rotated compared to those in (i,k) as the sample has been remounted between experiments and the wire may not lie perfectly along x in the laboratory frame. Despite this, the two data sets show similar features.

In both sets a wide wavepacket is initially injected which snakes between the walls in the y direction (Fig. 6.29(a,b)). As can be seen from the k-maps (Fig. 6.29(i,j)), three modes of the wire are initally excited. Looking at the dispersions (Fig. 6.29(e,f)), some emission is seen from two modes with the fundamental mode being the brightest. The horizontal line in (e) comes from residual laser scatter.

At later times, the injected wavepacket self-focusses into a much narrower wavepacket (Fig. 6.29(c,d)). The snaking of the main peak is reduced although it is not completely eliminated, especially in the dim tail. The dispersions (Fig. 6.29(g,h)) broaden along a diagonal line in E-$k_x$ space and in both cases, modulation of the intensity profile is seen along the line, although the period of modulation is different in the two cases. The k-maps (Fig. 6.29(k,l)) show that in both cases the emission at large $k_y$ is reduced and the wire mode pattern of nodes and antinodes becomes less obvious. A broader k range is occupied in case (k). The main features of the wavepacket dynamics are similar for the two laser configurations while small differences could be as a result of changes in other experimental parameters. The variation in the laser pulse does not therefore appear to have a significant effect on the excitation of self-focussing wavepackets.

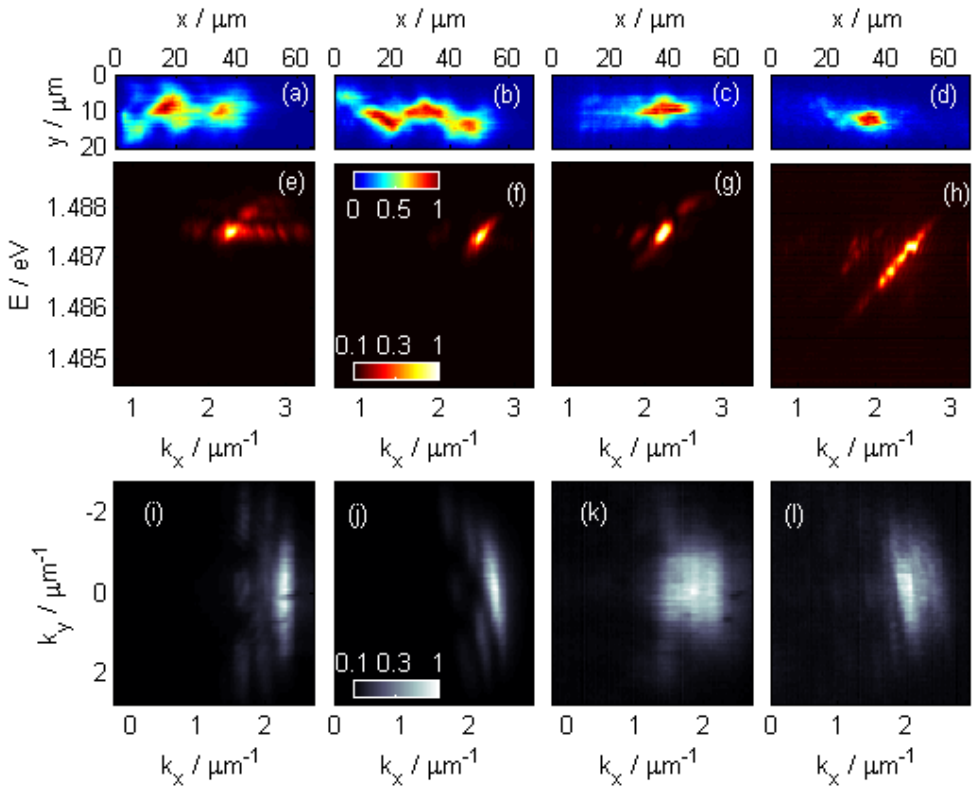


**Figure 6.29: Change laser pulse** (a,e,i) Realspace, dispersion and kmap for the wavepacket injected by a picosecond laser pulse. (b,f,j) show the injected wavepacket for a femtosecond laser pulse. (c,g,k) Self-focussed wavepacket, 70 ps after injection by a picosecond laser pulse . (d,h,l) Self-focussed wavepacket, 70 ps after injection by a femtosecond laser pulse. These measurements were made on a wire with a width of 8 µm.

## 6.7 Planar cavities

The behaviour of self-focussing wavepackets in a planar structure was also studied. In the propagation direction, they were seen to show similar self-focussing behaviour to both the wavepackets in microwires studied in this chapter and dissipative solitons in planar cavities [7].

In realspace, these wavepackets self focus in the x direction but defocus (spread out) in the y direction, as shown in Figure 6.30. If the WB power is reduced, the wavepackets remain roughly the same size in the x direction but still spread in the y direction (Fig. 6.31). Self-focussing only occurs at high power, as was the case in microwires (§6.2.3).

The y-spreading in the low power case is less than that in the high power case, which is attributed to the increased repulsive polariton-polariton interactions for higher polariton densities. For the low power case, the lack of spreading in the x-direction compared to the y-direction is attributed to the shape of the LPB. The phase velocity of different components of the wavepacket is proportional to the gradient of the E-k curve at that point. The more variable the gradient, i.e. the bigger the curvature, the larger the variation in propagation speeds of all the components, so spreading should increase with the curvature of the dispersion. The $k_x$ component of the wavepacket is high where the curvature is small, but the $k_y$ component is at the bottom of the LPB where the curvature is large. More spreading would therefore be expected in the y direction than the x direction.

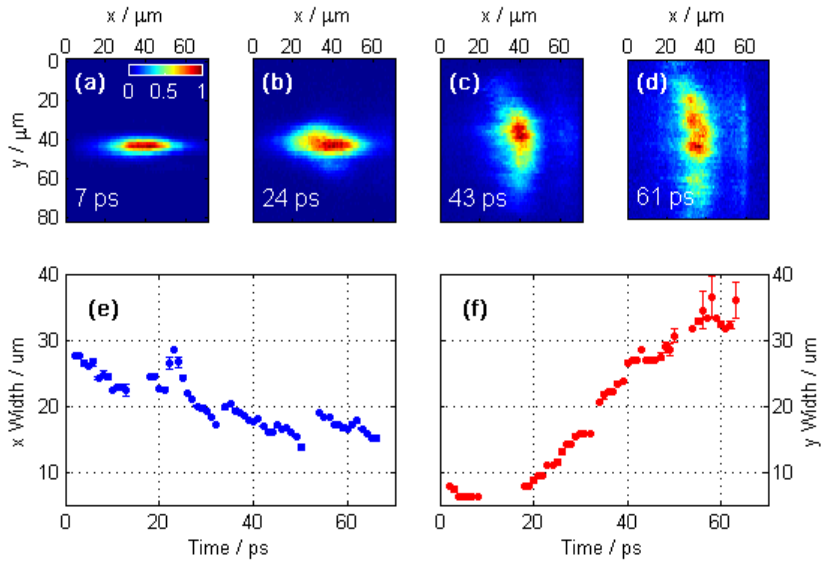


**Figure 6.30: Planar cavity: Dynamics**. **(a-d)** 2-dimensional realspace images at different times after the arrival of the WB. The WB power here is 720 µW. **(e,f)** Width of the wavepacket in the x (e) and y (f) directions vs time. These are calculated in the same way as the plots in Fig 6.6a.

The dependence of self-focussing behaviour on the excitation $k_x$ vector was measured in the same way as has been described for wavepackets in microwires. The results for the planar cavity are shown in Figure 6.31g. Self-focussing wavepackets are formed when the WB $k_x$ vector is centred at $\geq 2.3$ µm$^{-1}$, which is comparable to the point of inflection of the lower polariton branch at this detuning ($\sim$2.2 µm$^{-1}$, see Figure 6.31h).

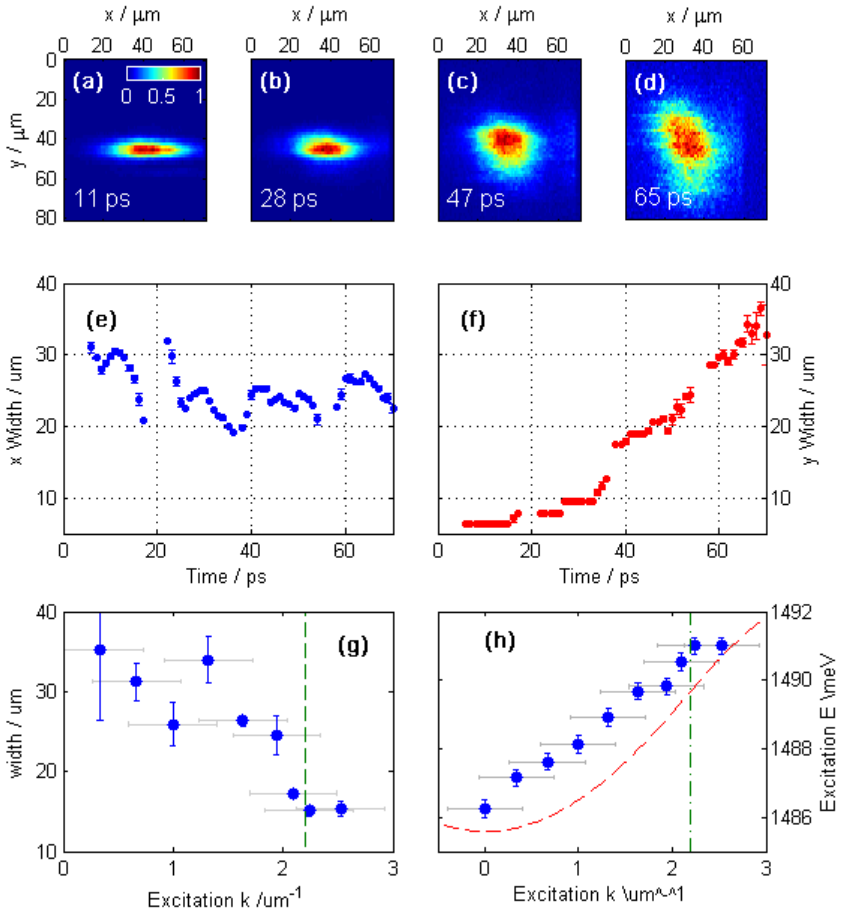


**Figure 6.31: Planar cavity: Excitation conditions. (a-f)** Evolution of the wavepacket shape with time when the excitation power is 40 µW. The data is plotted in the same way as for Fig 6.30. **(g)** Wavepacket width in the x direction as a function of the excitation $k_x$ vector. The wavepacket width shown here is the smallest width which the wavepacket reaches. The grey x-error bars indicate the range of $k_x$ vectors which make up the WB while the y-error bars indicate errors from the fit to the wavepacket width. The green dashed line indicates the approximate $k_x$ vector of the point of inflection of the LPB. **(h)** E-$k_x$ position of the WB for each measurement (blue dots) in relation to the LPB (red dashed line). The blue error bars indicate the energy range of the WB while the grey error bars again indicate the k range of the WB. The point of inflection is indicated by a green dash-dot line.

For the case of dissipative solitons (Chapter 5), theory suggests that localisation in the y direction arises from some interaction with the pump §2.4.1. The result shown here with no CW pump where self-focussing only occurs in the propagation direction and the wavepacket spreads significantly in the perpendicular direction gives strong experimental support for this theory.

## 6.8 Polariton Interaction Coefficient

Polariton-polariton interactions result in a blueshift in the polariton energy of U = gN where N is the polariton number density and g is the interaction coefficient. While the blueshift is relatively easy to measure (by comparing the measured dispersion with that recorded for low power non-resonant excitation), the number density N is much harder to estimate.

An attempt has been made to estimate the interaction coefficient g using the data set at power $P_2$ in §6.3. At the highly populated k vector of $k_x = 2.2\ \mu m^{-1}$, the energy of the polariton state is blue-shifted by ∼0.4 meV compared to the polariton dispersion measured under non-resonant excitation, so U can be taken to be 0.4 meV.

Simply measuring the excitation laser power does not give a good idea of the polariton number as it is not clear how efficient the excitation is. Instead, N was calculated by estimating the emission power. As this was too low to be directly measured with a power meter, I compared the recorded emission intensity measured on the streak camera with the recorded intensity of a laser pulse sent through the same optics with identical streak camera settings. The total emission intensity integrated over the whole propagation path was compared to the total intensity of the laser pulse, again integrated over the pulse duration. In this way, the number of photons calculated to be in the laser pulse was directly comparable to the number of photons emitted by the soliton and detected by the streak camera. The laser power was increased to a level which was measurable using a power meter, then a known level of attenuation was applied until the correct laser intensity was recorded on the streak camera. The attenuated laser power (corresponding to the polariton emission power) could then be deduced from these measurements.

The average power of the attenuated laser beam was found to be ∼50 nW. This was a continuous wave measurement of a pulsed emission source: the power is actually concentrated in pulses of ∼10 ps with a separation of 12 ns, so the power in each pulse was ∼ 50 μW. The energy in each pulse is 50 μW*10 ps = 3000eV, corresponding to ∼ 2000 photons with energy 1.5 eV in each laser pulse. This should be approximately equal to the number of photons collected from each excited wavepacket.

Here, only the photons emitted through the bottom (substrate side) DBR of the microcavity were collected. It was not possible to collect from both sides simultaneously so it is not possible to determine the total number of photons emitted. Similar experiments with the sample orientation reversed gave similar emission intensities, although the number of injected polaritons may be different in the two cases as the excitation efficiency may not be the same through both DBRs. As there are more DBR pairs on the back mirror than on the front, it is expected that more photons were emitted through the front mirror so were not collected in this experiment. To give an order of magnitude estimate, I assumed that 1.5 times as many photons were emitted from the top DBR compared to those collected

through the bottom (this is expected to be a low estimate), giving an approximate number of 5000 photons per polariton wavepacket.

The wavepacket width reached a minimum of $\sim$ 10 μm and was confined in a wire of width $\sim$ 5 μm, giving an approximate area of 50 $\mu m^2$. The number density would then be $\frac{5000 \text{ photons}}{50 \ \mu m^2} = 100 \ \mu m^{-2}$. The sample used contains three quantum wells (see §3.1.3) so, assuming that the excitons are evenly distributed between the three quantum wells, the number density N within each well would be $\sim 33 \mu m^{-2}$. I can now calculate an upper limit of the polariton-polariton interaction coefficient within each well, assuming that the blueshift is dominated by interactions within each well rather than between wells, as $g = U/N = \frac{0.4 \text{ meV}}{33 \ \mu m^{-2}} = 12 \ \mu eV \ \mu m^2$. This compares well with previous measurements of g in a microcavity, which found values of 2-10 $\mu eV \mu m^2$ [179].

## 6.9 Summary and Conclusions

The dynamics of the nonlinear wavepackets investigated in §6.2.1 and §6.2.2 show features which are characteristic of soliton formation. In particular, the shape of the wavepacket is not determined by that of the writing beam that triggers it. When triggered with a WB of width $\sim$ 20 μm, the wavepacket initially shrinks to $\sim$ 10 μm and then starts to grow as polaritons are lost from the system and the interaction energy within the wavepacket is decreased. The observed dependence of the wavepacket width on the polariton density is consistent with the trend expected theoretically for bright polariton solitons (see §2.4.1). If the polariton density drops below a certain threshold, polariton-polariton interactions become negligible. The observation that shrinking of the wavepacket is not seen in this linear regime (§6.2.3) confirms the role played by polariton-polariton interactions in the self-focussing wavepackets. A similar effect was seen in observations of bright dissipative polariton solitons [7].

Due to the repulsive interactions between polaritons, bright solitons would only be stable if there is some source of attraction to prevent the expansion of the high density wavepacket. Theoretically, the negative effective mass of polaritons on the LPB at high k vector should provide sufficient attraction to generate stable solitons [94] as has been observed experimentally [7]. The wavepackets investigated in this chapter have a clear dependence on k vector and will only shrink in size when polaritons are injected with negative effective mass, above the point of inflection of the LPB (§6.2.3). The spectrum of energy vs $k_x$ broadens as the wavepacket shrinks, as seen in observations of bright dissipative polariton solitons [7]. This is particularly pronounced when only the fundamental mode of the wires is excited (Fig 6.5) or at higher excitation powers §6.4.2, possibly due to a higher polariton-polariton scattering rate as there is greater spectral overlap between the occupied polariton states.

While this soliton-like behaviour is not seen at low excitation k vectors or low powers, it does appear to be robust against other small changes in the sample or the excitation conditions. This was studied extensively in §6.2.3 and §6.6 where self-focussing wavepackets were generated at a range of k vectors and powers and with laser pulses with different energy-intensity profiles (illustrated in Fig 3.9, data presented in Fig 6.29). If the injected wavepacket is multi-mode, the self-focussing wavepacket appears to form in a single mode although a dispersive tail can also form in other wire modes. This robustness to multi-mode

excitation makes the choice of wire width non-critical: similar behaviour is observed in wires with widths of 4 μm (e.g. Fig 6.28), 5 μm (all of the long wire data presented in this chapter) and 8 μm (e.g. Fig 6.22).

The wavepacket dynamics also appear to be robust against defects in the wires: even a reflection from the end of the wire (which could be described as a particularly large defect) in which energy is lost (as shown in Fig 6.25) does not hinder the self-focussing and may even aid in the broadening of the E-$k_x$ spectrum, as discussed in §6.3.2. Self-focussing along the x direction is even seen when the wire is removed completely and the wavepacket is injected into a planar cavity (§6.7), an observation that supports the theoretical description of the role played by the CW pump in the localisation of dissipative solitons perpendicular to the propagation direction [125] (see §2.4.1).

In the dissipative regime where soliton formation in a planar cavity is supported by a continuous wave pump, multi-peak soliton patterns have been observed as described in Chapter 5. Similar observations have been presented for these wire samples in §6.3 where multiple peaks are generated as the excitation power increases. There appear to be different regimes of wavepacket arrays, partly characterised by differences in the phase profile across the array (§6.4.2). Arrays excited at lower powers had a smoothly varying phase while discontinuities in the phase profile were seen between the peaks of arrays excited with higher powers. The pattern with no phase jump between the peaks consists of narrower peaks which are more closely spaced that the higher power regime. It has been predicted theoretically that single solitonic wavepackets can be brought together to form a stable pattern, but only if there is a phase jump of $\pi$ between them [97, 176, 177]. It could be that the lower power pattern is analogous to a single multi-peak parametric soliton of the sort simulated in [125, 8] while at higher powers, two completely separate soliton-like wavepackets form and a phase jump evolves between them, maintaining the stability of the pattern.

### 6.9.1 Conclusions

The formation of soliton-like self-focussing wavepackets in quasi one-dimensional microcavities has been extensively studied. In this chapter, I have shown that these non-linear wavepackets can be generated and will propagate in quasi-one dimensional microwires for $> 100$ μm. With a cavity with a sufficiently high Q factor, this can be achieved without a continuous wave pump to replenish the supply of polaritons as was required for observations of bright dissipative solitons both in the literature [7, 123] and in Chapter 5. The self-focussing behaviour is robust against small changes in excitation conditions, provided that the injected wavepacket has sufficient density and is quasi-resonant with the negative effective mass region of the lower polariton branch.

By modifying the excitation conditions, multiple wavepackets can be generated by each laser pulse. Wavepacket arrays show a range of behaviour, varying from one regime where the individual peaks are closely spaced, propagating with the same velocity and with no phase jump between peaks; to a second regime of wider wavepackets which can move apart from each other and have a phase jump of $\pi$ between neighbouring peaks.

Measurements of the quantum properties of the polariton emission show anti-bunching and sub-Poissonian statistics, revealing non-classical behaviour of the occupied states. The

slight anti-bunching suggests that these states are amplitude squeezed, although further experiments would be required to fully characterise these quantum properties.

# Chapter 7

# Conclusions

In this thesis, I have investigated the dynamics of nonlinear wavepackets and pattern formation in several microcavity structures.

In Chapter 4, a tunable periodic potential was applied to a planar microcavity using Surface Acoustic Waves (SAWs), which can be thought of as reservoirs of coherent phonons with the energy and momentum of the SAW. The absorption of these phonons during an Optical Parameteric Oscillator (OPO) scattering event was demonstrated by looking for energy differences between macroscopically occupied "signal" states forming at well defined non-zero k vectors. It was suggested that reflections of the SAW from features on the sample can contribute to pattern formation in the emission spot. It has been shown elsewhere [81] that the studied signal states correspond to gap soliton states, forming in band gaps that appear at the edge of the Mini Brillouin Zone defined by the periodic potential. The size of each gap soliton decreased with increasing SAW amplitude and arrays of these wavepackets could form in a sufficiently large emission spot.

In Chapter 5, patterns of bright dissipative polariton solitons were studied in planar microcavities, building on previous observations of single solitons by Sich *et al* [7]. It was found that by elongating the pulsed writing beam, coherent arrays of soliton peaks formed along the propagation direction. Similarly, arrays could form perpendicular to the propagation direction although it was emphasized that the localisation mechanisms were different in these two directions. While localisation along the propagation direction is due to interplay between repulsive polariton-polariton interactions and negative effective mass (similar to the Gap soliton case), this mechanism is not valid in the transverse direction where the effective mass is positive. Localisation mechanisms for this direction have been proposed theoretically elsewhere and are thought to be stabilised by parametric scattering from the continuous wave pump [125]. This is supported by observations of wavepackets localised only in the propagation direction when the pump was removed (presented in §6.7).

In Chapter 6, the dynamics of nonlinear wavepackets in microwire structures were investigated. These could be more practical than a planar cavity for use in a polariton circuit as the wires could be used to route the signals around other devices on the chip where necessary. In contrast to Chapter 5, no CW pump was used in these experiments as the polariton lifetime in this sample was long enough to observe the evolution of a wavepacket without needing to replenish losses. No localisation mechanism in the transverse direction

was required as the polaritons were already confined within the wire. Soliton-like behaviour was seen, where self focussing was observed along the propagation direction when a polariton wavepacket was injected with negative effective mass. The energy spectrum broadened about the WB energy, which was attributed to the population of states by parametric scattering processes. Measurements of the quantum properties of these nonlinear wavepackets revealed non-classical behaviour where the polaritons appeared to occupy amplitude squeezed states.

Multi-peak patterns were observed as the WB power was increased, accompanied by discontinuities in phase between the peaks for higher power cases. It appeared that as the power was increased, the structure evolved from a single peak soliton-like solution to a multi-peak soliton-like solution (analogous to higher order optical solitons) where the peaks remain in phase. With a further increase in power, the peaks separated (analogous to soliton fission) and a phase jump evolved between them as expected theoretically for a stable array of separate solitons. This was accompanied by a broadening of the energy spectrum in a similar manner to supercontinuum generation observed in optical fibers [92].

## 7.1 Future directions

### 7.1.1 Quantum Properties in Microwires

The initial measurements of the quantum properties of nonlinear wavepackets in microwires presented in §6.5 show promising results, suggesting an amplitude squeezing of the wavepacket states. However, further investigation is required to fully characterise this behaviour. Losses can be reduced in the collection path by using fewer optical elements, for example by focussing the emission straight onto the streak camera instead of directing it through the spectrometer. Increasing the detection efficiency in this way should give a clearer observation of sub-Poissonian photon statistics. Accumulating data over a longer period of time should also help to reduce the errors in the result as more emission events would be recorded.

With an improved setup, it may be possible to characterise the degree of squeezing in the different types of nonlinear wavepacket observed in wires and look for the parameters which optimise the level of squeezing. While the streak camera measurements reveal the presence of amplitude squeezed states, quadrature squeezing may also be observable using a homodyne detection setup [156]. Squeezed states can be advantageous in quantum circuits as the noise in a measurement of the parameter of interest is reduced (at the expense of increasing the noise in the conjugate parameter). In additional, these states can be implemented in quantum information systems based on continuous variables [157].

### 7.1.2 Polariton Polarisation in Microwires

While the polarisation properties of nonlinear wavepackets in microwires has not been investigated here, this could prove to be an important degree of freedom to control for polariton device applications. Many of the proposed polariton devices described in the literature (see §2.6) define logical states by the presence of polaritons with a given polarisation. A wavepacket with a given circular polarisation could be used to switch a multi-stable state initialised at low intensity to a high density state whose polarisation matches that of the incident wavepacket [88, 134].

It is expected that quasi-one dimensional wires will have an energy splitting between states linearly polarised along the wire and those polarised across the wire, rotating the pseudo-spin (mapped onto the circular polarisation) of polaritons propagating through the wire [139]. Theoretical work [136] has suggested how this could be used in a "NOT" gate, where the polarisation state is inverted during propagation through a wire. The microwires used in Chapter 6 did not show a significant polarisation splitting, so further investigation is required to determine whether the wavepacket polarisation evolves during propagation through these structures. It may be possible to increase the polarisation splitting by applying strain along one wire axis on demand [180], thereby inverting the polarisation state when required.

### 7.1.3 Dissipative Solitons in Microwires

Control of the polarisation properties of dissipative solitons in planar cavities has already been achieved [123], however as the trajectory and speed of these solitons is determined by the pump spot, it is not possible to collide them together, as may be required for logic gate applications. Using a microwire with a Y-splitter configuration, it may be possible to guide solitons together for use in a logic gate as has been proposed theoretically by Cancellieri *et al* [141]. Such a structure could be used to investigate collisions between solitons with different polarisations, which would be expected to annihilate. In addition to adding functionality to a polariton device, such collisions could be used to measure the interaction constant between polaritons with opposite spin, making it an interesting device from a fundamental physics point of view. An experimental realisation of bright dissipative solitons in microwire structures such as Y-splitters could therefore be a productive direction to pursue further.

### 7.1.4 Continuous Wave Soliton Generation

A useful extension of the soliton arrays studied in Chapter 5 would be to generate an array of soliton pulses using a continuous wave writing beam. The observed splitting of an elongated pulsed WB into several peaks indicates that this may be possible, however it is not easy to detect with the current experimental setup. Time resolved measurements of solitons on the streak camera are triggered when a pulse is emitted from the laser, but this is not available with continuous wave excitation. As an intermediate step, a pulsed laser emitting 100 ps pulses could be used for the excitation: this would still trigger the streak camera, but is much longer than the typical duration of a soliton pulse ($\sim$5 ps). This could be described as quasi-continuous wave excitation and would clearly demonstrate the feasibility of generating a soliton train on a polaritonic chip for use as a clocking device in a circuit.

### 7.1.5 Dark Solitons in Microwires

Dark polariton solitons have been investigated in planar microcavites [55] and theoretical suggestions have been made for generating trains of dark solitons in a microwire using a continuous wave pump [144]. These dark trains would have a similar functionality to their bright counterparts, so could also be implemented as a clocking device.

Observations of "collisions" between bright soliton-like wavepackets propagating in opposite directions in a microwire showed little interaction between the wavepackets (§6.3.3). This was attributed to the short interaction time as the wavepackets quickly propagated past one another. Dark solitons are stable with a positive polariton effective mass, so can be excited over a larger range of low energy k vectors than bright solitons, allowing more control over their propagation speed. Soliton-soliton interactions may be observable in a dark soliton system as the interaction time can be increased by exciting slower solitons. The ability to manipulate the state of one soliton with another would open up the possibility of constructing soliton-based logic gates, enhancing the potential functionality of these non-dispersive wavepackets as information bits in a polaritonic circuit.

# Appendix A

# Fourier Transform Relations

In this Appendix, I present the feature sizes for variables related by a fourier tranform, for example, the expected width in k-space of a gaussian wavepacket with a given realspace width.

## A.1 Gaussian Wavepacket

Start with a wavepacket with a Gaussian distribution of k vectors centred at k vector $k_0$:

$$\psi(k) = A_0 e^{-\alpha(k-k_0)^2}$$

The Fourier transform of this is

$$\psi(x) = \left(\frac{1}{2\pi\alpha}\right)^{\frac{1}{4}} e^{ik_0 x} A_0 e^{-\frac{x^2}{4\alpha}}$$

The measured quantities are I(k) = $|\psi(k)|^2$ and I(x) = $|\psi(x)|^2$

$$I(k) = A_0^2 e^{-2\alpha(k-k_0)^2}$$

$$I(x) = \left(\frac{1}{2\pi\alpha}\right)^{\frac{1}{2}} A_0^2 e^{-\frac{x^2}{2\alpha}}$$

Comparing these with the formula for a Gaussian distribution

$$I(q) = C_0 e^{-\frac{q-q_0}{2\sigma_q^2}}$$

widths $\sigma_k = \frac{1}{\sqrt{4\alpha}}$ and $\sigma_x = \sqrt{\alpha}$ can be extracted. These widths are related by

$$\sigma_x \sigma_k = \frac{1}{2}$$

Experimentally, the full width half maximum ($w_q = 2\sqrt{(2ln2)}\sigma_q$) is the measured quantity. These are related by

$$w_x w_k = 4ln2 \tag{A.1}$$

## A.2 Multiple Peaks

Regular multi-peak structures along x can be represented by a series of $N$ delta functions separated by distance $D$

$$\psi(x) \propto \sum_{m=0}^{N-1} \delta(x - mD)$$

The corresponding k space distribution is given by the Fourier transform

$$\begin{aligned}\psi(k) &\propto \int_{-\infty}^{\infty} \sum_{m=0}^{N-1} \delta(x - mD) e^{-ikx} dx \\ &= 1 + e^{-ikD + e^{-i2kD} + \ldots + e^{-iNkD}}\end{aligned}$$

Summing the geometric progression gives

$$\psi(k) \propto \frac{1 - e^{-iNkD}}{1 - e^{-ikD}}$$

$$= e^{-i\frac{(N-1)kD}{2}} \frac{\sin(\frac{NkD}{2})}{\sin(\frac{kD}{2})}$$

The measured quantity I(k) = $|\psi(k)|^2$ is given by

$$I(k) \propto \frac{\sin^2(\frac{NkD}{2})}{\sin^2(\frac{kD}{2})} \tag{A.2}$$

In the case of two peaks, this simplifies to

$$\begin{aligned}\psi(k) &\propto e^{-i\frac{kD}{2}} \cos(\frac{kD}{2}) \\ I(k) &\propto \cos^2(\frac{kD}{2})\end{aligned}$$

Equation A.2 has primary maxima when $k = \frac{2m\pi}{D}$ (for integer $m$) and minima for $k = \frac{2m\pi}{ND}$ for $m \neq N$

For a realspace peak separation of D, the peak separation in k space ($d$) is therefore given by

$$d = \frac{2\pi}{D} \tag{A.3}$$

with a peak width ($\Delta d$, separation between minima on either side of the primary maximum) of

$$\Delta d = \frac{4\pi}{ND} \tag{A.4}$$

# Appendix B

# Simulations of Dissipative Soliton Patterns

Many of the experimental results presented in Chapter 5 have been reproduced numerically by Andrey Gorbach and Dmitry Skryabin based at the University of Bath. These simulations are presented alongside the experimental results in the paper [Chana *et al*, Phys Rev Lett, **115**, 256401 (2015)] [8] and are reproduced in this appendix for ease of comparison.

## B.1 Soliton Trains

For numerical investigation of the system, we used Gross-Pitaevskii equations describing coupled TE and TM cavity modes interacting with the spin dependent polariton field [7] and looked for quasi-circularly polarised soliton solutions moving in the direction of the pump momentum (i.e. along the $x$-axis) [7]. The model is described in §B.1.1. Previously [7, 123] it has proved to include all the important features necessary to numerically reproduce the experimental conditions. The soliton existence range in terms of the pump intensity, $|E_p|^2$, is well approximated by the bistability interval of the intracavity field [7].

We have computed the bifurcation diagram showing a sequence of stable multi-peak solitons (Fig. B.1(a)). The diagram shows that for every given pump intensity (horizontal axis) within the bistability range, stable soliton solutions with different numbers of peaks can be excited (vertical axis). An example of a five-hump soliton is shown in Fig. B.1(b). In our time-dependent modelling we assumed a Gaussian profile of the WB. With an increasing WB intensity, there is an increasing number of peaks in stable multi-peak soliton solutions(Fig B.1(c, d)).

In practice, the profile of the pump is Gaussian and therefore conditions for the soliton formation are met only within a certain radius around the pump centre, where the pump intensity is large enough to bring the cavity into the bistable regime.

In Fig. B.1(b) we compare profiles found in the case of an infinite flat pump with those moving through the Gaussian pump. One can see that in both cases the peak widths and peak spacings are closely matched. The peak amplitudes, however, differ as the latter structure does not spend sufficient time inside the bistability range to fully stabilise itself.

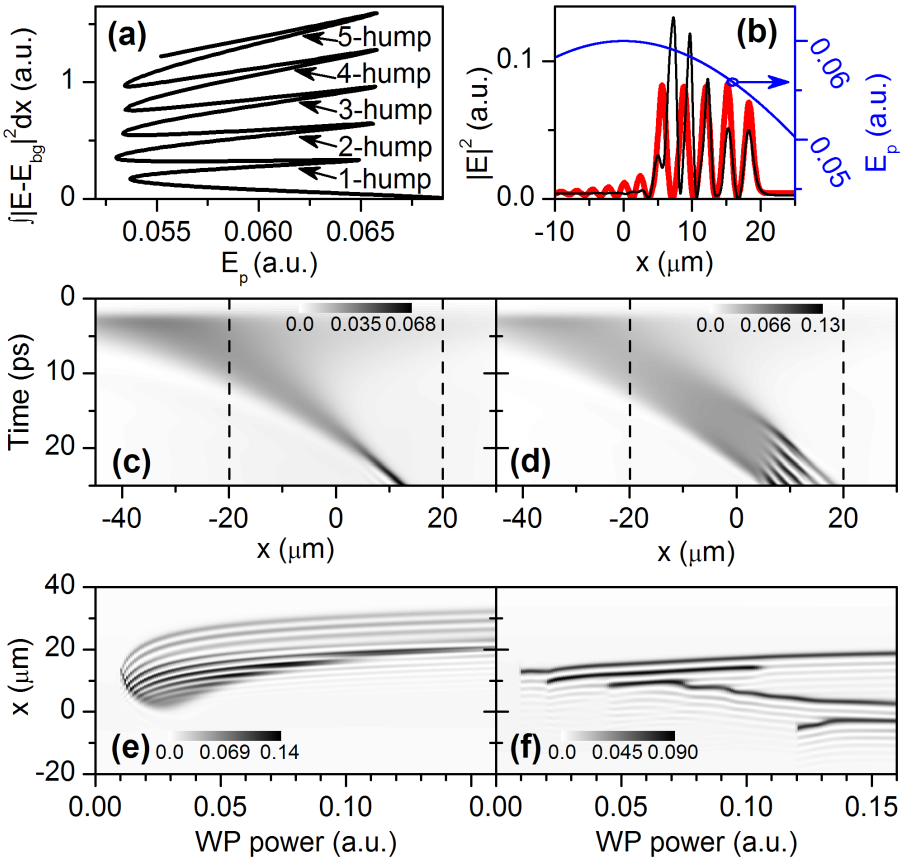


**Figure B.1:** (a) Snake-like bifurcation diagram for multi-peak solitons in the case of infinite flat pump. $E(x)$ is the electric field amplitude, $E_{bg}$ is the amplitude of the homogeneous solution (in the tails of the soliton), and $E_p$ is the pump amplitude.The homogeneous solution is bistable in the range $0.052 < E_p < 0.070$. (b) The red line is an example of the exact five-peak x-soliton array solution found for an infinite flat pump with amplitude $E_p = 0.06$; the black line is the five-peak x-soliton array generated in the numerical modelling reproducing the experimental conditions of Gaussian pump profile; the blue line shows the Gaussian profile of the pump field. (c, d) Spatio-temporal dynamics (grey-scale is $|E|^2$) resulting in the formation of the single-peak (c) and four-peak (d) x-soliton array. The pump field has a Gaussian profile with amplitude $E_p = 0.06$, the corresponding boundaries of the bistability region (as in (a)) are indicated by vertical dashed lines. The WB amplitude is $E_{wp} = 0.1$ (c), and $E_{wp} = 0.12$ (d). (e, f) Grey-scale profiles of multi-peak structures recorded in numerical simulations after 25 ps as a function of the WP power. In (e) $k_{wp} = k_p$, while in (f) the WB momentum is offset by 3° ($\Delta k \approx 0.4\ \mu\text{m}^{-1}$).

Fig. B.1(f) shows how the number and relative position of peaks varies with the WB power for slightly offset momenta of the pump and WB beams. Fig. B.1(f) is in good qualitative agreement with the experimental observations in Fig. 5.6. With increasing WB power there is an increase in both the number of peaks and the spacings between the solitons up to 10-20 $\mu$m. In numerical simulations minimising the difference between $k_{wp}$ and $k_p$ (preferably to zero) facilitates the generation of a regular pattern of peaks, while in the experiment $k_{wp} - k_p \approx 0.4$ $\mu\text{m}^{-1}$ due to physical constraints of the setup.

The solitons are formed by scattering polaritons from the pump state to populate the soliton spectrum. The characteristic time of polariton scattering is approximately given by $h/(gN)$, where $g$ is the interaction constant and $N$ is the density (then $gN$ is the blueshift). For a blueshift of 0.3 meV, about 13 ps are needed to fully populate the spectrum and form a soliton. The scattering can only occur once the trigger WB reaches the pump bistability area. For a Gaussian pump spot, solitons will only form after they have propagated a certain distance through the pump spot irrespective of how far away the WB is placed (Fig. B.1(c, d)). For this reason, when the WB power is high enough to excite a x-soliton array, the solitons in the array tend to appear at different times, see Fig. B.1(d). In the experiment, however, we observe that solitons start to form earlier, sometimes before reaching the bistability area (see §5.2.4). This was replicated in the modified simulations presented in §B.1.2.

### B.1.1 Numerical Model

Numerical studies were performed using mean-field equations describing the evolution of slowly varying amplitudes of the circularly polarized cavity mode $E$ and of the corresponding excitonic field $\psi$:

$$\partial_t E - i\frac{\hbar}{2m_c}\left(\partial_x^2 + \partial_y^2\right)E + (\gamma_c - i\delta_c)\,E = \\ = i\Omega_R\psi + E_p(x,y)e^{ik_p x} + E_w(x,y,t)e^{ik_{wx}x + ik_{wy}y + i\phi}\,, \quad \text{(B.1)}$$

$$\partial_t\psi + (\gamma_e - i\delta_e)\,\psi + ig|\psi|^2\psi = i\Omega_R E. \quad \text{(B.2)}$$

Here $m_c = 0.27 \cdot 10^{-34}$ kg is the effective cavity photon mass, $\hbar\Omega_R = 4.9867$ meV is the Rabi splitting, $\hbar\gamma_c = \hbar\gamma_e = 0.2$ meV are the cavity photon and the exciton coherence decay rates, $\delta_e = -1.84$ meV, $\delta_c = -2.34$ meV and $g > 0$ is the nonlinear parameter. $E_p(x,y)$ is the pump amplitude with the momentum $k_p$, the corresponding angle of incidence is $\theta = \arcsin[\kappa\lambda_p/(2\pi)]$. $E_{wp}$ is the writing pulse amplitude. The corresponding two non-zero in-plane components of the momentum $k_{wx}$ and $k_{wy}$ take into account mis-alignment between the pump and the writing pulse, and $\phi$ is the phase difference between the pump and the writing pulse.

For the case of the homogeneous pump $E_p(x,y) = const$ and $E_w(x,y,t) \equiv 0$ the soliton solutions are sought in the form $E = A(x - vt)e^{ik_p x}$, $\psi = Q(x - vt)e^{ik_p x}$. The soliton profiles and the velocity $v$ are found self-consistently by solving the Eqs. (B.1)-(B.2) using Newton-Raphson iterations [94].

In our simulations of the soliton excitation the system of Eqs. (B.1)-(B.2) has been solved directly using the split-step method [94].

### B.1.2 Nucleation of Arrays

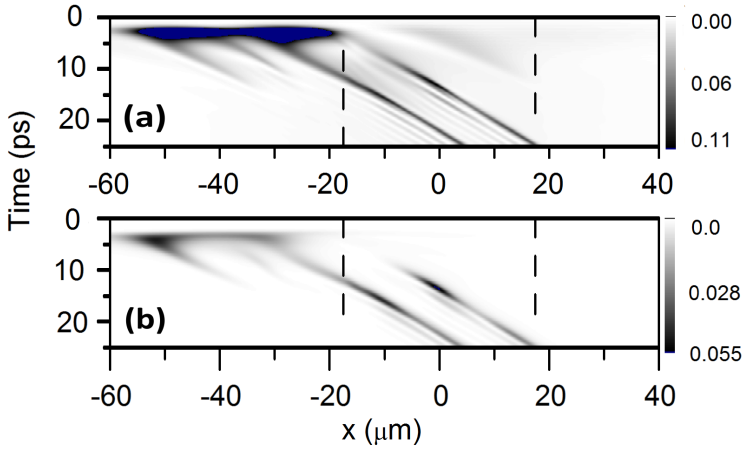


**Figure B.2:** (a) Numerical simulation of the equivalent trace taken from Fig. B.1f at WP power 0.115 and (b) the same trace but taking into account k-space filtering to block the WB reflection.

In most of the data sets presented in Chapter 5, the evolution of a smooth wavepacket excited by the WB into a multi-peak pattern along x was not recorded due to the limited field of view of the detection optics. However, some cases where this early emission was recorded are presented in §5.2.4. In particular, Figure 5.11c shows that the break-up of the WB pulse can start to occur before it reaches the bistability zone. This surprising observation was replicated in the numerical simulations presented in Figure B.2. It is believed that the break up occurs due to a combination of the two factors. Firstly, the difference in the k-vectors of the pump and WB leads to interference of the two, modulating the excitation power along the $x$-axis. Secondly, the onset of polariton-polariton interactions and scattering in close proximity of the bistability area may trigger the break-up before the wavepacket reaches the bistability area.

## B.2 Y-arrays

Previous simulations have shown that if the k vector of the pump and WB are the same and the WB is considered to be a top hat, the wavepacket from the WB focussed to a single soliton even if the WB is extended perpendicular to the propagation direction [125]. Here, it is shown that by changing the WB shape to a gaussian, the soliton wavefront was shown to be curved and could break up into several solitons.

In order to explain the mechanism of pattern formation along the $y$ direction, we first take a single hump one dimensional soliton localised along the $x$ direction and infinitely extended along $y$ and performed its linear stability analysis. This demonstrates that it is stable with respect to any transverse instabilities, which could lead to filamentation along the $y$ direction. If, however, we limit the extent of the soliton stripe by imposing a Gaussian

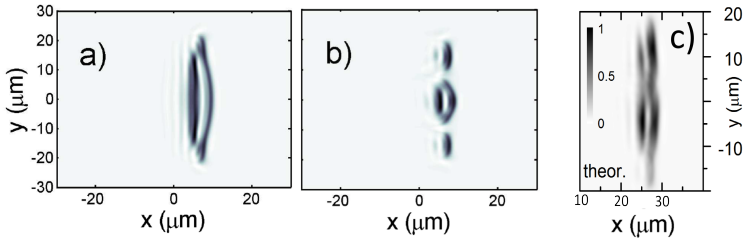


**Figure B.3: Numerical modelling of y-arrays.** Numerically modelled transverse distribution of the intracavity optical intensity after 15 ps of propagation under the conditions when the WB was elongated along the $y$-coordinate. In case (a), the pump and WB hit the sample at the same angle while in case (b) an angle of 3 degrees is introduced between the WB and the pump, introducing a difference in k vector of $\sim 0.4$ $\mu m^{-1}$. Figures (a,b) are obtained for a single WB phase, while in the experiments we average over all possible WB phases. A phase averaged numerical result is shown in Figure c where the pattern is broadened but some intensity modulation along the $y$ direction is maintained.
Note that figure (a) was not included in the paper, figure (b) was included in an arXiv version of the paper [arXiv:1407.7713v1], while figure (c) was taken from the published paper.

profile in the $y$ direction, then the change in the curvature of the soliton front leads to changes of the front velocity across the beam profile. This in turn leads to the breakup of the wavefront and the formation of y-soliton arrays, as in experiment. The latter process develops faster and is more pronounced if a small angle between the pump and WP beams in $y$ plane is introduced (see Figure. B.3). In this case the interference between the WP and pump beams creates initial modulation of polariton density across the $y$ direction, which assist the break-up of polariton wavepacket into a y-soliton array.

# Bibliography


[1] Hartley Jones, M. *A Practical Introduction to Electronic Circuits* (Cambridge University Press, 1995).

[2] Boyd, R. *Nonlinear Optics* (Academic Press, 2003).

[3] Kivshar, Y and Agrawal, G. *Optical Solitons: From Fibers to Photonic Crystals* (Academic Press, 2001).

[4] Agrawal, G. P. *Nonlinear fiber optics* (2001).

[5] Kavokin, A and Baumberg, J, J and Malpuech, G and Laussy, F. P. *Microcavities.* Semiconductor science and technology (Oxford University Press, 2007).

[6] Shor, P. W. Polynomial-Time Algorithms for Prime Factorization and Discrete Logarithms on a Quantum Computer. *SIAM Journal on Computing* **26**, 1484-1509 (1997).

[7] Sich, M. *et al.* Observation of bright polariton solitons in a semiconductor microcavity. *Nature Photonics* **6**, 50-55 (2012).

[8] Chana, J. K. *et al.* Spatial Patterns of Dissipative Polariton Solitons in Semiconductor Microcavities. *Physical Review Letters* **115**, 256401 (2015).

[9] Pekar, S. I. Theory of electromagnetic waves in a crystal in which excitons arise. *J. Exp. Teor. Fiz. USSR* **33**, 1022-1036 (1957).

[10] Hopfield, J. Theory of the Contribution of Excitons to the Complex Dielectric Constant of Crystals. *Physical Review* **112** (1958).

[11] Knoester, J. Optical Dynamics in Crystal Slabs: Crossover from Superradiant Excitons to Bulk Polaritons. *Physical Review Letters* **68**, 654-657 (1992).

[12] Weisbuch, C., Nishioka, M., Ishikawa, A. & Arakawa, Y. Observation of the Coupled Exciton-Photon Mode Splitting in a Semiconductor Quantum Microcavity. *Phys. Rev. Lett.* 3314-3317 (1992).

[13] Agrawal, G. P. *Fiber-Optic Communications Systems, Third Edition.*, vol. 6 (2002).

[14] Baxter, D. *et al.* Polarization-dependent phenomena in the reflectivity spectra of semiconductor quantum microcavities. *Phys. Rev. B* **56**, R10032-R10035 (1997).

[15] Panzarini, G. *et al.* Exciton-light coupling in single and coupled semiconductor microcavities: Polariton dispersion and polarization splitting. *Physical Review B* **59**, 5082-5089 (1999).

[16] Keeling, J. & Berloff, N. G. Exciton-polariton condensation. *Contemporary Physics* **52**, 131-151 (2011).

[17] Byrnes, T., Kim, N. Y. & Yamamoto, Y. Exciton-polariton condensates. *Nature Physics* **10**, 803-813 (2014).

[18] Egorov, O. A., Skryabin, D. V. & Lederer, F. Nonlinear Photonics and Novel Optical Phenomena **170**, 171-193 (2012).

[19] Tosi, G. *et al.* Geometrically locked vortex lattices in semiconductor quantum fluids. *Nature Communications* **3**, 1243 (2012).

[20] Hivet, R. *et al.* Interaction-shaped vortex-antivortex lattices in polariton fluids. *Physical Review B* **89**, 134501 (2014).

[21] Shelykh, I. A., Kavokin, A. V., Rubo, Y. G., Liew, T. C. H. & Malpuech, G. Polariton polarization-sensitive phenomena in planar semiconductor microcavities. *Semiconductor Science and Technology* **25**, 13001 (2010).

[22] Walker, P. M. *et al.* Exciton polaritons in semiconductor waveguides. *Applied Physics Letters* **102**, 012109 (2013).

[23] Dufferwiel, S. *et al.* Strong exciton-photon coupling in open semiconductor microcavities. *Applied Physics Letters* **104**, 2-5 (2014).

[24] Dufferwiel, S. *et al.* Exciton-polaritons in van der Waals heterostructures embedded in tunable microcavities. *Nature Communications* **6**, 8579 (2015).

[25] Shimada, R., Xie, J., Avrutin, V., Ozgur, U. & Morkoc, H. Cavity polaritons in ZnO-based hybrid microcavities. *Applied Physics Letters* **92**, 011127 (2008).

[26] Christopoulos, S. *et al.* Room-Temperature Polariton Lasing in Semiconductor Microcavities. *Physical Review Letters* **98**, 126405 (2007).

[27] D. G. Lidzey *et al.* Strong excitonphoton coupling in an organic semiconductor microcavity. *Letters To Nature* 53-55 (1998).

[28] Feynman, R. P., Leighton, R. B. & Sands, M. *The Feynman Lectures on Physics* (Addison-Wesley Publishing Company, 1965).

[29] Ciuti, C., Savona, V., Piermarocchi, C., Quattropani, A. & Schwendimann, P. Role of the exchange of carriers in elastic exciton-exciton scattering in quantum wells. *Physical Review B* **58**, 7926-7933 (1998).

[30] Vladimirova, M. *et al.* Polariton-polariton interaction constants in microcavities. *Physical Review B* **82**, 075301 (2010).

[31] Glazov, M. M. *et al.* Polariton-polariton scattering in microcavities: A microscopic theory. *Phys. Rev. B* **80**, 1-14 (2009).

[32] Vishnevsky, D. V. & Laussy, F. Effective attractive polariton-polariton interaction mediated by an exciton reservoir. *Physical Review B* **90**, 035413 (2014).

[33] Tassone, F. & Yamamoto, Y. Exciton-exciton scattering dynamics in a semiconductor microcavity and stimulated scattering into polaritons. *Physical Review B* **59**, 10830-10842 (1999).

[34] Schmitt-Rink, S., Chemla, D. S. & Miller, D. A. B. Theory of transient excitonic optical nonlinearities in semiconductor quantum-well structures. *Physical Review B* **32**, 6601-6609 (1985).

[35] Khitrova, G., Gibbs, H. M., Jahnke, F., Kira, M. & Koch, S. W. Nonlinear optics of normal-mode-coupling semiconductor microcavities. *Reviews of Modern Physics* **71**, 1591-1639 (1999).

[36] Wertz, E. *et al.* Spontaneous formation and optical manipulation of extended polariton condensates. *Nature Physics* **6**, 860-864 (2010).

[37] Tartakovskii, A. I., Kulakovskii, V. D., Forchel, A. & Reithmaier, J. P. Exciton-photon coupling in photonic wires. *Physical Review B* **57**, 6807-6810 (1998).

[38] Dasbach, G., Schwab, M., Bayer, M., Krizhanovskii, D. & Forchel, A. Tailoring the polariton dispersion by optical confinement: Access to a manifold of elastic polariton pair scattering channels. *Physical Review B* **66**, 201201 (2002).

[39] Lecomte, T. *et al.* Optical parametric oscillation in one-dimensional microcavities. *Physical Review B* **87**, 155302 (2013).

[40] Kuther, A. *et al.* Confined optical modes in photonic wires. *Physical Review B* **58**, 15744-15748 (1998).

[41] Cerda-Méndez, E. *et al.* Polariton Condensation in Dynamic Acoustic Lattices. *Physical Review Letters* **105**, 1-4 (2010).

[42] Lai, C. W. *et al.* Coherent zero-state and pi-state in an exciton-polariton condensate array. *Nature* **450**, 529-32 (2007).

[43] Cerda-Méndez, E. *et al.* Dynamic exciton-polariton macroscopic coherent phases in a tunable dot lattice. *Physical Review B* **86**, 100301 (2012).

[44] de Lima, M., van der Poel, M., Santos, P. & Hvam, J. Phonon-Induced Polariton Superlattices. *Physical Review Letters* **97**, 045501 (2006).

[45] Bogoliubov, N. On the theory of superfluidity *. *Journal of Physics* **XI**, 23-32 (1947).

[46] Penrose, O. & Onsager, L. Bose-einstein condensation and liquid helium. *Physical Review* **104**, 576-584 (1956).

[47] Yang, C. Concept of Off-Diagonal Long-Range Order and the Quantum Phases of Liquid He and of Superconductors. *Reviews of Modern Physics* **34**, 694 (1962).

[48] Anderson, M. H., Ensher, J. R., Matthews, M. R., Wieman, C. E. & Cornell, E. A. Observation of bose-einstein condensation in a dilute atomic vapor. *Science (New York, N.Y.)* **269**, 198-201 (1995).

[49] Butov, L. V., Lai, C. W., Ivanov, A. L., Gossard, A. C. & Chemla, D. S. Towards Bose-Einstein condensation of excitons in potential traps. *Nature* **417**, 47-52 (2002).

[50] Butov, L. V., Gossard, A. C. & Chemla, D. S. Macroscopically ordered state in an exciton system. *Nature* **418**, 751-754 (2002).

[51] Byrnes, T., Wen, K. & Yamamoto, Y. Macroscopic quantum computation using Bose-Einstein condensates. *Physical Review A* **85**, 040306 (2012).

[52] Sanvitto, D. *et al.* Persistent currents and quantized vortices in a polariton superfluid. *Nature Physics* **6**, 527-533 (2010).

[53] Liew, T., Shelykh, I. & Malpuech, G. Polaritonic devices. *Physica E: Low-dimensional Systems and Nanostructures* **43**, 1543-1568 (2011).

[54] Amo, A. *et al.* Superfluidity of polaritons in semiconductor microcavities. *Nature Physics* **5**, 805 (2009).

[55] Amo, A. *et al.* Polariton superfluids reveal quantum hydrodynamic solitons. *Science (New York, N.Y.)* **332**, 1167-70 (2011).

[56] Savvidis, P. *et al.* Angle-resonant stimulated polariton amplifier. *Physical Review Letters* **84**, 1547-50 (2000).

[57] Baumberg, J. *et al.* Parametric oscillation in a vertical microcavity: A polariton condensate or micro-optical parametric oscillation. *Phy. Rev. B* **62**, R16247-R16250 (2000).

[58] Stevenson, R. *et al.* Continuous wave observation of massive polariton redistribution by stimulated scattering in semiconductor microcavities. *Phys. Review Lett.* **85**, 3680-3 (2000).

[59] Kasprzak, J. *et al.* Bose-Einstein condensation of exciton polaritons. *Nature* **443**, 409-14 (2006).

[60] Tassone, F. & Schwendimann, P. Bottleneck effects in the relaxation and photoluminescence of microcavity polaritons. *Physical Review B* **56**, 7554-7563 (1997).

[61] Tartakovskii, A. *et al.* Relaxation bottleneck and its suppression in semiconductor microcavities. *Physical Review B* **62**, R2283-R2286 (2000).

[62] Christmann, G. *et al.* Oscillatory solitons and time-resolved phase locking of two polariton condensates. *New Journal of Physics* **16**, 103039 (2014).

[63] Cristofolini, P. *et al.* Optical Superfluid Phase Transitions and Trapping of Polariton Condensates. *Physical Review Letters* **110**, 186403 (2013).

[64] Krizhanovskii, D. *et al.* Dominant Effect of Polariton-Polariton Interactions on the Coherence of the Microcavity Optical Parametric Oscillator. *Physical Review Letters* **97**, 097402 (2006).

[65] Baas, A., Karr, J., Eleuch, H. & Giacobino, E. Optical bistability in semiconductor microcavities. *Physical Review A* **69**, 023809 (2004).

[66] Gippius, N. A., Tikhodeev, S. G., Kulakovskii, V. D., Krizhanovskii, D. N. & Tartakovskii, A. I. Nonlinear dynamics of polariton scattering in semiconductor microcavity: Bistability vs. stimulated scattering. *Europhys. Lett.* **67**, 997-1003 (2004).

[67] Krizhanovskii, D. *et al.* Self-organization of multiple polariton-polariton scattering in semiconductor microcavities. *Physical Review B* **77**, 115336 (2008).

[68] London, F. On the bose-einstein condensation. *Physical Review* **54**, 947-954 (1938).

[69] Amo, A. *et al.* Collective fluid dynamics of a polariton condensate in a semiconductor microcavity. *Nature* **457**, 291-5 (2009).

[70] Wouters, M. & Carusotto, I. Excitations in a Nonequilibrium Bose-Einstein Condensate of Exciton Polaritons. *Physical Review Letters* **99**, 140402 (2007).

[71] Utsunomiya, S. *et al.* Observation of Bogoliubov excitations in exciton-polariton condensates. *Nature Physics* **4**, 700-705 (2008).

[72] Lagoudakis, K. G. *et al.* Quantized vortices in an exciton-polariton condensate. *Nature Physics* **4**, 706-710 (2008).

[73] Krizhanovskii, D. N. *et al.* Effect of Interactions on Vortices in a Nonequilibrium Polariton Condensate. *Physical Review Letters* **104**, 126402 (2010).

[74] Roumpos, G. *et al.* Single vortex-antivortex pair in an exciton-polariton condensate. *Nature Physics* **7**, 129-133 (2011).

[75] Lagoudakis, K. G. *et al.* Observation of half-quantum vortices in an exciton-polariton condensate. *Science (New York, N.Y.)* **326**, 974-6 (2009).

[76] Flayac, H., Solnyshkov, D. D., Shelykh, I. A. & Malpuech, G. Transmutation of Skyrmions to Half-Solitons Driven by the Nonlinear Optical Spin Hall Effect. *Physical Review Letters* **110**, 016404 (2013).

[77] Manni, F., Léger, Y., Rubo, Y. G., André, R. & Deveaud, B. Hyperbolic spin vortices and textures in exciton-polariton condensates. *Nature Communications* **4**, 2590 (2013).

[78] Pigeon, S., Carusotto, I. & Ciuti, C. Hydrodynamic nucleation of vortices and solitons in a resonantly excited polariton superfluid. *Physical Review B* **83**, 144513 (2011).

[79] Kim, N. Y. *et al.* Dynamical d-wave condensation of exciton-polaritons in a two-dimensional square-lattice potential. *Nature Physics* **7**, 681-686 (2011).

[80] Cerda-Méndez, E. A. *et al.* Wavefunction of polariton condensates in a tunable acoustic lattice. *New Journal of Physics* **14**, 075011 (2012).

[81] Cerda-Méndez, E. A. *et al.* Exciton-Polariton Gap Solitons in Two-Dimensional Lattices. *Physical Review Letters* **111**, 146401 (2013).

[82] Russell, J. Report on waves. *Rep. Br. Ass. Advmt Sci.* **14**, 311-390 plus plates XLVII-LVII (1845).

[83] Bykov, V. Nonlinear waves and solitons in models of fault block geological media. *Russian Geology and Geophysics* **56**, 793-803 (2015).

[84] Pang, X.-f. The theory of bio-energy transport in the protein molecules and its properties. *Physics of life reviews* **8**, 264-86 (2011).

[85] Song, T. The function of soliton on bio-energy transport in the protein molecules. Comment on "The theory of bio-energy transport in the protein molecules and its properties" by Xiao-feng Pang. *Physics of Life Reviews* **8**, 191-292 (2011).

[86] Boskovic, A., Chernikov, S. V., Taylor, J. R., Gruner-Nielsen, L. & Levring, O. A. Direct continuous-wave measurement of n(2) in various types of telecommunication fiber at 1.55 microm. *Optics letters* **21**, 1966-1968 (1996).

[87] Yulin, A., Egorov, O., Lederer, F. & Skryabin, D. Dark polariton solitons in semiconductor microcavities. *Physical Review A* **78**, 061801 (2008).

[88] Amo, A. *et al.* Exciton-polariton spin switches. *Nature Photonics* **4**, 361-366 (2010).

[89] Walker, P. M. *et al.* Ultra-low-power hybrid light-matter solitons. *Nature Communications* **6**, 8317 (2015).

[90] Mollenauer, L. F., Stolen, R. H. & Gordon, J. P. Experimental observation of picosecond pulse narrowing and solitons in optical fibers. *Physical Review Letters* **45**, 1095-1098 (1980).

[91] Hasegawa, A. An historical review of application of optical solitons for high speed communications. *Chaos* **10**, 475-485 (2000).

[92] Ranka, J. K., Windeler, R. S. & Stentz, A. J. Visible continuum generation in air-silica microstructure optical fibers with anomalous dispersion at 800 nm. *Optics letters* **25**, 25-27 (2000).

[93] Liu, X. *et al.* Soliton self-frequency shift in a short tapered air-silica microstructure fiber. *Optics letters* **26**, 358-360 (2001).

[94] Egorov, O., Skryabin, D., Yulin, A. & Lederer, F. Bright Cavity Polariton Solitons. *Physical Review Letters* **102**, 153904 (2009).

[95] Wai, P. K., Menyuk, C. R., Chen, H. H. & Lee, Y. C. Soliton at the zero-group-dispersion wavelength of a single-model fiber. *Optics letters* **12**, 628-630 (1987).

[96] Akhmediev, N. & Karlsson, M. Cherenkov radiation emitted by solitons in optical fibers. *Physical Review A* **51**, 2602-2607 (1995).

[97] Zakharov, V. & Shabat, A. Exact theory of two-dimensional self-focussing and one-dimensional self-modulation of waves in non-linear media. *Soviet Phsyics JETP* **34**, 62-69 (1972).

[98] Kodama, Y. & Hasegawa, A. Nonlinear pulse propagation in a monomode dielectric guide. *IEEE Journal of Quantum Electronics* **23**, 510-524 (1987).

[99] Bennink, R. *et al.* Honeycomb Pattern Formation by Laser-Beam Filamentation in Atomic Sodium Vapor. *Physical Review Letters* **88**, 113901 (2002).

[100] Gordon, J. P. Interaction forces among solitons in optical fibers. *Optics letters* **8**, 596-598 (1983).

[101] Aitchison, J. S. *et al.* Experimental observation of spatial soliton interactions. *Optics letters* **16**, 15-7 (1991).

[102] Mitschke, F. M. & Mollenauer, L. F. Experimental observation of interaction forces between solitons in optical fibers. *Optics letters* **12**, 355-357 (1987).

[103] Shalaby, M., Reynaud, F. & Barthelemy, A. Experimental observation of spatial soliton interactions with a $\pi/2$ relative phase difference. *Optics Letters* **17**, 778 (1992).

[104] Strecker, K. E., Partridge, G. B., Truscott, A. G. & Hulet, R. G. Formation and propagation of matter-wave soliton trains. *Nature* **417**, 150-3 (2002).

[105] Al Khawaja, U., Stoof, H., Hulet, R., Strecker, K. & Partridge, G. Bright Soliton Trains of Trapped Bose-Einstein Condensates. *Phys. Rev. Lett.* **89**, 200404 (2002).

[106] Nguyen, J. H. V., Dyke, P., Luo, D., Malomed, B. A. & Hulet, R. G. Collisions of matter-wave solitons. *Nature Physics* **10**, 1-5 (2014).

[107] Birks, T. A., Wadsworth, W. J. & Russell, P. S. Supercontinuum generation in tapered fibers. *Optics letters* **25**, 1415-1417 (2000).

[108] Husakou, A. V. & Herrmann, J. Supercontinuum generation of higher-order solitons by fission in photonic crystal fibers. *Physical review letters* **87**, 203901 (2001).

[109] Herrmann, J. *et al.* Experimental Evidence for Supercontinuum Generation by Fission of Higher-Order Solitons in Photonic Fibers. *Phys. Rev. Lett.* **88**, 173901 (2002).

[110] Aitchison, A. *et al.* Observation of spatial optical solitons in a nonlinear glass waveguide. *Optics Letters* **15**, 471-473 (1990).

[111] Khitrova, G. *et al.* Spatial Solitons in a Self-Focusssing Semiconductor Gain Medium. *Phys. Rev. Lett.* **70**, 920-924 (1993).

[112] Kutsche, C. *et al.* Self-guiding Effects in Semiconductor Waveguide Amplifiers. *Proc. SPIE 3384, Photonic Processing Technology and Applications II* **3384**, 153-160 (1998).

[113] Mendoza-Alvarez, J. G. & Nunes, F. D. & Patel, N. B. Refractive index dependence on free carriers for GaAs. *Journal of Applied Physics* **51**, 4365 (1980).

[114] Ultanir, E. *et al.* Stable Dissipative Solitons in Semiconductor Optical Amplifiers. *Phys. Rev. Lett* **90**, 253903 (2003).

[115] Khaykovich, L. *et al.* Formation of a matter-wave bright soliton. *Science (New York, N.Y.)* **296**, 1290-3 (2002).

[116] Tiesinga, E., Verhaar, B. J. & Stoof, H. T. C. Threshold and resonance phenomena in ultracold ground-state collisions. *Physical Review A* **47**, 4114-4122 (1993).

[117] Sich, M., Skryabin, D. V. & Krizhanovskii, D. N. Soliton physics with semiconductor exciton-polaritons in confined systems. *In preparation, C. R. Physique* (2016).

[118] Taranenko, V., Weiss, C. & Schäpers, B. From coherent to incoherent hexagonal patterns in semiconductor resonators. *Physical Review A* **65**, 013812 (2001).

[119] Taranenko, V., Ahlers, F. & Pierz, K. Coherent switching of semiconductor resonator solitons. *Applied Physics B* **75**, 75-77 (2002).

[120] Taranenko, V. B., Slekys, G. & Weiss, C. O. Spatial Resonator Solitons. *Dissipative Solitons* **13**, 777 (2003).

[121] Barland, S., Tredicce, J. R. & Brambilla, M. Cavity solitons as pixels in semiconductor microcavities. *Nature* **419**, 699-702 (2002).

[122] Pedaci, F. *et al.* All-optical delay line using semiconductor cavity solitons. *Applied Physics Letters* **92**, 011101 (2008).

[123] Sich, M. *et al.* Effects of Spin-Dependent Interactions on Polarization of Bright Polariton Solitons. *Physical Review Letters* **112**, 046403 (2014).

[124] Rogel-Salazar, J. The Gross-Pitaevskii equation and Bose-Einstein condensates. *European Journal of Physics* **34**, 247-257 (2013).

[125] Egorov, O., Gorbach, A., Lederer, F. & Skryabin, D. Two-Dimensional Localization of Exciton Polaritons in Microcavities. *Physical Review Letters* **105**, 11-14 (2010).

[126] Egorov, O. A., Skryabin, D. V. & Lederer, F. Parametric polariton solitons in coherently pumped semiconductor microcavities. *Physical Review B* **84**, 165305 (2011).

[127] Fu, Y., Zhang, W. & Wu, X. Polarization-dependent solitons in the strong coupling regime of semiconductor microcavities. *Chaos, Solitons & Fractals* **81**, 345-350 (2015).

[128] Liew, T., Kavokin, A. & Shelykh, I. Optical Circuits Based on Polariton Neurons in Semiconductor Microcavities. *Physical Review Letters* **101**, 016402 (2008).

[129] Gippius, N. *et al.* Polarization Multistability of Cavity Polaritons. *Physical Review Letters* **98**, 236401 (2007).

[130] Gavrilov, S., Gippius, N. A., Tikhodeev, S. G. & Kulakovskii, V. D. Multistability of the optical response in a system of quasi-two-dimensional exciton polaritons. *J. Exp. Theor. Phys* **110**, 825 (2010).

[131] Gavrilov, S. S. *et al.* Polarization instability in a polariton system in semiconductor microcavities. *J. Exp. Theor. Phys Lett.* **92**, 171 (2010).

[132] Paraiso, T., Wouters, M., Leger, Y., Morier-Genou, F. & Deveaud-Pledran, B. Multistability of a coherent spin ensemble in a semiconductor microcavity. *Nature Materials* **9**, 655 (2010).

[133] Wouters, M. *et al.* Influence of a nonradiative reservoir on polariton spin multistability. *Physical Review B* **87**, 045303 (2013).

[134] Cerna, R. *et al.* Ultrafast tristable spin memory of a coherent polariton gas. *Nature communications* **4**, 2008 (2013).

[135] Gavrilov, S. S. *et al.* Spin multistability of cavity polaritons in a magnetic field. *Physical Review B* **87**, 201303 (2013).

[136] Espinosa-Ortega, T. & Liew, T. C. H. Complete architecture of integrated photonic circuits based on and and not logic gates of exciton polaritons in semiconductor microcavities. *Physical Review B* **87**, 195305 (2013).

[137] Sarkar, D. *et al.* Polarization Bistability and Resultant Spin Rings in Semiconductor Microcavities. *Physical Review Letters* **105**, 216402 (2010).

[138] Gao, T. *et al.* Polariton condensate transistor switch. *Phys. Rev. B* **85**, 235102 (2012).

[139] Sturm, C. *et al.* All-optical phase modulation in a cavity-polariton Mach-Zehnder interferometer. *Nature communications* **5**, 3278 (2014).

[140] Antón, C. *et al.* Quantum reflections and shunting of polariton condensate wave trains: Implementation of a logic AND gate. *Physical Review B* **88**, 245307 (2013).

[141] Cancellieri, E. *et al.* Logic Gates with Bright Dissipative Polariton Solitons in Bragg-Cavity Systems. *Phys. Rev. B* **92**, 174528 (2015).

[142] Cilibrizzi, P. *et al.* Linear wave dynamics explains observations attributed to dark-solitons in a polariton quantum fluid *Phys. Rev. Lett.* **113**, 103901 (2014) Reply *Phys. Rev. Lett.* **115**, 089402 (2015)

[143] Amo, A. *et al.* Comment on Linear Wave Dynamics Explains Observations Attributed to Dark Solitons in a Polariton Quantum Fluid. *Phys. Rev. Lett.* **115**, 089401 (2015).

[144] Pinsker, F. & Flayac, H. On-Demand Dark Soliton Train Manipulation in a Spinor Polariton Condensate. *Phys. Rev. Lett.* **112**, 140405 (2014).

[145] Flayac, H., Solnyshkov, D. D. & Malpuech, G. Oblique half-solitons and their generation in exciton-polariton condensates. *Physical Review B - Condensed Matter and Materials Physics* **83**, 2-5 (2011).

[146] Hivet, R. *et al.* Half-solitons in a polariton quantum fluid behave like magnetic monopoles. *Nature Physics* **8**, 724-728 (2012).

[147] Gorbach, A., Malomed, B. & Skryabin, D. Gap polariton solitons. *Physics Letters A* **373**, 3024-3027 (2009).

[148] Eiermann, B. *et al.* Bright Bose-Einstein Gap Solitons of Atoms with Repulsive Interaction. *Physical Review Letters* **92**, 1-4 (2004).

[149] Fleischer, J. W., Segev, M., Efremidis, N. K. & Christodoulides, D. N. Observation of two-dimensional discrete solitons in optically induced nonlinear photonic lattices. *Nature* **422**, 147-50 (2003).

[150] Tanese, D. *et al.* Polariton condensation in solitonic gap states in a one-dimensional periodic potential. *Nature communications* **4**, 1749 (2013).

[151] Fox, M. *Quantum Optics: An Introduction.* Oxford Master Series in Physics (Oxford University Press, 2006).

[152] Loudon, R. *The Quantum Theory of Light* (Oxford University Press, 2000), 3rd edn.

[153] Hilico, L. *et al.* Squeezing with \Chiˆ{3} Materials. *Applied Physics B: Lasers and Optics* **55**, 202-209 (1992).

[154] Karr, J. P., Bass, A., Houdré, R. & Giacobino, E. Squeezing in semiconductor microcavities in the strong-coupling regime. *Physical Review A - Atomic, Molecular, and Optical Physics* **69**, 031802-1 (2004).

[155] Bamba, M., Pigeon, S. & Ciuti, C. Quantum squeezing generation versus photon localization in a disordered planar microcavity. *Phys. Rev. Lett.* **104**, 1-4 (2010).

[156] Boulier, T. *et al.* Polariton-generated intensity squeezing in semiconductor micropillars. *Nature communications* **5**, 3260 (2014).

[157] Braunstein, S. L. & van Loock, P. Quantum information with continuous variables. *Reviews of Modern Physics* **77**, 513 (2005).

[158] Anton, C. *et al.* Dynamics of a polariton condensate transistor switch. *Applied Physics Letters* **101**, 261116 (2012).

[159] Ballarini, D. *et al.* All-optical polariton transistor. *Nature Commun.* **4**, 1778 (2013).

[160] Berrada, T. *et al.* Integrated Mach-Zehnder interferometer for Bose-Einstein condensates. *Nature Communications* **4**, 1-8 (2013).

[161] Solnyshkov, D. D., Bleu, O. & Malpuech, G. All optical Controlled-NOT gate based on an exciton-polariton circuit. *Superlattices and Microstructures* **83**, 466-475 (2015).

[162] Melnikov, I. V. & Aitchison, J. S. Gap soliton memory in a resonant photonic crystal. *Applied Physics Letters* **87**, 201111 (2005).

[163] Rudolph, J., Hey, R. & Santos, P. Long-Range Exciton Transport by Dynamic Strain Fields in a GaAs Quantum Well. *Physical Review Letters* **99**, 047602 (2007).

[164] Rocke, C. *et al.* Acoustically Driven Storage of Light in a Quantum Well. *Physical Review Letters* **78**, 4099-4102 (1997).

[165] Vurgaftman, I., Meyer, J. R. & Ram-Mohan, L. R. Band parameters for III-V compound semiconductors and their alloys. *Journal of Applied Physics* **89**, 5815 (2001).

[166] Aßmann, M. *et al.* Measuring the dynamics of second-order photon correlation functions inside a pulse with picosecond time resolution. *Optics Express* **18**, 20229 (2010).

[167] Krizhanovskii, D. N. *et al.* Effect of polariton-polariton interactions on the excitation spectrum of a nonequilibrium condensate in a periodic potential. *Physical Review B* **87**, 155423 (2013).

[168] Shilton, J. M. *et al.* High-frequency single-electron transport in a quasi-one-dimensional GaAs channel induced by surface acoustic waves. *Journal of Physics: Condensed Matter* **8**, L531-L539 (1996).

[169] Pedros, J. *et al.* Surface acoustic waves in liquid helium for enhanced single-electron transport applications. *IEEE International Ultrasonics Symposium, IUS* 2-5 (2012).

[170] Yahagi, Y., Harteneck, B., Cabrini, S. & Schmidt, H. Control of the magnetization dynamics in patterned nanostructures with magnetoelastic coupling. In *Photonic and Phononic Properties of Engineered Nanostructures V*, vol. 9371 of *Proceedings of SPIE*, 937110 (SPIE, 2015).

[171] Kryshtal, R. G. & Medved, A. V. Surface acoustic wave in yttrium iron garnet as tunable magnonic crystals for sensors and signal processing applications. *Applied Physics Letters* **100** (2012).

[172] Mah, C. & Thurbide, K. B. Acoustic methods of detection in gas chromatography. *Journal of Separation Science* **29**, 1922-1930 (2006).

[173] Länge, K., Rapp, B. E. & Rapp, M. Surface acoustic wave biosensors: A review. *Analytical and Bioanalytical Chemistry* **391**, 1509-1519 (2008).

[174] Skryabin, D. V. & Gorbach, A. V. Colloquium: Looking at a soliton through the prism of optical supercontinuum. *Reviews of Modern Physics* **82**, 1287-1299 (2010).

[175] Anton, C. *et al.* Role of supercurrents on vortices formation in polariton condensates. *Optics Express* **20**, 16366 (2012).

[176] Carr, L. D., Clark, C. W. & Reinhardt, W. P. Stationary solutions of the one-dimensional nonlinear Schrodinger equation. I. Case of repulsive nonlinearity. *Physical Review A* **62**, 063610 (2000).

[177] Carr, L. D., Clark, C. W. & Reinhardt, W. P. Stationary solutions of the one-dimensional nonlinear Schrodinger equation. II. Case of attractive nonlinearity. *Physical Review A* **62**, 063611 (2000).

[178] Koashi, M., Kono, K., Hirano, T. & Matsuoka, M. Photon antibunching in pulsed squeezed light generated via parametric amplification. *Physical Review Letters* **71**, 1164-1167 (1993).

[179] Ferrier, L. *et al.* Interactions in Confined Polariton Condensates. *Physical Review Letters* **106**, 126401 (2011).

[180] Dasbach, G. *et al.* Enhancement of the exciton exchange energy splitting by the confined light field in strained microcavities. *Physica E-Low-Dimensional Systems & Nanostructures* **13**, 394-397 (2002).